UNIVERSITY OF OKLAHOMA

GRADUATE COLLEGE

SURFACE AND INTERFACIAL ENGINEERING IN REVERSIBLE PROTONIC CERAMIC CELLS FOR ELECTROCHEMICAL ENERGY CONVERSION

A DISSERTATION

SUBMITTED TO THE GRADUATE FACULTY

in partial fulfillment of the requirements for the

Degree of

DOCTOR OF PHILOSOPHY

By SHUANGLIN ZHENG

Norman, Oklahoma

2026

Downloaded from SHAREOK. Persistent Handle URL: https://hdl.handle.net/11244/342534

SURFACE AND INTERFACIAL ENGINEERING IN REVERSIBLE PROTONIC CERAMIC CELLS FOR ELECTROCHEMICAL ENERGY CONVERSION

A DISSERTATION APPROVED FOR THE
SCHOOL OF AEROSPACE AND MECHANICAL ENGINEERING

BY THE COMMITTEE CONSISTING OF

Dr. Hanping Ding, Chair

Dr. Yingtao Liu

Dr. Iman Ghamarian

Dr. Jivtesh Garg

Dr. Binbin Weng

©Copyright by SHUANGLIN ZHENG 2026
All Rights Reserved.

Acknowledgement

This doctoral journey has been one of the most demanding and meaningful seasons of my life. It taught me how to think with rigor, how to endure uncertainty, and how to keep moving forward when results were slow, instruments failed, and confidence felt fragile. More than anything, it reminded me that a dissertation is never written by one person alone. It is built day by day through guidance, patience, friendship, and love from many people, and I am deeply grateful to everyone who carried me to the finish line.

First and foremost, I would like to express my sincerest gratitude to my advisor, Dr. Hanping Ding. Thank you for believing in me from the beginning and for giving me the freedom to grow into an independent researcher. Your standards pushed me to become more careful, more creative, and more resilient. You taught me how to see the "story" behind the data, how to turn setbacks into clarity, and how to pursue work that truly matters. I am especially thankful for your patience through the long nights of troubleshooting, the countless revisions, and the moments when progress felt impossible. Your mentorship shaped not only this dissertation, but also the kind of scientist and person I hope to become.

I am grateful to my lab family, who made the hardest days lighter and the best days unforgettable. To Dr. Idris Temitope Bello, thank you for your example of discipline and professionalism and for always being willing to share your experience. To Anshu, thank you for your generosity, kindness, and the steady support that made the lab feel like a safe place even under pressure. To Saroj, thank you for your thoughtful help, your consistency, and your ability to keep things moving forward when everything felt stuck. And to my best helper, Sooraj from Dr. Iman Ghamarian's group, thank you for being the kind of teammate everyone hopes for—reliable, sharp, and always ready to step in when I needed help.

I would like to thank my dissertation committee for their time, guidance, and support: Dr. Yingtao Liu, Dr. Iman Ghamarian, Dr. Jivtesh Garg, and Dr. Binbin Weng. Thank you for your thoughtful feedback, your careful questions, and your willingness to help me strengthen both the science and the direction of this work. Your encouragement and high expectations challenged me to refine my thinking and communicate my research with greater clarity and confidence.

I also sincerely appreciate the additional support from colleagues beyond my department. I am grateful to the Department of Chemistry, especially Dr. John Peters, for valuable input and assistance that contributed to this dissertation. I would also like to thank Dr. Thirumalai Venkatesan and the Center for Quantum Research and Technology for their support and collaboration. The help I received from these groups broadened the capabilities of this work and reminded me how powerful interdisciplinary science can be.

To the leadership, faculty, and staff who built the environment that made this research possible, I am truly thankful. I want to acknowledge all GCoE faculty and staff, and especially Dr. John Kiler, Dean, and Dr. Zahed Siddique, Dean for Research, for their support of research and graduate training.

I am also grateful to all AME faculty and staff for the resources, guidance, and daily help that keeps everything running. In particular, I want to thank Dr. Wilson Merchan-Merchan, who—besides my advisor—was the first person to introduce me to the School of AME and help me feel welcomed as I began this journey. Thank you for your kindness and the early support that made a lasting difference. I also thank Dr. Parthasarathy for your leadership as Director. To Samarpita and Aaron, thank you for your care and efficiency as student service and administration coordinators—your help solved so many problems before they became stressful. And to Greg, thank you for always offering help on the mechanical supply side. I also want to take a moment to remember Billy. His kindness, presence, and the support he gave so generously meant more than words can fully express, and he will always be remembered and missed. I gratefully acknowledge the support from the CMEI Office-U.S. Department of Energy, the University of Oklahoma and Idaho National Laboratory, whose funding, resources, and institutional support made this research possible.

Finally, none of this would have been possible without my parents, thank you for your unconditional love, your sacrifices, and your faith in me, even when you were far away and could not see what my daily life looked like. When I was exhausted, uncertain, or discouraged, I carried your support with me. This dissertation is as much yours as it is mine.

To everyone who supported me, through advice, assistance, encouragement, or simple kindness, thank you. I will carry your generosity forward, and I will always remember that this milestone was reached together.

Abstract

Protonic ceramic electrochemical cells (PCCs)—operating reversibly as protonic ceramic fuel cells (PCFCs) for power generation and protonic ceramic electrolysis cells (PCECs) for hydrogen production—offer an attractive pathway for efficient, solid-state energy conversion in the intermediate-temperature regime (≈400–600 °C). By transporting protons through a dense ceramic electrolyte, PCCs provide a unique coupling between electricity and hydrogen that can enable reversible "power-to-gas" and "gas-to-power" operation within a single device platform. This reversibility is especially compelling for renewable energy integration and long-duration storage, where the ability to switch efficiently between electrical output and fuel generation can mitigate intermittency and improve system flexibility. Compared with conventional oxide-ion solid oxide cells, PCCs can reduce thermomechanical stress and expand materials compatibility by operating at lower temperatures; compared with low-temperature electrochemical devices, they can benefit from enhanced reaction kinetics and broadened oxide-based catalyst options that become viable at intermediate temperatures. Despite this promise, practical PCC deployment remains constrained by oxygen-side polarization and durability challenges under steam-rich and high-current conditions—conditions that are intrinsic to electrolysis and to reversible cycling.

In protonic systems, oxygen-electrode reactions are intrinsically proton-coupled: in fuel-cell mode, oxygen is reduced and reacts with protons to form water predominantly at the oxygen electrode; in electrolysis mode, steam is oxidized at the oxygen electrode to evolve oxygen while generating protons that must be transported through the electrolyte. Consequently, oxygen-electrode performance is governed by the coordinated overlap of (i) gas delivery and product removal through porous microstructures, (ii) electron transport through percolated solid networks, and (iii) proton accessibility to the reaction zone. At intermediate temperatures, where surface exchange and charge-transfer kinetics become more prominent, the oxygen electrode frequently dominates the polarization resistance. Moreover, oxygen-electrode durability is challenged by steam-induced surface reconstruction, nanoparticle coarsening, cation segregation, and defect-driven chemical expansion, all of which can accelerate under high current density and reversible cycling. Compounding these issues, the buried electrode–electrolyte interface often becomes the practical bottleneck: conventional porous electrodes typically contact the dense electrolyte through discontinuous point contacts, creating current constriction, high local overpotential hot spots, and

vulnerability to interfacial reaction-layer growth and delamination. These coupled transport–kinetic–interfacial limitations produce a familiar pattern: impressive initial performance can be achieved by optimizing a single factor, but improvements quickly plateau as the limiting step shifts, and long-term operation reveals degradation pathways that erode the initial gains.

This doctoral dissertation addresses these limitations by developing an integrated oxygen-side design framework that unifies three elements: (1) microstructure engineering and multiscale transport architecture, (2) defect- and redox-enabled catalytic modulation, and (3) electrode–electrolyte interfacial engineering. The central thesis is that high reversible performance and durability cannot be achieved through isolated optimization of composition, porosity, or electrolyte thickness alone, because PCC operation is governed by coupled processes whose limiting step depends on temperature, steam activity, current density, and operating direction. Instead, durable low-polarization operation emerges when gas access, electronic/protonic percolation, surface exchange activity, and interfacial integrity are engineered as a coordinated multiscale system. Within this framework, "activity" is not defined only by intrinsic catalytic chemistry; it is equally defined by accessibility of reaction sites and stability of the defect landscape and interface under steam-rich reversible conditions.

Four studies constitute the technical core of this dissertation, each addressing a different leverage point within the integrated framework while building toward a coherent multiscale strategy. The first study focuses on transport and reaction-zone engineering through a nano-architectured oxygen electrode design that combines high porosity with triple-conducting functionality. In intermediate-temperature PCECs, it is often insufficient to increase intrinsic catalytic activity if gas transport remains limiting or if proton accessibility is confined to a narrow zone adjacent to the electrolyte. The nano-architectured electrode developed in this work is designed to extend the effective reaction zone while maintaining scalable fabrication. By introducing a structure that enhances mass transfer and maintains percolated pathways for charge transport, the oxygen electrode exhibits robust bifunctional performance, achieving a peak power density of 1.50 W cm^{-2} at 600 °C in fuel-cell mode and a current density of 5.04 A cm^{-2} at 1.60 V in electrolysis mode, alongside improved stability under transient operation and thermal cycling. This work establishes a foundational message for PCC electrodes: microstructure is not merely supportive; it actively governs apparent kinetics by controlling the overlap of gas access, charge pathways, and proton

participation, and it strongly influences durability by moderating gradients and avoiding localized hot spots.

The second study advances from architecture to hybrid catalytic modulation, targeting the oxygen electrode's limited active sites and sluggish kinetics under steam. The work introduces a hybrid oxygen electrode architecture based on a $PrNi_{0.7}Co_{0.3}O_{3-\delta}$ (PNC) backbone infused with oxygen-vacancy–rich praseodymium oxide (PrO_x) nanoparticles. This design leverages complementary roles: the backbone provides robust transport continuity and structural stability, while the PrO_x phase supplies vacancy-rich catalytic sites that enhance oxygen adsorption/activation and accelerate proton-coupled ORR/OER kinetics. Beyond simply increasing surface activity, the hybrid design is intended to couple surface and bulk processes so that catalytic enhancement remains effectively utilized throughout operation. Cells incorporating this hybrid oxygen electrode deliver a peak power density of 1.56 W cm^{-2} at 600 °C and achieve 2.25 A cm^{-2} at 1.30 V in electrolysis mode. Importantly, the study emphasizes practical electrolysis metrics: Faradaic efficiency and energy efficiency reach 96.8% and 89.9%, respectively, reflecting effective conversion of charge to hydrogen with minimized parasitic losses. The polarization resistance is substantially reduced (reported as 0.079 Ω cm^2), and the electrode exhibits exceptional thermal cycling stability. This work demonstrates that catalytic improvement in PCCs is most impactful when vacancy chemistry and redox flexibility are introduced in a way that is compatible with transport pathways and stability constraints, thereby narrowing the traditional activity–durability tradeoff.

The third study addresses a widely observed but often underestimated limitation in reversible PCCs: the buried electrode–electrolyte junction. Even when bulk electrolyte conductivity is high and oxygen-electrode surfaces are active, interfacial polarization and interfacial degradation can dominate the loss budget, particularly under high steam activity in electrolysis mode. Conventional porous electrodes frequently form discontinuous contact networks and chemically reactive interfaces, producing constriction resistance and promoting interphase growth and delamination. To overcome this coupled problem, this dissertation develops a pulsed laser deposition (PLD) enabled interfacial nanostructuring strategy that constructs a dense, nanocrystalline $Pr_{0.5}La_{0.5}BaCo_2O_{5+\delta}$ (PLBC) interlayer directly on a chemically robust $BaZr_{0.8}Y_{0.2}O_3$ (BZY) electrolyte. The interlayer forms conformal contact and creates a defect-enriched reaction zone beneath a

porous oxygen electrode, thereby reducing interfacial constriction and stabilizing the junction without sacrificing gas accessibility. Mechanically, the engineered interface increases bonding strength by approximately threefold, demonstrating that interfacial design can simultaneously enhance electrochemical performance and thermomechanical integrity. Electrochemically, the interfacial nanostructuring substantially reduces interfacial polarization, enabling peak power densities of 1.16 W cm^{-2} at 600 °C, and critically supports long-term steam electrolysis stability for ~1000 h under 0.3–0.7 atm steam, maintaining stable operando impedance at 1.30 V with Faradaic efficiency exceeding 92%. This work establishes that controlling the interface is not a secondary refinement but a primary route to durable reversibility, particularly when paired with chemically robust electrolytes such as BZY where long-term stability and interface compatibility are central goals.

The fourth study integrates the dissertation's multiscale logic most fully by coupling hierarchical architecture with a chemically active, redox-buffered interphase, aiming to stabilize oxygen electrocatalysis under steam while maintaining high reversible performance. A three-dimensional, mesh-like PNC scaffold is conformally integrated with a vacancy-rich PrO_x nanophase, producing both an extended reaction zone and an interphase that enables vacancy–redox coupling between Pr and Co. This coupling is proposed to buffer local oxygen chemical potential swings and stabilize the defect landscape during reversible operation, addressing a central durability driver in steam electrolysis: repeated perturbation of cation valence and oxygen nonstoichiometry at active regions and interfaces. The enhanced activity is associated with vacancy-assisted steam activation and defect-mediated oxygen surface exchange and is described within an electronic-structure/defect framework where modulation of metal–oxygen covalency (often rationalized through an O 2p-band center perspective) influences oxygen exchange kinetics. The electrode achieves 1.75 W cm^{-2} in fuel-cell mode and 2.77 A cm^{-2} at 1.30 V in electrolysis at 600 °C, maintains >92% Faradaic efficiency, and exhibits minimal degradation over 200 h. This work generalizes a key concept emerging across the dissertation: the most durable high-rate operation is achieved when active defect chemistry is not merely maximized but buffered and stabilized through engineered heterostructures and interphases that prevent excessive redox swings and suppress steam-driven reconstruction.

Across these four contributions, the dissertation clarifies several governing principles and practical design rules for reversible PCCs:

1. Microstructure controls apparent kinetics by determining the overlap of gas pathways, electronic transport, and proton accessibility. High intrinsic activity cannot be fully realized if the reaction zone is confined or if transport bottlenecks create strong gradients; hierarchical and 3D architectures expand utilization and moderate local extremes that accelerate degradation.

2. Catalytic performance is best understood through defect and bonding descriptors, including oxygen vacancy chemistry, redox flexibility, and metal–oxygen covalency. However, activity gains must be balanced against steam-driven instability, motivating strategies that couple vacancy-rich phases with stable backbones and that buffer redox swings during reversible operation.

3. The buried electrode–electrolyte interface is a dominant determinant of both initial polarization and long-term durability. Constriction at point contacts, chemical incompatibility, interdiffusion, and reaction-layer growth can dominate losses even when bulk properties are favorable; engineered interlayers and nanostructured junctions provide a direct route to low-polarization, mechanically robust interfaces.

4. Integrated multiscale design creates synergy: transport-ready architectures amplify catalytic utilization; engineered interphases stabilize defect landscapes; and stabilized interfaces reduce hot spots and suppress the degradation mechanisms that typically erase activity gains. This synergy is essential for reversible operation, where ORR and OER impose different chemical potential fields and where cycling accelerates defect redistribution and interfacial stress.

Beyond the specific demonstrations reported here, this dissertation contributes a broader message for PCC development: electrolyte selection, oxygen-electrode architecture, and interface engineering are deeply interdependent. For example, chemically robust electrolytes such as BZY strengthen long-term stability but raise processing and interface demands; interfacial nanostructuring and compatible interlayers can unlock their potential by ensuring proton transparent contact and strong adhesion. Conversely, higher-conductivity electrolytes such as

BZCYYb reduce ohmic loss but still require microstructure and interface strategies to stabilize oxygen-side kinetics and durability under steam. In this sense, PCC performance is ultimately a system property anchored not only in bulk material conductivity, but also in grain-boundary control, interface compatibility, and multiscale electrode design.

Overall, this dissertation provides a multiscale, mechanism-based pathway for constructing oxygen electrodes and interfaces that deliver both high kinetics and durability in reversible protonic ceramic electrochemical systems. The work establishes design principles for transport-ready architectures, vacancy/redox-managed catalytic interphases, and structurally integrated, proton transparent interfaces, validated through high-performance reversible operation and long-term steam electrolysis testing. The insights developed here also point to future directions: deeper probing of catalytic/material descriptors under realistic steam conditions, broader interface-engineering strategies that combine chemical compatibility with mechanical compliance and scalability and expanded post-operation and operando-informed diagnosis to connect evolving electrochemical signatures with nanoscale structural and defect-chemical changes. Together, these advances are expected to accelerate PCC progress toward practical deployment in renewable energy storage and conversion applications.

Table of Contents

Acknowledgement iv

Abstract vi

List of Figures xvii

Chapter 1- Objectives of Doctoral Research 1

Chapter 2- General Introduction 4

2.1 Protonic Ceramic Cells (PCCs) as Reversible Energy-Conversion Devices 4

2.1.1 Motivation and positioning 4

2.1.2 Operating principles in PCFC and PCEC modes 9

2.1.3 Charge carriers and defect chemistry basics 12

2.1.4 Performance metrics and benchmarking conventions 17

2.1.5 Degradation and durability fundamentals 23

2.2 Electrode Microstructure Engineering 26

2.2.1 Why microstructure controls kinetics 26

2.2.2 Key microstructural descriptors 30

2.2.3 Fabrication routes and knobs 34

2.2.4 3D / hierarchical architectures 37

2.2.5 Stability and quantification 41

2.3 Electrode Catalysis and Defect Engineering 45

2.3.1 ORR/OER kinetics in protonic systems 45

2.3.2 Catalytic descriptors 49

2.3.3 Bulk tuning strategies 53

2.3.4 Surface-focused strategies 56

2.3.5 Activity–stability tradeoffs 61

2.4 Electrode–Electrolyte Interfacial Engineering 63

2.4.1 Origins of interfacial polarization 63
2.4.2 Chemical compatibility and interdiffusion 67
2.4.3 Interlayers and graded junctions 72
2.4.4 Mechanical integrity under operation 76
2.4.5 Interface characterization and degradation signatures 79
2.5 Integrated Multiscale Electrode Design for High Performance 83
2.5.1 Why single-factor optimization plateaus 83
2.5.2 Multiscale architecture 86
2.5.3 Synergy mechanisms 90
2.5.4 Design for reversibility 92
2.5.5 Diagnostics-guided optimization 96
2.6 Electrolyte Materials and Emerging Alternatives 97
2.6.1 Electrolyte requirements and tradeoffs 97
2.6.2 Grain boundaries and processing control 101
2.6.3 Thin electrolytes and supported architectures 105
Chapter 3- Enhancing Surface Activity and Durability in Triple Conducting Electrode for Protonic Ceramic Electrochemical Cells 109
3.1 Abstract 109
3.2 Introduction 109
3.3 Materials and Methods 112
3.3.1 Fabrication of NAUP-PNC73 mesh-structure electrode 112
3.3.2 Integration of NAUP electrode to PCEC full cells 112
3.3.3 Cells assembly and electrochemical measurements 113
3.3.4 Faradaic efficiency and energy efficiency measurements 114
3.3.5 Characterizations 115

3.4 Results and Discussion 116
3.4.1 Formation of self-assembled NAUP electrode structure 116
3.4.2 Synergistic effects of enlarged dual-transfer pathways and enhanced interfacial bonding on reduced polarization resistance of R_o and R_p 120
3.4.3 Superior electrochemical performances in fuel cell and steam electrolysis modes 126
3.4.4 Electrochemical performance durability in various degradation measurements 129
3.4.5 Structural resilience of the NAUP electrode on thermal cycles 131
3.5 Conclusion 133
3.6 Data and materials availability 134
Chapter 4- Hybridizing Electrode Interface Structures in Protonic Ceramic Cells for Durable, Reversible Hydrogen and Power Generation 135
4.1 Abstract 135
4.2 Introduction 135
4.3 Materials and Methods 138
4.3.1 Materials synthesis 138
4.3.2 Cells assembly and electrochemical measurements 139
4.3.3 Structural characterizations 140
4.3.4 Measurement of surface oxygen vacancy 140
4.3.5 Measurement of bulk oxygen vacancy 141
4.4 Results and Discussion 142
4.4.1 Reconstruction of high-catalytic hetero-interface 142
4.4.2 Comprehensive characterizations on multiphase PrO_x catalytic zone 144
4.4.3 Minimizing ASR_o and ASR_p to enhance ORR efficiency 149
4.4.4 Hybridized electrode for PCEC: electrochemical efficiency and durability validation 152

4.4.5 DFT simulations and determination of oxygen vacancy concentration for studying synergistic interaction on hybridized electrode structure 157
4.5 Conclusion 161
4.6 Data and materials availability 162
Chapter 5- Interfacial Nanostructuring Enables Integrated, Low-Polarization Reversible Protonic Ceramic Cells 163
5.1 Abstract 163
5.2 Introduction 163
5.3 Materials and Methods 166
5.3.1 Synthesis of PLBC powder 166
5.3.2 Cell fabrication 167
5.3.3 Cells assembly and electrochemical measurements 168
5.3.4 Characterizations 168
5.4 Results and Discussion 169
5.4.1 Fabrication route for the conformal PLD interface in PCCs 169
5.4.2 Phase stability and defect chemistry of double perovskite PLBC 172
5.4.3 Nanocrystalline PLD-PLBC interlayer: crystallography and interfacial continuity 174
5.4.4 Performance gains from PLD interface engineering 177
5.4.5 Long-term reversible cycling and high-pressure steam electrolysis with sustained FE 183
5.5. Conclusion 187
5.6 Data and materials availability 188
Chapter 6- Vacancy–Redox Coupling at Interface-Engineered Heterostructures Enhances Reversible Energy Conversion in Protonic Ceramic Cells 189
6.1 Abstract 189
6.2 Introduction 189

6.3 Materials and Methods 192
6.3.1 Fabrication of 3D-architectured electrodes (3DE) and hierarchically engineered nanostructure electrode (HEN) 192
6.3.2 Cells assembly and electrochemical measurements 193
6.3.3 Structural and microstructural characterizations 194
6.3.4 Electronic structure and oxygen defect analyses 194
6.4 Results and Discussion 194
6.4.1 Vacancy enrichment and band modulation induced by hybrid interface in a hierarchically engineered oxygen electrode for PCCs 194
6.4.2 Atomic-scale structural evolution and vacancy engineering in PrO_x–PNC hybrid interface 200
6.4.3 Degradation-resistant microstructure for high performance and Faradaic efficiency 204
6.4.4 Linking electrochemical stability to vacancy-driven catalysis 215
6.5 Conclusions 223
6.6 Data and materials availability 224
Chapter 7- Summary and Prospects 225
Bibliography 228

List of Figures

Figure 2.1. Schematic diagram of R-PCEC in fuel cell (FC) and electrolysis cell (EC) operation modes along with the bulk and in-situ surface modification strategy for air electrode. 5

Figure 2.2. Schematic of RePCECs and comparison with low-temperature proton exchange membrane electrolysis cells, intermediate-temperature solid oxide electrolysis cells and high-temperature solid oxide electrolysis cells. 7

Figure 2.3. Illustrative comparison of oxygen electrode operating conditions in SOECs and PCECs. 8

Figure 2.4. Schematic representation of (2MZr′, VO••) configuration for the calculation of total energy. M1 and M2 denote two doped trivalent cations. The VO•• site is equidistant and the nearest from the two M cations in each M–M configuration (1–5NN). 2NN and 3NN sites locate on a plane with different z-coordinates of 1/8 and 1/4, respectively. 14

Figure 2.5. Schematic demonstration of the process of hydration through the reaction of H2O molecules. 16

Figure 2.6. Predicted cell voltage, power density, and faradaic efficiency as functions of current density at four temperatures. 20

Figure 2.7. Formation of the high-performance air electrode of BCFN covered with fine BCFN NPs with less Nb. 22

Figure 2.8. Schematic illustration of (a) inactive cation surface segregation, (b) surface poisoning, and (c) cation interdiffusions. 25

Figure 2.9. Phase field simulation of 3DEC with different porosities. 29

Figure 2.10. Overview of the characterized microstructure properties for the two solid-phases SP1 and SP2 (summarized as SPi, where i denotes 1 or 2), the total composite solid-phase SP tot, the pore-phase and the interface properties. The used variables are explained in the following sections. 33

Figure 2.11. Schematic diagram of steam transport pathways in LSCF(SP)/LSCF – BZY (a) and LSCF(PT)/LSCF – BZY (b) air electrodes. EIS (Ohmic impedance removed) of the electrodes before and after 100 h of operation in 40% H_2O–air (c) 36

Figure 2.12. (a) 3D X-ray microscopic image for the cell consisting of hydrogen electrode (bottom layer), electrolyte (invisible) and 3D steam electrode (top layer). (b) The bulk electrode frame with hierarchical gaps, which would facilitate fast mass transfer; (c) SEM image for the cross section of the cell shows the contact area between steam electrode frame and electrolyte and (d) reconstructed 3D image for the cell with dimension of 0.4 × 0.4 × 0.1 mm3. Three layers of cell components, that is, fibrous PBSCF electrode with a porosity of 57.7%, dense BZCYYb electrolyte, and sponge-like pore Ni-BZCYYb hydrogen electrode support, are obviously distinguished. ... 40

Figure 2.13. Schematic illustration of atom trapping. 43

Figure 2.14. Five representative reaction pathways for proton-coupled oxygen reduction reaction in PCFC cathodes are governed by the proton conductivity of the cathode material. 47

Figure 2.15. (a) Simplified evolution of an exemplary transition metal perovskite oxide band structure from the molecular orbital diagram for octahedral MO6. (b) Qualitative change of the electronic structure with increasing B-site cation electronegativity. EF and the metal d-band shift down, leading to a shallower O 2p band center. (c) Model of a 2 × 2 × 2 perovskite unit cell used for hybrid calculations (tilting angles slightly differ between $LaCoO_3$ and $LaCrO_3$). (d) Projected densities of states for $LaCrO_3$ and $LaCoO_3$, with the energy of the respective centroid of the occupied O 2p states taken as the reference energy. 51

Figure 2.16. (a) Protonic properties of the surface of NF and NSTF0.3 measured by TOF-SIMS. (b) A depth profile of the H_3O^+ detected in NSTF0.3. (c) The Schematic diagram of H3O+ diffusion. Copyright 2023, John Wiley and Sons. (d) The phase content-controlled hybrid electrode composed of cubic and hexagonal perovskites induced by tuning the ratio of A-site to B-site of cubic perovskite. (e) Comparison of PPDs at different temperatures for single cells with C-BSCF, C/H-BSCF, and H-BSCF electrodes. 55

Figure 2.17. (a) Schematic of the energy profile for the fuel cell and water electrolysis modes on LSCF (001). "*" denotes an adsorbed species on the surface. TS1 and TS2 are transition states. The energies in brackets are for the water electrolysis mode. In this reaction scheme, a Co ion on LSCF (001) was applied as a catalytically active center. (b) Schematic illustration of the reversible ORR and OER processes via the fuel cell and water electrolysis modes in BCO-LSCF//BZCYYb//Ni-BZCYYb. 57

Figure 2.18. (a) Schematic diagram of BCFNi95 ($Ba_5Ca_2Fe_6NiO_{23}$), BCFNi ($Ba_6Ca_2Fe_6Ni_2O_{24}$), and BCF ($Ba_8Fe_8O_{24}$); (b) Calculated oxygen vacancy formation energies and hydrations energies for BCFNi95, BCFNi and BCF perovskites; Electronic DOS for (c) BCF, (d) BCFNi and (e) BCFNi95; (f) Planar average charge density difference plots of NiO|BCFNi95; (g) Comparison of Fe-O bonds in BCF, BCFNi and BCFNi95; (h) -ICOHP calculations results of Fe-O bonds in BCFNi and BCFNi95..... 59

Figure 2.19. Correlation between simultaneously lowered ohmic and polarization resistance along electrode–electrolyte interface. 65

Figure 2.20. SIMS depth profiles of the LSCF-CFL cells (a) before and (b) after fuel cell measurements..... 69

Figure 2.21. Electrochemical properties of the PBSCF cathode based on BZCYYb4411 proton conducting electrolyte using humidified (3% H2O) H2 as fuel and dry air as oxidant at various temperatures. 74

Figure 2.22. EIS characterization results of the symmetrical cells with thick BCZYYb7111 electrolyte pellets (pristine and homogeneously laser-polished electrolyte surfaces) sandwiched between two identical porous BCFZY0.1 cathode films. 81

Figure 2.23. Redesigned nano-micro positive electrode simultaneously reducing ASRO and ASRP. The errors bars in these figures correspond to SDs from the averaging across all measurements. 88

Figure 2.24. Reversible operation and analysis in hydrogen and power generation. The cycling reversible operation of the electrochemical cell between electrolysis mode (hydrogen production) and fuel cell mode (electricity generation) at different current densities to examine the capability of converting hydrogen generated by electrolysis into electricity. 95

Figure 2.25. Stability under high-steam pressure electrolysis. 99

Figure 2.26. Segregation-controlled conductivity changes in different scientifically important $BaZrO_3$ based proton conductors. a–d) Electrochemical impedance spectroscopy in wet Ar/H2 of $BaZr_{0.8}Y_{0.2}O_{3-\delta}$ (BZY20)..... 102

Figure 2.27. Comparison between PCFCs with optimized and non-optimized nano-AFLs. The optimized nano-AFL was fabricated by post annealing at 1300 °C for 1 h after PLD with a

volumetric composition of 50:50 (Ni:BZY), while the non-optimized nano-AFL by post annealing at 1200 °C for 1 h. 106

Figure 3.1. Scalable fabrication and characterization of nano-structured ultra-porous PNC73 oxygen electrode. 117

Figure 3.2. TEM characterization of NAUP-PNC oxygen electrode. 119

Figure 3.3. Correlated elucidation on synergistic impacts of electrode structures via electrochemical impedance spectra and analysis of distribution of relaxation times (DRT) and activation energy. 121

Figure 3.4. Illustration of the integrated NAUP PNC electrode and hybrid structure for optimal dual mass/charge transfer and interfacial strength in PCEC. 124

Figure 3.5. Electrochemical performances of NAUP-PNC73 full cells in both fuel-cell and electrolysis modes as compared to full cells with conventional powder-packed electrodes. 127

Figure 3.6. Extraordinary stability and durability on accelerated stress tests of NAUP-PNC full cells under both fuel cell and electrolysis modes. 130

Figure 3.7. Thermal cycle stability evaluation of NAUP-PNC electrode under both fuel cell and electrolysis modes, explicated by dynamically operation across different temperatures. 132

Figure 4.1. Mechanistic approach for designing a synergistic interlayer to enhance the ORR. . 144

Figure 4.2. Schematic of the readily hybridized electrode and its characterizations. 146

Figure 4.3. In-depth characterization of the hybrid Type VI electrode through XRD and TEM analysis. 148

Figure 4.4. Correlation between electrochemical impedance spectra, distribution of relaxation times (DRT) analysis, and activation energies. 151

Figure 4.5. Electrochemical performance of the hybrid Type VI electrode full cells in both fuel cell and electrolysis modes. 153

Figure 4.6. Exceptional stability and durability of the hybrid Type VI electrode full cells in both fuel cell and electrolysis modes. 155

Figure 4.7. DFT analysis. 159

Figure 5.1. PLD-enabled interfacial nanostructuring strategy for protonic ceramic cells. 170

Figure 5.2. Structural stability, chemical expansion, and defect chemistry of PLBC. 173

Figure 5.3. PLD-derived nanocrystalline PLBC interlayer with compositional continuity stabilizes the PLBC | BZY interface. 176

Figure 5.4. Interfacial reinforcement and polarization reduction enabled by PLD. 178

Figure 5.5. Performance enhancement enabled by interfacial nanostructuring in PCCs..... 182

Figure 5.6. Long-term reversible operation and benchmarked performance of the PLD-enabled protonic ceramic cell under thermal cycling test. 184

Figure 5.7. Stable reversible performance enabled by a robust bilayer interface under steam and repeated thermal cycling. 186

Figure 6.1. PCCs energy pathway: from grid electricity to hydrogen and chemicals. 197

Figure 6.2. Structure, morphology, and oxygen-vacancy-induced lattice structure evolution of the hybrid interface in PrOx–PNC hierarchical structure. 199

Figure 6.3. Structural characterizations of the hybrid PrO_x–PNC interfaces..... 202

Figure 6.4. Electrochemical performance and structural stability of a PCC incorporating the HEN electrode. 207

Figure 6.5. Electrochemical performances of pristine, 3DE, and HEN cells and the durability under reversible and dynamic operations..... 214

Figure 6.6. Comprehensive investigation of oxygen vacancy behavior and mobility for understanding the mechanism related with the hybrid interfaces. 216

Figure 6.7. XPS analyses and schematic illustrations revealing the synergistic modulation of Pr, Co, and O chemical states in the PrO_x–PNC hybrid. 222

Chapter 1- Objectives of Doctoral Research

My doctoral research focuses on advancing reversible protonic ceramic cells (R-PCCs) for efficient power generation and hydrogen production at intermediate temperatures. The central challenge addressed in this dissertation is that, under steam-rich and high-current operation, the oxygen side of the cell often becomes the practical limiter: polarization losses rise due to coupled constraints in mass transport, catalytic kinetics, and electrode–electrolyte interfacial stability, while durability is threatened by microstructural coarsening, steam-driven surface reconstruction, and interfacial degradation. The overarching objective of my work is therefore to develop design principles and engineering strategies that simultaneously enhance oxygen-electrode activity and maintain long-term stability during reversible cycling between fuel-cell (PCFC) and electrolysis (PCEC) modes.

The key thesis developed across this dissertation is that closing the activity–durability gap requires integrated multiscale design, rather than isolated optimization of a single factor. High reversible performance emerges only when three elements are engineered together: (i) transport-ready electrode architectures that preserve gas accessibility and percolated charge pathways at high utilization, (ii) defect- and redox-tailored catalytic surfaces/interphases that accelerate proton-coupled ORR/OER under steam, and (iii) chemically compatible, mechanically robust buried interfaces that minimize constriction and suppress interdiffusion-driven polarization growth. In this framework, the oxygen electrode is treated as a coupled system in which microstructure sets accessibility, defect chemistry sets intrinsic kinetics, and interface integrity sets both initial losses and degradation trajectories.

Accordingly, this dissertation is built around four interrelated studies that collectively establish this integrated strategy. Together, these works demonstrate: (1) how nano-/3D electrode architectures can expand the effective reaction zone while maintaining scalability and durability under high current, (2) how hybridizing vacancy-rich phases with a stable backbone can couple surface activity with bulk transport to boost reversible kinetics, (3) how interfacial nanostructuring can create a continuous, proton transparent, and mechanically integrated electrode–electrolyte junction that enables low polarization and long-term steam electrolysis stability, and (4) how vacancy–redox coupling at engineered heterostructures can buffer local chemical potential swings

and stabilize the defect landscape during reversible operation. Collectively, these contributions provide a coherent pathway for designing oxygen electrodes that achieve both high kinetics and durability in protonic ceramic electrochemical systems.

The remainder of this dissertation is organized to first establish the fundamental background of PCC operation, electrode design, and interface chemistry in **Chapter 2**, and then to present these four studies from **Chapter 3** to **Chapter 6** as specific implementations of the integrated multiscale design principles developed herein.

Chapter 3 focuses on enhancing oxygen-electrode activity and durability through nano-architectured, triple-conducting electrode design and microstructure optimization under high-current operation. This chapter is organized around one paper: "Enhancing Surface Activity and Durability in Triple Conducting Electrode for Protonic Ceramic Electrochemical Cells" (Shuanglin Zheng, Wei Wu, Yuchen Zhang, Zeyu Zhao, Chuancheng Duan, Saroj Karki, Hanping Ding). Nature Communications 16, 4146 (2025). https://doi.org/10.1038/s41467-025-59477-9

Chapter 4 focuses on hybridizing the oxygen-electrode interface to couple vacancy-rich catalytic functionality with a robust backbone, aiming to accelerate proton-coupled ORR/OER while improving reversible stability. This chapter is organized around one paper: "Hybridizing Electrode Interface Structures in Protonic Ceramic Cells for Durable, Reversible Hydrogen and Power Generation" (Shuanglin Zheng, Bin Liu, Guntae Kim, Iman Ghamarian, Sooraj Patel, Hanping Ding). Advanced Materials 2025, 37, 2503649. https://doi.org/10.1002/adma.202503649

Chapter 5 focuses on engineering the buried electrode–electrolyte junction via interfacial nanostructuring to reduce interfacial polarization and strengthen mechanical adhesion for long-term, steam-rich reversible operation. This chapter is organized around one paper: "Interfacial Nanostructuring Enables Integrated, Low-Polarization Reversible Protonic Ceramic Cells" (Shuanglin Zheng, Anshu Kumari, Yuqi Geng, Yuchen Zhang, Nengneng Xu, Idris Temitope Bello, Sooraj Patel, Saroj Karki, Iman Ghamarian, Hanping Ding). Advanced Energy Materials (2026): e70850. https://doi.org/10.1002/aenm.70850

Chapter 6 focuses on defect-mediated design at interface-engineered heterostructures, highlighting vacancy–redox coupling as a route to simultaneously boost reversible kinetics and stabilize the oxygen-electrode defect landscape under steam. This chapter is organized around one

paper: “Vacancy–Redox Coupling at Interface-Engineered Heterostructures Enhances Reversible Energy Conversion in Protonic Ceramic Cells” (Shuanglin Zheng, Yuqi Geng, Sabrina Islam, Nishya Mohamed Raseek, Anshu Kumari, Saroj Karki, Idris Temitope Bello, John W. Peters, Chuancheng Duan, Sooraj Patel, Iman Ghamarian, Yingtao Liu, Zongping Shao, Hanping Ding). Angewandte Chemie International Edition. (2026): e7079252, https://doi.org/10.1002/anie.7079252

Chapter 7 presents the overall summary and prospects of this dissertation thesis.

Chapter 2- General Introduction

2.1 Protonic Ceramic Cells (PCCs) as Reversible Energy-Conversion Devices

2.1.1 Motivation and positioning

Deep decarbonization requires not only clean electricity generation, but also dependable ways to store and deliver energy across timescales from hours to seasons. Batteries are highly effective for short-duration buffering, yet long-duration storage and hard-to-electrify sectors often favor energy carriers that are energy-dense, transportable, and broadly usable[1,2]. Hydrogen is therefore increasingly viewed as a key component of low-carbon energy systems: it can store surplus renewable electricity in chemical form, provide carbon-free heat and power, and serve as a feedstock for ammonia and synthetic fuels[3–5]. The practical value of hydrogen, however, depends on how efficiently and durably it can be produced and converted. This motivates electrochemical platforms that can flexibly switch between power generation and fuel production with high efficiency, stability, and scalable manufacturing[6].

Protonic ceramic cells (PCCs)—often described as protonic ceramic fuel cells (PCFCs) in fuel-cell mode and protonic ceramic electrolysis cells (PCECs) in electrolysis mode—offer a compelling pathway toward this goal. PCCs are solid-state devices that employ dense ceramic electrolytes capable of transporting protons (H^+) at intermediate temperatures, typically ~400–600 °C[7,8]. This temperature window is strategically important: it is high enough to accelerate electrode kinetics and reduce polarization losses compared with low-temperature systems, while remaining substantially below conventional oxide-ion solid oxide cells. As a result, PCCs occupy a valuable “middle regime” that can potentially combine favorable ceramic robustness with reduced thermal stress, improved start-up dynamics, and broader materials compatibility[9].

A defining advantage of PCCs is their ability to couple electricity and hydrogen within a single reversible platform[10,11]. In PCFC operation, hydrogen is oxidized at the fuel electrode to generate protons and electrons; protons migrate through the electrolyte, while electrons flow through the external circuit to deliver electrical power. At the oxygen electrode, oxygen is reduced and reacts with incoming protons to form water. In PCEC operation, these processes reverse under an applied

voltage: steam is supplied (commonly to the oxygen electrode), where it is electrochemically split to produce oxygen and mobile protons; the protons are transported through the electrolyte and recombine at the fuel electrode to form hydrogen. This reversibility enables "power-to-gas" during renewable surplus and gas-to-power during demand peaks, supporting integrated energy storage and conversion using the same cell concept (Figure 2.1). Importantly, reversibility is not simply running the device backward; the dominant losses, interfacial chemistry, and degradation pathways can differ between fuel-cell and electrolysis modes. A practical reversible PCC must therefore sustain performance in both directions and remain stable under steam-rich conditions and repeated cycling[12].

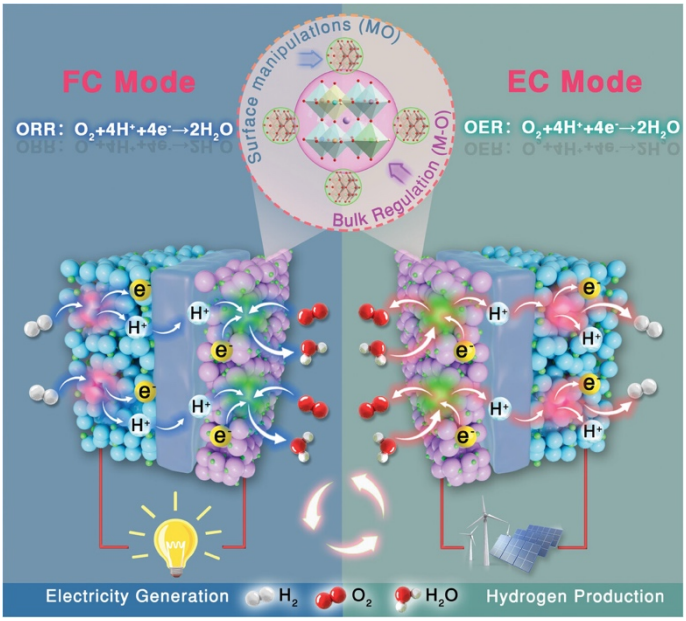


Figure 2.1. Schematic diagram of R-PCEC in fuel cell (FC) and electrolysis cell (EC) operation modes along with the bulk and in-situ surface modification strategy for air electrode[11].

Positioning PCCs among established technologies highlights why they are attracting increasing interest. Relative to low-temperature electrochemical systems such as PEM or alkaline devices, PCCs can leverage intermediate temperatures to activate oxide-based electrocatalysts that are sluggish near room temperature, potentially reducing precious-metal dependence and enabling new catalyst chemistries. The solid ceramic electrolyte also avoids issues associated with liquid electrolytes, such as flooding/drying management[13–15]. Meanwhile, compared with conventional high-temperature solid oxide cells, PCCs aim to mitigate severe thermomechanical stresses, accelerated microstructural coarsening, and aggressive chemical reactivity that complicate

durability and rapid cycling. Operation at intermediate temperature can broaden the palette of compatible seals, interconnects, and electrode constituents, improving prospects for manufacturability and system integration[16,17].

PCCs also differ fundamentally from oxide-ion solid oxide cells because proton conduction reshapes where water is produced or consumed and how electrodes experience local chemical environments (Figure 2.2). In fuel-cell mode, water formation occurs primarily at the oxygen electrode, which can reduce fuel-side dilution and may benefit fuel utilization strategies. In electrolysis mode, steam splitting proceeds via proton transport, offering favorable kinetics and thermodynamics in the intermediate-temperature regime[7,18]. These features make PCCs promising for distributed hydrogen generation and for reversible operation coupled to variable renewable electricity.

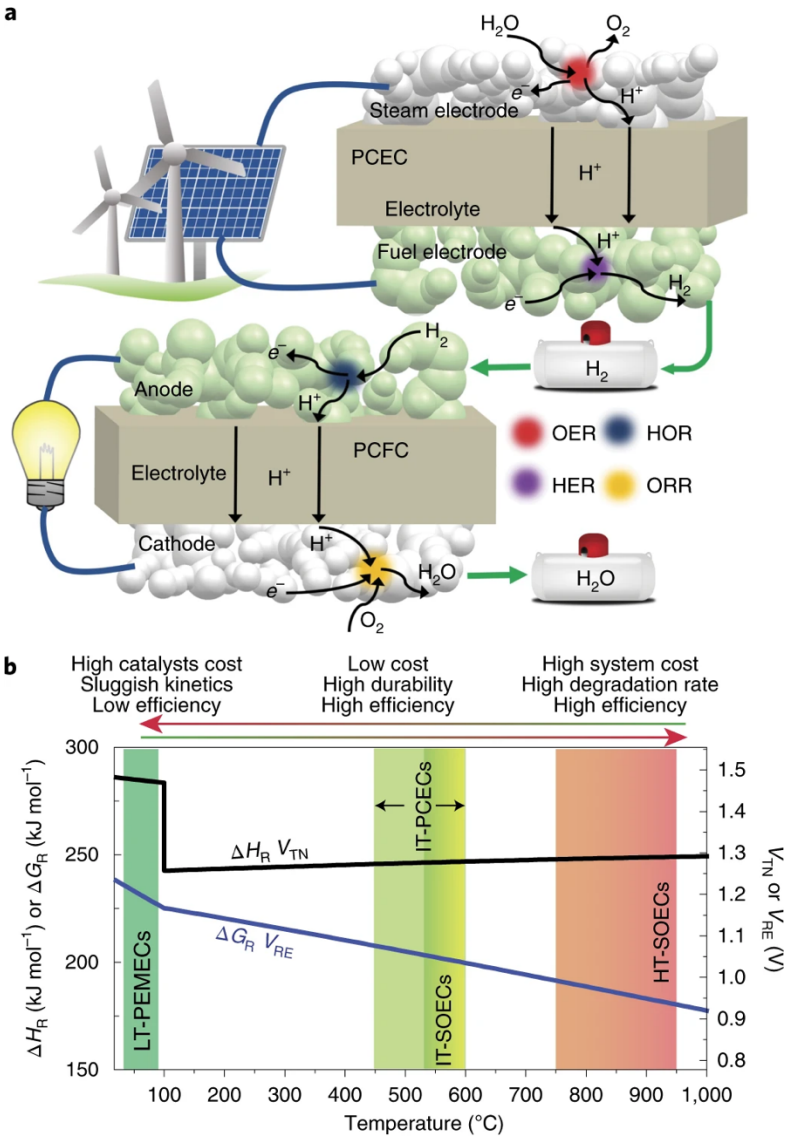


Figure 2.2. Schematic of RePCECs and comparison with low-temperature proton exchange membrane electrolysis cells, intermediate-temperature solid oxide electrolysis cells and high-temperature solid oxide electrolysis cells. (a) Schematic of the RePCEC: a reversible energy storage device that can operate in both fuel cell and electrolysis modes. OER, oxygen evolution reaction; ORR, oxygen reduction reaction; HOR, hydrogen oxidation reaction; HER, hydrogen evolution reaction. (b) Thermodynamics of water electrolysis as a function of temperature. ΔG_R is correlated with the reversible voltage (V_{RE}) while ΔH_R is correlated with thermal neutral voltage (V_{TN}) in electrolysis mode. ΔG_R and V_{RE} share the same plot and different *y* axes. ΔH_R and V_{TN} share the same plot and different *y* axes. PEMECs, proton exchange membrane

electrolysis cells; IT-SOECs, intermediate-temperature solid oxide electrolysis cells; HT-SOECs, high-temperature solid oxide electrolysis cells[7].

Despite these advantages, PCC performance is often limited by the oxygen electrode and by the buried electrode–electrolyte interface, especially under humid conditions relevant to electrolysis. Intermediate temperatures reduce some high-temperature degradation modes but amplify the importance of surface exchange and interfacial polarization (Figure 2.3). The oxygen electrode must simultaneously provide fast catalytic reaction rates, robust ionic/electronic transport, efficient gas access, and chemical/mechanical stability under steam and redox cycling—requirements that frequently conflict[19,20]. Highly active surfaces can reconstruct, segregate, or coarsen, while highly stable compositions may be kinetically sluggish at intermediate temperature. Similarly, interfacial reactions, poor bonding, or defect redistribution can create blocking layers and reduce the true electrochemically active contact area, turning the interface into a dominant resistance even when the bulk electrolyte is highly conductive.

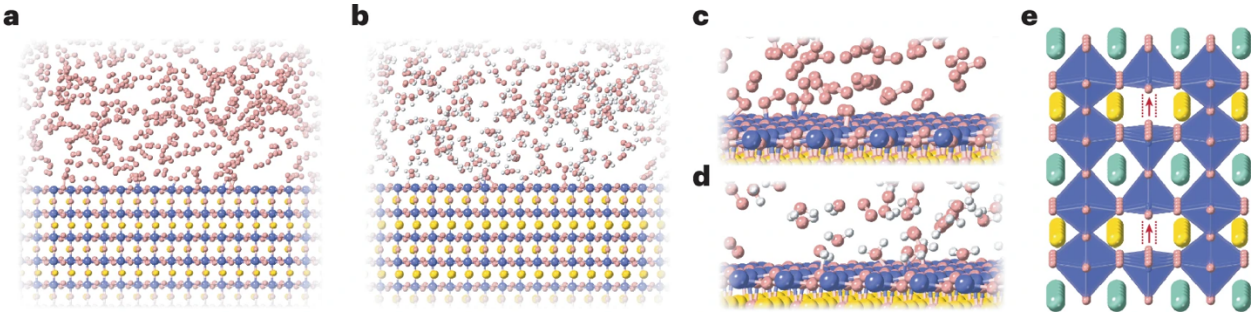


Figure 2.3. Illustrative comparison of oxygen electrode operating conditions in SOECs and PCECs. (a) Surface of the oxygen electrode material exposed to O_2 in SOECs. (b) Surface of the oxygen electrode material exposed to a H_2O/O_2 mixture with a high steam concentration in PCECs. (c-d) Enlarged views of the surface areas from a (c) and b (d), showing interactions between the surface of the oxygen electrode material and O_2 or H_2O molecules. In a–d, red and white spheres represent oxygen and hydrogen atoms, respectively, whereas yellow and blue spheres denote cations in the oxygen electrode materials. (e) Lattice structure of a layered double perovskite $AA'BO_{5+\delta}$ with oxygen migration channels indicated by the red arrows. Atoms on A and A′ sites are depicted by yellow and green spheres, respectively; cations on B sites are represented by the blue polyhedral units; oxygen atoms are shown as red spheres[20].

From a broader design standpoint, PCCs are best viewed as a coupled system in which performance emerges from co-optimizing bulk transport, porous-electrode architecture, surface catalysis, and interfacial integrity[21]. Improvements in one domain can expose bottlenecks in another—for example, enhancing catalytic activity can shift limitations toward gas diffusion or percolation; thinning the electrolyte can make interface polarization more visible; increasing steam content can improve electrolysis throughput while accelerating steam-driven reconstruction[22,23]. Consequently, the central motivation of PCC research is not only to discover better materials, but also to establish integrated, multiscale design principles that remain robust across operating modes.

This dissertation is positioned within that motivation by focusing on oxygen-electrode design as a key lever to improve both performance and durability in reversible PCCs. The overarching objective is to bridge the gap between transport-enabled architectures and chemically stabilized catalytic interfaces through coordinated design across scales, linking porous microstructures, catalytic modulation, and interface engineering to sustain high activity and stability during long-term reversible operation.

2.1.2 Operating principles in PCFC and PCEC modes

Protonic ceramic cells operate as solid-state electrochemical reactors in which a dense proton-conducting ceramic electrolyte separates two porous electrodes and forces charge transport to proceed along distinct pathways: protons (H^+) migrate through the electrolyte, while electrons (e^-) flow through the external circuit[24]. This separation is the core operating principle in both directions. The electrodes provide catalytic sites where gas molecules are converted into ionic and electronic charge carriers (or the reverse), and the cell voltage is determined by the reversible thermodynamic potential together with irreversible losses associated with ohmic resistance and electrode polarization[25].

In PCFC (fuel-cell) mode, the device converts chemical energy to electrical energy by electrochemically oxidizing hydrogen and reducing oxygen. Hydrogen is supplied to the fuel electrode, where it dissociates and is oxidized to form mobile protons while releasing electrons to the external circuit.

$$H_2 \rightarrow 2H^+ + 2e^-$$

The protons enter the electrolyte and migrate to the oxygen electrode under the electrochemical potential gradient, while the electrons travel through the load and return to the oxygen electrode. There, oxygen molecules are reduced and combine with incoming protons and electrons to form water[26].

$$\frac{1}{2}O_2 + 2H^+ + 2e^- \rightarrow H_2O$$

The overall reaction in PCFC mode is:

$$H_2 + \frac{1}{2}O_2 \rightarrow H_2O$$

A key distinction from oxide-ion solid oxide cells is that, because the transported ion is H^+, water is produced primarily on the oxygen-electrode side, which influences local humidity, reaction pathways, and stability requirements at that electrode.

The open-circuit voltage in PCFC mode is set by the chemical potential difference between the reactants and products and follows a Nernst-type dependence on temperature and gas activities by approximated partial pressures. Under load, the measurable cell voltage decreases from the reversible value due to irreversible losses, which can be grouped into ohmic loss (electrolyte resistance, contact resistances, current collection) and polarization loss (surface exchange, charge transfer, and mass transport through porous structures). In intermediate-temperature PCCs, polarization losses, especially at the oxygen electrode, often become prominent because surface exchange and interfacial kinetics can be slower than in higher-temperature solid oxide systems[14].

In PCEC (electrolysis) mode, the same device is driven in reverse to convert electrical energy into chemical energy, producing hydrogen from steam. Typically, steam is introduced at the oxygen electrode side, where water is electrochemically split under an applied voltage. The oxygen electrode now performs the anodic reaction, generating protons, releasing oxygen, and sending electrons into the external circuit (to the power supply)[27,28].

$$H_2O \rightarrow 2H^+ + \frac{1}{2}O_2 + 2e^-$$

The protons migrate through the electrolyte toward the fuel electrode, where they recombine with incoming electrons to form hydrogen.

$$2H^+ + 2e^- \rightarrow H_2$$

The overall reaction in PCEC mode is:

$$H_2O \rightarrow H_2 + \frac{1}{2}O_2$$

A key feature of this process is that proton transport through the ceramic electrolyte does not occur as simple free-particle diffusion, but rather through a Grotthuss-type mechanism involving successive proton transfer and reorientation steps on the oxygen sublattice. In this mechanism, protons are incorporated as hydroxyl defects bound to lattice oxygen, and long-range migration proceeds through the coupled rotation of O–H bonds and hopping of protons between neighboring oxide ions. These steps are associated with distinct energy barriers, commonly described as reorientation and transfer barriers, both of which depend strongly on the local crystal chemistry, including dopant species, oxygen-vacancy distribution, and hydrogen-bond geometry[26]. In acceptor-doped perovskites, trivalent dopants introduced to generate oxygen vacancies can also create proton-trapping effects through local defect association, thereby hindering proton mobility.

At the device level, these atomistic transport processes are reflected in several categories of polarization loss that together govern PCC performance, namely ohmic, activation, and concentration polarization[29]. Ohmic polarization arises from resistance to proton transport through the electrolyte, particularly across grain boundaries, as well as from electronic/ionic transport limitations in the electrodes and interfacial contact resistances. Activation polarization is associated with the intrinsic kinetic barriers of the electrode reactions, including gas adsorption and dissociation, surface exchange, charge transfer, and incorporation of ionic species into the electrode/electrolyte network; in PCCs, this contribution is especially significant at intermediate temperatures because the oxygen-electrode reactions remain comparatively sluggish[30]. Concentration polarization originates from mass-transport limitations when reactant delivery or product removal cannot keep pace with the electrochemical rate, giving rise to local gas-composition gradients within porous electrodes; this contribution is strongly influenced by electrode thickness, porosity, and tortuosity. Although the global reactions are straightforward, the performance of both modes is therefore governed by coupled microscopic steps: gas diffusion through the porous electrodes, adsorption and surface reactions, charge transfer at active sites, and incorporation/transport of ionic species within the electrode–electrolyte network[31]. Achieving

high current density consequently requires continuous electronic pathways, sufficient protonic accessibility, abundant catalytically active surfaces, and open gas pathways, which is why composite and mixed- or triple-conducting electrode designs are so important for extending the active reaction region beyond a narrow triple-phase boundary, especially at intermediate temperatures.

Although the global reactions are straightforward, the performance of both modes is governed by coupled microscopic steps: gas diffusion through the porous electrodes, adsorption and surface reactions, charge transfer at active sites, and incorporation of ionic species into the electrolyte/electrode network. Achieving high current density therefore requires continuous electronic pathways to and from reaction sites, sufficient ionic accessibility for protons to reach the reactive region, abundant catalytically active surfaces for fast hydrogen and oxygen electrocatalysis, and open gas pathways that minimize concentration gradients. These requirements motivate composite and mixed-conducting electrode designs and microstructures that extend the active region beyond a narrow triple-phase boundary, especially at intermediate temperatures.

Reversible operation imposes constraints beyond single-mode optimization. The dominant loss mechanisms and the local chemical environments can shift between PCFC and PCEC operation, and repeated switching can amplify redox and steam-driven stresses. Because proton conduction places water formation or consumption at the oxygen electrode depending on direction, that electrode and its buried interface with the electrolyte often experience the most severe combination of humidity exposure, chemical potential gradients, and structural driving forces. For this reason, oxygen-electrode catalysis, transport, and interface integrity frequently emerge as the central determinants of reversible PCC efficiency and durability, motivating the design strategies developed in the following sections of this chapter.

2.1.3 Charge carriers and defect chemistry basics

The distinctive feature of protonic ceramic cells is that their dense electrolyte supports mobile protonic defects as the primary ionic charge carrier over a useful intermediate-temperature window. In practice, however, a proton-conducting ceramic is rarely a single-carrier conductor. Depending on temperature and gas environment, the electrolyte (and often the electrodes) can also carry oxide-ion defects (oxygen vacancies) and electronic defects (electrons and holes)[16,32]. Understanding

how these charge carriers form, interconvert, and redistribute is essential because PCC performance depends not only on high proton conductivity, but also on minimizing parasitic electronic leakage, maintaining chemical stability, and ensuring that interfacial reaction zones remain catalytically and mechanically robust[33,34].

Most practical proton-conducting electrolytes are acceptor-doped oxides, commonly perovskite-type materials such as $BaZrO_3$- and $BaCeO_3$-based solid solutions. Acceptor doping (e.g., substituting a lower-valence cation on the B-site) introduces positive effective charge relative to the host lattice and is charge-compensated primarily by the formation of oxygen vacancies[35]. In Kröger–Vink notation, the creation of oxygen vacancies is often represented in an idealized way as:

$$M_2O_3 \xrightarrow{ABO_3} 2M_B' + V_O^{\cdot\cdot} + 3O_O^x$$

Here, M_B' denotes an acceptor dopant on the B-site with one effective negative charge, and $V_O^{\cdot\cdot}$ is a doubly positively charged oxygen vacancy. These oxygen vacancies are not just defects; they are the key chemical handles that enable hydration and therefore proton incorporation. In humid atmospheres, water molecules dissociatively incorporate into the oxide lattice by filling an oxygen vacancy and forming two hydroxyl groups, i.e., two protonic defects bound to lattice oxygen:

$$H_2O(g) + V_O^{\cdot\cdot} + O_O^x \rightleftharpoons 2OH_O^{\cdot}$$

The defect $OH_O^{\cdot}$ (often described as a lattice hydroxide) is the microscopic form of the mobile protonic carrier. At the atomistic level, proton transport proceeds predominantly by a Grotthuss-type mechanism: the proton rotates around an oxygen (reorientation of the O–H bond) and then hops to a neighboring oxygen (proton transfer), producing long-range migration without transporting the oxygen framework[36,37]. This mechanism explains why proton conduction can be substantial at intermediate temperatures and why local lattice geometry, oxygen–oxygen distances, and the hydrogen-bonding landscape strongly influence conductivity.

Because hydration consumes oxygen vacancies, the population of available carriers is inherently coupled to environmental variables—especially steam partial pressure and temperature. At a fixed acceptor dopant level, the system chooses how to distribute charge compensation among vacancies, protonic defects, and electronic defects to satisfy defect equilibria and electroneutrality (Figure

2.4). Qualitatively, higher steam activity favors larger $OH_O^{\cdot}$ concentration (higher proton conductivity), whereas dry conditions shift compensation back toward $V_O^{\cdot\cdot}$, increasing the relative importance of vacancy-related processes and, in some materials, increasing susceptibility to reduction/oxidation-driven electronic conduction[33].

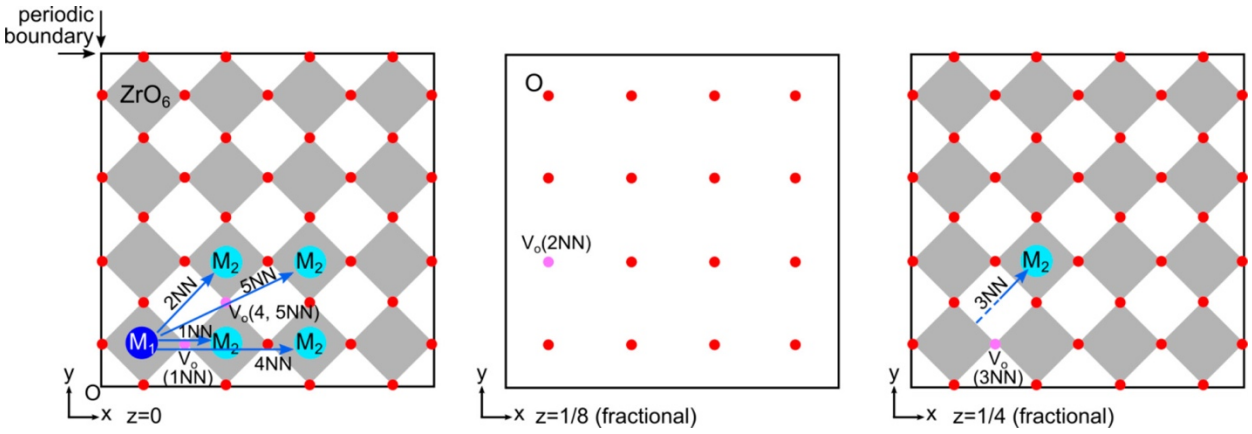


Figure 2.4. Schematic representation of (2MZr′, VO••) configuration for the calculation of total energy. M1 and M2 denote two doped trivalent cations. The VO•• site is equidistant and the nearest from the two M cations in each M–M configuration (1–5NN). 2NN and 3NN sites locate on a plane with different z-coordinates of 1/8 and 1/4, respectively[33].

Electronic defects become particularly important when the oxide exchanges oxygen with the gas phase and changes its oxidation state. Under oxidizing conditions, oxygen incorporation can annihilate oxygen vacancies and generate holes:

$$\frac{1}{2}O_2(g) + V_O^{\cdot\cdot} \rightleftharpoons O_O^x + 2h^{\cdot}$$

Conversely, under reducing conditions, oxygen can be released from the lattice, creating oxygen vacancies and electrons:

$$O_O^x \rightleftharpoons \frac{1}{2}O_2(g) + V_O^{\cdot\cdot} + 2e'$$

These reactions illustrate why pO_2 strongly affects the balance between ionic and electronic carriers. In an ideal electrolyte for PCC operation, the protonic transference number should be close to unity in the relevant temperature and gas windows, meaning most current is carried by protons rather than electrons or holes. Any significant electronic conduction acts as a “short-circuit”

pathway, lowering the open-circuit voltage and reducing efficiency[38,39]. This is one reason why electrolyte selection is often framed as a tradeoff among proton conductivity, chemical stability, and electronic leakage under realistic $pO_2$and pH_2O.

Defect chemistry also provides a direct link between materials selection and mechanical and structural behavior. Changes in oxygen nonstoichiometry and hydration state can induce chemical expansion, because altering cation valence and local bonding environments changes lattice parameters. Hydration and reduction can therefore produce dimensional changes that accumulate as stress during thermal cycling or reversible operation, especially near interfaces where gradients in $pO_2$and $pH_2O$are steep. In PCC stacks, even modest chemical expansion mismatches between electrode and electrolyte can contribute to interfacial strain, microcracking, or delamination over long operation.

Experimental and computational studies further suggest that, although rotational motion is often relatively fast, the proton-transfer step can become rate-limiting in many perovskite proton conductors (Figure 2.5). Consequently, the efficiency of steam electrolysis depends not only on electrode catalytic activity, but also on how effectively the electrolyte supports continuous proton hopping across its defect-modified oxygen framework. In this mode, the applied voltage must at least match the reversible requirement set by the Gibbs free energy change, and in practice must exceed it to overcome ohmic and polarization losses. The thermoneutral voltage provides an additional practical reference because it indicates whether the cell tends to absorb heat or generate heat during electrolysis, which matters for thermal management and durability at sustained high current.

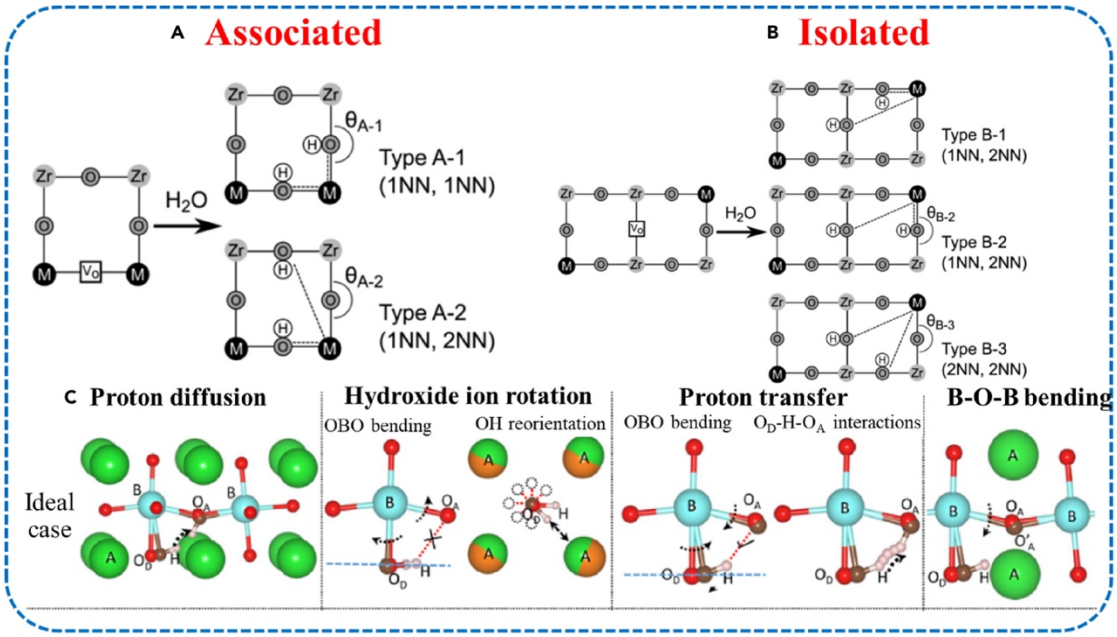


Figure 2.5. Schematic demonstration of the process of hydration through the reaction of H_2O molecules. (A) type A (associated) and (B) type B (isolated) configurations related to the defects, which are complex before hydration. The locations of the H atom at the first and second closest neighbors from the M dopant are designated as 2NN and 1NN, respectively. The M–O–Zr angle is illustrated by θ. (C) Representation of the proton diffusion mechanism in perovskite oxide (ABO). The schematic on the left demonstrates the diffusion of protons and its mechanism in 3D structures: rotation of hydroxide ion in the AO plan as well as transfer of protons in the BO2 plan. The schematics in the center describe the underlying elementary stages. (1) Rotation of hydroxide ion: bending motion of O–B–O outward and reorientation of the hydroxide ion (OH^-) in the AO plane. (2) Proton transfer involves the O–B–O system bending inward, the OH^- revolving outside of the AO plane, and the interaction of the O–D–H–OA system in the BO2 plane. The further O–B–O bending motion that is engaged in the proton transfer and rotation of the OH^- is shown on the right. The initial position is shown by red balls, while the ending position is shown by brown balls[26].

Importantly, the same defect concepts that describe bulk electrolyte transport also govern what happens in electrodes and at the buried electrode–electrolyte interface. Electrodes in PCCs often rely on mixed conduction—electronic conduction plus some ionic accessibility—to expand the active region beyond a narrow triple-phase boundary. In protonic systems, proton availability to the oxygen electrode (either through a proton-conducting phase or through interfacial pathways)

becomes part of the kinetic picture for oxygen reduction/evolution under humid conditions. Meanwhile, the interfacial defect landscape can deviate from the bulk due to space-charge effects, cation interdiffusion, or secondary phase formation, which can locally suppress carrier concentrations and increase polarization resistance even when the bulk electrolyte is highly conductive.

It is useful to summarize the practical implication: PCC operation is enabled by a defect-mediated knob set in which acceptor doping creates oxygen vacancies, steam hydrates those vacancies to generate protonic defects, and oxygen chemical potential shifts the balance between ionic and electronic carriers. The performance and durability of a PCC therefore depend on maintaining a regime where (i) $OH_O^{\cdot}$ defects are sufficiently abundant and mobile to support high proton conductivity, (ii) electronic defects remain minimal to avoid leakage, and (iii) defect-driven chemical expansion and interfacial defect redistribution are controlled to preserve mechanical integrity and stable polarization over time.

2.1.4 Performance metrics and benchmarking conventions

A consistent set of performance metrics is essential for evaluating protonic ceramic cells and for making meaningful comparisons across different material systems, microstructures, and test platforms. In PCC literature, apparent improvements can easily arise from differences in cell geometry, electrolyte thickness, steam utilization, electrode loading, or even how resistance is reported. For this reason, benchmarking should always distinguish intrinsic electrochemical kinetics from device-level engineering factors and should report metrics in forms that allow normalization across laboratories and cell formats[40,41].

The most fundamental voltage-based metrics are the open-circuit voltage (OCV) and the polarization curve. OCV provides a quick diagnostic of electrolyte integrity and electronic leakage: values significantly below the thermodynamic Nernst potential often indicate gas leakage, internal shorting, or non-negligible electronic conduction through the electrolyte. Under load, polarization curves report the relationship between cell voltage and current density[14,42]. In PCFC mode, the voltage decreases with increasing current due to irreversible losses; in PCEC mode, the applied voltage must exceed the reversible requirement and increases with current as losses grow. When reporting polarization behavior, it is best practice to specify the full operating conditions, as

temperature, gas compositions, flow rates, total pressure, and electrode areas—and to state whether values are corrected for ohmic drop (iR-corrected) or reported as measured.

Power and hydrogen production metrics are commonly used to summarize device capability. In PCFC mode, the peak power density (PPD) is typically reported as the maximum of $P = V \times j$, where $j$is the current density. PPD is useful for rapid comparison but can be misleading if reported without context (e.g., electrolyte thickness, electrode thickness, or mass-transport limits). In PCEC mode, electrolysis performance is often reported as the current density at a given voltage (e.g., at 1.3 V or 1.5 V) or the voltage required to reach a target current density[43]. Because electrolysis operation can be either endothermic or exothermic depending on the applied voltage relative to the thermoneutral voltage, reporting the operating voltage alongside current density is essential for interpreting energy efficiency and thermal management requirements.

Electrochemical impedance spectroscopy (EIS) is the most widely used tool to deconvolute losses and extract resistive metrics. The two headline quantities are the ohmic resistance (R_Ω or R_o) and the polarization resistance (R_p). $R_\Omega$is typically associated with electrolyte resistance plus contact and current-collection contributions, while $R_p$reflects the combined electrode processes, including surface exchange, charge transfer, and mass transport. In practice, the separation of $R_\Omega$and $R_p$depends on how the high-frequency intercept is interpreted and whether additional inductive artifacts or lead resistances are properly removed[44]. For benchmarking, it is strongly recommended to report area-specific resistances (ASR), i.e., $ASR = R \times A(\Omega \cdot cm^2)$, where $A$is the active electrode area. ASR enables comparison across different cell sizes and geometries. When possible, both $ASR_\Omega$and ASR_pshould be reported, because a high-performing cell can be limited either by electrolyte thickness/quality (ohmic) or by electrode kinetics/transport (polarization), and these require different design solutions.

Because PCC performance is highly temperature dependent, activation energies derived from Arrhenius-type plots are often reported to infer controlling processes. For example, the temperature dependence of ASR_pcan suggest whether surface exchange or bulk diffusion is rate-limiting over a given range, while ASR_Ωtrends can validate electrolyte transport behavior[45]. However, benchmarking based on activation energy alone requires caution: different temperature windows may capture different regimes, and microstructural evolution during heating can alter

apparent kinetics. Thus, activation energies are most informative when extracted over clearly stated temperature intervals and when accompanied by stable, reproducible EIS spectra.

For electrolysis operation, Faradaic efficiency (FE) and energy efficiency (EE) are critical metrics because they directly quantify whether the measured current is producing the desired product and how much electrical energy is converted into chemical energy. Faradaic efficiency describes the fraction of total charge that results in hydrogen production and is typically determined by measuring hydrogen production rate and comparing it to the theoretical rate from the applied current[43,46]. Energy efficiency can be defined in several ways depending on whether the lower heating value (LHV) or higher heating value (HHV) of hydrogen is used and whether thermal inputs are considered. Regardless of the chosen convention, benchmarking should clearly state the definition used, the method of gas quantification, and whether any corrections are applied for leakage or crossover (Figure 2.6). In PCCs, FE and OCV can also provide indirect evidence of electronic leakage through the electrolyte, since leakage reduces both the attainable voltage and the fraction of current contributing to product formation.

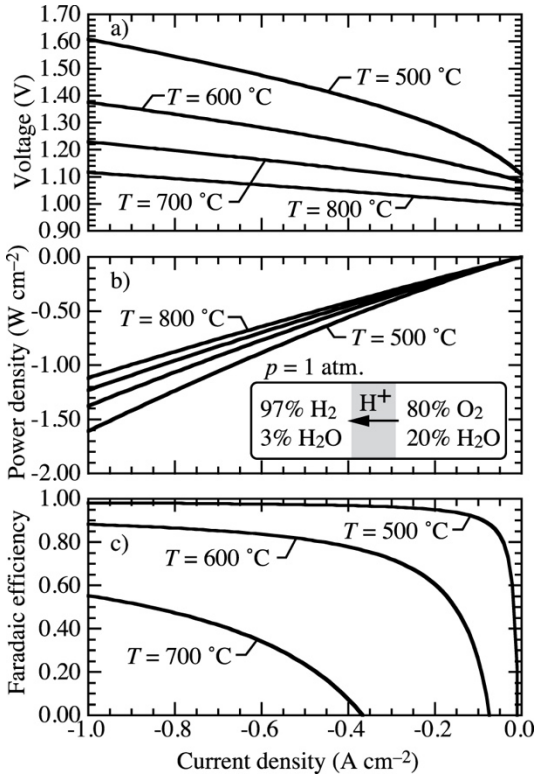


Figure 2.6. Predicted cell voltage, power density, and faradaic efficiency as functions of current density at four temperatures[43].

Benchmarking conventions also require careful reporting of cell design and test conditions. At minimum, meaningful comparisons should include electrolyte material and thickness; electrode composition, thickness, and fabrication route (e.g., infiltrated scaffold versus conventional composite); active area; current collectors and contact methods; gas compositions (including steam fraction and oxygen partial pressure); flow rates and utilization; total pressure; and whether values were recorded under steady state. In reversible PCC studies, it is particularly important to report both PCFC and PCEC performance under comparable conditions and to specify cycling protocols, because an oxygen electrode that performs well in one direction may degrade rapidly in the other due to different local chemical potentials and humidity exposure.

An emerging direction in PCC benchmarking is the incorporation of data-driven degradation prediction in addition to conventional electrochemical metrics[46]. It is demonstrated that combining embedded interfacial electrical sensors with machine-learning models enables real-time degradation diagnosis and remaining-useful-life prediction for PCECs under steam electrolysis (Figure 2.7). By using electrochemical signals from the full cell, oxygen electrode, and buried interfaces as internal health indicators, and then applying preprocessing, outlier filtering, and predictive models including long short-term memory and modular regression with Bayesian uncertainty estimation, they established a framework that links evolving electrochemical response to component-specific degradation. Their analysis predicted a remaining useful life of up to 2132 h and attributed 82.9% of the total degradation to the oxygen electrode, demonstrating that data-driven methods can identify dominant failure origins even when early electrolysis-voltage changes do not clearly reveal them. Such approaches point toward a next generation of PCC benchmarking in which performance metrics are not only descriptive, but also prognostic, allowing more reliable lifetime assessment, earlier anomaly detection, and more targeted materials and interface optimization.

Quantitative performance metrics normally do not by themselves reveal why a cell performs well or degrades over time. For this reason, rigorous benchmarking should be complemented by post-test analysis, which links electrochemical behavior to the structural, chemical, and interfacial state

of the cell after operation. In practice, post-test characterization helps distinguish whether performance changes originate primarily from electrolyte degradation, electrode coarsening, interfacial instability, current-collector/contact failure, or gas-transport limitations. Techniques such as SEM or FIB-SEM can reveal pore coarsening, particle growth, cracking, or delamination; TEM can probe nanoscale interfacial reconstruction and secondary-phase formation; and XRD, XPS, or EELS can identify phase instability, cation segregation, and valence or oxygen nonstoichiometry changes after operation. For example, Pei et al. combined XRD, SEM, high-resolution TEM, and HAADF-STEM/EDS to show that exposure to wet operating conditions induced surface restructuring of the BCFN air electrode, while cross-sectional SEM of the tested single cell further confirmed that the cell layers remained well bonded, highlighting why post-test analysis is not only useful for identifying failure, but also for verifying whether apparent durability is associated with genuine structural and interfacial stability or with beneficial surface evolution under realistic operating conditions (Figure 2.7)[12].

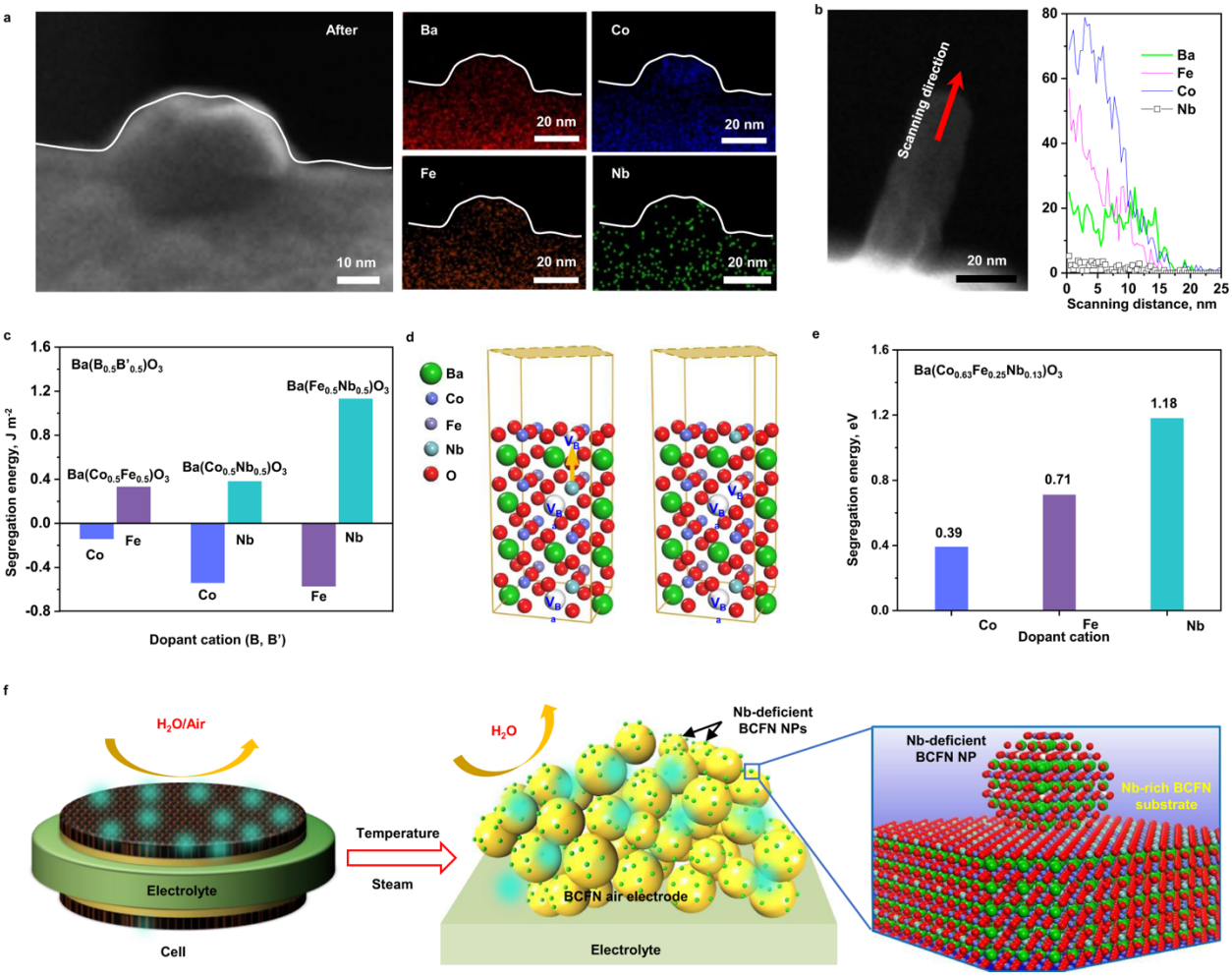


Figure 2.7. Formation of the high-performance air electrode of BCFN covered with fine BCFN NPs with less Nb. (a) TEM image and elemental (Ba, Co Fe, and Nb) mapping of a BCFN grain after electrochemical testing at 650 °C; (b) Elemental profile along the scanning line shown in the TEM image; (c) Comparison of computed segregation energies (J m^{-2}) for stoichiometric $Ba(B_{0.5}B'_{0.5})O_3$ (B,B′ = Co, Fe, or Nb); (d) Illustration of CoO-terminated BCFN(001) surface models representing segregation of Nb from the bulk to the surface; (e) Computed segregation energy (eV) for three different dopant cations of $Ba_{0.9}(Co_{0.63}Fe_{0.25}Nb_{0.13})O_3$; and (f) A schematic illustration of the formation of Nb-deficient BCFN NPs on the BCFN air electrode[12].

As electrode microstructure and interfaces strongly influence EIS and polarization behavior, best-practice benchmarking increasingly includes complementary diagnostics such as distribution of

relaxation times (DRT) analysis, pO_2or pH_2Odependence tests, and durability data under fixed current or fixed voltage. When these are reported with consistent normalization and transparent experimental details, performance metrics become more than headline numbers: they become mechanistic signatures that allow the community to identify the true origin of improvement and to translate promising materials concepts into reproducible, scalable PCC devices.

2.1.5 Degradation and durability fundamentals

High performance in protonic ceramic cells is only meaningful if it can be sustained under realistic operating conditions and over repeated switching between fuel-cell (PCFC) and electrolysis (PCEC) modes. Durability in PCCs is fundamentally a multi-physics problem: electrochemical driving forces, local gas chemistry (especially steam), defect chemistry, microstructure evolution, and mechanical stresses all couple together. As a result, degradation often manifests as a gradual increase in polarization resistance, a rise in ohmic loss, and in severe cases, sudden failure through cracking, delamination, or gas leakage[47–49].

A common durability limitation arises from thermally driven microstructural coarsening in porous electrodes. In Ni-based hydrogen electrodes, Ni particles can agglomerate and coarsen during long-term operation, reducing Ni–ceramic interfacial area and triple-phase-boundary length[50]. On the oxygen-electrode side, the porous backbone can undergo grain growth and partial densification, while infiltrated nanoscale catalysts can coarsen or sinter, all of which lower active surface area, impede gas access, and increase polarization resistance[12]. In protonic ceramic cells, the steam-rich oxygen-electrode environment can further accelerate oxygen-electrode instability through hydrothermal degradation and surface restructuring. Coarsening reduces active surface area, shortens the length of electrochemically active regions, and can diminish percolation pathways, all of which increase polarization resistance over time. The coarsening tendency can be accelerated by humid environments because steam can enhance surface diffusion or promote dissolution–reprecipitation pathways for certain oxide species[51,52]. Consequently, an electrode that exhibits exceptional initial activity may suffer rapid performance decay unless its nanostructure is stabilized by anchoring, strong interfacial bonding, or self-regenerating mechanisms.

A second major degradation route is surface and bulk chemical reconstruction driven by steam, oxygen chemical potential gradients, and redox cycling. Oxygen electrodes in PCCs are frequently

exposed to high steam fractions during electrolysis and to dynamic local environments during reversible operation. Under these conditions, surfaces can undergo hydroxylation, cation segregation, or phase transitions that alter catalytic activity and charge-transfer kinetics. In mixed-conducting oxides, changes in oxygen nonstoichiometry and cation valence can modify defect populations and electronic structure, which directly impacts oxygen exchange and charge transport. Even when bulk phase stability is retained, subtle changes at the near-surface region—where reactions occur—can shift the rate-limiting step and cause progressive polarization growth[52,53].

The electrode–electrolyte interface is another frequent origin of durability loss (Figure 2.8). Interfaces can degrade through chemical reactions that form resistive secondary phases, through interdiffusion of alkaline-earth or rare-earth species, or through defect redistribution that lowers local carrier concentration[51,54]. These interfacial changes reduce the true electrochemically active contact area and introduce additional transport barriers, often appearing in EIS as a growing mid-to-low frequency polarization contribution. Because the interface is buried, such degradation can proceed unnoticed until performance has significantly decayed. This is why interlayers, compositional grading, and low-temperature processing strategies are widely used: they aim to maintain chemical compatibility and stable defect chemistry at the junction while preserving mechanical adhesion.

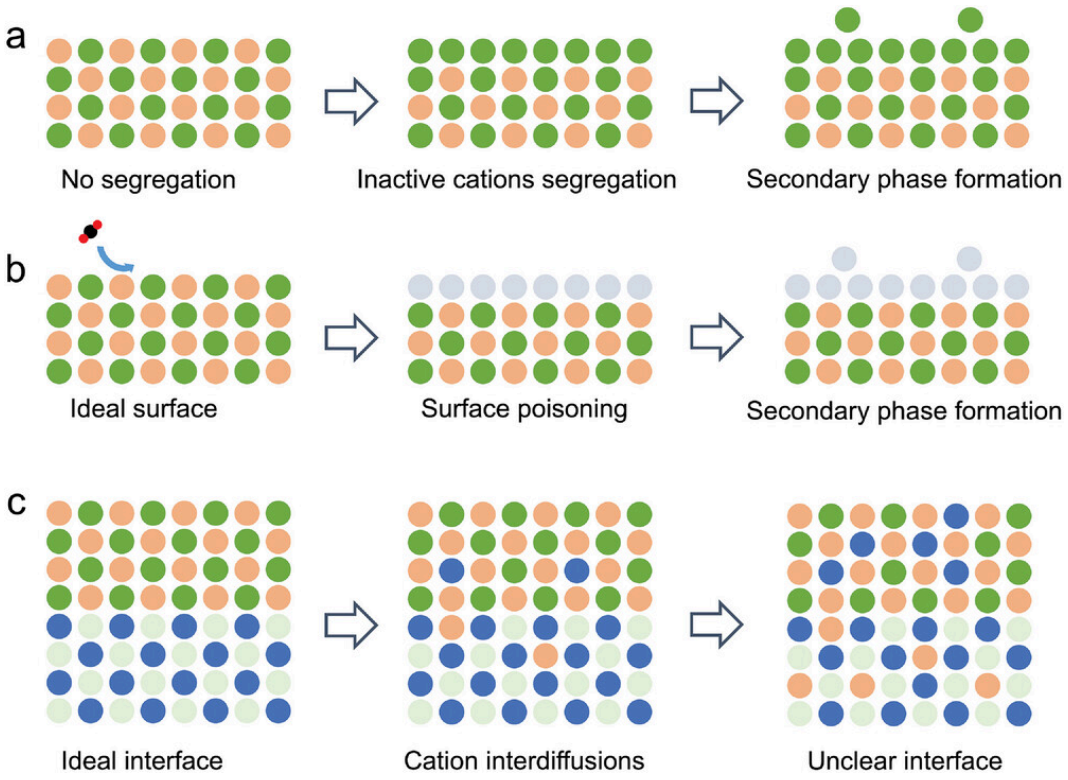


Figure 2.8. Schematic illustration of (a) inactive cation surface segregation, (b) surface poisoning, and (c) cation interdiffusions[51].

Durability is also strongly influenced by mechanical and thermochemical stresses. During operation, gradients in temperature, steam activity, and oxygen partial pressure create spatially varying defect populations[55,56]. Hydration/dehydration and redox changes can lead to chemical expansion, while mismatched thermal expansion coefficients between layers generate cyclic stress during heating and cooling. In reversible cells, mode switching can amplify these effects because local chemical potentials shift directionally, repeatedly moving the system between different defect states. Over time, accumulated stress can cause microcracking in electrodes, loss of contact at current collectors, or delamination at the electrode–electrolyte interface. Once a delamination initiates, both ohmic and polarization losses can rise sharply because the effective current-carrying area decreases and current constriction becomes severe.

Electrolyte-related degradation can occur even when the electrolyte remains dense and nominally stable. Grain boundaries may exhibit higher resistance than bulk due to impurity segregation or secondary phases, and these effects can evolve under long-term exposure to humid or reactive

gases[57]. In some proton-conducting perovskites, chemical instability under CO_2-containing atmospheres or extreme steam conditions can lead to carbonate/hydroxide formation or surface degradation, which can compromise conductivity and interfacial compatibility. In addition, any increase in electronic conduction—caused by reduction at low pO_2or defect chemistry shifts—can decrease OCV and efficiency and may accelerate local heating and degradation by enabling internal leakage currents.

For electrolysis operation, additional durability considerations emerge from high steam utilization and large chemical potential gradients. Local depletion of steam in porous electrodes can create strong gradients in $p_{\mathrm{H_2O}}$and $p_{\mathrm{O_2}}$, intensifying concentration polarization and driving localized changes in defect chemistry and phase stability[58]. High current densities also increase the risk of non-uniform current distribution and hotspot formation, which can accelerate coarsening, segregation, and mechanical damage. These issues are particularly relevant in oxygen electrodes, where steam splitting occurs and where the combined demands of catalysis, transport, and stability are most stringent.

Because multiple mechanisms can contribute simultaneously, durability assessment requires more than a single lifetime number. Best practice is to report degradation under well-defined protocols—constant current, constant voltage, or cycling between PCFC and PCEC—together with periodic EIS to separate evolving ohmic and polarization contributions. Complementary characterization (post-test microscopy and spectroscopy, interfacial cross-sections, and composition profiling) is critical for linking performance decay to physical mechanisms. Ultimately, the durability challenge in PCCs can be summarized as maintaining a stable multiscale structure: preserving nanoscale catalytic functionality, sustaining porous-network transport, and protecting the buried interface from chemical and mechanical damage, all while the defect landscape continuously adapts to steam and oxygen chemical potentials during reversible operation.

2.2 Electrode Microstructure Engineering

2.2.1 Why microstructure controls kinetics

Electrode kinetics in protonic ceramic cells are often described in terms of “intrinsic catalytic activity,” yet the polarization resistance measured in a real cell is rarely dictated by surface

chemistry alone. In porous electrodes, the apparent kinetics emerge from how efficiently the microstructure connects reactants, charge carriers, and reaction sites across multiple length scales. Even an excellent catalyst can look sluggish if gas access is restricted, if electronic/protonic pathways are discontinuous, or if only a small fraction of the electrode volume is electrochemically active[25]. For this reason, microstructure is not a secondary detail—it is a primary design variable that governs how much of the material is utilized and how the electrochemical driving force is distributed within the electrode.

At the most basic level, porous electrodes must coordinate three coupled processes: mass transport, charge transport, and interfacial reaction. Gas-phase reactants (H_2 on the fuel side; O_2 and/or H_2O on the oxygen side) must diffuse through a tortuous pore network to reach reactive surfaces. In parallel, electrons must travel through a percolated electronic network, and protons must be supplied through the electrolyte and/or a proton-conducting phase within the electrode to complete the electrochemical reaction. If any of these pathways is poorly connected, the local reaction rate is throttled regardless of the catalyst's intrinsic activity[59,60]. Because these processes occur in the same physical space, microstructure determines whether they overlap effectively, creating a large, well-utilized reactive region or remain spatially separated, forcing reactions to occur only at limited sites.

This overlap is often captured by the concept of the reaction zone. In conventional composite electrodes, reactions are concentrated near triple-phase boundaries where gas, an electronic conductor, and an ionic conductor meet. In protonic ceramic cells, the reaction zone can be broadened beyond a narrow boundary if protons can access internal surfaces, either through mixed protonic/electronic conduction, intimate ceramic–catalyst mixing, or engineered interphases. The extent of this reactive region is strongly microstructure-dependent: particle size, phase distribution, necking and contacts, and continuity of the proton-conducting phase all influence how far protons can penetrate the electrode and how much internal surface becomes electrochemically addressable[60,61]. A coarse or poorly connected structure can confine proton access to a thin layer near the electrolyte, leaving most of the porous volume underutilized even when porosity and electronic conductivity appear adequate.

Microstructure governs the effective transport properties that are inseparable from the measured electrochemical kinetics. Gas transport is controlled by porosity, pore-size distribution, and tortuosity; when pores are too small or transport pathways are excessively tortuous, concentration gradients develop within the electrode, leading to local reactant depletion and product accumulation near electrochemically active regions. Such gradients lower the local chemical driving force and introduce concentration polarization that can be mistakenly attributed to intrinsically sluggish charge-transfer kinetics. Charge transport exhibits an analogous dependence on microstructure. Electronic conduction is determined not only by the intrinsic conductivity of the constituent phase, but also by the continuity of the percolation network, the quality of interparticle contacts, and constriction effects at grain junctions. Proton transport similarly depends on the continuity, thickness, and accessibility of proton-conducting pathways, as well as on the resistance associated with phase boundaries and interfacial contacts.

Importantly, the influence of porosity is not simply monotonic. As demonstrated in the analysis summarized in Figure 2.9, increasing cathode porosity improves oxygen access and expands the spatial extent of the electrochemically active region, thereby promoting oxygen-gas absorption and reducing mass-transport limitations. However, beyond an optimal level, further increases in porosity diminish the continuity of the solid-state transport network and weaken charge-transfer capability within the electrode. As a result, the oxygen-ion generation rate no longer improves and may instead decline, even though gas diffusion becomes easier. The experimentally observed peak power density follows the same non-monotonic trend, confirming that superior performance arises from a balanced microstructure that simultaneously supports efficient gas diffusion and robust charge transport, rather than from maximizing porosity alone[59]. This behavior highlights a central principle in protonic ceramic electrode design: the most severe transport penalties often do not originate from the intrinsic properties of the constituent materials, but from microstructural bottlenecks that prevent reactants, electrons, and protons from converging effectively at active reaction sites. A related modeling study reached a similar conclusion, showing that proper tuning of cathode porosity improves not only overall cell performance but also the uniformity of gas distribution, further underscoring that apparent electrode kinetics are governed as much by transport architecture as by catalyst chemistry itself.

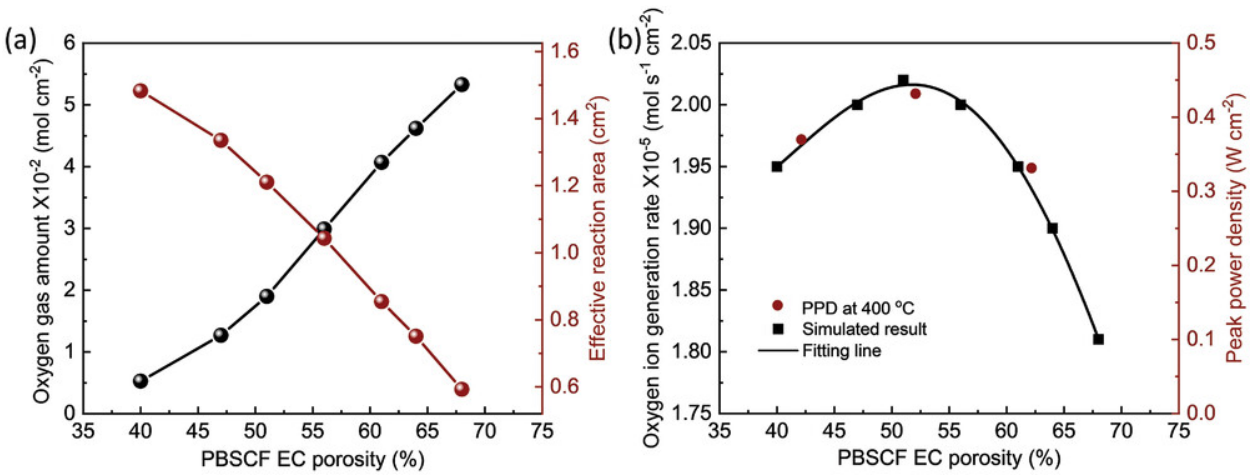


Figure 2.9. Phase field simulation of 3DEC with different porosities. (a) Oxygen gas absorption and effective reaction area in cathode bulk. (b) Oxygen ion generation rate and experimental PPD at 400 °C versus cathode porosity[59].

A related microstructural control is current distribution. Ideally, current spreads uniformly across the electrode–electrolyte contact, but in practice non-uniform contact, local densification, or discontinuous percolation can cause current to funnel through a limited number of pathways. This increases local overpotential, which not only raises instantaneous polarization but also accelerates degradation by amplifying coarsening, segregation, and interfacial reactions in those stressed regions. In other words, microstructure controls kinetics in two senses: it determines the initial utilization of reaction sites, and it governs how the electrode shares electrochemical load over time.

These effects are especially pronounced at the intermediate temperatures typical of PCC operation, where many oxygen electrodes sit near the transition between kinetics-limited and transport-limited regimes. As intrinsic activity improves via materials chemistry (e.g., higher surface exchange, more favorable defect chemistry), the limiting factor often shifts to gas diffusion, proton accessibility, or contact resistance[57,60,62]. This is why advanced designs increasingly use hierarchical architectures: larger pores and embedded gas channels reduce diffusion resistance; finer features provide high surface area and dense populations of reaction sites; and robust backbones maintain electronic conduction and mechanical integrity. Scaffold-based and infiltrated electrodes are particularly powerful because they decouple functions, mechanical support and electronic conduction from catalytic activity, allowing nanoscale catalysts to be added without sacrificing macroscopic transport.

Finally, microstructure influences the local chemical environment, which is critical in protonic systems. Because water is produced or consumed at the oxygen electrode depending on operation mode, local steam activity within pores can vary strongly with pore geometry and utilization. These gradients affect hydration state, defect populations, and surface hydroxylation, thereby feeding back into apparent kinetics and stability. Electrodes with well-designed pore networks can moderate these gradients, improving both performance and durability.

Electrode microstructure controls kinetics because it translates intrinsic material activity into device-level performance. It sets the size and accessibility of the reaction zone, governs effective gas and charge transport, shapes current distribution and constriction, and even influences local steam and defect equilibria. For protonic ceramic cells, where proton availability, humid environments, and interface integrity strongly shape polarization, microstructural engineering is inseparable from catalytic design: the most successful electrodes are those whose architecture ensures that reactants, electrons, and protons converge efficiently at stable, well-connected reaction sites throughout the electrode volume.

2.2.2 Key microstructural descriptors

To design and compare porous electrodes in protonic ceramic cells, it is useful to describe the microstructure using a common set of quantitative descriptors. These parameters connect what is visible in microscopy to what is measured electrochemically, because they determine gas transport, charge percolation, the size of the active reaction zone, and the stability of the electrode under steam and cycling. Importantly, no single descriptor is sufficient: high performance typically requires a balanced combination of open gas pathways, continuous electronic/protonic networks, and a large, accessible catalytic surface area.

A first-order descriptor is porosity (ε), which represents the volume fraction of void space available for gas transport[63]. Higher porosity generally lowers gas-diffusion resistance, but excessive porosity can reduce mechanical strength, decrease electronic connectivity, and limit the density of reaction sites. In practice, optimal porosity depends on electrode thickness, operating current density, and whether the electrode is scaffold-based or a conventional composite. Closely related is the pore size distribution, which governs whether transport is dominated by bulk diffusion or by Knudsen diffusion in small pores, and whether steam and oxygen can penetrate

deeply at high utilization. A narrow distribution of very small pores may provide high surface area but can create severe concentration gradients, whereas a bimodal or hierarchical pore network (large channels plus fine pores) often provides both rapid gas delivery and abundant reactive surface.

Because pores are not straight tubes, gas transport is also strongly affected by tortuosity (τ), which captures how convoluted the transport pathways are relative to a straight line[64]. For a given porosity, a higher tortuosity increases diffusion resistance and amplifies local gradients in $p_{\mathrm{H_2O}}$and $p_{\mathrm{O_2}}$, which can shift defect equilibria and alter apparent kinetics. Porosity and tortuosity together determine effective diffusivity and permeability, which are the transport-relevant properties that ultimately shape concentration polarization. In practical PCC oxygen electrodes, controlling tortuosity is often as important as increasing porosity, because highly tortuous fine pores can trap products and create local steam-rich environments that accelerate surface reconstruction.

Beyond gas pathways, high performance requires continuous networks for charge transport. Electronic percolation describes whether an electronically conducting phase forms a connected pathway from current collector to reaction sites. This is often evaluated qualitatively from micrographs, but quantitatively it depends on volume fraction, particle connectivity, and the quality of interparticle contacts[65]. A structure can have a high electronic conductor fraction yet still suffer high resistance if contacts are poor or if constriction forces current through narrow bottlenecks. In protonic cells, protonic percolation or ionic accessibility is equally critical: protons must reach the reaction zone either through a proton-conducting phase distributed within the electrode or through an engineered interphase that provides proton pathways to internal surfaces. The continuity and thickness of the ionic network, as well as the density of ionic/electronic interfaces, therefore, directly influence polarization resistance.

The microstructure also determines how much catalytic surface is usable. A common descriptor is the specific surface area (surface area per unit volume or mass), but the more relevant quantity is the electrochemically accessible surface area, i.e., surface that simultaneously has gas access and access to both electronic and protonic charge carriers. In many electrodes, the total surface area can be high while the accessible fraction is low due to blocked pores, isolated catalyst islands, or insufficient protonic connectivity. For composite electrodes, descriptors such as interfacial area

density between phases (e.g., catalyst–proton conductor contact area per unit volume) or an effective triple-phase boundary density remain useful proxies for reaction-site density, especially when reactions are localized near phase junctions.

Geometric parameters such as electrode thickness and functional layer architecture are also essential descriptors because they set the balance between available reactive volume and transport distances[66]. A thicker electrode can provide more reaction sites but also increases diffusion path length and can exacerbate concentration polarization, especially under high steam utilization in electrolysis mode. Many high-performing PCC electrodes therefore use layered designs—e.g., a thin "functional layer" with fine features near the electrolyte to maximize reaction-site density, supported by a coarser "backbone layer" optimized for gas transport and current collection. The transition between these layers or the presence of graded microstructures is itself a descriptor of how the electrode distributes function spatially.

To quantitatively connect microscopy to electrochemical performance, porous PCC electrodes can be described in terms of solid phases, pore phase, and their interfaces, with the most important descriptor classes including volume fraction, size distribution, tortuosity, and interfacial characteristics[63]. These structural parameters ultimately determine the effective transport properties for ions, electrons, and gases. A useful way to express this influence is through microstructure factors (M-factors), defined as the ratio of an effective transport property in the porous electrode to the intrinsic property of the dense parent material (Figure 2.10). Because these factors depend entirely on architecture, they provide a concise measure of how microstructure limits transport and therefore link observed morphology directly to electrode kinetics and overall PCC performance.

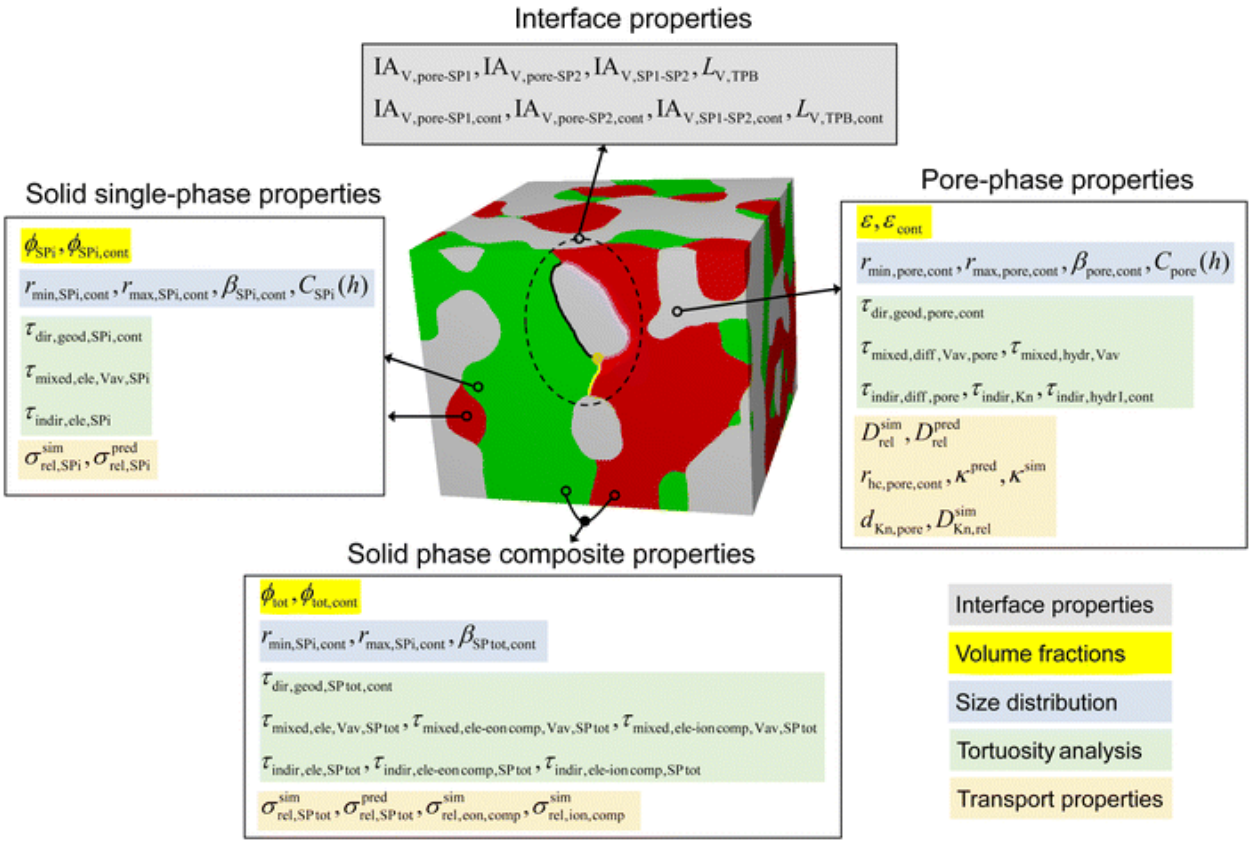


Figure 2.10. Overview of the characterized microstructure properties for the two solid-phases SP1 and SP2 (summarized as SPi, where i denotes 1 or 2), the total composite solid-phase SP tot, the pore-phase and the interface properties. The used variables are explained in the following sections[63].

Descriptors tied to connectivity, robustness, and evolution are critical for durability. Grain size, neck size, and coordination number (average contacts per particle) influence both conductivity and coarsening rates. Structures with weak necking may show high initial surface area but rapid performance decay due to coarsening and loss of percolation. Likewise, contact area at the electrode–electrolyte interface controls current constriction and interfacial polarization; poor contact can dominate losses even when the porous bulk is well designed. Because PCCs operate under humid conditions and often under reversible cycling, microstructural descriptors should be considered not only at beginning-of-life but also in terms of their tendency to evolve—how quickly nanoscale features coarsen, how pore networks densify, and how interfaces change under steam and redox gradients.

Key microstructural descriptors for PCC electrodes include porosity, pore size distribution, tortuosity and effective diffusivity, electronic and protonic percolation/connectivity, accessible surface and interfacial area density, thickness and layered architecture, and stability-related parameters such as grain/neck size and contact area at interfaces. Together these descriptors provide a quantitative language to connect processing and structure to performance, enabling rational microstructure optimization rather than trial-and-error tuning.

2.2.3 Fabrication routes and knobs

Electrode microstructure in protonic ceramic cells is not an accidental byproduct of processing; it is the direct outcome of fabrication choices that set pore formation, phase connectivity, adhesion, and long-term stability. Because PCC electrodes must simultaneously provide gas transport, electronic/protonic percolation, and abundant reactive surfaces, fabrication strategies are often judged by how well they allow these functions to be tuned independently. In practice, the most useful way to view fabrication is as a set of routes, each associated with a characteristic microstructure and a set of controllable knobs—parameters that can be adjusted to systematically shift porosity, tortuosity, reaction-zone thickness, and robustness under steam[67,68].

The most established route is the conventional porous composite electrode, typically made by screen printing, doctor blading, or slurry coating a mixed powder ink onto a dense electrolyte, followed by co-firing or sequential sintering. This approach is attractive for scalability and compatibility with established ceramic manufacturing. Its main microstructural knobs include powder characteristics (primary particle size, agglomeration state, morphology), the ratio of electronic conductor to proton conductor (or to ionic conductor in general), and the use of pore formers (graphite, PMMA, starch, polymer spheres) to create controlled porosity. Firing temperature and dwell time are decisive: higher temperatures strengthen necks and improve adhesion and electronic connectivity but also reduce surface area and can increase tortuosity by densifying fine pores. Ink rheology and printing conditions (solid loading, binder content, printing passes) further influence thickness uniformity and pore connectivity[25,69]. For PCCs, where oxygen-electrode performance is often sensitive to proton accessibility, the phase distribution in the composite, whether proton-conducting particles form a continuous network versus isolated islands, becomes a key microstructural control target.

A closely related but increasingly important strategy is the use of functional layers and graded microstructures. Instead of one uniform porous layer, the electrode is designed with a thin fine-feature region near the electrolyte to maximize reaction-site density and minimize interfacial polarization and a thicker, coarser backing region to minimize gas-transport resistance and provide mechanical support[60,70]. Practically, this can be achieved by sequential printing of inks with different pore-former loadings and particle sizes, or by applying a fine functional layer followed by a coarse current-collection layer. The knobs here are the thickness of each layer, the pore size hierarchy, and the continuity of electronic and protonic pathways across the gradient. This route is particularly effective when intermediate-temperature operation makes surface kinetics and interfacial transport dominant, because it allows the designer to place reaction sites where protons are available while keeping gas transport efficient deeper in the electrode.

To decouple transport from catalytic surface chemistry more strongly, many high-performance PCC electrodes adopt structurally differentiated architectures, in which a porous framework is designed first to provide robust gas and electron transport, while catalytic functionality is concentrated in a separate active region. A concept was realized using a finger-like porous current-collection layer fabricated by phase-inversion tape casting, followed by deposition of a screen-printed catalytic active layer[71]. The advantage of this approach is that the large, open pores in the current-collection layer promote gas access and relieve diffusion limitations, while the active layer supplies the electrochemically active surface and maintains good contact with the electrolyte (Figure 2.11). The key microstructural knobs therefore include the pore morphology and thickness of the current-collection layer, the thickness and composition of the active layer, and the interfacial contact between them. Because steam-rich operation can strongly intensify transport limitations in oxygen electrodes, this type of dual-layer design is especially valuable for maintaining stable electrolysis performance by spatially separating gas-transport and catalytic functions.

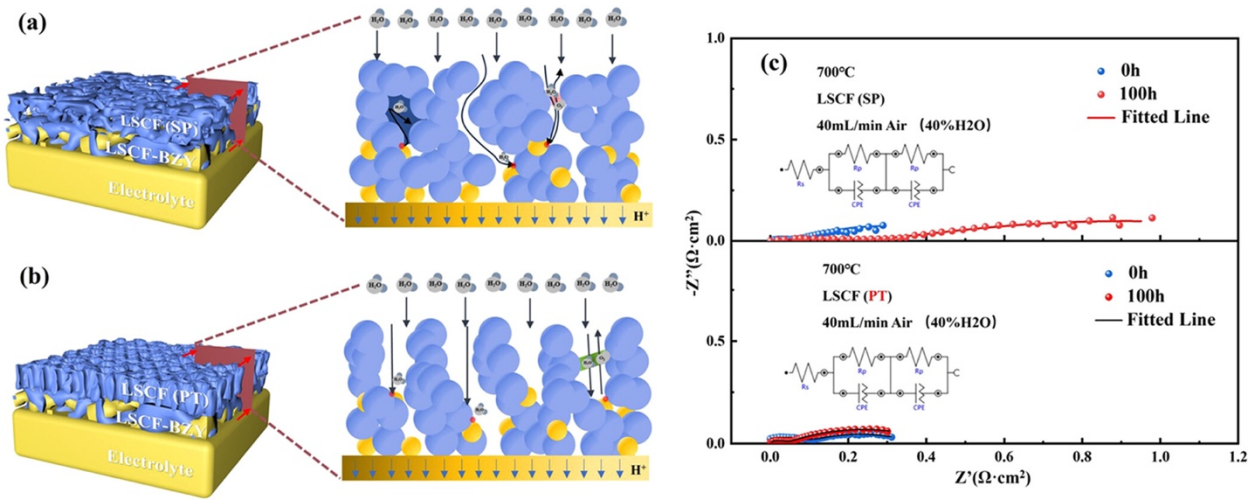


Figure 2.11. Schematic diagram of steam transport pathways in LSCF(SP)/LSCF – BZY (a) and LSCF(PT)/LSCF – BZY (b) air electrodes. EIS (Ohmic impedance removed) of the electrodes before and after 100 h of operation in 40% H2O–air (c)[71].

A third family of approaches uses 3D current-collecting frameworks or deliberately engineered macroporosity to reduce transport limitations at high current. Examples include metal meshes, fiber mats, foams, or patterned backbones integrated with porous ceramic layers[72]. The microstructural advantage is the creation of low-resistance electron pathways and large gas channels that reduce concentration gradients, while finer microstructures are reserved for the functional region near the electrolyte. The knobs here include framework geometry (wire diameter, spacing, foam pore size), infiltration or coating thickness onto the framework, and the degree to which the framework is integrated with the ceramic electrode (contact area, adhesion, thermal expansion compatibility). For reversible operation, such 3D architectures can also improve robustness by reducing current constriction and distributing electrochemical load more uniformly.

Microstructures can also be engineered through templating and directional pore-forming techniques. Freeze casting can produce aligned, low-tortuosity channels; sacrificial templates can introduce ordered macropores; and phase-inversion or polymeric templates can generate interconnected networks with controlled pore size distributions[71]. While these methods may be less common in standard cell manufacturing, they highlight a powerful concept for PCC electrodes: tortuosity is often as critical as porosity. The principal knobs include template size and loading, binder chemistry, and sintering schedules that preserve the intended architecture without collapse.

Across all routes, the sintering and thermal history act as universal knobs that determine neck growth, connectivity, adhesion, and long-term stability. A microstructure optimized for low polarization at beginning-of-life may not be stable if it relies on weakly bonded nanoparticles or highly metastable pore networks[73]. Thus, fabrication choices should consider not only initial performance but also how the microstructure evolves under steam and cycling. In PCCs, where oxygen electrodes face humid exposure and large chemical potential gradients, designs that provide stable backbones, strong interfacial bonding, and controllable nanoscale catalysts tend to outperform approaches that maximize surface area at the expense of structural robustness.

In conclusion, the main fabrication routes for PCC electrodes, conventional porous composites, layered/graded architectures, scaffold plus infiltration designs, 3D frameworks, and templated structures, offer complementary advantages and tradeoffs. The key knobs span powder characteristics, pore formers, ink formulation, deposition method, layer thickness, scaffold porosity and connectivity, infiltration chemistry and calcination conditions, and sintering schedules. Viewing these as adjustable levers provides a rational pathway to tailor porosity, tortuosity, percolation, and catalytic utilization toward high, durable performance in reversible protonic ceramic cells.

2.2.4 3D / hierarchical architectures

In protonic ceramic cells, better materials alone rarely deliver their full potential unless the electrode architecture is designed to move gas, electrons, and protons efficiently to the same places. This is the motivation for 3D and hierarchical electrodes: rather than relying on a single-scale sponge-like microstructure, the electrode is engineered across multiple length scales so that mass transport is fast at the macro/meso scale, while reaction-site density and catalytic functionality are maximized at the nano scale. Recent reviews of oxygen electrodes for protonic ceramic electrochemical cells increasingly highlight 3D structural design as a central strategy to overcome sluggish ORR/OER kinetics at intermediate temperatures while maintaining stability under steam[74].

A useful way to think about hierarchical design is a three-level separation of functions. At the largest scale, the electrode needs “highway” pathways—open channels or macropores—to minimize pressure drop and concentration gradients, especially under high steam utilization in

electrolysis[59]. At the intermediate scale, a percolated porous backbone must provide continuous electronic conduction, robust mechanical support, and stable adhesion to the electrolyte. At the finest scale, nanoscale features (nanoparticles, conformal coatings, or nano-porous skins) supply the high density of active sites needed for fast surface exchange and charge transfer. When these scales are combined properly, the architecture prevents a common failure mode of conventional porous electrodes: a large fraction of internal surface exists, but only a small portion is truly electrochemically addressable because gas access, electronic pathways, and protonic pathways do not overlap well.

In protonic ceramic systems, 3D engineering has been shown to directly regulate the competition between mass transport and charge transfer at reduced temperature, where oxygen-electrode polarization often dominates. For example, Bian and co-workers demonstrated that structural 3D engineering of a PCFC cathode can enhance ORR performance, notably at low temperature, emphasizing that porosity must be tuned to avoid trading transport gains for charge-transfer penalties[57]. This illustrates an important architectural principle: increasing porosity is not automatically beneficial unless the remaining solid network still preserves continuous charge pathways and sufficient reaction-site density near proton-accessible regions.

A particularly powerful class of hierarchical designs in PCCs is the porous-backbone plus infiltration approach, where a mechanically robust, percolated skeleton is created first and then functionalized with a high-activity catalytic phase. This strategy decouples structural requirements (porosity, tortuosity, backbone conduction, adhesion) from catalytic requirements (surface exchange, active site density), enabling higher utilization of nanoscale catalysts without collapsing gas pathways. A clear example is the $LaCoO_3$-infiltrated porous BZY20 backbone oxygen electrode for PCECs, which achieved low polarization resistance and showed strong durability in humid air testing (reported stability at 600 °C in 10 vol% humidified air for extended operation). Architecturally, the key advantage is that the proton-conducting backbone improves proton accessibility throughout the electrode thickness, while the infiltrated catalyst decorates internal surfaces, expanding the effective reaction zone beyond a narrow electrolyte interface[75].

Beyond infiltration, hierarchical electrodes often employ functional-layer concepts: a thin, fine-feature layer adjacent to the electrolyte, where proton access is highest and interfacial losses are

most sensitive, supported by a coarser, highly permeable backing layer for gas delivery and current collection[75,76]. This fine-to-coarse hierarchy is especially valuable for oxygen electrodes under steam, where local gradients in p_{H_2O} and p_{O_2} can become severe at high current density. By providing fast gas highways and reducing tortuosity, hierarchical pores help suppress concentration polarization that would otherwise masquerade as slow kinetics.

Recent work also shows that 3D/hierarchical concepts can be integrated with surface or interphase nanoengineering to simultaneously boost activity and mitigate degradation. For reversible PCC operation, nanoengineered oxygen electrodes, such as nanoparticle-coated or infiltrated surfaces, have been reported to reduce polarization resistance and improve reversible cycling stability, illustrating how nanoscale catalytic features can be hosted by a stable porous framework[77]. This style of design is attractive because it addresses the classic activity–stability tension: the backbone preserves transport and mechanical integrity, while the nano-layer provides high initial activity and can be refreshed or stabilized more readily than a bulk composition change.

Importantly, hierarchical architecture is not only a strategy for maximizing peak performance; it can also directly improve durability. In the self-architectured ultraporous 3D steam electrode reported, the initial microstructure already combined several durability-relevant features: a highly porous fibrous framework with hierarchical gaps for rapid steam transport, no obvious bulk-frame disconnection, and well-adhered contact between the steam electrode and electrolyte through particle-filled interfacial junctions[78]. More importantly, post-test analysis showed that the architecture did not simply resist degradation passively; it reorganized beneficially during operation (Figure 2.12). After electrolysis, PBSCF particles migrated to bridge neighboring fibers and to eliminate gaps at the electrode/electrolyte contact, producing a more uniform interface and increasing the active reaction area. This “bridging” effect generated additional electron/proton transport pathways and was correlated with a decrease in ohmic resistance rather than the rapid decay typically expected under humid electrolysis conditions. In this sense, the Wu et al. study shows that a well-designed 3D architecture can enhance durability not only by improving gas transport and reducing local concentration gradients, but also by enabling interfacial self-optimization under bias, thereby preserving or even improving electrode utilization during operation.

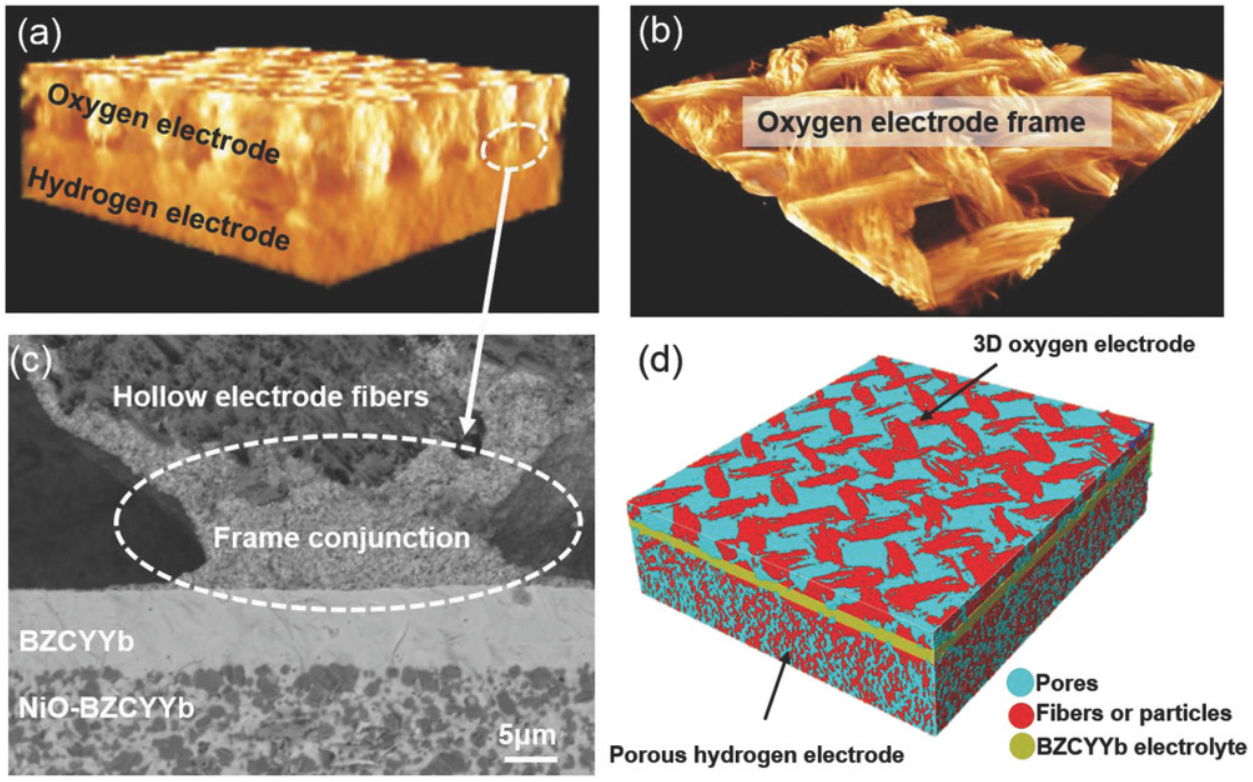


Figure 2.12. (a) 3D X-ray microscopic image for the cell consisting of hydrogen electrode (bottom layer), electrolyte (invisible) and 3D steam electrode (top layer). (b) The bulk electrode frame with hierarchical gaps, which would facilitate fast mass transfer; (c) SEM image for the cross section of the cell shows the contact area between steam electrode frame and electrolyte and (d) reconstructed 3D image for the cell with dimension of 0.4 × 0.4 × 0.1 mm3. Three layers of cell components, that is, fibrous PBSCF electrode with a porosity of 57.7%, dense BZCYYb electrolyte, and sponge-like pore Ni-BZCYYb hydrogen electrode support, are obviously distinguished[78].

From a practical fabrication standpoint, 3D/hierarchical architectures can be realized through several routes, each offering different degrees of control over pore hierarchy and connectivity: (i) engineered pore formers and graded printing to create bimodal pores, (ii) scaffold sintering followed by infiltration/coating to generate nano-catalyst layers, and (iii) self-architectured ultraporous electrodes that create low-tortuosity pathways favorable for steam electrolysis at intermediate temperatures. The broader literature on proton-conducting electrolysis cells includes examples of 3D self-architectured steam electrodes enabling efficient hydrogen production below

600 °C, underscoring how macroporous architectures can relieve mass-transfer limits while maintaining active area.

Despite these advantages, hierarchical electrodes introduce design constraints that must be managed. High surface area is beneficial only if it remains electrochemically accessible and structurally stable under steam and cycling. Infiltrated nanoparticles can sinter and lose activity; macroporous structures can reduce mechanical strength or contact quality; and aggressive architectures can increase processing complexity or reduce reproducibility. Therefore, successful 3D designs typically emphasize a stable backbone, controlled pore hierarchy, and robust electrode–electrolyte bonding, because even the best internal architecture cannot compensate for interfacial constriction or delamination.

Overall, 3D and hierarchical architectures provide a concrete pathway to break the traditional tradeoff between activity and transport in PCC electrodes. By separating functions across length scales—fast gas access at the macro scale, percolated conduction and mechanical support at the meso scale, and high-density active sites at the nano scale. These designs expand the effective reaction zone, suppress concentration polarization, and improve robustness under steam-rich reversible operation.

2.2.5 Stability and quantification

Microstructural engineering in PCC electrodes is only successful if the architecture remains functional over time under steam exposure, electrochemical polarization, and repeated switching between PCFC and PCEC modes. Many oxygen electrodes can be made highly active at beginning-of-life by increasing surface area or introducing nanoscale catalysts, but these gains often decay because porous networks are thermodynamically driven to coarsen, densify, or chemically reconstruct[48]. In practice, long-term performance is governed by whether the microstructure can preserve (i) open, low-tortuosity gas pathways, (ii) continuous electronic and protonic percolation, (iii) stable, accessible catalytic surface area, and (iv) robust contact at the electrode–electrolyte interface. If any one of these functions degrades, polarization resistance increases even when the bulk composition remains unchanged.

The dominant stability challenge is microstructural evolution. At intermediate temperatures, porous ceramics and infiltrated nanoparticles tend to reduce surface energy through grain growth and neck thickening, which lowers surface area and can shrink the electrochemically active region. Infiltrated catalysts are especially vulnerable: nanoparticles can sinter, migrate, or agglomerate, reducing the density of active sites and altering phase connectivity[71]. Steam often accelerates these processes by enhancing surface diffusion and by changing surface termination chemistry, which can promote ripening or local dissolution–reprecipitation for some oxides. In addition, electrochemical operation itself can bias evolution: high local overpotential and non-uniform current distribution create hot spots that coarsen faster, leading to a feedback loop where current becomes even more localized as pathways degrade.

A second stability dimension is pore-network integrity. Porosity is not static; it can evolve via partial sintering, pore collapse, or blockage by secondary phases. Fine pores that initially provide high surface area may gradually close, increasing tortuosity and amplifying gas concentration gradients. This matters strongly in electrolysis mode, where high steam utilization can generate steep local gradients in $p_{H_2O}$and p_{O_2}. If transport becomes restricted, concentration polarization rises and local chemical potentials become extreme, which can further drive reconstruction and accelerate degradation. Hierarchical architectures are often more stable in this sense because macropores act as persistent highways even as finer features evolve.

The stability of PCC electrodes is governed not only by the preservation of porous morphology, but also by the integrity of the buried electrode–electrolyte and hetero-phase interfaces. A recent work demonstrates this clearly through an atomic trapping strategy in which scalable co-sintering restructures the interfacial chemistry between BSCF and Ru@CeO_2, driving Ru migration into the perovskite matrix and forming strongly coupled heterointerfaces (Figure 2.13). This interfacial reconfiguration promotes electron redistribution, generates oxygen vacancies, and improves both triple conductivity and hydration kinetics, thereby strengthening bifunctional oxygen-electrode performance while suppressing degradation[79]. The resulting cell delivered high reversible activity together with a very low degradation rate of 0.09 mV h^{-1} over 400 h at 600 °C. These findings show that interface design should be treated as a core element of microstructural stability, because a chemically optimized and defect-active heterointerface can simultaneously enhance transport, catalytic function, and long-term durability in reversible protonic ceramic cells.

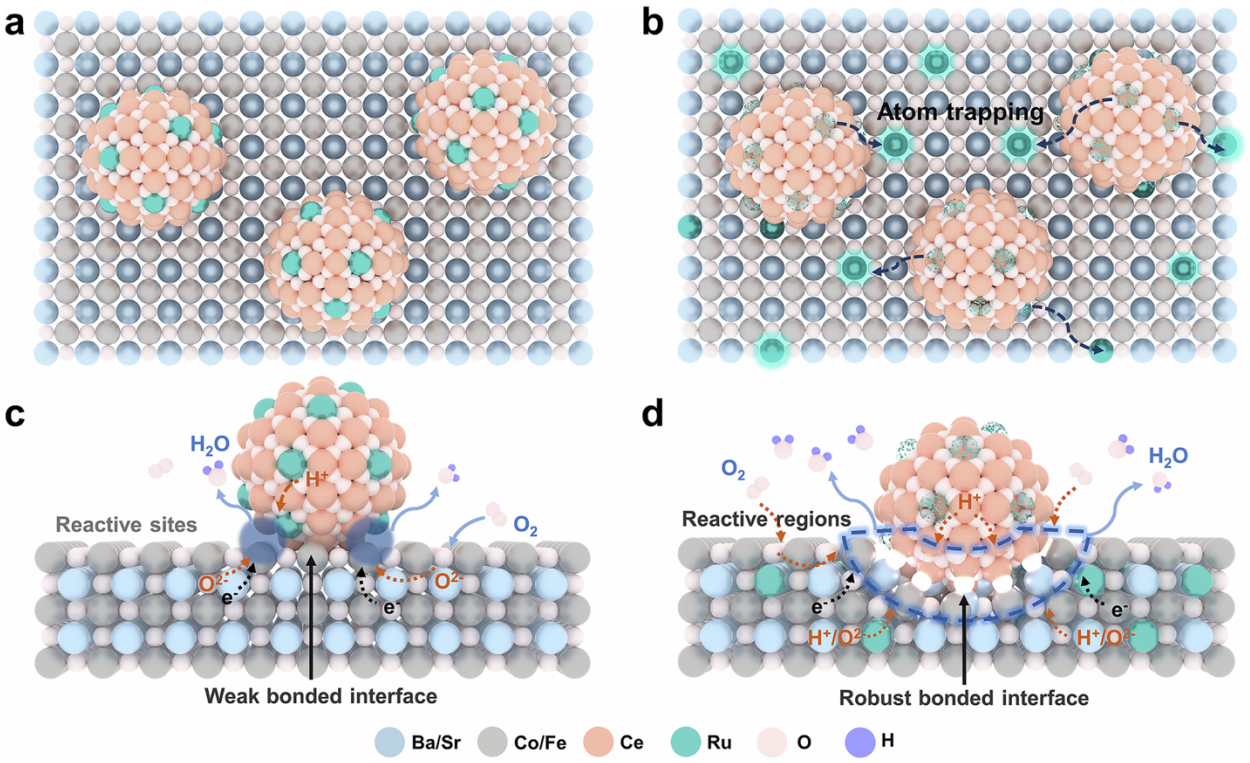


Figure 2.13. Schematic illustration of atom trapping. (a, b) Distribution of Ru element in heterogeneous catalyst before and after heat treatment. (c, d) Heterogeneous interface structure before and after atom trapping[79].

Because stability is multiscale, quantification must also be multiscale and should be reported in a way that connects structure to function[66]. At the simplest level, 2D SEM (plan-view and cross-section) remains invaluable for tracking thickness, gross porosity, grain growth, cracking, and interface quality. Quantitative image analysis as pore fraction, average pore size, particle size distributions, and neck size statistics can convert qualitative micrographs into comparable metrics. For composite electrodes, phase segmentation can estimate connectivity and the spatial distribution of proton-conducting versus electronically conducting phases, which is often more predictive than composition alone.

However, many critical descriptors (tortuosity, percolation pathways, constriction points) are inherently three-dimensional, and 2D images can be misleading. This is where 3D methods such as FIB-SEM tomography, X-ray micro-CT/nano-CT, or serial sectioning become powerful: they allow direct reconstruction of pore and solid networks so that porosity, tortuosity, connectivity,

and interfacial area density can be computed rather than inferred. Once a 3D volume is reconstructed and segmented, transport-relevant quantities—effective diffusivity or permeability, can be estimated using numerical tools (e.g., random-walk diffusion models or lattice-Boltzmann simulations)[80]. For hierarchical electrodes, 3D data are particularly valuable because performance often hinges on whether macropore networks truly provide through-thickness highways and whether fine catalytic regions remain connected to both gas and charge pathways.

Surface area and catalytic accessibility require careful interpretation. BET surface area can be informative for powders, but for intact electrodes it may not reflect the electrochemically accessible surface area, which depends on gas access and charge-carrier access simultaneously. In practice, accessibility is better assessed by combining microstructural metrics (pore openness + percolation) with electrochemical signatures (polarization components and their dependence on gas composition)[81]. For infiltrated electrodes, quantification of catalyst loading (wt% or $mg \cdot cm^{-2}$), particle size evolution, and surface coverage—ideally before and after aging—helps distinguish whether degradation is driven by catalyst coarsening versus backbone or interface changes.

Electrochemical tools provide the complementary functional quantification that links microstructure to performance. EIS is central because it separates the time constants associated with ohmic losses, interfacial charge transfer, and gas transport. When combined with distribution of relaxation times (DRT), evolving microstructure can often be diagnosed: growth of low-frequency features frequently correlates with increasing mass-transport limitation (e.g., rising tortuosity, pore blockage), while increases in mid-frequency processes can indicate shrinking reaction-zone accessibility or deteriorating interface contact[41]. Importantly, these interpretations are most convincing when paired with structural measurements—showing, for example, that a rise in the low-frequency arc accompanies pore closure or loss of macropore continuity.

Best practice for stability and quantification is therefore to report microstructure and electrochemistry as paired before/after datasets under well-defined aging protocols (constant current/voltage, steam fraction, temperature, and cycling history). At minimum, this means tracking (i) ASR_Ω and ASR_p evolution, (ii) one or more structural descriptors tied to transport (porosity/tortuosity or macropore fraction), (iii) one or more descriptors tied to reaction-site density (particle size, neck size, catalyst coverage), and (iv) interface quality (contact area,

presence of cracks or secondary layers). When these metrics move together in a consistent way, microstructural stability becomes a quantifiable design target rather than an after-the-fact explanation for performance loss.

2.3 Electrode Catalysis and Defect Engineering

2.3.1 ORR/OER kinetics in protonic systems

In protonic ceramic cells, the oxygen-side electrode is responsible for oxygen reduction in fuel-cell mode and water oxidation/oxygen evolution in electrolysis mode. These reactions often dominate the polarization resistance at intermediate temperatures because they require the coordinated delivery of multiple species—gas-phase molecules, electronic carriers, and protonic defects within a porous, humid environment[9,82]. Unlike oxide-ion solid oxide cells, where the oxygen electrode primarily couples oxygen molecules to oxide ions (O^{2-}), protonic systems inherently involve proton participation at the oxygen electrode, meaning the local kinetics depend strongly on proton availability, hydration state, and the stability of protonic transport pathways near the electrode. Reviews focused on oxygen electrodes for PCCs consistently identify ORR/OER kinetics at reduced temperature as a central barrier to high performance and durability.

For PCFC and PCEC modes, two directions share many microscopic steps (adsorption, surface intermediates, charge transfer), but the chemical potentials and flux directions reverse, so the dominant limitations and degradation drivers can differ markedly between ORR and OER—especially under steam-rich conditions typical of electrolysis and reversible cycling. At the mechanistic level, ORR/OER in protonic systems is often described as a sequence of coupled processes occurring on or near the oxygen-electrode surface: (i) gas transport to the surface through the pore network, (ii) adsorption and activation of O_2 (ORR) or H_2O (OER), (iii) charge transfer involving electrons/holes in the electrode, and (iv) incorporation/removal of ionic species that ultimately connect to the electrolyte's protonic current[83]. In ORR, oxygen must be reduced and ultimately transformed into water through protonation steps; in OER under steam electrolysis, water must be activated and oxidized, producing oxygen while releasing protonic defects that must be transported away efficiently. Because both electrons and protons are required (either consumed or produced) at the oxygen electrode, the reaction rate is strongly influenced by how well electronic

conduction, protonic access, and gas access overlap in space, linking catalysis inseparably to electrode architecture and defect transport.

A key concept now emerging for PCFC cathodes is that the oxygen reaction should be understood as a proton-coupled oxygen reduction reaction rather than as conventional oxygen-ion chemistry alone. Because protons, oxygen-related defects, and electronic carriers all participate, the mechanism is intrinsically multiparticle and can follow different pathway classes depending on the cathode's proton transport and proton release behavior. It shows that this complexity is not just conceptual: for two widely studied cathodes, PBSCF and BCFZY, the rate-determining step was found to be different—vacancy-assisted O_2 dissociation for PBSCF, but proton-coupled OH adsorbate formation for BCFZY—and this contrast was traced to differences in their proton uptake and release mechanisms rather than to a single universal ORR pathway (Figure 2.14)[84]. The study therefore argues against assigning the mechanism by assuming a priori most probable route and instead supports a pathway-agnostic microkinetic interpretation grounded in experimental observables. In practical terms, this means that the measured polarization of PCFC cathodes can arise from fundamentally different limiting steps depending not only on temperature, steam content, and oxygen partial pressure, but also on the specific cathode chemistry and its proton-coupled transport characteristics.

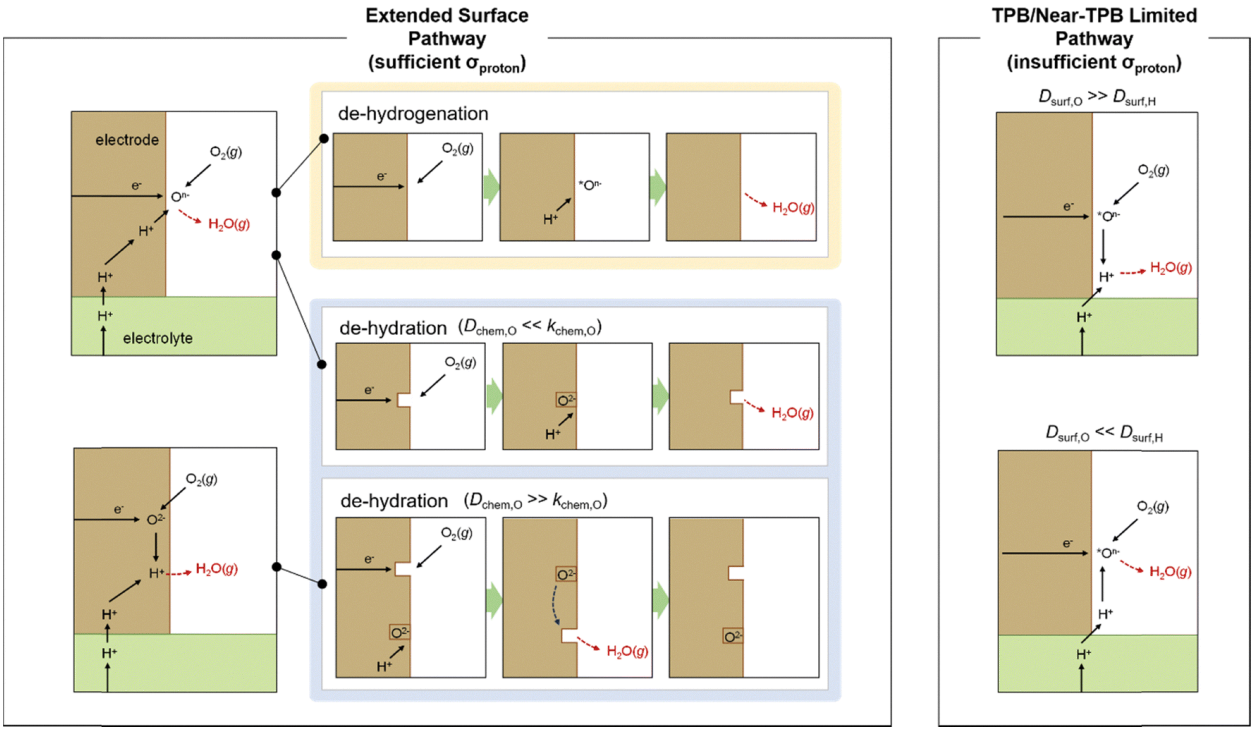


Figure 2.14. Five representative reaction pathways for proton-coupled oxygen reduction reaction in PCFC cathodes are governed by the proton conductivity of the cathode material. In the TPB/Near-TPB limited pathway (insufficient σ_{proton}), the dominant route depends on the relative diffusivity of protons and oxygen species at the cathode surface. In the extended surface pathway (sufficient σ_{proton}), proton release occurs *via* either a dehydrogenation mechanism (not involving oxygen vacancies) or a dehydration mechanism (involving oxygen vacancies), the latter of which is further classified based on the relative rates of bulk oxygen diffusion ($D_{chem,O}$) and surface oxygen exchange ($k_{chem,O}$)[84].

In many PCC oxygen electrodes, the bottleneck can be framed in one of two intertwined ways. First, the system may be limited by surface exchange and charge transfer, where oxygen or water activation and intermediate conversion at the surface is slow. Second, it may be limited by proton delivery or removal to the reactive region, especially if protons are only available very close to the electrolyte interface. In the latter case, even a highly active surface cannot be fully utilized because only a thin interfacial region has the necessary protonic current[28]. This is why composite oxygen electrodes that incorporate a proton-conducting phase, or oxygen electrodes engineered to transport protons themselves, often show disproportionate gains: they expand the effective reaction

zone from a narrow boundary into a finite electrode volume, reducing local current constriction and lowering polarization.

Steam plays a particularly important, and sometimes, counterintuitive role in these kinetics. A humid atmosphere can enhance proton uptake in proton-conducting phases and thereby improve proton availability within the electrode region; however, excessive local water/steam can also alter surface coverage, shift defect equilibria, and change which elementary step becomes limiting. A recent study on cathode water management in PCFCs explicitly showed that ORR performance can be optimized by balancing hydration and ORR through operating conditions that control local water and oxygen contents around the cathode, highlighting that the oxygen electrode is simultaneously a catalytic interface and a dynamic defect-chemical system. This sensitivity helps explain why ORR kinetics and measured polarization may vary significantly with air flow rate, steam fraction, and current density, even for nominally identical materials.

One major materials strategy to improve oxygen-electrode kinetics in protonic systems is the development of triple-conducting oxides (TCOs) that transport $H^+/O^{2-}/e^-$. By enabling proton transport within the oxygen electrode itself, rather than confining protons to the electrolyte boundary, TCOs can fundamentally reshape the reaction-zone geometry and reduce sensitivity to microstructural percolation limitations. A widely cited example is a $PrNi_{0.5}Co_{0.5}O_{3-\delta}$-based oxygen electrode reported as a triple-conducting material that supports both fuel-cell and electrolysis operation at 400–600 °C, illustrating how enhancing proton transport in the oxygen electrode can boost bifunctional performance. Broader discussions of triple-conducting behavior and its impact on oxygen-electrode performance also appear in dedicated reviews of TCOs and PCFC cathodes[10,28].

In steam electrolysis mode, oxygen-electrode kinetics are often challenged by the need to sustain high steam conversion rates while maintaining stable surface and interface chemistry. The electrode must efficiently activate water, transfer charge, and form O–O bonds leading to oxygen evolution, all while continuously generating protons that must be transported away through the electrolyte. Reviews on protonic ceramic electrolysis cells emphasize that sluggish OER kinetics and electrode instability under steam remain key barriers to scale-up, especially at reduced temperatures where kinetic penalties are more severe. In practice, the rate limitation in electrolysis

can shift toward mass transport (steam delivery through pores), interfacial transport (proton transfer across the electrode–electrolyte junction), or surface chemistry (accumulation of hydroxylated species, reconstruction, segregation), depending on architecture and material selection[76].

Because ORR and OER impose different local chemical potentials and defect flux directions, reversible operation can produce kinetic asymmetry: an electrode optimized for fast ORR may not automatically exhibit equally fast OER, and vice versa. This is one reason why bifunctional oxygen electrodes are an active research focus in reversible PCCs and why kinetic descriptors must be interpreted alongside stability and defect-chemical response under both modes. From a practical standpoint, the most robust route to improved oxygen-electrode kinetics in protonic systems is therefore not a single lever, but a coupled approach: ensure abundant and stable reactive surface sites, enable effective proton accessibility via composite design or triple conduction, minimize transport polarization through hierarchical porosity, and stabilize the interface so that the defect landscape at the reaction zone remains favorable during long-term, steam-rich reversible operation.

2.3.2 Catalytic descriptors

Because oxygen-electrode polarization in protonic ceramic cells reflects a chain of coupled steps (gas transport → surface chemistry → charge transfer → incorporation/transfer of ionic species), it is useful to describe catalytic quality using descriptors—measurable or computable quantities that correlate with ORR/OER rates and help rationalize why one oxide outperforms another. In PCCs, the most useful descriptors are those that link (i) surface exchange activity, (ii) defect chemistry and redox flexibility, and (iii) electronic structure / metal–oxygen bonding, while also acknowledging that the best catalyst must remain stable in steam and under cycling[85].

A primary kinetic descriptor is the oxygen surface exchange coefficient (often reported as k^*or k_{chem}), which captures how rapidly oxygen-containing species are incorporated at the surface and transferred into the solid. In many perovskite-type oxygen electrodes, k^*correlates strongly with polarization resistance at intermediate temperatures because surface exchange is frequently rate-limiting[8,86]. Complementary to $k^*$is the chemical diffusion coefficient (D_{chem}), which reflects the mobility of oxygen-related defects (and, in some systems, coupled ambipolar transport). In

simplified terms, k^* describes how fast the surface works, while D_{chem} describes how fast the bulk or near-surface region can accommodate the exchanged species. A material with fast surface exchange but sluggish defect transport can still polarize strongly, and vice versa; high performance typically requires both to be sufficiently large in the operating window.

Defect-chemical descriptors are especially powerful in PCC oxygen electrodes because ORR/OER rates are tightly coupled to oxygen vacancy chemistry and redox response. The oxygen vacancy concentration (often expressed via oxygen nonstoichiometry, δ, in $ABO_{3-\delta}$) is a practical descriptor because vacancies provide sites for oxygen incorporation and strongly influence adsorption, dissociation, and charge-transfer steps[87]. Related to this is the oxygen vacancy formation energy or vacancy formation enthalpy, which describes how energetically easy it is to create vacancies. In general, a lower vacancy formation energy tends to promote higher vacancy concentrations and faster exchange kinetics up to a point. If vacancy formation is too favorable, the lattice oxygen sublattice can become overly labile, which may accelerate steam-driven reconstruction, cation segregation, or phase instability during electrolysis. Thus, in PCCs the design goal is often optimized vacancy energetics rather than maximized vacancies.

Closely connected is redox flexibility of the transition-metal and sometimes A-site cations, which determines how the oxide accommodates charge during oxygen exchange. Useful descriptors here include the average transition-metal valence, the accessible redox couples under operating pO_2 and steam activity, and a qualitative or quantitative measure of redox buffering capacity of how strongly the material resists large swings in local valence during polarization[88]. In steam-rich reversible operation, materials that can redistribute charge smoothly, without large, localized redox changes, often show improved stability and slower polarization growth because they reduce the driving force for reconstruction at the surface and interface.

Electronic-structure descriptors provide a deeper basis for these catalytic trends. Recent analysis by Siebenhofer et al. shows that fast oxygen exchange on mixed-conducting oxides can be understood through three coupled material properties: reducibility, adsorption energetics, and surface acidity (Figure 2.15). In this framework, the bulk O 2p-band center relative to the Fermi level is a useful descriptor because it correlates with oxide reducibility and therefore with oxygen-vacancy formation energetics, oxidation enthalpy, and the availability of electronic charge carriers

needed for oxygen exchange[89]. At the same time, the study emphasizes that the O 2p-band center alone is not sufficient to describe surface reaction kinetics. A second key descriptor is the work function, which reflects the surface electron chemical potential and is closely linked to surface acidity/basicity and adsorption strength of oxygenated intermediates. The resulting design principle is that fast oxygen exchange generally requires a shallow O 2p-band center together with a low work function. Importantly, these descriptors must still be balanced against stability, since tuning the lattice toward higher reducibility and greater oxygen activity can also increase the susceptibility of the surface to reconstruction or degradation under reactive conditions.

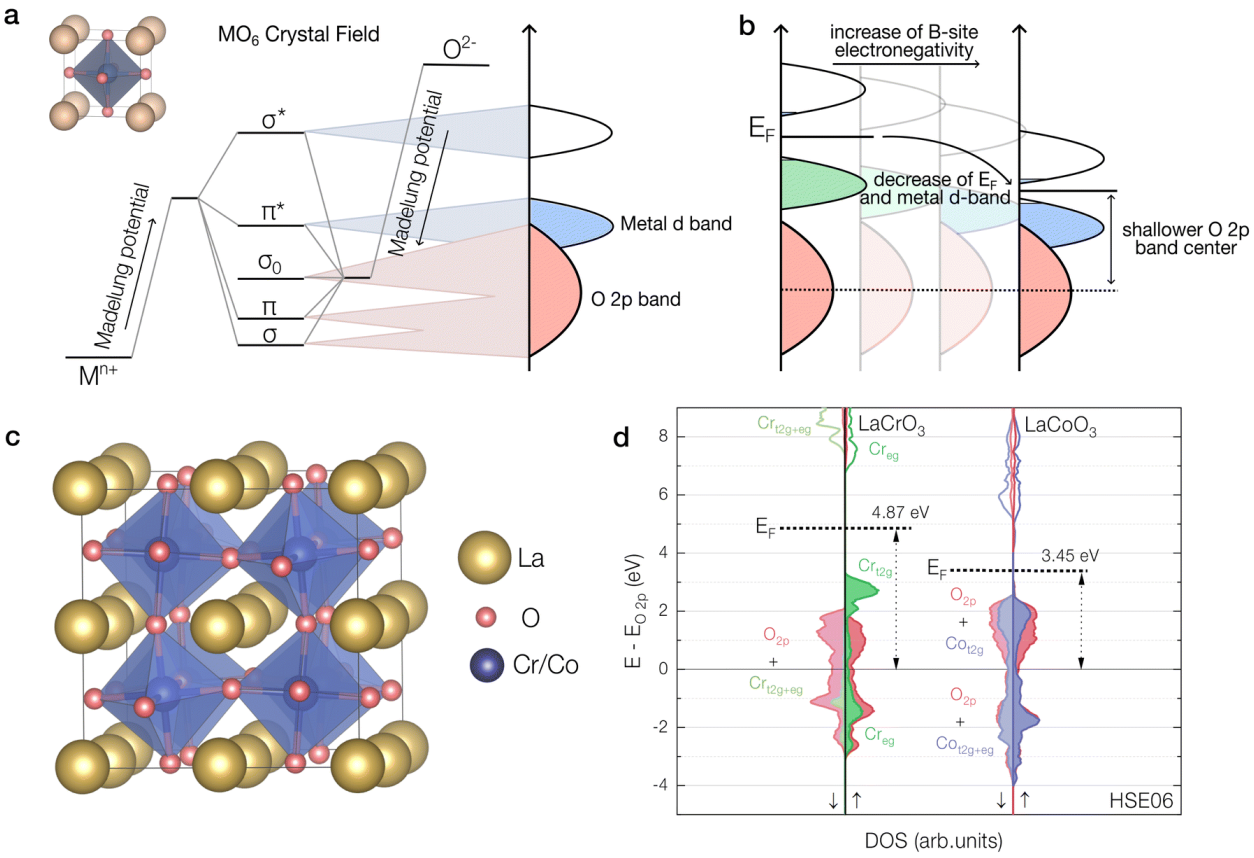


Figure 2.15. (a) Simplified evolution of an exemplary transition metal perovskite oxide band structure from the molecular orbital diagram for octahedral MO6. (b) Qualitative change of the electronic structure with increasing B-site cation electronegativity. EF and the metal d-band shift down, leading to a shallower O 2p band center. (c) Model of a 2 × 2 × 2 perovskite unit cell used for hybrid calculations (tilting angles slightly differ between LaCoO3 and LaCrO3). (d) Projected

densities of states for LaCrO3 and LaCoO3, with the energy of the respective centroid of the occupied O 2p states taken as the reference energy[89].

Because PCC oxygen-electrode reactions are proton-coupled, descriptors linked to hydration and proton availability can matter as much as classic ORR descriptors. For composite electrodes containing proton-conducting phases, the local protonic conductivity and the hydration thermodynamics of the proton conductor influence how far protons can access the electrode and therefore how large the effective reaction zone becomes[84,90]. For so-called triple-conducting or proton-permeable oxygen electrodes, descriptors include the material's hydration capability and its proton mobility under relevant $pH_2O$and temperature. In practice, a catalyst that is excellent for oxygen exchange but poorly coupled to proton supply may exhibit high apparent polarization because only a thin interfacial region can participate.

There are also pragmatic, device-facing descriptors that translate directly into performance. Electronic conductivity (and its pO_2dependence) matters because insufficient electronic transport introduces internal voltage drop and constricts current to limited pathways, increasing local overpotential[20,51,91]. Work function and surface charge-transfer propensity can influence how readily electrons participate in surface steps, especially when space-charge effects or interfacial barriers are present. At the porous-electrode level, the effective catalytic descriptor becomes a combination of intrinsic activity and accessibility, meaning that high k^*or favorable vacancy energetics must be paired with microstructures that provide gas access and percolated charge pathways.

PCCs catalytic descriptors must be considered together with stability descriptors, because the oxygen electrode operates in humid atmospheres and experiences large chemical potential swings during reversible cycling. Useful stability-oriented descriptors include the tendency for A-site cation segregation, the susceptibility to steam-induced surface hydroxylation or carbonate formation when CO_2 is present, and the propensity for phase reconstruction under high polarization. In practical terms, the most valuable catalysts are those that sit in an activity–stability sweet spot: sufficiently strong covalency and vacancy activity to enable fast exchange, but sufficiently buffered defect chemistry and surface stability to resist steam-driven degradation.

Catalytic performance in protonic oxygen electrodes can be rationalized using a compact set of descriptors: surface exchange (k^*), defect transport (D_{chem}), vacancy concentration and vacancy formation energetics, redox flexibility/buffering, electronic-structure metrics such as O 2p-band center and metal–oxygen covalency, and proton-related descriptors (hydration capability and proton mobility) when proton participation is limiting. Framing materials selection through these descriptors helps convert empirical optimization into design logic, clarifying which knob (surface exchange, defect chemistry, proton access, or stability) must be tuned to lower polarization in both ORR and OER directions.

2.3.3 Bulk tuning strategies

Bulk tuning strategies aim to improve oxygen-electrode performance by engineering the *intrinsic* properties of the solid, its defect chemistry, transport coefficients, and redox response, rather than relying solely on microstructural refinements or surface additives. In protonic ceramic cells, bulk tuning is especially impactful because ORR/OER rates are strongly coupled to oxygen vacancy chemistry, metal–oxygen covalency, and the ability of the electrode to accommodate proton participation under steam. The central idea is to place the electrode material in an activity–stability window where oxygen exchange and charge transfer are fast at 400–600 °C, while the lattice remains sufficiently buffered to resist steam-driven reconstruction and polarization growth during reversible cycling[82].

A first and widely used lever is composition tuning through aliovalent doping, which directly controls oxygen vacancy concentration and redox flexibility. Substituting lower-valence cations on the A-site or B-site increases the driving force for oxygen vacancy formation, often enhancing surface exchange and lowering polarization resistance[28]. Conversely, higher-valence substitutions can suppress excessive vacancy formation when the lattice is too labile. In practice, the goal is not simply more vacancies, but a vacancy population that is high enough to promote fast oxygen exchange while avoiding instability from overly low vacancy formation energy. Doping also tunes the average transition-metal valence, thereby adjusting the availability of redox couples that participate in charge compensation during ORR/OER. This is particularly important in steam-rich electrolysis, where the electrode experiences large chemical potential gradients and repeated redox perturbations.

A second bulk strategy is B-site transition-metal mixing to tailor metal–oxygen bonding and electronic structure[91]. Many high-performance oxygen electrodes are based on perovskites or layered perovskites containing mixed Co/Fe/Ni/Mn chemistries. Mixing can shift the O 2p-band center relative to the Fermi level, alter covalency, and optimize adsorption strength of oxygenated intermediates, effectively tuning the intrinsic catalytic landscape without changing the microstructure. At the same time, B-site mixing can improve thermodynamic stability by distributing redox burden across multiple cations, reducing extreme valence swings on any single species. This redox sharing is often beneficial for maintaining stable surface states during reversible operation, especially when steam accelerates reconstruction in highly reducible or highly covalent lattices.

A third approach is selecting or engineering structure families that intrinsically support fast transport and stable defect chemistry. Beyond simple perovskites, layered perovskites or Ruddlesden–Popper phases can provide anisotropic oxygen diffusion pathways and distinct surface terminations that alter oxygen exchange kinetics[88,90]. Some structures naturally host higher oxygen vacancy concentrations or more facile oxygen migration, which can reduce polarization at intermediate temperatures. However, structure selection must be balanced against chemical compatibility and steam stability, since layered oxygen-deficient frameworks can undergo ordering/disordering transitions or chemical expansion that influence adhesion and long-term durability at the electrode–electrolyte interface.

A fourth bulk tuning lever is engineering the balance of conduction modes, electronic conduction, oxygen-ion defect transport, and proton uptake/transport in the oxygen electrode. For many PCC oxygen electrodes, the apparent kinetics are limited not only by surface exchange but also by the spatial extent of proton accessibility[88]. Bulk strategies that increase mixed conduction, without introducing problematic electronic leakage when used as an electrolyte, can expand the effective reaction zone within the electrode. This is one motivation behind triple-conducting or proton-permeable oxygen electrodes: by enabling protonic participation within the electrode bulk under humid conditions, the reaction is not confined to a narrow region near the electrolyte, reducing current constriction and lowering polarization. Even when bulk proton conduction is modest, improved hydration affinity and compatible defect chemistry can enhance proton transfer at the near-interface region, which is often the kinetic bottleneck.

Another important bulk strategy is chemical stabilization through A-site design, because A-site chemistry affects not only tolerance factor and phase stability, but also surface basicity**,** hydration affinity, and proton uptake behavior. A work highlights this point using the $NSTF_{0.3}$/NF system: the Na-containing NF second phase exhibited stronger surface protonation than the parent perovskite, and TOF-SIMS/H_3O^+ depth profiling showed that this enhanced hydronation promoted proton enrichment from the surface into the near-surface region (Figure 2.16)[92]. The resulting electrode concept was not simply more hydration is better, but rather that A-site-related chemistry can be tuned to balance ORR activity with proton availability at low steam content, thereby minimizing the competition between oxygen adsorption and excessive water adsorption on the cathode surface. This provides a more refined view of A-site design in PCC oxygen electrodes: partial substitution or nonstoichiometry can stabilize the lattice while also adjusting proton affinity and defect chemistry, helping the material retain activity under humid operation without pushing it into an overly labile, segregation-prone regime. In practical terms, bulk stabilization therefore often means moving away from the most oxygen-reactive composition toward one that better balances activity, hydration, and structural robustness over long-term operation.

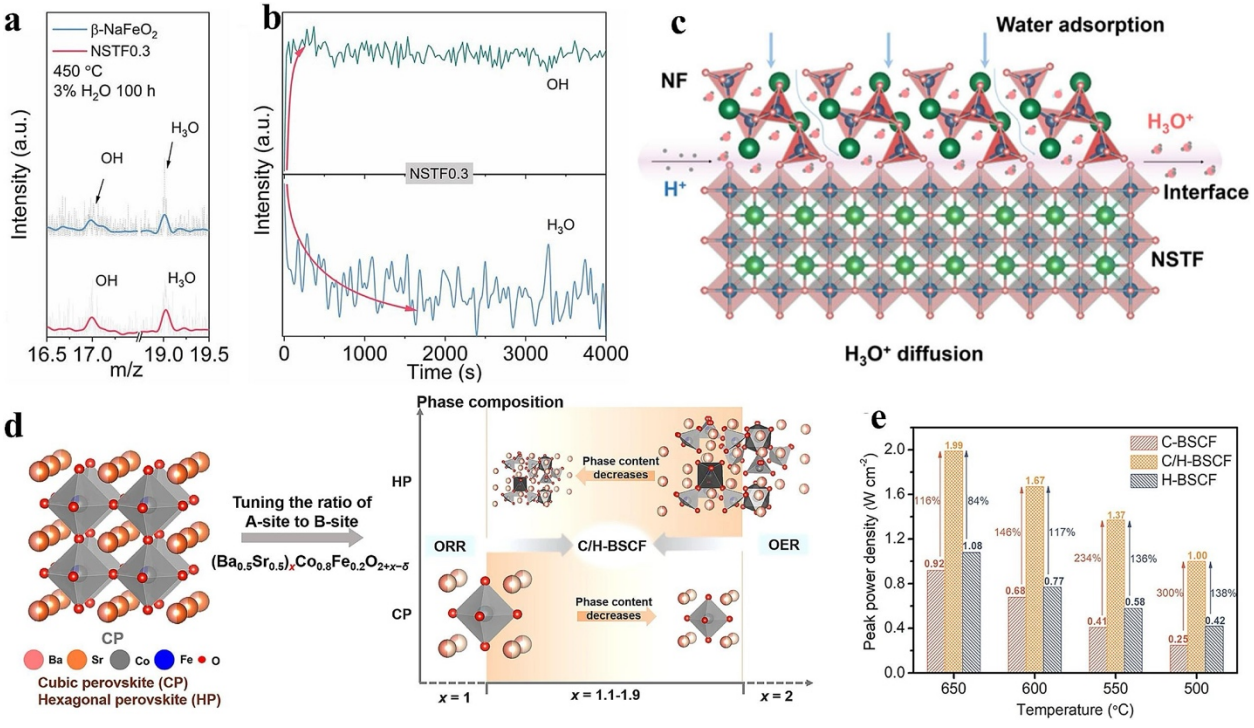


Figure 2.16. (a) Protonic properties of the surface of NF and NSTF0.3 measured by TOF-SIMS. (b) A depth profile of the H3O+ detected in NSTF0.3. (c) The Schematic diagram of

H3O+ diffusion. Copyright 2023, John Wiley and Sons. (d) The phase content-controlled hybrid electrode composed of cubic and hexagonal perovskites induced by tuning the ratio of A-site to B-site of cubic perovskite. (e) Comparison of PPDs at different temperatures for single cells with C-BSCF, C/H-BSCF, and H-BSCF electrodes[92].

Bulk tuning also includes controlling oxygen nonstoichiometry and defect ordering, which can dramatically affect transport and kinetics. Some oxygen-deficient perovskites exhibit vacancy ordering (brownmillerite-like arrangements) that can reduce effective oxygen mobility or create anisotropic transport. Strategies that disrupt unfavorable ordering, through cation disorder, compositional complexity, or controlled stoichiometry, can increase defect mobility and improve oxygen exchange[93]. At the same time, excessive disorder can increase chemical expansion and mechanical strain, so the structural consequences of defect tuning must be considered alongside electrochemical gains.

Finally, bulk tuning is most effective when evaluated with metrics that separate intrinsic effects from microstructural artifacts. A meaningful assessment typically combines temperature- and pO_2/pH_2O -dependent EIS to identify whether surface exchange or transport is improved, measurements or estimates of oxygen nonstoichiometry to confirm vacancy tuning, and complementary spectroscopy to verify redox states and bonding trends[12]. When these indicators move consistently, higher exchange activity with moderated redox swings and improved stability, bulk tuning becomes a rational design tool rather than empirical composition screening.

Collectively, bulk tuning strategies for PCC oxygen electrodes center on aliovalent doping to optimize vacancy chemistry, transition-metal mixing to tune covalency and redox buffering, selection of structure families to enable fast transport, balancing mixed conduction including proton-related behavior under steam, and A-site design to improve structural and chemical stability. These levers shape the intrinsic catalytic landscape and defect response that ultimately control ORR/OER rates and durability in reversible protonic ceramic cells.

2.3.4 Surface-focused strategies

Because ORR/OER in protonic ceramic cells occurs at or near the electrode surface, many of the most effective performance gains come from engineering the outermost tens of nanometers rather

than changing the entire bulk composition. Surface-focused strategies aim to (i) increase the density of active sites, (ii) tune surface defect chemistry and adsorption energetics, and (iii) stabilize the surface against steam-driven reconstruction and segregation. This approach is especially attractive in PCCs because intermediate-temperature operation makes surface exchange and interfacial charge transfer disproportionately important, and because the oxygen electrode experiences persistent humidity (water formation in PCFC mode and steam consumption in PCEC mode) that can rapidly alter surface states[19,82].

A common route is infiltration of catalytic nanoparticles or thin catalyst layers into a pre-sintered porous backbone. In this approach, the porous scaffold preserves gas pathways and electronic/protonic connectivity, while the infiltrated phase distributes nanoscale catalysts over the internal surface, generating a hierarchical nanostructure that expands active reaction zones and accelerates oxygen-surface processes[51,94]. Representative of this strategy, Zhou et al. deposited a proton-conducting barium cobaltite (BCO) catalyst onto an LSCF oxygen electrode through a one-step infiltration process; the resulting BCO-coated LSCF showed markedly lower polarization resistance, improved stability in humid air, and enhanced reversible-cell performance, with the improvement attributed mainly to faster oxygen surface exchange[95]. Accordingly, the effectiveness of infiltration depends strongly on precursor chemistry, loading, calcination conditions, and the number of infiltration cycles, which together govern particle size, surface coverage, and continuity of the catalytic network (Figure 2.17).

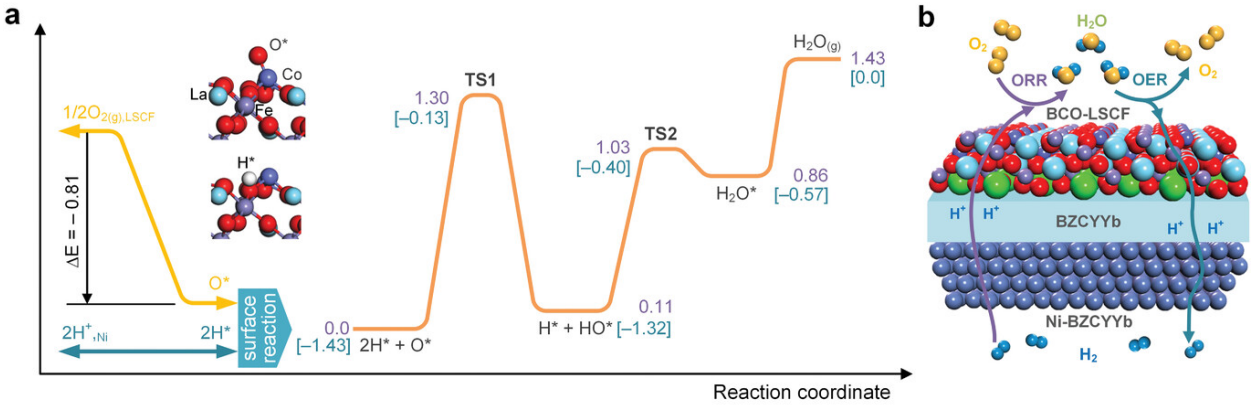


Figure 2.17. (a) Schematic of the energy profile for the fuel cell and water electrolysis modes on LSCF (001). "*" denotes an adsorbed species on the surface. TS1 and TS2 are transition states. The energies in brackets are for the water electrolysis mode. In this reaction scheme, a Co ion on

LSCF (001) was applied as a catalytically active center. (b) Schematic illustration of the reversible ORR and OER processes via the fuel cell and water electrolysis modes in BCO-LSCF//BZCYYb//Ni-BZCYYb[95].

Closely related are conformal surface coatings that create a catalytic skin or chemically stabilizing interphase. In protonic ceramic electrodes, such coatings can be introduced by infiltration or by thin-film methods when finer control over thickness and conformality is needed[39,96]. Their function is not only to increase surface-exchange activity by presenting a more active termination, but also to improve steam tolerance and surface stability by suppressing degradation of the underlying electrode. In this sense, the BCO-coated LSCF work is especially relevant because it shows that an infiltrated catalyst layer can simultaneously serve as a catalytic coating and a stabilizing interphase under humid reversible-PCC conditions. More broadly, the most effective coatings are typically thin and defect-accessible, so they enhance near-surface kinetics without blocking charge transfer.

Another powerful surface strategy is the deliberate creation of heterostructures and composite interfaces at the nanoscale. When two oxides are brought into coherent or semi-coherent contact, interfacial regions can exhibit altered electronic structure, enhanced defect concentrations, or modified adsorption energetics relative to either parent phase[97]. These interfacial effects can accelerate surface exchange and charge transfer, effectively creating hot zones for ORR/OER. In protonic systems, heterostructures can also promote proton accessibility by placing proton-conducting and oxygen-exchanging functionalities in closer proximity, expanding the effective reaction zone beyond a narrow electrolyte boundary. In practice, heterostructure design often overlaps with infiltration and coating approaches, since infiltrated particles and conformal skins naturally generate high densities of interfaces.

Exsolution-enabled surfaces represent another route to high and stable activity in protonic ceramic electrodes. Rather than acting only as anchored nano-catalysts, exsolved particles can generate electronically active heterointerfaces that modify near-surface defect chemistry and charge-transfer behavior. For example, Ge et al. showed that A-site defect engineering in BCFNi95 induces in situ exsolution of NiO nanoparticles, forming a NiO|BCFNi95 heterointerface with substantially enhanced electrochemical performance[23]. As discussed, this exsolution-derived

interface lowers oxygen-vacancy formation energy and hydration energy, strengthens d–p orbital hybridization, and accelerates interfacial charge transfer, collectively promoting proton/oxygen-ion transport and surface exchange kinetics (Figure 2.18). Thus, in reversible PCCs, exsolution is attractive not only because socketed nanoparticles resist sintering, but also because the resulting nano-interfaces can actively regulate the defect and electronic landscape governing ORR/OER.

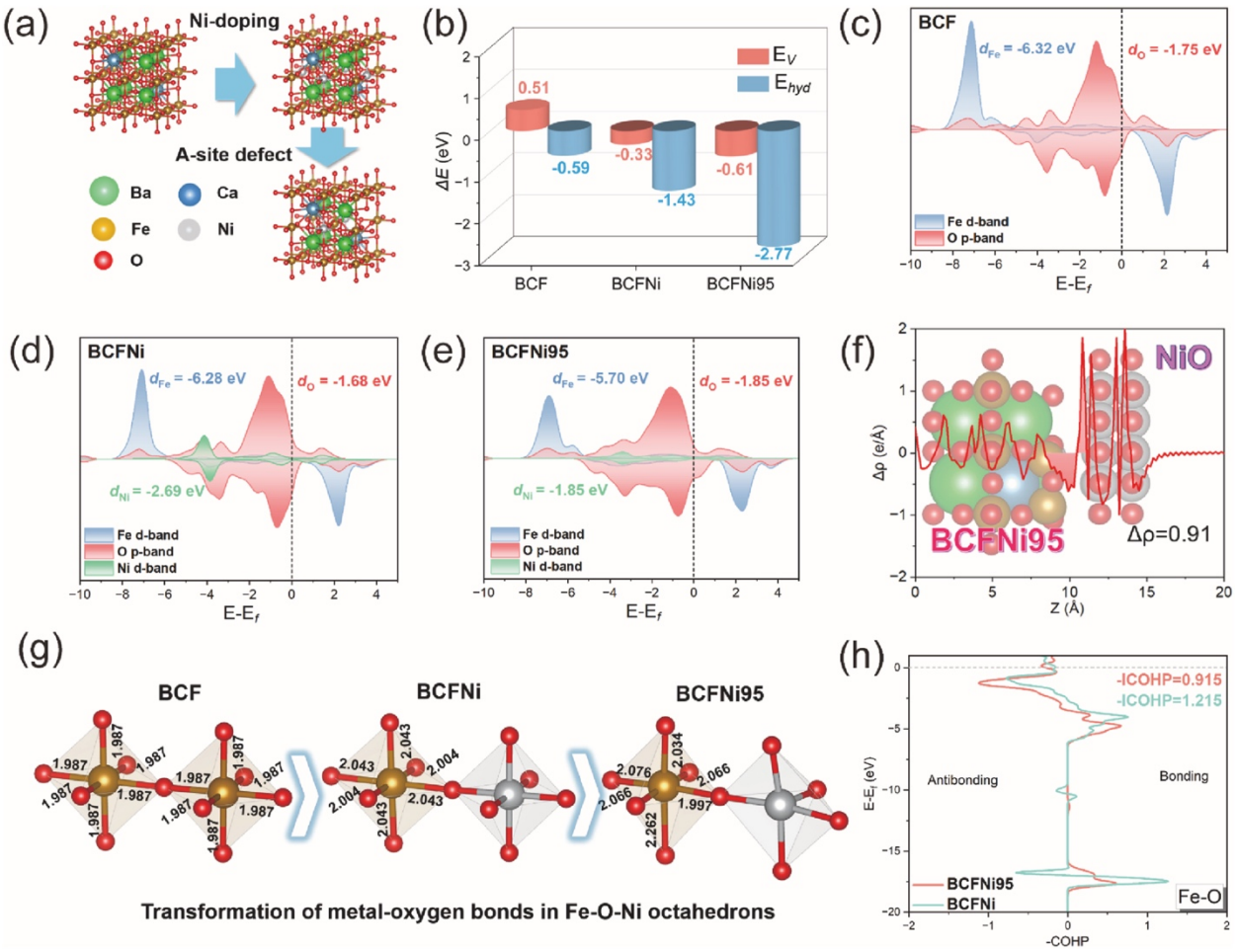


Figure 2.18. (a) Schematic diagram of BCFNi95 ($Ba_5Ca_2Fe_6NiO_{23}$), BCFNi ($Ba_6Ca_2Fe_6Ni_2O_{24}$), and BCF ($Ba_8Fe_8O_{24}$); (b) Calculated oxygen vacancy formation energies and hydrations energies for BCFNi95, BCFNi and BCF perovskites; Electronic DOS for (c) BCF, (d) BCFNi and (e) BCFNi95; (f) Planar average charge density difference plots of NiO|BCFNi95; (g) Comparison of Fe-O bonds in BCF, BCFNi and BCFNi95; (h) -ICOHP calculations results of Fe-O bonds in BCFNi and BCFNi95[23].

Surface chemistry can also be tuned through controlled defect enrichment near the surface. Strategies include mild reduction/oxidation treatments to adjust oxygen nonstoichiometry, surface doping to modify vacancy formation energetics, and creating thin surface layers with different cation compositions than the bulk[98,99]. These approaches aim to optimize the local balance between oxygen vacancy concentration and metal–oxygen bonding strength—key determinants of adsorption and exchange kinetics—without destabilizing the entire electrode. In humid environments, an additional goal is to manage surface hydroxylation: surfaces that bind hydroxyl species too strongly can accumulate blocking layers, whereas surfaces that are too labile may reconstruct under steam. Thus, defect enrichment must be paired with stability-aware surface design.

Because PCC oxygen electrodes operate under steam, surface-focused strategies increasingly emphasize stability engineering alongside activity. Cation segregation is a recurring issue in many perovskite oxygen electrodes, where A-site enrichment at the surface can block active sites and reduce exchange kinetics over time[77]. Approaches such as surface caps that suppress segregation, compositional grading that reduces segregation driving forces, and coatings that act as diffusion barriers can slow or prevent this degradation pathway. Likewise, protective surface layers can reduce reactivity with contaminants or suppress the formation of resistive surface phases in the presence of CO_2 or other impurities, improving durability in practical gas feeds.

Surface-focused strategies provide a direct handle on the kinetic bottlenecks of ORR/OER in protonic systems by targeting the region where reactions occur. Infiltration and nanoparticle decoration increase active site density; conformal coatings and nano-skins tune surface exchange and stabilize the surface; heterostructures leverage interfacial effects to enhance defect chemistry and adsorption energetics; exsolution offers anchored, potentially regenerable nano-catalysts; and surface defect engineering and segregation control protect activity under steam and cycling. When integrated with a stable porous backbone and strong electrode–electrolyte bonding, these surface strategies can deliver large reductions in polarization resistance while preserving durability in reversible PCC operation.

2.3.5 Activity–stability tradeoffs

A persistent theme in oxygen-electrode development for protonic ceramic cells is that the same features that raise ORR/OER activity can also accelerate degradation. At intermediate temperatures, polarization losses are often dominated by surface exchange and interfacial charge transfer, which encourages designs with high oxygen vacancy concentrations, strongly covalent metal–oxygen bonding, and high surface area[12,19]. However, these high-activity states frequently come with a cost: the lattice oxygen sublattice can become too labile, surfaces can reconstruct under steam, and nanoscale catalysts can coarsen, leading to performance decay. Managing this activity–stability tension is therefore not a secondary optimization step, which is the central requirement for practical reversible PCC operation.

From a defect-chemical perspective, high activity often correlates with low oxygen vacancy formation energy and a large population of mobile oxygen defects. These properties generally improve oxygen exchange kinetics and reduce polarization resistance, but they can also amplify chemical expansion, redox swings, and susceptibility to steam-driven structural changes[100,101]. Under electrolysis conditions, where the oxygen electrode experiences high steam activity and strong chemical potential gradients, an overly reducible or overly oxygen-deficient lattice may undergo phase transitions, vacancy ordering/disordering, or local amorphization at the surface. Even when the bulk phase remains intact, near-surface changes, such as altered termination, hydroxylation, or segregation, can shift the rate-limiting step and produce continuous polarization growth.

Surface-centered strategies illustrate the same tradeoff. Infiltration and nanoparticle decoration can dramatically reduce R_p by increasing active site density and creating highly reactive interfaces, yet nanoparticles are thermodynamically driven to sinter and coarsen, especially under humid atmospheres[21,48]. As particle size increases, active surface area decreases, percolation among catalytic features can be lost, and the electrode gradually reverts toward the lower-activity behavior of the underlying backbone. Similarly, conformal coatings or catalytic skins can tune surface exchange favorably, but if they are not carefully designed to remain permeable to both electronic and ionic charge carriers, they can become transport-blocking layers. Thus, activity gains obtained

by maximizing surface reactivity must be balanced against morphological and transport stability under realistic operation.

Another major stability constraint is cation segregation, particularly in many perovskite oxygen electrodes. High vacancy concentrations, strong electrostatic driving forces, and elastic strain can promote A-site enrichment at the surface, forming insulating or weakly active surface layers that progressively suppress oxygen exchange[102]. Segregation is often accelerated under polarization and can be further influenced by steam, which changes surface termination and defect equilibria. In reversible PCCs, repeated switching between PCFC and PCEC modes introduces additional perturbations that can enhance segregation kinetics and make degradation faster than in single-mode testing.

The electrode–electrolyte interface is an additional axis of the activity–stability balance. Highly active compositions may be chemically incompatible with the electrolyte or may react under high-temperature processing, forming resistive secondary phases that dominate polarization[76]. Conversely, low-temperature processing used to preserve surface area and catalytic phases may compromise adhesion or interfacial contact, increasing constriction resistance and creating vulnerability to delamination under cycling. In many cases, the most stable interface is achieved by sacrificing some intrinsic activity and instead using interlayers, grading, or hybrid interphases that provide both catalytic enhancement and chemical and mechanical buffering.

In protonic systems, water and steam introduce a uniquely important stability dimension. Because water is produced or consumed at the oxygen electrode depending on mode, the oxygen electrode continuously experiences humid conditions and large gradients in $p_{\mathrm{H_2O}}$ and $p_{\mathrm{O_2}}$ at high current. These gradients can shift hydration state, change local defect populations, and alter surface coverage of hydroxyl species[14]. A catalyst that is optimal under dry air conditions may behave very differently under humid air or steam electrolysis. Therefore, stability-aware activity optimization must be performed under relevant steam fractions and, ideally, under reversible cycling protocols rather than single-point measurements.

Designing within the activity–stability trade space typically requires buffering strategies that preserve sufficient reactivity while suppressing the fastest degradation routes. At the bulk level,

this can mean moderating oxygen lability through composition tuning (e.g., adjusting dopant level or transition-metal mix) so the material retains fast exchange but avoids extreme redox swings[103]. At the surface level, it can mean anchoring nanoparticles, using socketed or exsolved catalysts, or creating heterostructures where interfacial effects enhance kinetics without requiring an excessively labile bulk lattice. At the interface level, it can mean inserting thin interlayers that prevent chemical reactions and maintain strong bonding while providing a fast transport pathway for protons and electrons to reach active sites.

The meaningful evaluation of the activity–stability balance requires metrics that capture both short-term performance and long-term retention. Reporting only peak power density or an initial R_p can be misleading if the structure degrades rapidly. Best practice is to pair initial performance with durability tests, periodic EIS to track which polarization components grow, and post-test microstructural or chemical analyses that identify the dominant degradation mechanism (coarsening, segregation, interface growth, or transport blockage). When these data are used together, the activity–stability tradeoff becomes a design guide: it clarifies whether additional activity should be pursued through more aggressive defect chemistry, or whether the next gains must come from stabilizing the surface and interface so that existing activity can be preserved over practical operating timescales.

2.4 Electrode–Electrolyte Interfacial Engineering

2.4.1 Origins of interfacial polarization

In protonic ceramic cells, the electrode–electrolyte junction is not a passive contact. It is an electrochemically active, defect-sensitive, mechanically stressed region that often controls the measured polarization resistance. Even when an oxygen electrode shows high intrinsic catalytic activity and the electrolyte exhibits high bulk proton conductivity, the cell can still display a large R_p if the buried interface restricts charge transfer, blocks proton transport, or reduces the effective area through which current can pass. Interfacial polarization therefore refers to the voltage loss associated with processes that occur at or immediately adjacent to the electrode–electrolyte interface, and it is frequently observed in impedance spectra as one or more arcs that grow disproportionately with time, steam exposure, or cycling[19,21].

A first, deceptively simple origin is geometric and microstructural constriction. The apparent electrode area seen in a cross-section is not the same as the true electrical contact area[104]. In porous electrodes, contact with the dense electrolyte occurs through discrete particle necks, asperities, and locally bonded regions. Current must funnel through these limited contact spots before spreading into the electrolyte, producing an additional resistive loss commonly described as constriction resistance. This effect becomes severe when the interface is rough, poorly sintered, partially detached, or covered by pores near the electrolyte surface. The result is an elevated local current density at contact points, which increases local overpotential and accelerates further degradation (coarsening, cracking, or chemical reaction), creating a positive feedback loop that enlarges interfacial polarization over time. A recent work makes this point especially concrete: Bian et al. showed that poor contact at the low temperature processed oxygen-electrode/electrolyte junction can prevent the cell from fully utilizing the electrolyte's theoretical bulk proton conductivity, even when the electrolyte itself is highly conductive[39]. Their work therefore highlights that interfacial contact loss is not merely geometric; it can directly manifest as a major proton-transport bottleneck in full cells (Figure 2.19).

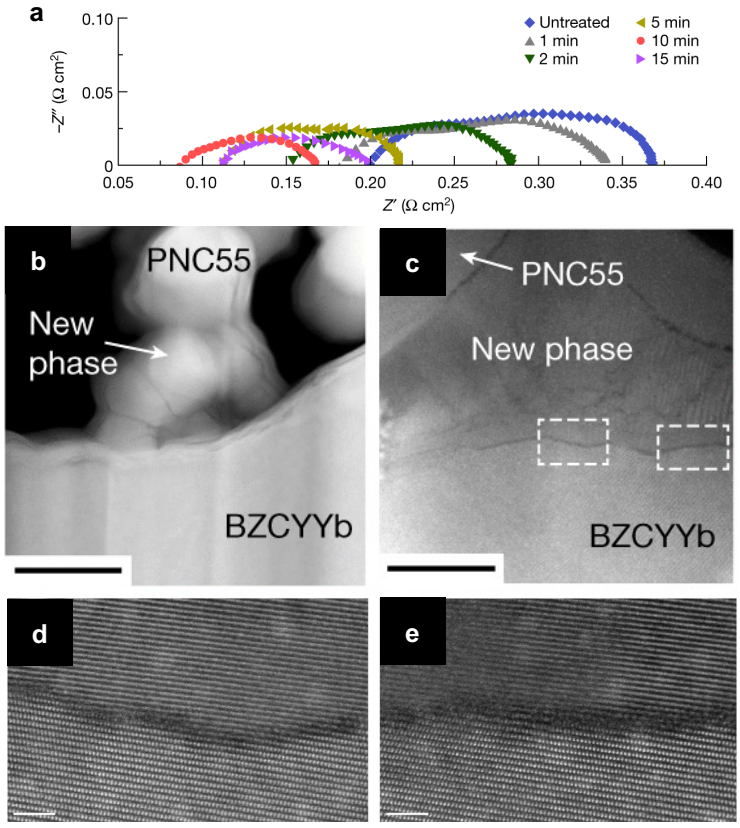


Figure 2.19. Correlation between simultaneously lowered ohmic and polarization resistance along electrode–electrolyte interface. (a) EIS at OCV at 600 °C. Z' and Z'' denote the real and imaginary parts of the complex impedance, respectively. R_o is taken from left intercept of the EIS curve with x axis and R_p is taken from right intercept of the EIS curve with x axis minus R_o. (b) HAADF–STEM image of a sample slice near the oxygen electrode–electrolyte interface. (c) HAADF–STEM image of a thinned sample slice at another region near the interface. (d, e) High-resolution HAADF–STEM of the two regions marked in c (left dashed box (d) and right dashed box (e)), showing a rough and well-bonded interface. Scale bars, 200 nm (b); 40 nm (c) and 2 nm (d,e)[39].

Beyond geometry, interfacial polarization commonly originates from chemical incompatibility and secondary phase formation. During electrode sintering or long-term operation, elements can inter-diffuse and form reaction products at the interface[48,105]. Even nanometer-to-micrometer thick interlayers can be highly detrimental if they are poor proton conductors or electronic insulators, because they interrupt the coupled proton/electron transfer required for ORR/OER. In protonic systems, this is especially critical: the oxygen electrode must exchange charge with the electrolyte via protons, so any interphase that is proton-blocking can dominate $R_p$even if it occupies only a small volume fraction. These reaction layers may form during high-temperature processing or gradually during operation under steam and large chemical potential gradients. Importantly, interfacial reaction does not need to consume the electrode to matter—forming a thin, continuous film at the contact is enough to impose a major transport barrier.

A third key origin is defect redistribution and space-charge effects at the junction. When two oxides with different defect chemistries come into contact, the chemical potentials of charged defects are not automatically continuous across the boundary[106,107]. To equilibrate, defects may redistribute near the interface, creating a region with modified carrier concentration relative to the bulk, often described as a space-charge layer. In proton-conducting electrolytes, this can manifest as a local depletion of mobile protonic defects or an enrichment of compensating defects near the interface, effectively reducing the local proton conductivity exactly where protons must cross to sustain the electrode reaction. The same concept applies to oxygen-vacancy redistribution and electronic carrier alignment in mixed-conducting electrodes. The practical consequence is that the

interface can behave like a kinetic bottleneck even when both bulk phases are individually conductive.

Interfacial polarization is also amplified by mismatch in transport pathways and reaction-zone geometry. In many PCC oxygen electrodes, the reaction is proton-coupled, meaning protons must reach reactive sites where oxygen or steam is activated. If proton transport is confined to the electrolyte surface and cannot access internal electrode surfaces, the electrochemically active region collapses into a thin band adjacent to the electrolyte[25,108]. This concentrates charge-transfer demand at the interface and makes the cell highly sensitive to any interfacial imperfection. In contrast, designs that provide proton-conducting pathways within the electrode effectively spread reaction sites away from the interface, reducing interfacial current density and lowering interfacial polarization. Thus, what appears as an interfacial limitation in EIS is often the combined outcome of interface chemistry plus the extent of proton accessibility in the electrode's near-interface microstructure.

Mechanical integrity is another frequent contributor. The interface is where thermal expansion mismatch, chemical expansion, and elastic constraint accumulate. Over time, these stresses can create microcracks, debonding, or partial delamination, reducing effective contact area and increasing constriction losses[49,109]. Reversible operation can exacerbate this: switching between PCFC and PCEC modes changes local steam activity and oxygen chemical potential, shifting defect populations and associated lattice strain. Even small cyclic strains, repeated many times, can fatigue the interface. Once partial delamination begins, current constriction becomes more pronounced and local heating or overpotential can accelerate both chemical and structural degradation, rapidly increasing interfacial polarization.

Interfacial polarization is influenced by electrode processing choices that trade activity for contact quality. Low-temperature processing helps preserve high surface area and prevents undesirable bulk reactions, but it can leave the interface under-sintered with weak bonding and high contact resistance[110,111]. High-temperature co-firing can improve adhesion and reduce constriction resistance, but it increases the risk of forming reaction phases and can coarsen microstructures that are needed for high catalytic utilization. This processing tension is why many PCC strategies

introduce a deliberate engineered interface: the goal is to maintain intimate contact and stable defect chemistry at the junction while preserving the electrode's catalytic and transport advantages.

Interfacial polarization in PCCs typically arises from a combination of (i) limited true contact area and current constriction, (ii) chemically formed resistive interphases from reactions or interdiffusion, (iii) defect redistribution/space-charge effects that locally suppress mobile carriers, (iv) reaction-zone confinement caused by poor proton accessibility in the near-interface region, and (v) mechanically driven contact loss under thermal/chemical cycling. Recognizing these origins is crucial because each calls for a different remedy—microstructural densification at the contact, chemical barrier layers, defect-compatible interlayers, graded functional regions, or mechanically compliant architectures—rather than a one-size-fits-all catalyst approach.

2.4.2 Chemical compatibility and interdiffusion

Chemical compatibility between electrode and electrolyte is a prerequisite for durable protonic ceramic cells, yet it is often challenged by the very conditions needed to manufacture and operate high-performance devices. The electrode–electrolyte junction experiences high temperatures during fabrication (co-firing, sintering, post-annealing) and then strong chemical potential gradients during operation (changes in pO_2, pH_2O, polarization state, and redox environment). Under these stimuli, elements can inter-diffuse across the interface and form secondary phases that are electronically insulating, proton-blocking, mechanically weak, or all three. Even when the bulk electrode and electrolyte are stable in isolation, their contact can generate a new local chemical environment that drives interfacial reactions[112].

A practical definition of compatibility is therefore strict: an electrode is chemically compatible with an electrolyte if, across relevant processing and operating conditions, the interface does not develop a continuous reaction layer that impedes coupled charge transfer. This requirement is particularly demanding in PCCs because oxygen-electrode reactions are proton-coupled; even a thin interphase with poor proton conductivity can dominate polarization[48,105]. In many PCC stacks, the electrolyte is a barium-based perovskite, and barium chemistry adds an extra constraint: Ba-containing phases can react with a wide range of oxides and impurities, and Ba species can be mobile under certain defect conditions. As a result, compatibility is not only about thermodynamic

phase stability but also about kinetic access to reaction pathways during sintering and long-term operation.

Interdiffusion is often initiated during high-temperature processing, when concentration gradients and high defect concentrations accelerate cation mobility. Multiple species can move simultaneously. Alkaline-earth cations (Ba/Sr) may diffuse toward the electrode; rare-earth cations (La/Pr) and transition metals (Co/Fe/Ni/Mn) may diffuse toward or into the electrolyte[19,113]. Importantly, diffusion is not uniform: grain boundaries and porous pathways act as fast diffusion channels, so the microstructure of the electrolyte (grain size, boundary density, residual porosity) and the interfacial contact (necking, wetting, local densification) can strongly influence how quickly interdiffusion proceeds. In practice, an interface can look clean in bulk powder compatibility tests but still form thin, continuous reaction films in a dense cell where grain-boundary diffusion intersects the junction.

Once interdiffusion begins, the local thermodynamic driving force can precipitate secondary phases that are more stable than the parent oxides under interfacial conditions. The electrochemical

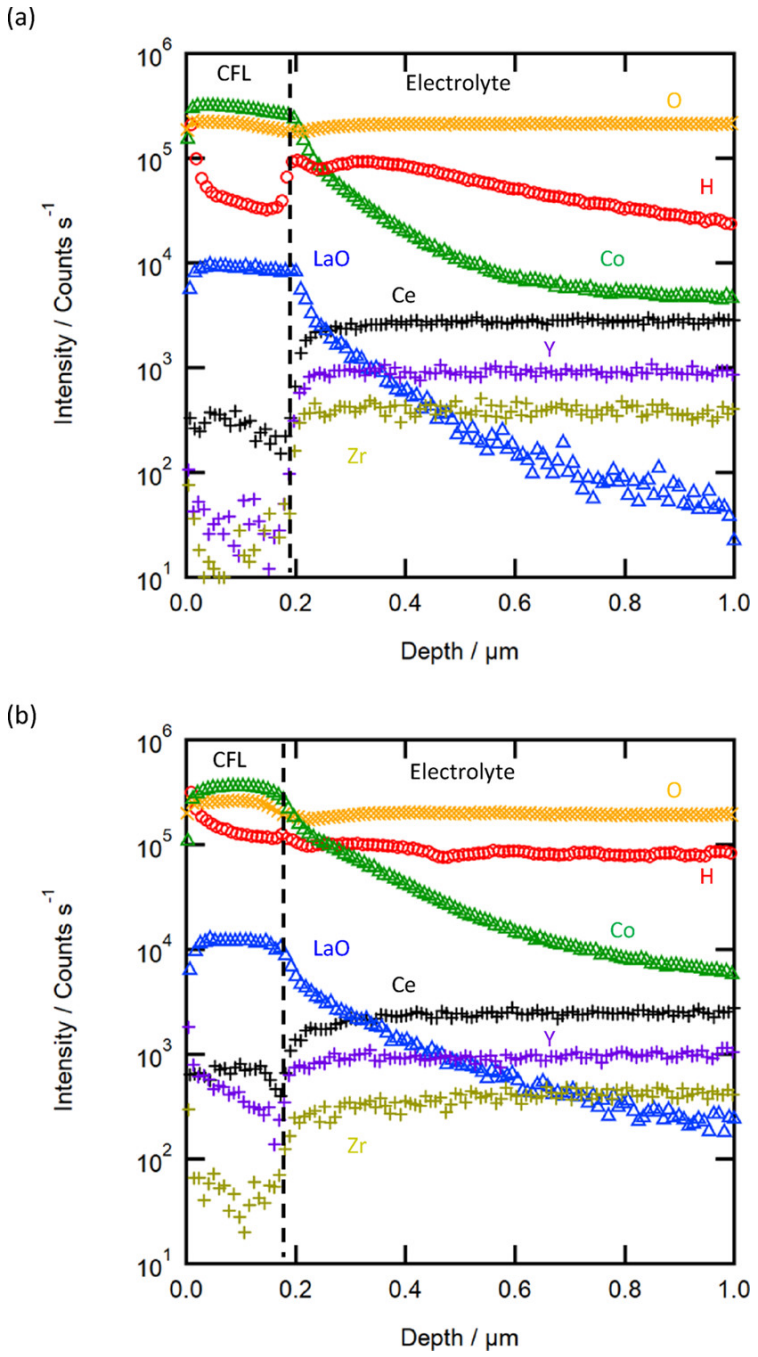


Figure 2.20. SIMS depth profiles of the LSCF-CFL cells (a) before and (b) after fuel cell measurements. The assignment is as follows: O (orange, cross), H (red, open circle), LaO (blue, open triangle), Co (green, open triangle), Ce (black, plus), Y (purple, plus), and Zr (yellow, plus). The dashed lines at a 0.2 µm depth indicate the border between CFL and the electrolyte. For SIMS measurements, the LSCF cathode was removed by scratching and sonication[114].

consequences are often severe because many reaction products have low proton conductivity and/or low electronic conductivity. A nanometer- to micrometer-thick interphase that is proton-blocking can introduce a large additional resistance because it sits exactly where proton flux must cross to sustain ORR/OER. At the same time, it also shows the other side of this principle: a deliberately designed interlayer need not become a blocking film[114]. In the discussion of SIMS result, depth profiling after operation indicated hydrogen incorporation into the cathode functional layer, and the paper associates this proton accessibility with reduced ohmic and polarization losses. That result is especially relevant here because it demonstrates that the key issue is not simply whether an extra interfacial layer exists, but whether the interfacial region remains chemically compatible and proton-transport-active under operating conditions (Figure 2.20). By contrast, when interdiffusion produces a continuous proton-poor or electronically resistive reaction layer, impedance typically evolves as a growing interfacial contribution and a progressive increase in polarization resistance, while the brittle or poorly bonded nature of such layers can also introduce weak planes that promote microcracking and delamination during thermal cycling or chemical expansion associated with hydration and redox changes.

Operating conditions can accelerate incompatibility even if processing is controlled. In PCCs, the oxygen electrode frequently sees humid air or steam, and during electrolysis it experiences high steam activity together with large oxygen chemical potential gradients[115]. These conditions can shift defect equilibria and increase cation mobility, especially for transition metals that change valence under polarization. Steam can also alter surface termination and promote hydroxylation, which may change interfacial reactivity and enable dissolution–reprecipitation-type transport in extreme cases. Reversible operation adds another stressor: switching between PCFC and PCEC changes the direction of ionic flux and local chemical potentials, which can repeatedly perturb the interface and favor gradual interphase growth even when each individual mode appears stable in shorter tests.

Because compatibility is both chemical and kinetic, mitigation strategies typically combine thermodynamic buffering with diffusion control. One route is lower-temperature fabrication—for example, densifying the electrolyte at reduced temperature (via sintering aids, optimized powder processing, or thin-electrolyte designs) and then forming the oxygen electrode by post-sinter methods (infiltration, low-temperature firing) to avoid prolonged high-temperature contact

between reactive chemistries[18]. Another widely used approach is interlayers: thin films or functional layers that are stable against both the electrolyte and electrode and that maintain high proton transport. These interlayers serve multiple functions simultaneously—diffusion barrier, chemical compatibility buffer, and sometimes a wetting layer that improves adhesion and reduces constriction resistance. A related strategy is compositional grading, which reduces abrupt chemical potential jumps by transitioning gradually from electrolyte-like to electrode-like chemistry, lowering the driving force for discrete reaction-phase formation and improving mechanical compliance.

Assessing compatibility requires evidence at multiple scales. Simple powder-mixing anneals are useful screening tools, but real interfaces can form nanometer-scale reaction films that strongly affect electrochemistry while remaining invisible to coarse characterization. Therefore, cross-sectional analysis is essential: SEM/EDS can identify micrometer-scale layers and elemental diffusion profiles; TEM/EELS can resolve nanometer-scale interphases and valence changes; and depth profiling methods can detect surface/interfacial enrichment that precedes phase formation. Electrochemically, compatibility issues typically present as a progressive increase in polarization resistance and sometimes apparent constriction effects; tracking how specific impedance features evolve with time, steam fraction, and cycling can help distinguish interfacial growth from purely catalytic or transport degradation.

In a nutshell, chemical compatibility and interdiffusion at the electrode–electrolyte interface are central determinants of PCC durability because even thin interphases can block proton transfer and destabilize adhesion. High-temperature processing initiates diffusion and reaction pathways; steam-rich and polarized operation can accelerate them through defect-chemical and redox effects. Durable interfaces therefore rely on strategies that reduce reaction driving forces (lower-temperature processing), interrupt diffusion (stable barrier interlayers), and smooth chemical/strain discontinuities (graded functional regions), supported by high-resolution cross-sectional characterization and impedance-based diagnostics to confirm that the interface remains both chemically stable and electrochemically transparent.

2.4.3 Interlayers and graded junctions

A recurring topic in protonic ceramic cells is that the electrode–electrolyte interface must be engineered as a functional region, not treated as a simple contact. Even when the bulk electrolyte has high proton conductivity and the electrode material is intrinsically active, performance can be limited by constriction at discrete contact points, defect depletion near the boundary, and chemical reactions that form proton-blocking interphases. Interlayers and graded junctions address these problems by inserting a deliberately designed region—typically from a few tens of nanometers to several micrometers thick—that improves (i) chemical compatibility, (ii) transport continuity for protons/electrons, and (iii) mechanical/adhesive integrity. This interface-centric view is strongly emphasized in reviews of solid–solid interfaces in protonic ceramic devices, which note that cathode development and interface engineering are inseparable challenges in practice[21].

One widely used concept is the electrolyte-based porous interlayer. Here, a thin, porous layer made of the same proton-conducting composition as the electrolyte is deposited on the dense electrolyte before applying the oxygen electrode. The logic is twofold: (1) chemical compatibility is maximized because the interlayer is composition-matched to the electrolyte, and (2) the porous interlayer increases the density of accessible reaction sites near the interface by improving contact area and extending the effective reaction zone. A clear example is the porous BZCYYb interlayer approach, where a porous layer of the electrolyte material is placed on a dense BZCYYb electrolyte specifically to modify the cathode-electrolyte interface and expand the electrochemically active region.[105] In practical terms, this interlayer reduces current constriction at isolated contact points, creates more continuous protonic pathways into the near-electrode region, and provides a microstructurally compliant transition from a dense electrolyte to a porous electrode.

Interlayers are also used as buffer or barrier layers to suppress interdiffusion and stabilize long-term durability, even if they add a small ohmic penalty. This reflects a common tradeoff: adding an interlayer increases total thickness in the ionic path (raising R_{Ω}slightly), but it can dramatically reduce the rate of polarization growth by preventing the formation of resistive secondary phases or weak bonding[116]. For instance, durability improvements with a BZCYYb buffer interlayer have been reported in long-term PCFC operation, where the interlayer decreases degradation rates over extended testing up to thousands of hours in the reported study. This kind of result underscores

that interface stability can dominate lifetime, and that a small increase in ohmic resistance is often acceptable if it prevents progressive interfacial polarization and delamination.

Beyond porous electrolyte interlayers, a second major category is catalytically active interlayers, where the inserted layer is chosen not only for compatibility but also for its ability to accelerate oxygen-electrode kinetics and facilitate proton-coupled charge transfer[116]. In reversible PCCs, this is particularly attractive because the oxygen electrode must perform both ORR and OER under humid conditions, and weak bonding or poor near-interface kinetics can limit both modes. A recent example of this philosophy is a thin, nanostructured interlayer deposited between the air electrode and electrolyte to reduce both polarization and ohmic resistances, coupled with additional electrode modifications for improved contact and kinetics. Mechanistically, catalytic interlayers can (i) increase the density of electrochemically active sites near the electrolyte where proton availability is highest, (ii) provide a more favorable defect-chemical environment for proton transfer and oxygen exchange, and (iii) protect the electrolyte surface from direct exposure to reactive electrode chemistries[114].

A third and increasingly important approach is the use of thin-film interlayers and functional layers prepared by methods such as pulsed laser deposition (PLD), atomic layer deposition (ALD), or related coating techniques. These routes offer unusually precise control over thickness, density, and composition, enabling interlayers that are thin enough to avoid a large ohmic penalty yet continuous enough to homogenize the buried contact and suppress direct electrolyte–electrode incompatibility. The value of this strategy is illustrated clearly by a PLD work, who introduced a thin dense PBSCF interlayer film on a BZCYYb electrolyte prior to the porous cathode; notably, this design was feasible because PBSCF is sufficiently proton permeable, allowing the dense film to improve contact without blocking proton transfer[117]. In that work, the PLD interlayer produced a dramatic reduction in offset resistance, indicating that a major part of the initial loss originated from the buried cathode–electrolyte junction rather than from bulk electrolyte transport alone (Figure 2.21). The result therefore shows that thin-film interlayers can do more than simply separate two reactive phases: they can function as proton-transport-active contact layers that reduce constriction, improve interfacial uniformity, and create a more effective near-interface pathway for proton-coupled ORR. More broadly, PLD-based functional layers and interlayers are now viewed as a powerful means to reduce both ohmic and polarization losses in intermediate-

temperature protonic ceramic cells while also tailoring the near-interface microstructure and defect chemistry.

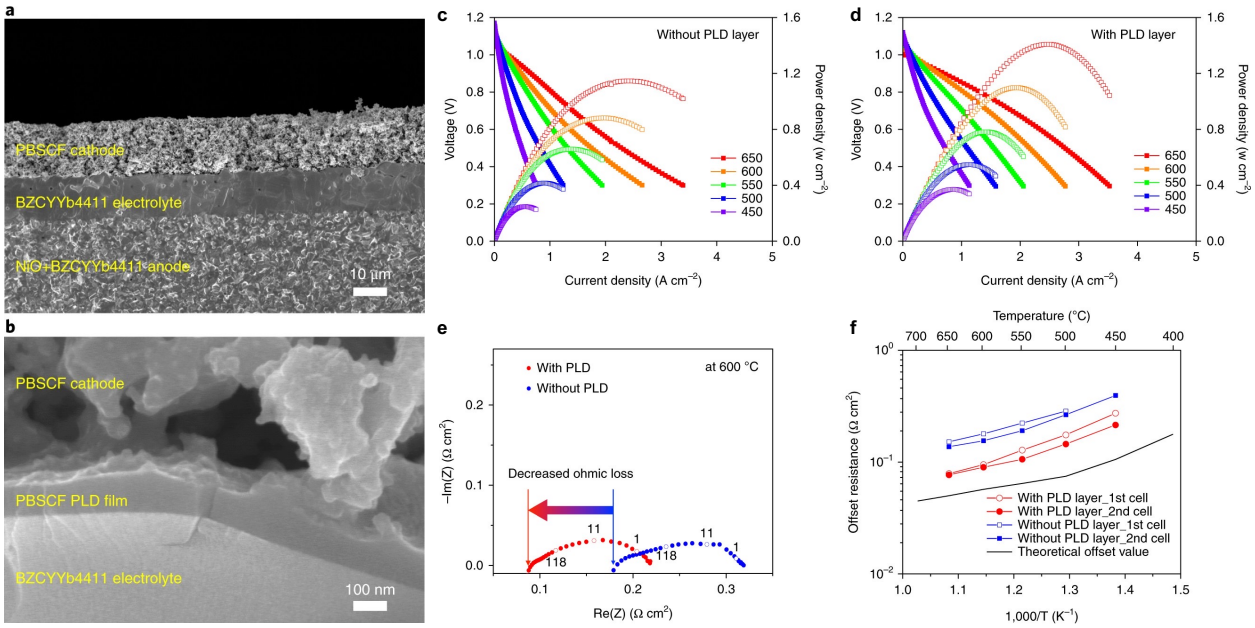


Figure 2.21. Electrochemical properties of the PBSCF cathode based on BZCYYb4411 proton conducting electrolyte using humidified (3% H2O) H2 as fuel and dry air as oxidant at various temperatures. (a) Cross-section. (b) Expanded view of cross-section showing PLD layer at the cathode of electrolyte–cathode interface. (c) Polarization and power density curves of a representative cell without a PLD layer. (d) Polarization and power density curves of a representative cell with a PLD layer. (e) Impedance spectra collected at 600 °C, showing dramatic decrease in offset resistance on introduction of the cathode PLD layer. (f) Offset (ohmic) resistance under OCV[117].

It is also important to recognize that interlayer engineering does not always require inserting a new composition; sometimes it involves reconditioning the electrolyte surface to restore interfacial transport and adhesion[118]. For example, interface rejuvenation strategies have demonstrated that modifying the electrolyte surface state can recover high proton conductivity at the surface and improve bonding strength, translating into better performance and thermomechanical stability. Conceptually, this points to a broader principle: the interfacial region is governed by local defect chemistry and microstructure, and engineering either composition, morphology, or defect state can reduce interfacial polarization.

Graded junctions extend these ideas further by replacing an abrupt boundary with a continuous transition in composition and/or microstructure. Instead of a discrete interlayer, a graded region gradually changes from electrolyte-like to electrode-like chemistry and often from dense to porous morphology[119]. This approach reduces sharp discontinuities in chemical potential and defect concentrations, which can mitigate space-charge-driven carrier depletion and lower the driving force for forming discrete secondary phases. From a mechanics standpoint, grading can also reduce thermal/chemical expansion mismatch by distributing strain across a finite thickness rather than concentrating it at a single plane. In practice, grading can be implemented by sequential deposition of layers with progressively changing compositions (e.g., mixing ratios of protonic conductor and electrode oxide) or by infiltrating a porous electrolyte scaffold near the interface to create a gradual increase in catalytic phase content with distance from the electrolyte.

Whether implemented as a discrete interlayer or a graded junction, several design rules repeatedly appear. First, the interfacial region must remain proton transparent: any continuous layer with low proton conductivity can dominate R_p, even if it is thin. Second, the region must provide robust adhesion and high true contact area, since constriction losses and local hot spots accelerate both chemical reactions and mechanical damage. Third, the interlayer should be tailored to the operating mode: steam electrolysis imposes stronger humidity exposure and chemical potential gradients, so the oxygen-side interface often benefits most from barrier/catalytic interlayers and mechanically compliant grading. Finally, interlayers must be considered together with processing—high-temperature co-firing may improve bonding but increase reaction risk, while low-temperature routes preserve chemistry but can leave weak contact unless an interlayer or surface treatment is used to promote adhesion[120].

Interlayers and graded junctions are central tools for translating intrinsically good PCC materials into durable devices. Porous electrolyte interlayers improve contact and expand the near-interface reaction zone, buffer interlayers suppress interdiffusion and slow long-term degradation, catalytic interlayers enhance proton-coupled ORR/OER near the electrolyte, and thin-film/graded designs offer precise control of transport continuity and mechanical compliance. Collectively, these strategies directly target the dominant origins of interfacial polarization—constriction, defect discontinuity, and chemical incompatibility—making them foundational to high-performance reversible PCFC/PCEC operation.

2.4.4 Mechanical integrity under operation

Mechanical integrity is a quiet make-or-break requirement for protonic ceramic cells because the highest electrochemical activity is only useful if the multilayer structure remains well bonded, crack-free, and gas-tight over long operation and repeated cycling. In practice, the cell behaves like a constrained laminate: a dense ceramic electrolyte is joined to porous electrodes, supported by current collectors and seals. Each component experiences different thermal histories, defect-chemical states, and microstructural evolution, so stresses accumulate not only from temperature changes but also from chemistry and electrochemical polarization[21,121]. Mechanical degradation typically appears as microcracking, loss of interfacial contact, partial delamination, warping, or gas leakage and catastrophic failure.

The most recognized stress source is thermal expansion mismatch. Electrolytes, oxygen electrodes, fuel electrodes, interlayers, and current collectors each have distinct thermal expansion coefficients (TECs). During heating to operating temperature and during cooldown, the constrained mismatch generates tensile/compressive stresses at interfaces. Even small TEC differences matter because ceramic layers are stiff and brittle; repeated thermal cycling can fatigue the interface and promote crack initiation at pores, sharp corners, and local defects[122]. This is one reason intermediate-temperature operation is attractive: it reduces absolute thermal gradients and the amplitude of thermally induced strain compared with very high-temperature solid oxide systems, yet the mismatch problem does not disappear, especially when devices are cycled frequently for reversible operation.

A second, often more subtle driver is chemical expansion associated with defect chemistry. Protonic electrolytes and many mixed-conducting oxygen electrodes change lattice parameters as they hydrate/dehydrate and as they undergo reduction/oxidation (changes in oxygen nonstoichiometry and cation valence)[55]. In PCCs, hydration is not an occasional event; it is embedded in operation because steam partial pressure can vary with gas supply, utilization, and local reaction rates. Likewise, oxygen chemical potential gradients shift with current density and mode (PCFC vs PCEC). These defect-state changes produce dimensional strains that can be comparable to or even larger than thermal strains locally, especially near interfaces where gradients are steep. Because the electrolyte is dense and the electrode is porous, the strain is

nonuniform: the porous layer can partially accommodate expansion through its void space, while the dense electrolyte cannot, concentrating stress at the buried junction. Over time, cyclic chemical expansion can drive interfacial fatigue even under isothermal conditions.

Microstructural evolution introduces a third mechanical pathway. Porous electrodes coarsen under operation: particles sinter, necks grow, and porosity can decrease or redistribute. This evolution changes elastic modulus and shrinkage tendencies, altering the stress state even if the device is held at constant temperature[110]. In infiltrated or nanostructured electrodes, catalyst coarsening can also change local stiffness and create weak planes. If interfacial bonding was initially marginal, microstructural relaxation of the electrode can progressively reduce true contact area, intensifying current constriction and increasing local overpotential, conditions that can accelerate both chemical reactions and mechanical damage in a coupled feedback loop.

Electrochemical operation itself adds electro-chemo-mechanical coupling. High current densities produce nonuniform local reaction rates across the interface due to microstructural heterogeneity. Regions carrying higher current experience larger local chemical potential shifts (in pO_2 and pH_2O) and therefore larger local chemical expansion, creating hot spots of strain. Joule heating and polarization heating can further raise local temperature, increasing diffusion rates and softening some components while others remain rigid[48,123]. In electrolysis mode, steam consumption and oxygen evolution at the oxygen electrode can amplify concentration gradients through porous layers, which translates into spatially varying hydration state and defect concentrations—again producing stress localization. These coupled gradients make reversible cycling particularly challenging: the direction of ionic flux and the distribution of chemical potentials change between PCFC and PCEC, so the interface experiences repeated, asymmetric perturbations rather than a single steady stress state.

Mechanical integrity also depends on the quality of interfacial adhesion and compliance. A highly porous electrode bonded to a dense electrolyte tends to have limited true contact area unless a functional interlayer or sintering strategy creates sufficient necking and wetting. Poor adhesion leads to micro-gaps that act as stress concentrators and promote delamination[124]. Conversely, overly aggressive firing to improve adhesion can create thick reaction layers that are brittle or proton-blocking, swapping a mechanical problem for an electrochemical one. This is why

interface-engineering tools (interlayers, graded junctions, and compliant functional layers) are often justified not only for lowering polarization but also for distributing stress more gently across the junction. A graded region, for example, can reduce both chemical and thermal mismatch by smoothing changes in composition, TEC, and porosity over a finite thickness rather than concentrating strain at a sharp boundary.

From a design standpoint, achieving mechanical robustness usually requires co-optimization of materials selection, architecture, and processing. Matching TECs as closely as possible is a first step, but it must be paired with microstructures that can tolerate strain: controlled porosity near the interface for compliance, stable backbones that resist densification, and current collectors that distribute load without introducing point contacts[49,125]. Thin electrolytes reduce ohmic loss but can be mechanically fragile; this pushes designs toward supported architectures where mechanical support is provided by a thicker, porous substrate while keeping the dense layer thin and defect-free. For reversible cells, stability also benefits from minimizing steep gradients by using hierarchical porosity for gas transport and ensuring uniform current distribution to avoid localized chemo-mechanical damage.

Mechanical integrity must be verified with operation-relevant testing, not only room-temperature adhesion checks. Useful indicators include post-test cross-sections for microcracks and delamination, curvature/warping changes after cycling, and impedance signatures consistent with constriction/contact loss (often a rising interfacial contribution)[46]. Durability protocols that include thermal cycling and mode switching are especially informative because they probe the coupled stresses that the interface will face in real reversible operation.

Mechanical failure in PCCs is typically driven by the combined effects of TEC mismatch, defect-chemical expansion, microstructural evolution, and electrochemically induced nonuniform gradients. Durable electrode–electrolyte interfaces therefore require more than strong bonding: they demand architectures and interlayers that maintain contact, provide compliance, suppress stress localization, and remain chemically stable so that mechanical and electrochemical degradation do not reinforce each other during long-term reversible operation.

2.4.5 Interface characterization and degradation signatures

Because the electrode–electrolyte interface is buried and often only tens to hundreds of nanometers thick, it can dominate PCC performance while remaining invisible to routine surface characterization. A reliable interface story therefore requires two complementary elements: (i) direct structural/chemical observation of the junction and (ii) electrochemical signatures that track how interfacial processes evolve during operation. The most convincing diagnoses come from pairing these two views, linking a change in impedance to a specific interfacial feature such as a reaction layer, cation segregation, loss of contact, or defect depletion.

Cross-sectional electron microscopy is the starting point for most interface studies. Conventional SEM provides rapid assessment of electrode–electrolyte contact quality, interfacial roughness, pore penetration, cracking, and delamination. When coupled with EDS mapping, SEM can also reveal micrometer-scale interdiffusion and the emergence of reaction products thick enough to be resolved[126]. However, many critical interphases in PCCs are sub-micrometer, and element gradients can be subtle. For this reason, focused ion beam (FIB) preparation followed by higher-resolution analysis is widely used to produce site-specific cross-sections and to target suspected hot spots such as regions near current collectors or areas that experienced high local polarization.

Transmission electron microscopy provides the most direct view of nanoscale interfacial chemistry and structure. High-angle annular dark-field STEM imaging can resolve interphases, grain-boundary pathways, and local densification at the junction, while STEM-EDS quantifies elemental diffusion with nanometer-scale spatial resolution. Even more diagnostic in many PCC interfaces is STEM-EELS, which can detect changes in cation valence and oxygen coordination, information that is essential when degradation involves redox-driven reconstruction or defect-chemical redistribution[127]. For example, an apparently thin interphase may be functionally blocking because its electronic structure differs from the parent phases or because its oxygen-vacancy/proton defect landscape has shifted. In short, TEM/EELS can distinguish whether the interface is merely a compositional gradient or a truly distinct phase with different transport properties.

Depth-sensitive spectroscopy complements microscopy by probing chemical states and segregation. XPS is commonly used to detect surface enrichment and changes in oxidation state, and with sputter depth profiling it can extend sensitivity toward near-interface regions, particularly for thin-film interlayers or treated electrolyte surfaces. Secondary ion mass spectrometry (SIMS), especially when used as a depth profile, can be particularly powerful for quantifying diffusion of key species (Ba/Sr, transition metals) and for tracking hydrogen-related species in protonic systems[94]. While absolute quantification of hydrogen in oxides is challenging, SIMS can still provide comparative insights on hydration-related distributions and interfacial incorporation pathways. When combined with careful standards and controls, these tools help establish whether degradation is driven by cation migration, impurity accumulation, or changes in oxygen/hydrogen chemistry.

Crystallographic tools also contribute important information, particularly for phase identification. XRD may detect bulk reaction products when interfacial reactions are extensive, but many interphases are too thin for detection by standard lab XRD. In such cases, micro-XRD, grazing-incidence approaches, or electron diffraction within TEM are more sensitive[46,128]. Electron diffraction can identify nanocrystalline reaction phases and reveal whether the interface remains coherent/semi-coherent or has transformed into an incoherent, porous layer, which is an important distinction for both transport and mechanical integrity.

Because structure alone does not fully define function, electrochemical diagnostics are essential for identifying degradation signatures associated with interface evolution. EIS is the primary tool:

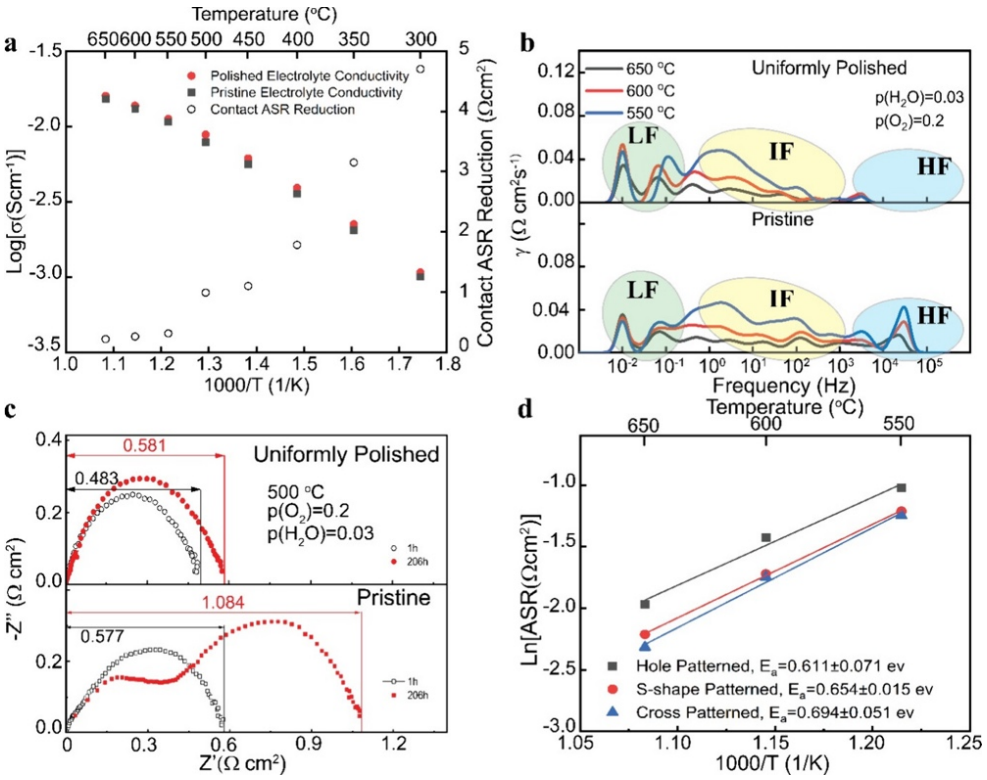


Figure 2.22. EIS characterization results of the symmetrical cells with thick BCZYYb7111 electrolyte pellets (pristine and homogeneously laser-polished electrolyte surfaces) sandwiched between two identical porous BCFZY0.1 cathode films. (a) comparison of the apparent conductivities and the contact ASR reduction caused by laser polishing, (b) DRT spectra of the uniformly polished and pristine symmetrical cells, (c) ASR degradation of the uniformly polished and pristine symmetrical cells, and (d) activation energies of the patterned symmetrical cells[129].

interfacial degradation commonly manifests as a growing mid- or low-frequency contribution, an increase in apparent polarization resistance, and, in severe cases, changes consistent with current constriction. When impedance is measured periodically during aging, it can often distinguish whether degradation is dominated by ohmic rise, which is more consistent with electrolyte/contact deterioration, or by polarization growth, which more often points to electrode/interface processes. This logic is illustrated well by Zhou et al., who used laser engineering of the electrolyte/cathode interface and reported simultaneous reductions in ohmic resistance, positive-electrode/electrolyte contact resistance, and electrode polarization resistance; their results show that buried-interface improvement can appear electrochemically not as a change in only one component, but as a

coordinated decrease in both contact-related and kinetic losses (Figure 2.22). In that sense, impedance analysis is especially valuable because it can reveal whether an interface modification is mainly improving bonding/current collection, mainly accelerating electrode kinetics, or doing both at once[129]. Distribution of relaxation times (DRT) analysis further helps deconvolute overlapping processes and can highlight the emergence of new time constants consistent with reaction-layer growth or contact loss, but its strongest role remains interpretive rather than definitive. The key is not to overinterpret DRT peaks in isolation, but to use them as a hypothesis generator that is then validated by cross-sectional evidence.

Several practical red flags repeatedly indicate interface-limited degradation. A steady increase in polarization resistance with relatively stable $R_\Omega$often suggests interfacial reaction growth or loss of electrochemically active contact area rather than bulk electrolyte degradation. Conversely, a rise in $R_\Omega$can indicate increased constriction resistance from partial debonding or the formation of a continuous resistive layer at the junction[130]. Hysteresis between increasing and decreasing current sweeps, or strong performance dependence on contact pressure/current-collector configuration, can also signal that current constriction at the interface is significant. In reversible operation, asymmetric degradation between PCFC and PCEC modes often points to oxygen-side interface vulnerability under steam electrolysis, where chemical potentials and defect fluxes are more severe.

Post-test failure analysis is most informative when it is spatially correlated with electrochemical history. Instead of analyzing a single arbitrary cross-section, it is valuable to target regions where current density, steam utilization, or temperature gradients were highest. FIB lift-outs from these regions can reveal whether degradation is uniform or localized, whether reaction layers nucleate at specific microstructural features as grain boundaries or triple junctions, and whether delamination initiates at chemically altered zones[131]. Such spatial correlation is essential in PCCs because interfaces often degrade heterogeneously, and “average” microstructures may not reveal the true failure trigger.

Interface characterization should be viewed as a before/after comparison under controlled protocols. A persuasive interface section typically includes: (i) initial junction microstructure (contact area, interlayer thickness, compositional gradients), (ii) time-resolved EIS showing how R_Ω and R_p evolve, and (iii) post-test cross-sectional chemistry and structure that identify the

physical origin of the electrochemical change[18]. When these three elements align—e.g., a new interfacial layer appears alongside a growing interfacial impedance feature—interface degradation becomes a mechanistic conclusion rather than a speculative explanation.

Robust interface characterization in PCCs relies on cross-sectional microscopy (SEM/FIB-SEM, STEM-EDS/EELS), depth-sensitive chemistry (XPS depth profiling, SIMS), and crystallographic identification (electron diffraction, micro-XRD where needed), paired with electrochemical signatures from time-resolved EIS and DRT. Together, these tools reveal the dominant degradation signatures—reaction-layer growth, cation segregation/interdiffusion, carrier-depleted interfacial zones, and mechanical contact loss—and provide a quantitative, evidence-based foundation for designing interlayers, graded junctions, and mechanically compliant interfaces that remain stable during long-term reversible operation.

2.5 Integrated Multiscale Electrode Design for High Performance

2.5.1 Why single-factor optimization plateaus

In protonic ceramic cells, it is natural to chase performance by improving one lever at a time—selecting a more active oxygen electrode, increasing porosity, thinning the electrolyte, adding an infiltrated catalyst, or inserting an interlayer. When a baseline cell is clearly limited by a single dominant loss, these changes can produce dramatic gains. The plateau appears when that dominant loss is reduced and the device transitions from being single bottleneck limited to being limited by a network of coupled processes. At that stage, further improvement of the original lever yields diminishing returns because the next constraint, often previously hidden, now governs the overall voltage loss[19,126].

This behavior can be understood by viewing the cell as a chain of resistive and kinetic elements that must all be traversed by the same current. Even if one avoids over-simplifying impedance spectra, the practical reality is that total loss contains multiple contributions: ohmic resistance from electrolyte and contacts, polarization from charge transfer and surface exchange, transport losses inside porous electrodes (electronic/protonic percolation), and gas-phase mass transport through tortuous pores[82]. Because these contributions add and interact, lowering one term increases the relative importance of the others. For example, once $R_{\Omega}$is reduced through electrolyte thinning or

improved densification, the oxygen-electrode polarization becomes more visible and begins to dictate achievable current density. Conversely, if oxygen-electrode kinetics are enhanced strongly through defect tuning or surface nanoengineering, the device can shift into a regime where gas diffusion or proton accessibility becomes limiting, so the same catalyst improvement no longer translates into proportional cell-level gains.

A common plateau mechanism is the mismatch between intrinsic activity and electrochemical accessibility. Many catalytic strategies increase the density of reactive sites, but these sites contribute only if gas molecules, electrons, and protons can reach them simultaneously. In protonic systems, proton access is often the hardest constraint on the oxygen electrode[9,60]. If protons are supplied mainly through the electrolyte interface and cannot penetrate the electrode volume, the effective reaction zone collapses into a thin layer near the electrolyte. In that situation, adding more catalyst deeper in the porous network improves intrinsic activity on paper but does not expand the truly active region, so measured polarization stops improving. This is why infiltration or surface coatings often show strong initial gains that saturate unless paired with architectures that extend protonic pathways.

Microstructural tuning can plateau for similar reasons. Increasing porosity or introducing larger pores may reduce concentration polarization, but it can also reduce mechanical robustness, worsen current constriction at the electrolyte contact, or break electronic percolation if the solid network becomes too sparse. In practical terms, there is an architectural trade space where improving one transport channel degrades another[10]. When optimization is performed along a single axis (e.g., “maximize porosity” or “minimize particle size”), the system eventually hits a point where further change harms percolation, adhesion, or stability, flattening net performance. Hierarchical designs were developed precisely to escape this: they separate gas highways (macro/meso pores) from catalytic fine structure (nano features) so transport can improve without sacrificing reaction-site density or connectivity.

Interfaces are another source of plateaus because they often become the hidden limiter once bulk properties improve. A cell can have a highly conductive electrolyte and an active oxygen electrode yet still exhibit large polarization due to limited true contact area, defect depletion near the interface, or thin reaction layers that block proton transfer[59]. Many great cathodes demonstration

plateau because the electrolyte surface state or the cathode–electrolyte junction becomes the controlling resistance. Interlayers and graded junctions frequently produce large jumps in performance not because they change the bulk catalyst, but because they reduce constriction and maintain proton transparent contact. Once that interface bottleneck is addressed, the limiting step may shift again, often toward surface exchange or mass transport, so additional interface optimization alone provides smaller returns unless coupled with changes in electrode architecture and catalytic chemistry.

Reversible operation amplifies plateau behavior because PCFC and PCEC modes do not stress the electrode identically. An oxygen electrode improvement that lowers polarization in fuel-cell mode may not translate directly to electrolysis mode, where steam activity is higher, oxygen evolution changes surface coverage, and chemical potential gradients across the porous electrode can be steeper[129]. Similarly, a microstructure that is adequate for ORR under humid air can become transport-limited for OER under high steam utilization, producing a plateau in PCEC mode even if PCFC performance continues to rise. This mode dependence is one reason why single-factor optimization can look successful when evaluated under a single operating point but plateaus when the device is pushed across a wider current range, steam fraction, or during cycling.

Durability introduces a second, very practical plateau: the stability-limited ceiling. The most aggressive activity strategies—highly oxygen-labile compositions, very high vacancy concentrations, ultrafine nanostructures, and heavily infiltrated nanoparticles—often degrade faster under steam and polarization[40,132]. Coarsening reduces active area, segregation blocks sites, and interfacial reactions slowly add resistive layers. In such cases, the best initial performance is not the best sustained performance, and the device converges toward a similar long-term resistance regardless of how far initial activity was pushed. This creates the impression of an unavoidable plateau unless stabilization mechanisms are built in.

As performance improves, nonuniformity becomes the ceiling. High current densities magnify any local weakness: a slightly denser region, a partially blocked pore network, uneven catalyst distribution, or a small interfacial gap can concentrate current and create hot spots. Those hot spots experience higher overpotential, faster chemical change, and faster microstructural evolution, which further concentrates current—an accelerating feedback loop that limits the usable average

performance[18,46]. Single-factor optimization usually improves an average property (average activity, average porosity, average conductivity) but does not necessarily eliminate the weakest-link regions that dominate at high load. Integrated design addresses this by improving uniformity of percolation, ensuring robust contact across the full active area, and building transport redundancy into the architecture.

For these reasons, single-factor optimization in PCCs often follows a predictable trajectory: large early gains, then diminishing returns as the limiting step shifts, and finally a plateau set by a different process. Moving beyond that plateau requires integrated multiscale design—co-optimizing microstructure (gas pathways and percolation), catalysis (surface exchange and defect chemistry), and the buried interface (compatibility, contact, and mechanical integrity) so that gains in one domain are not throttled by constraints in another, and so that the improved state can be sustained under steam-rich reversible operation.

2.5.2 Multiscale architecture

Multiscale architecture is the idea that high-performance PCC electrodes must be designed as hierarchical systems, where different length scales are assigned distinct functions and engineered to work cooperatively. This approach moves beyond making it more porous or using a better catalyst by recognizing that ORR/OER performance in protonic systems depends simultaneously on (i) fast gas delivery/removal, (ii) continuous electron and proton transport, (iii) abundant and stable catalytic sites, and (iv) a robust, low-loss interface to the electrolyte. Because these requirements cannot be maximized with a single uniform microstructure, multiscale architecture intentionally separates functions across macro-, meso-, and nano-length scales and then reconnects them through percolated pathways[133].

At the macroscale (hundreds of micrometers to millimeters), architecture governs how the device moves gases, collects current, and manages thermal and mechanical constraints. Gas flow fields, manifold design, and current collection geometry determine whether reactants are delivered uniformly across the active area or whether local starvation occurs. In electrolysis, where steam consumption and oxygen evolution can generate steep concentration gradients, macroscale gas distribution becomes particularly important to avoid localized high polarization and accelerated degradation[59]. Similarly, macroscale current collection influences current uniformity: poor

current spreading creates hot spots that raise local overpotential and amplify interfacial stress. Thus, a well-designed macroscale architecture provides low-resistance, uniform pathways for both gases and electrons, while minimizing thermal gradients and mechanical constraint.

At the mesoscale (roughly 1–100 μm), the porous electrode backbone sets the dominant transport properties and defines the size of the effective reaction zone. This is the scale at which porosity, tortuosity, pore connectivity, and percolation networks are established[134]. A robust mesoscale backbone should provide three things simultaneously: (1) open, low-tortuosity pathways for gas transport, (2) continuous electronic conduction from current collector to the interface region, and (3) sufficient mechanical integrity and adhesion so the structure remains stable under steam and cycling. In PCC oxygen electrodes, mesoscale design also influences how strongly the electrode is constrained near the electrolyte and how well it can accommodate chemical expansion. Hierarchical porosity is often implemented at this level, combining macropores that act as gas highways with finer pores that increase internal surface area, because a single pore size distribution rarely provides both low diffusion resistance and high utilization at intermediate temperature.

At the nanoscale (nanometers to sub-micrometers), architecture controls where electrochemical reactions actually occur by regulating surface chemistry and the density of active sites. Many PCC electrodes require nano-enabled features, such as infiltrated nanoparticles, conformal catalytic skins, heterostructures, or exsolved particles, to achieve sufficiently fast surface exchange at 400–600 °C. However, nanoscale features are only valuable when they are electrochemically addressable, meaning they are simultaneously connected to gas pathways and to both electronic and protonic charge carriers[60]. This point is illustrated well by Liu et al., who compared a nanosized BCFZY positive electrode, a nano–nano BCFZY/BCZYYb composite, and a nano–micro architecture in which nanosized BCFZY was hosted on microsized BCZYYb (Figure 2.23). As discussed, the microsized proton-conducting phase did not merely dilute the catalyst; instead, it created effective proton-conduction channels and acted as particle reinforcement, while the nanosized mixed-conducting phase preserved high catalytic activity[22]. In contrast, the nanosized proton-conducting phase in the nano–nano design was too dispersed to build an equally effective proton-transport network. As a result, the nano–micro architecture simultaneously lowered both ASR_P and ASR_O; at 350 °C, ASR_P decreased from 5.1 to 1.5 $\Omega \cdot \mathrm{cm}^2$, and the fuel-cell peak power

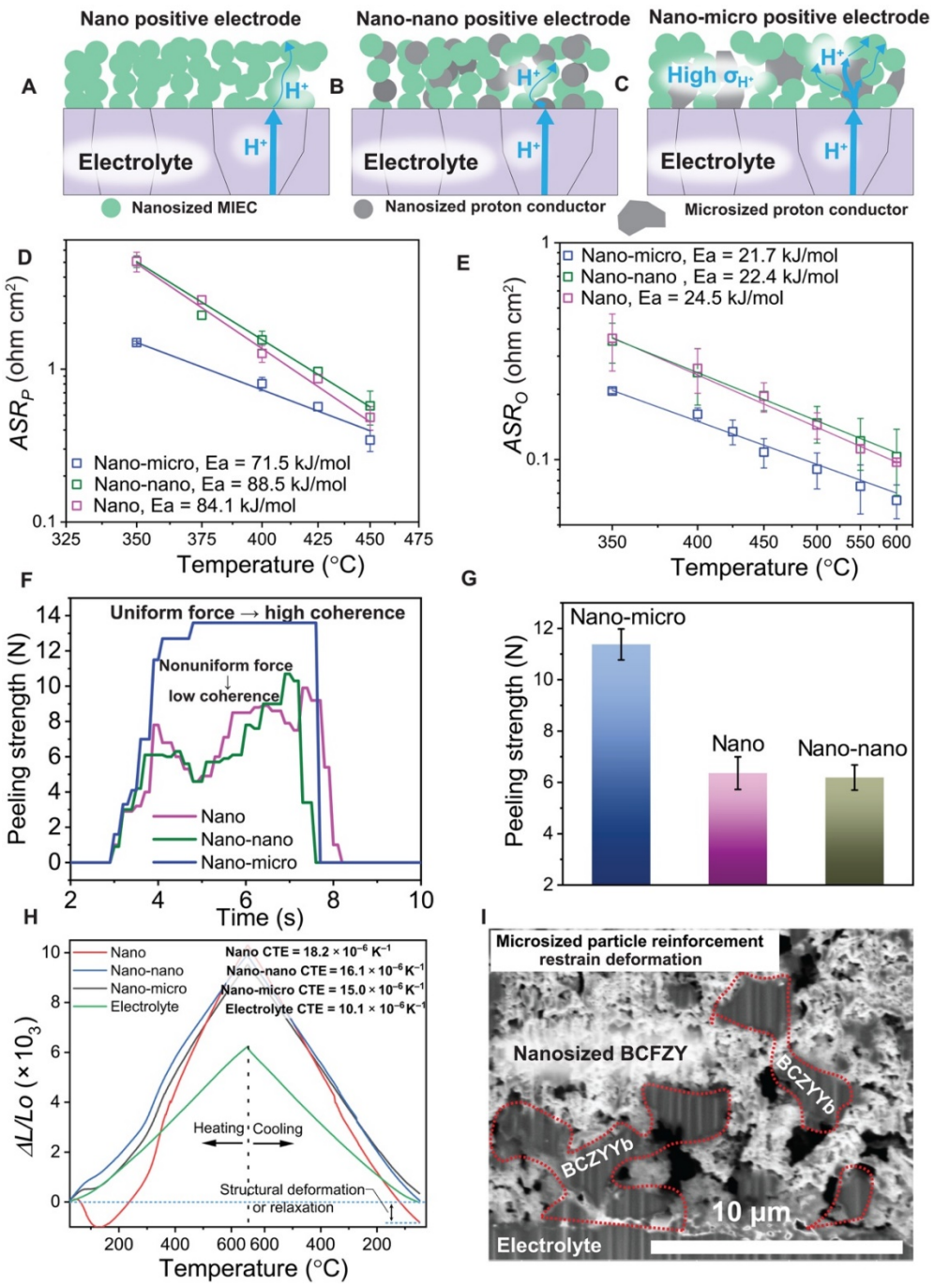


Figure 2.23. Redesigned nano-micro positive electrode simultaneously reducing ASRO and ASRP. The errors bars in these figures correspond to SDs from the averaging across all measurements. (A) Illustration of the nano positive electrode, which is a nanosized $BaCo_{0.4}Fe_{0.4}Zr_{0.1}Y_{0.1}O_{3-\delta}$ (BCFZY). (B) Illustration of the nano-nano positive electrode, which is a composite of a nanosized BCFZY and a nanosized $BaCe_{0.4}Zr_{0.4}Y_{0.1}Yb_{0.1}O_{3-\delta}$ (BCZYYb). (C) Illustration of the nano-micro positive electrode, which is a composite of a nanosized BCFZY and

a microsized BCZYYb. (D) The ASR_P of PCECs is equipped with three kinds of positive electrodes shown in (A) to (C). All results are measured in fuel cell mode and under OCV condition (cell 3 and cells 11 to 15). (E) The ASR_O shown in (A) to (C). (F) Examples of peeling strength measurement plots for three positive electrodes (cell 16). (G) Peeling strength of electrolyte-positive electrode interface (cells 16 to 18). (H) Linear thermal expansion of three positive electrodes as a function of temperature during heating and cooling, and corresponding thermal expansion coefficients (TECs) (nano, cell 19; nano-nano, cell 20; nano-micro, cell 21). (I) SEM image of the nano-micro positive electrode, which shows how the microsized phase functions as particle reinforcement to restrain the structural deformation[22].

density increased by about 3.1-fold. The same Figure 5 discussion further showed stronger electrolyte–positive-electrode bonding for the nano–micro design, with a peeling strength of 11.4 N versus 6.4 N and 6.1 N for the nano and nano–nano electrodes, respectively, together with a lower thermal expansion coefficient. Multiscale design therefore treats nanoscale catalysts as functional coatings hosted on a stable backbone and proton-conducting framework, rather than as standalone powders that must form the entire electrode on their own. This hosting concept is especially important for durability, because anchoring nanoscale features to a mechanically and proton effective scaffold can limit mobility, reduce local overpotential gradients, and suppress the sintering, segregation, and interfacial weakening that would otherwise accompany highly active nanostructures.

A unique requirement in protonic systems is that multiscale architecture must also enable proton accessibility to the oxygen-electrode reaction zone. In many configurations, the electrolyte is the primary proton conductor, and protons enter the electrode only at the buried interface. If the electrode microstructure does not provide proton-conducting pathways (via a protonic phase, a proton-permeable oxygen electrode, or an engineered interphase), the reaction zone remains confined close to the electrolyte[114,135]. Multiscale architecture therefore often includes a functional near-interface region—a thin layer where proton transport, catalytic activity, and strong adhesion are simultaneously maximized. This can be realized by a porous electrolyte-like interlayer, a graded junction, or a composite functional layer with fine features and high interfacial area density. The purpose is to reduce constriction, suppress defect depletion, and expand the active region outward into the electrode thickness.

From a design language perspective, multiscale electrodes in PCCs are often best described as backbone + functionalization + interface, where each component plays a distinct role. The backbone supplies mechanical support, gas permeability, and electronic conduction. Functionalization supplies high density of catalytic sites and tailored defect chemistry. The interface ensures chemical compatibility, high true contact area, and proton transparent transport across the junction. When these elements are co-designed, improvements in one domain reinforce rather than expose weaknesses in another, avoiding the plateau behavior typical of single-factor optimization.

Importantly, multiscale architecture is not only a performance strategy but also a durability strategy. Gas highways reduce concentration polarization and suppress extreme local $p_{\mathrm{H_2O}}/p_{\mathrm{O_2}}$ conditions that drive reconstruction. Distributed current collection reduces hot spots and slows localized coarsening[9,76]. Stable backbones preserve percolation as catalysts evolve. Engineered interfaces prevent interdiffusion and maintain adhesion under chemical expansion and cycling. In reversible PCC operation, these features become even more critical because the oxygen electrode repeatedly experiences changes in reaction direction, humidity, and defect flux, which can accelerate degradation if architecture concentrates stresses and current into narrow regions.

Multiscale architecture in PCC electrodes assigns function by length scale: macroscale structures ensure uniform gas delivery and current collection; mesoscale backbones provide low-tortuosity transport and robust percolation; nanoscale functionalization supplies high catalytic activity; and a tailored near-interface region provides proton access and stable bonding. This hierarchical, systems-level design framework is the practical route to simultaneously achieving high activity, low transport loss, and long-term stability in reversible protonic ceramic cells.

2.5.3 Synergy mechanisms

In protonic ceramic cells, improvements in microstructure, catalysis**,** and interface engineering rarely act as simple add-ons. Instead, they interact to create synergy where optimizing one element makes the others more effective, and the combined design becomes both higher-performing and more durable. This systems behavior is widely emphasized in PCC literature because oxygen-electrode losses at intermediate temperature are typically governed by coupled requirements: fast

gas delivery, continuous electronic pathways, reliable proton access, and a chemically/mechanically stable buried interface.

A first synergy is microstructure–catalysis coupling. Surface nanoengineering (infiltrated nanoparticles, catalytic skins, nano-heterostructures) can markedly increase intrinsic surface exchange and charge-transfer rates, but these gains translate to device performance only if the architecture keeps those active surfaces accessible—to gases and to charge carriers—throughout the electrode thickness[9,126]. Hierarchical porous backbones provide this amplifier effect by combining macropore gas highways with high internal surface area for catalyst decoration, enabling a much larger fraction of catalyst sites to operate near their intrinsic rate. This logic underpins recent scaffold/infiltration and nano-architectured oxygen electrodes designed to simultaneously raise activity and maintain stability in humid operation.

A second synergy is microstructure–interface coupling, where a tailored near-interface architecture reduces interfacial polarization and suppresses hot spots. Porous electrodes contact dense electrolytes through discrete necks; without an engineered transition region, current constriction localizes overpotential and accelerates both chemical reaction-layer growth and mechanical debonding[60,77]. A thin functional interlayer increases true contact area, improves protonic continuity into the electrode, and spreads current more uniformly, so the same catalytic surface chemistry performs better and degrades more slowly. Porous BZCYYb interlayers are a clear example of this concept, explicitly introduced to modify the cathode/electrolyte interface and improve performance by restructuring the near-interface region.

A third synergy is catalysis–interface coupling, which is particularly strong in protonic systems because proton supply is highest near the electrolyte. If catalytic enhancement is distributed deep in a thick, porous electrode while proton access remains confined to a narrow interfacial region, the added activity is underutilized and improvements saturate[136]. Interlayers and graded junctions can instead place catalytic functionality where protons are available, and transport barriers are minimal, maximizing utilization per catalyst loading. Relatedly, triple-conducting oxygen electrodes supporting coupled proton/oxide-ion/electronic transport create synergy by expanding the effective reaction zone beyond a thin boundary layer, improving both ORR and steam electrolysis kinetics in the 400–600 °C regime.

Synergy also appears as defect-chemical buffering across scales. Many high-activity oxygen electrodes rely on high defect activity and strong metal–oxygen covalency, which can accelerate steam-driven reconstruction, segregation, or interfacial reactivity under polarization[10,114]. Interface engineering can stabilize this by preventing detrimental interdiffusion and maintaining a proton transparent junction, while architecture reduces local overpotential and concentration extremes that drive defect redistribution. The importance of such interface-controlled phenomena is repeatedly highlighted in dedicated discussions of solid–solid interfaces in protonic ceramic devices.

Finally, synergy is often most evident under reversible operation, where mode switching changes local chemical potentials and defect flux directions. Integrated designs that combine hierarchical transport, stable catalytic functionalization, and engineered interfaces tend to show not only lower initial polarization, but also slower growth of interfacial and polarization contributions during aging[76]. For example, interface rejuvenation strategies that recover near-surface proton transport and improve bonding demonstrate how correcting an interfacial limitation can unlock performance otherwise hidden by the interface, illustrating synergy between defect chemistry at the junction and electrode kinetics.

2.5.4 Design for reversibility

Designing a protonic ceramic cell for true reversibility means more than demonstrating that the same button cell can run in both directions. A reversible PCC must sustain high activity, low losses, and stable interfaces in two different electrochemical environments: oxygen reduction in PCFC mode and steam oxidation/oxygen evolution in PCEC mode. Because these modes impose different local chemical potentials, defect flux directions, and humidity fields, the oxygen-side electrode and its buried interface often become the “stress concentrator” of reversible operation. Recent reviews of oxygen electrodes and air electrodes for reversible protonic ceramic cells repeatedly emphasize that sluggish and unstable ORR/OER kinetics—especially under steam—remain the main barrier to practical R-PCC implementation[20].

A central reversibility requirement is bifunctional oxygen-electrode kinetics. In fuel-cell mode, the oxygen electrode must rapidly reduce oxygen and form water in a humid local environment; in electrolysis mode, it must activate steam and evolve oxygen while continuously generating protons

that must be transported away. Even when the overall reaction is reversible, the *rate-limiting steps* can differ adsorption/charge transfer and surface exchange may dominate during ORR, while steam activation, oxygen evolution steps, and mass transport under high steam utilization can dominate during OER[9]. This kinetic asymmetry means that an electrode optimized only for PCFC can plateau or degrade rapidly in PCEC. Therefore, reversible design favors oxygen electrodes whose catalytic mechanism remains efficient in both directions—often by ensuring high surface exchange activity and stable defect chemistry under a wide range of $pO_2$and pH_2O.

A second requirement is proton accessibility throughout the active reaction zone. In protonic systems, ORR/OER is proton-coupled, so the oxygen electrode cannot be treated as a purely electronic catalyst layer. If protons can only enter at a narrow electrolyte boundary, then most of the porous electrode volume is underutilized and reversibility becomes fragile: small changes in interface contact or hydration state can cause large swings in polarization. This is why reversible designs increasingly favor (i) composite oxygen electrodes containing proton-conducting phases, (ii) engineered near-interface functional layers, and/or (iii) triple-conducting air electrodes that provide coupled transport pathways[76]. Triple-conducting oxygen electrodes have been highlighted as a promising route to reduce polarization and improve stability for both power generation and steam electrolysis at intermediate temperatures.

Third, reversibility requires architecture that controls gradients—in gases, current density, and defect chemistry. Electrolysis operation can create steep gradients in steam content and oxygen chemical potential through the porous oxygen electrode, and these gradients can trigger localized reconstruction, cation segregation, and accelerated coarsening. Hierarchical/3D architectures mitigate this by combining macroporous highways for rapid gas delivery/removal with mesoporous regions that supply large reactive surface area, while maintaining continuous electronic pathways and mechanical robustness[18]. When gradients are suppressed, the electrode experiences fewer hot spots, lower local overpotential extremes, and slower microstructural evolution—benefits that directly translate into more stable cycling between ORR and OER. This architecture–durability link is a recurring theme in reversible cell demonstrations and in broader reviews of oxygen-electrode development.

Fourth, design for reversibility is inseparable from interface engineering, because the electrode–electrolyte junction experiences the largest coupled stresses during mode switching. During PCFC↔PCEC transitions, the direction of ionic flux and the local hydration/redox state near the interface change, which can drive defect redistribution, chemical expansion mismatch, and interfacial reactions[124,132]. Thin reaction layers or carrier-depleted interfacial zones may remain tolerable in one mode but become catastrophic in the other. Interlayers and graded junctions help by increasing true contact area, maintaining proton transparent transport across the junction, and buffering chemical incompatibility. The importance of solid–solid interfaces in protonic ceramic devices and the fact that interface phenomena can dominate cell performance has been emphasized in dedicated interface-focused reviews.

Fifth, reversible operation demands a deliberate approach to stability under steam and redox perturbations. Many activity-boosting strategies (high vacancy activity, highly covalent B-site chemistries, nanoscale catalysts) also increase susceptibility to steam-driven reconstruction, segregation, and coarsening. In a reversible device, these degradation pathways can be accelerated because switching changes surface coverage and defect populations repeatedly rather than allowing the system to settle into a single steady state[48]. As a result, reversible design often prioritizes buffered activity: compositions and surfaces that are active enough to lower R_p, but resistant to large redox swings and to rapid morphological evolution. Stabilization strategies include anchored nano-catalysts, defect-buffering secondary phases/interphases, and architectures that distribute current uniformly to avoid localized overpotential that would amplify reconstruction. Degradation-focused discussions of PCECs commonly underline that steam-related instability at the oxygen electrode is a central durability challenge.

A representative example of reversibility-by-design is provided by Ding et al., who developed a triple-conducting oxygen electrode specifically to support both water oxidation and oxygen reduction at intermediate temperatures[10]. As discussed in reversible operation, the cell exhibited stable reversible switching between electrolysis and fuel-cell modes at 500 °C, with transient current responses that remained well behaved as the operating mode changed (Figure 2.24). More importantly, they demonstrated a self-sustainable reversible process in which hydrogen generated during electrolysis was directly consumed for electricity generation without external hydrogen feeding, highlighting that good reversibility depends not only on bifunctional catalytic activity but

also on maintaining sufficient oxygen-electrode robustness and interfacial stability during repeated mode transitions. The same figure further shows stable voltage behavior during repeated electrolysis/fuel-cell switching, while the authors note similar cycling behavior and an even more stable fuel-cell process at 550 °C. Together, these results support a central design principle for reversible PCCs: an oxygen electrode should be judged not only by low initial polarization in one mode, but by its ability to sustain coupled ORR/OER operation with minimal penalty upon switching.

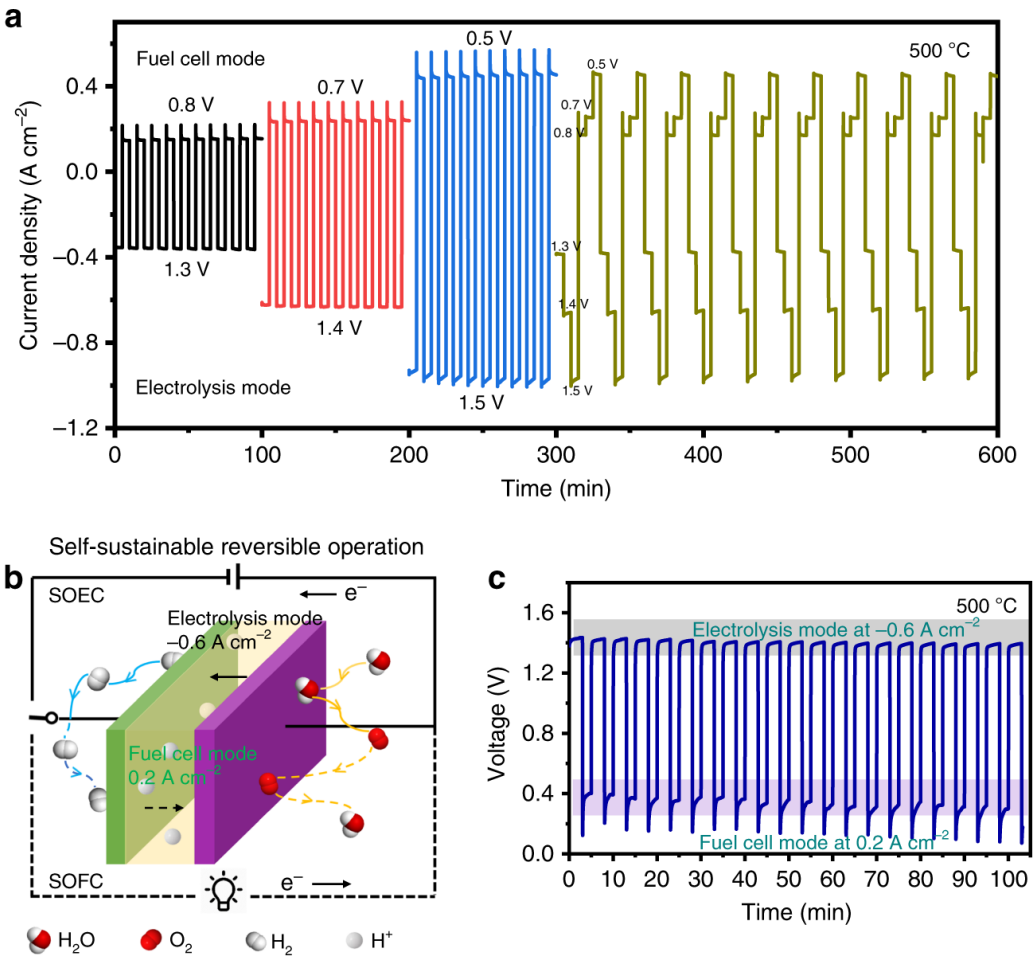


Figure 2.24. Reversible operation and analysis in hydrogen and power generation. The cycling reversible operation of the electrochemical cell between electrolysis mode (hydrogen production) and fuel cell mode (electricity generation) at different current densities to examine the capability of converting hydrogen generated by electrolysis into electricity. (a) Reversible operation with external hydrogen supply: current density responses as working mode transiently changing between electrolysis and fuel cell at 500 °C. (b) Schematic of self-

sustainable reversible operation without external hydrogen feeding. (c) Voltage observation under switchable electrolysis and fuel cell current densities at 500 °C[10].

Design for reversibility must be expressed in how the cell is validated, not only how it is built. A reversible design is credible when it demonstrates (i) comparable, well-understood loss breakdowns in both modes (via EIS/DRT), (ii) stable operation under steam-rich electrolysis conditions, and (iii) cycling stability under repeated PCFC-PCEC switching with minimal growth of interfacial and polarization components. Reversibility, in other words, is a systems property: it emerges when oxygen-electrode catalysis, proton access, transport architecture, and interface integrity are co-optimized so that improvements in one domain do not expose a hidden bottleneck in the other mode.

2.5.5 Diagnostics-guided optimization

Integrated multiscale design is most effective when it is implemented through a simple, repeatable workflow: diagnose the dominant loss, apply a targeted fix, and re-check under both PCFC and PCEC conditions. This matters because the limiting step in PCCs can shift as performance improves and can differ between fuel-cell and electrolysis operation, especially under steam-rich conditions.

Electrochemical tools provide the quickest loss map. Polarization curves show overall capability, but EIS is the workhorse for separating ohmic contributions from polarization contributions and for tracking how these change with time. Pairing EIS with controlled perturbations, temperature, pO_2, steam fraction, and flow rate, helps identify whether the bottleneck is primarily kinetic, transport, or interfacial[40]. When features overlap, DRT is useful as a comparative tool to see which time-constant region responds to a modification or grows during aging.

Electrochemical signatures should be anchored by targeted cross-sectional validation, especially for interfaces. Cross-sectional SEM often suffices to verify thickness, porosity gradients, cracking, and contact quality[48]. When interphase growth or segregation is suspected, focused FIB/TEM with EDS/EELS can confirm whether a thin reaction layer or compositional gradient is responsible for the impedance change[127]. The goal is not exhaustive characterization, but a tight link between what changed in resistance and what changed physically, so the next design step stays mechanistic.

Scalability then acts as a constraint on which multiscale concepts are practical. A useful rule is to keep precision where it pays the most: thin functional/interfacial regions (interlayers, graded junctions, surface skins) can justify higher control, while the bulk electrode should rely on scalable routes (printing/casting backbones, pore-former-based hierarchy, solution infiltration for catalytic functionalization)[46]. Designs that are robust to firing variability and to steam-driven aging are more likely to translate beyond button cells, because they preserve the multiscale functions—transport-ready architecture, accessible active sites, and a stable, proton transparent interface—without depending on fragile microstructures[137].

2.6 Electrolyte Materials and Emerging Alternatives

2.6.1 Electrolyte requirements and tradeoffs

The electrolyte is the functional heart of a protonic ceramic cell because it sets the ohmic loss, defines the operating window, and strongly influences electrode selection and long-term stability. For reversible PCC operation, an ideal electrolyte must combine (i) high proton conductivity in the 400–600 °C range, (ii) negligible electronic leakage under both oxidizing and reducing conditions, (iii) chemical stability in steam (and preferably tolerance to CO_2/impurities), (iv) mechanical integrity and thermal/chemical expansion compatibility with electrodes, and (v) manufacturability—meaning it can be densified into thin, gas-tight layers without forming resistive grain-boundary phases[16]. In practice, no single composition optimizes all these requirements, so electrolyte selection is fundamentally a set of tradeoffs. Two widely used proton-conducting perovskites that represent this trade space are BZY ($BaZrO_3$-based, typically Y-doped) and BZCYYb (a $BaZrO_3$–$BaCeO_3$ solid solution co-doped with Y/Yb).

A first requirement is high proton conductivity (σ_{H^+}) in the targeted temperature window. Proton conductivity determines the electrolyte area-specific resistance:

$$ASR_{\Omega} \approx \frac{t}{\sigma_{H^+}}$$

where t is electrolyte thickness. This relationship highlights a key coupling: conductivity and thickness are inseparable at the device level. A moderately conductive electrolyte can still yield low ohmic loss if it can be fabricated as a thin, fully dense film; conversely, even a highly

conductive electrolyte becomes limiting if it must be thick to remain gas-tight. In general, BZCYYb tends to offer higher conductivity than more Zr-rich compositions at intermediate temperatures, which is advantageous for reducing $ASR_{\Omega}$and enabling high current density. BZY, while often lower in conductivity at the same temperature, can still be competitive when processed into thin layers and when grain-boundary resistance is minimized through careful densification and microstructure control[14].

A second requirement is high ionic transference number, meaning the electrolyte should conduct protons but not electrons/holes. Electronic leakage reduces OCV and energy efficiency and becomes especially detrimental in electrolysis because it wastes electrical input without producing hydrogen. Leakage can increase under strongly reducing or strongly oxidizing conditions depending on defect chemistry, so reversible operation effectively tests both extremes. In practice, Zr-rich electrolytes like BZY are often favored when electronic leakage or redox-driven instability is a concern, because Zr-based perovskites tend to be more resistant to reduction than Ce-rich compositions[138]. BZCYYb improves conductivity partly by incorporating Ce, but this can introduce a greater tendency toward reduction and mixed conduction under very low pO_2, making careful operating-window selection and electrode design important[121].

A third requirement is chemical stability in humid and impurity-containing environments. Steam is unavoidable in reversible PCCs, so the electrolyte must preserve both bulk phase stability and interfacial integrity without forming products that degrade conductivity, adhesion, or Faradaic efficiency. This tradeoff is illustrated clearly by Tang et al., who compared Zr-rich BZY-15 with Ce-containing BCZYYb under high-steam electrolysis conditions. In their discussion, the BZY-15 cell showed only a very small voltage increase, about 10 mV over 500 h at 600 °C under 0.7 atm steam, whereas the BCZYYb cell exhibited a much larger increase of about 110 mV over 320 h under the same harsh conditions. The impedance evolution was consistent with this contrast: for BZY-15, the ohmic resistance changed only slightly and the polarization resistance remained essentially unchanged at 0.026 $\Omega \cdot cm^2$, while BCZYYb showed substantial increases in both contributions (Figure 2.25). The authors further note that the stability challenge of BCZYYb becomes much more pronounced as steam pressure rises, and oxygen-electrode delamination was observed after severe humid testing, underscoring that electrolyte choice can directly affect interface durability as well as bulk transport. These results sharpen the usual conductivity–stability

tradeoff: BZCYYb remains attractive for lab-scale demonstrations because of its higher conductivity and easier processing, but BZY becomes increasingly appealing when long-term operation under steam-rich or impurity-sensitive conditions is the priority[139].

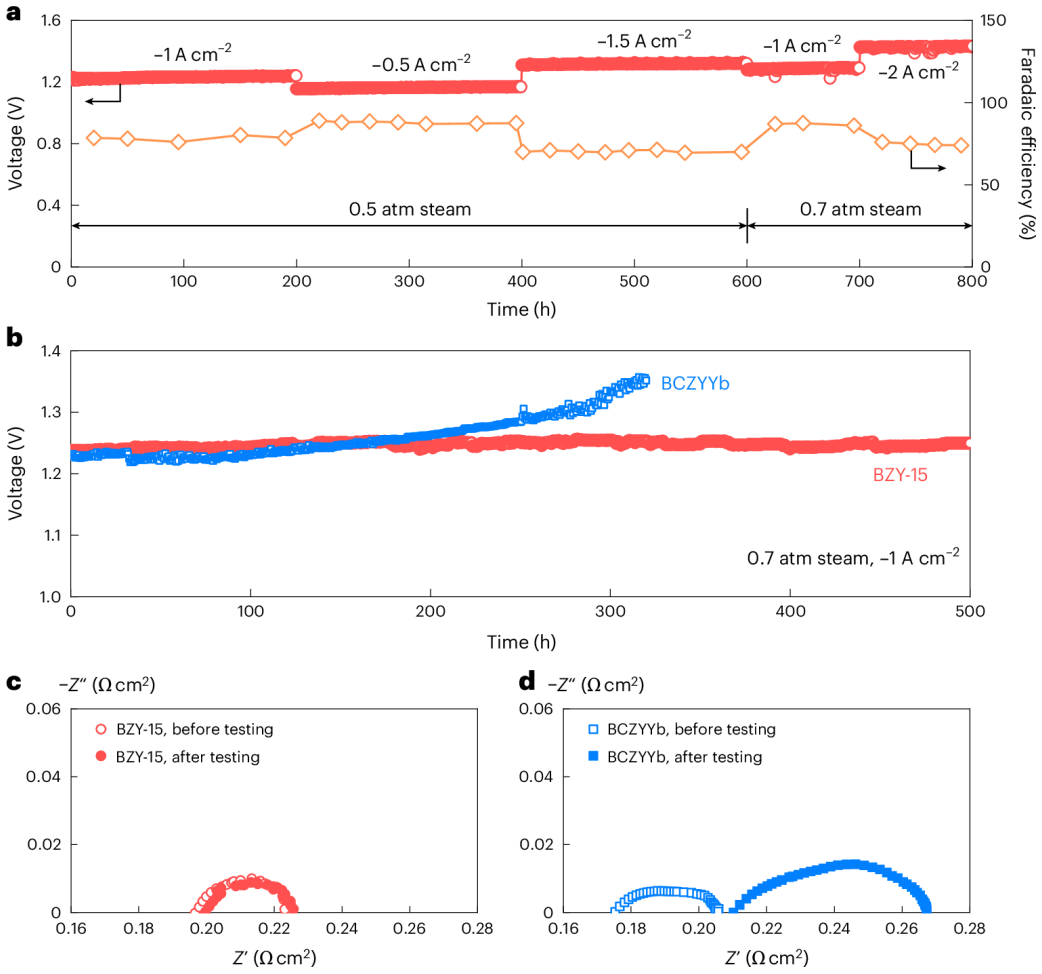


Figure 2.25. Stability under high-steam pressure electrolysis. (a) Cell voltage and Faradaic efficiency during long-term PCEC operations of BZY-15 cell at 600 °C. Feedstock for fuel electrode: pure H_2. Other testing conditions are specified in the main text. (b) Cell voltage during long-term PCEC operations of BZY-15 and BCZYYb cells at −1 A cm^{-2} and 0.7 atm steam at 600 °C. Feedstock for fuel electrode: pure H_2. (c) EIS measured at a d.c. bias of −1 A cm^{-2} before and after 500 h of testing of the BZY-15 cell in (b). (d) EIS measured at a d.c. bias of −1 A cm^{-2} before and after 320 h of testing of the BCZYYb cell in (b)[139].

A fourth requirement is microstructural and grain-boundary control. In many protonic perovskites, grain boundaries can contribute disproportionately to resistance, especially if impurities segregate

or if secondary phases form during sintering. Therefore, the effective conductivity in a real electrolyte is not only a bulk property but also a processing outcome. Here the tradeoff often flips: BZY is chemically stable but notoriously difficult to densify because it is refractory and requires higher sintering temperatures or sintering aids, which can introduce unintended secondary phases if not carefully controlled[140,141]. BZCYYb is often easier to densify at lower temperatures and can yield lower grain-boundary resistance under comparable processing, which benefits manufacturability and reduces variability in ASR_{Ω}. In practice, many successful cell designs using BZY rely on optimized powder processing, sintering aids, or thin-film approaches to overcome densification challenges while preserving chemical stability.

A fifth requirement is mechanical compatibility and defect-chemical expansion behavior. Electrolytes and electrodes experience thermal expansion during heat-up/cooldown and chemical expansion associated with hydration and redox changes. Reversible operation can impose repeated changes in local chemical potentials, so a mechanically robust electrolyte must resist cracking while maintaining strong adhesion to electrodes and interlayers[142–144]. Both BZY and BZCYYb are perovskites with similar crystal frameworks, but their defect chemistry differs; Ce-containing compositions can exhibit larger redox-related expansion under reducing conditions, which can increase interfacial stress if not buffered by appropriate electrode/interlayer design. From a practical standpoint, the electrolyte choice influences not only mechanical reliability but also the need for interlayers and graded junctions to manage stress and chemical compatibility.

Taken together, these requirements explain why BZCYYb and BZY are often treated as complementary electrolyte anchors in PCC development. BZCYYb is typically chosen when the priority is high conductivity and easier densification to minimize ohmic loss and enable high power density at intermediate temperatures. BZY is typically chosen when the priority is chemical robustness and stability against impurities, even if additional processing sophistication is required to achieve dense, low-resistance films[37,110]. In many modern designs, these tradeoffs are further managed by architecture: using thin electrolytes to reduce ASR_{Ω}, adopting stable oxygen electrodes and engineered interlayers to protect the interface, and selecting operating windows that avoid conditions where electronic leakage or chemical instability becomes dominant.

Electrolyte selection in reversible PCCs is a balance among conductivity, electronic leakage suppression, steam/CO_2 stability, grain-boundary resistance and densification, and mechanical compatibility. BZCYYb and BZY represent two ends of a practical design spectrum, conductivity/manufacturability-forward versus stability/robustness-forward, and the optimal choice depends on the targeted operating conditions, fabrication route, and the interface-engineering strategy used to integrate the electrolyte with high-performance oxygen electrodes.

2.6.2 Grain boundaries and processing control

In proton-conducting perovskite electrolytes, the measured ohmic loss is rarely a pure bulk property. Especially in the intermediate-temperature range relevant to PCCs, grain boundaries can contribute a large fraction of the total resistance, sometimes dominating the electrolyte ASR even when the intrinsic bulk proton conductivity is high. This is because grain boundaries often act as proton-blocking regions: they can be chemically different from the grain interior due to impurity segregation, secondary-phase wetting, dopant redistribution, or space-charge effects that deplete mobile protonic defects locally. As a result, electrolyte selection (e.g., BZY vs BZCYYb) must be paired with processing strategies that minimize grain-boundary resistance and ensure full densification[16,145].

A key origin of high grain-boundary resistance is unintentional impurity segregation. Trace species (from powders, binders, milling media), alumina contamination, or residual carbonate/hydroxide precursors can concentrate at grain boundaries during sintering, forming thin intergranular films that are poor proton conductors[146]. In Ba-based perovskites, such films can be especially detrimental because they wet grain boundaries and create a continuous barrier network across the electrolyte. This phenomenon helps explain why two electrolytes of the same nominal composition can show very different conductivities depending on powder purity and processing history. Practically, it means that controlling raw materials (high-purity precursors), milling tools (wear-

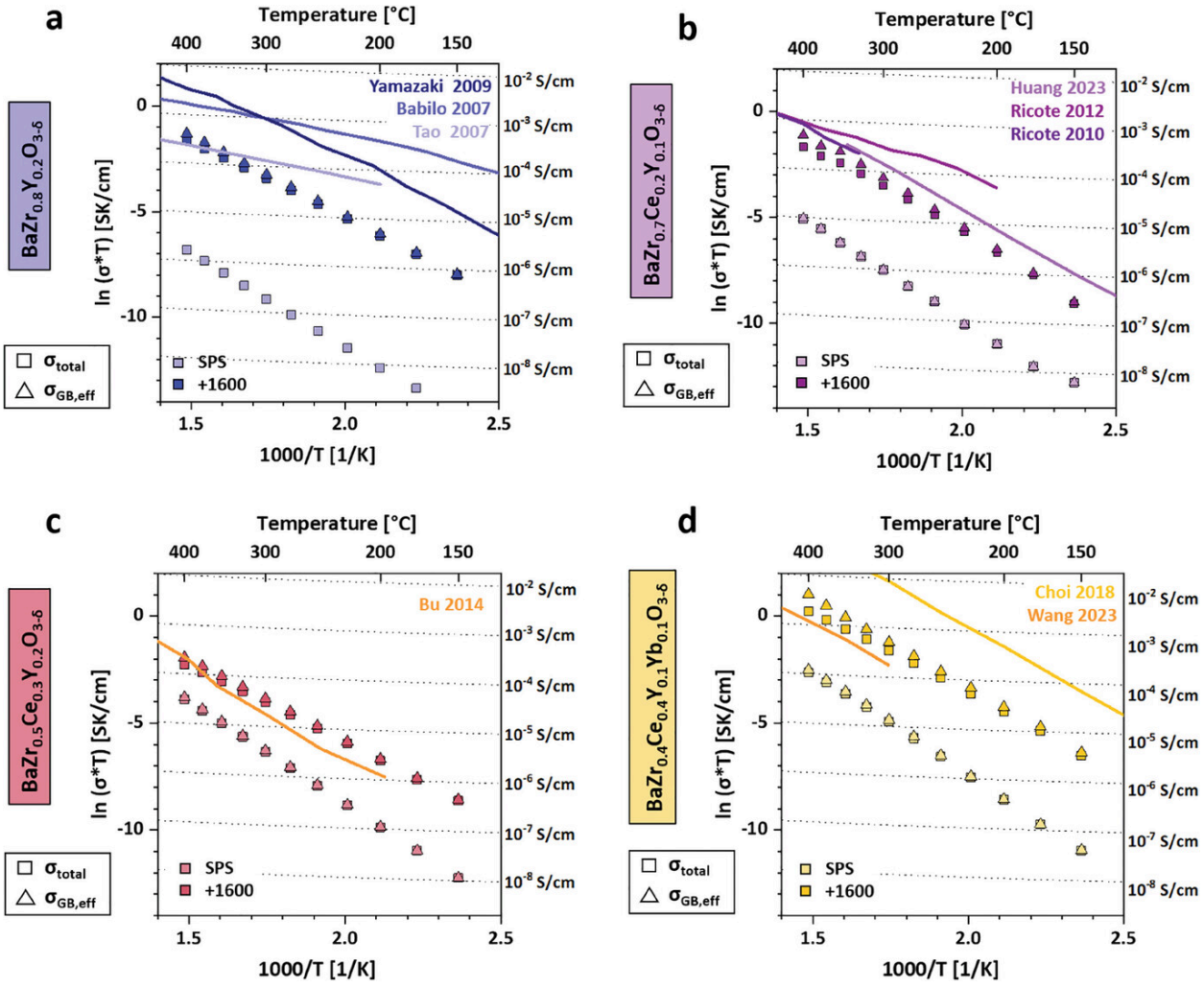


Figure 2.26. Segregation-controlled conductivity changes in different scientifically important $BaZrO_3$ based proton conductors. a–d) Electrochemical impedance spectroscopy in wet Ar/H_2 of $BaZr_{0.8}Y_{0.2}O_{3-\delta}$ (BZY20) (a) $BaZr_{0.7}Ce_{0.2}Y_{0.1}O_{3-\delta}$ (BZCY721) (b) $BaZr_{0.5}Ce_{0.3}Y_{0.2}O_{3-\delta}$ (BZCY532) (c) and $BaZr_{0.4}Ce_{0.4}Y_{0.1}Yb_{0.1}O_{3-\delta}$ (BZCYYB4411) (d) samples after SPS and post thermally treated for 5 h at 1600 °C in air. Total and effective grain boundary conductivity are represented by squares and triangles, respectively. Literature data in all plots is visualized by lines[147].

resistant media), and organic burnout (clean deboning to avoid residues) is not optional—it is central to achieving low ASR. At the same time, not all segregation should be viewed simply as harmful impurity blocking. Kindelmann et al. found that, in acceptor-doped barium zirconate ceramics, grain-boundary proton transport is governed not only by whether segregation occurs,

but by which species segregate and how that segregation reshapes the local defect chemistry (Figure 2.26). Their study argues that the positive grain-boundary space-charge potential that initially hinders proton transport also drives acceptor accumulation during high-temperature treatment, and that this controlled acceptor segregation can substantially enhance proton conductivity in both a model material and several application-relevant barium zirconate compositions[147]. In this sense, grain-boundary engineering in PCC electrolytes should be framed less as a goal of eliminating segregation altogether and more as a goal of suppressing harmful impurity-rich or boundary-wetting secondary phases while steering the boundary toward a defect-chemical state that is more proton-conductive. This point is especially important for BZY-based electrolytes, where thermal history, equilibration, and post-sinter treatment can determine whether the grain boundary remains strongly blocking or evolves into a more transport-permissive pathway.

The densification challenge is particularly acute for BZY, which is chemically robust but refractory and difficult to sinter to full density without very high temperatures or additives. High sintering temperatures can improve density and reduce pore-related leakage, but they also risk exaggerated grain growth, Ba loss, and unwanted secondary phases—each of which can reintroduce boundary resistance or weaken mechanical integrity[108,148]. In contrast, BZCYYb generally densifies more readily at lower temperatures due to the presence of Ce-rich chemistry and higher defect mobility, which can reduce processing burden and help achieve lower grain-boundary resistance under comparable sintering schedules. However, easier densification does not guarantee low grain-boundary resistance; impurity control and microstructural uniformity remain essential for both materials.

Processing control therefore focuses on two coupled goals: **(**i) eliminate boundary-blocking phases and (ii) achieve fully dense, fine-to-moderate grain structures that balance conductivity and stability. Common levers include powder synthesis route (solid-state vs wet-chemical), calcination temperature to ensure phase purity while avoiding hard agglomerates, and milling/deagglomeration to achieve uniform packing and reduce large pores. Sintering profile design is equally important: heating rates and dwell times influence pore elimination and grain growth, while atmosphere control can limit Ba volatilization and surface reactions. For BZY in particular, many laboratories rely on carefully chosen sintering aids to lower the densification

temperature and suppress residual porosity; the tradeoff is that sintering aids can themselves segregate or form insulating phases if dosed improperly, so they must be optimized with grain-boundary impedance as the key metric—not density alone[149].

Because grain boundaries and bulk transport respond differently to temperature and environment, impedance-based separation of bulk and grain-boundary contributions is a practical diagnostic for processing optimization. A well-processed electrolyte typically shows a reduced grain-boundary arc relative to the bulk contribution, and this improvement should remain stable after exposure to humid conditions representative of operation. When processing is suboptimal, the grain-boundary contribution often dominates and can also drift with time due to continued segregation, hydration-related changes, or slow intergranular phase evolution. In that sense, grain-boundary control is not only a manufacturing issue but also a durability issue[150].

Grain-boundary engineering interacts directly with interface engineering. A dense electrolyte with low grain-boundary resistance provides a stable foundation for low interfacial polarization, while a boundary-rich electrolyte surface can worsen electrode bonding and increase interfacial loss even if bulk conductivity is high. This coupling is one reason why electrolyte processing, surface preparation, and interlayer strategies often need to be considered together—especially for BZY, where aggressive sintering conditions used to densify the electrolyte can also create surface states that require deliberate interface treatment.

Grain boundaries are a primary determinant of electrolyte ASR in protonic ceramics, and they are strongly governed by processing. For BZY, the central challenge is achieving full density and low boundary resistance without introducing boundary-wetting secondary phases; for BZCYYb, the advantage of easier densification must still be protected by strict impurity control and microstructural uniformity. Effective processing control—high-purity powders, clean milling/debinding, optimized sintering (and carefully tuned sintering aids when needed), and impedance-guided validation—turns nominal electrolyte chemistry into reliable, low-loss electrolyte performance.

2.6.3 Thin electrolytes and supported architectures

For protonic ceramic cells operating at intermediate temperatures, the electrolyte thickness is one of the most direct device-level levers for performance because the ohmic area-specific resistance scales approximately with thickness ($ASR_{\Omega} \propto t/\sigma$). As PCCs are pushed toward 400–600 °C, lowering ASR_{Ω} becomes increasingly important for achieving high current density without excessive voltage penalty. This is why much of the field has moved from early electrolyte-supported geometries toward supported architectures that enable dense electrolytes in the ~1–20 μm range, while shifting mechanical strength to a separate support layer. Reviews of protonic ceramic electrochemical cells emphasize that reducing operating temperature while retaining performance is tightly coupled to electrolyte development and cell architecture[22].

In an electrolyte-supported cell, the dense electrolyte (often hundreds of micrometers thick) provides structural support, simplifying fabrication and sealing but imposing a substantial ohmic loss[151]. As a result, electrolyte-supported designs are valuable for fundamental studies and materials screening, but they tend to underperform at reduced temperature unless the electrolyte is exceptionally conductive or the operating temperature is relatively high. By contrast, electrode-supported cells (most commonly anode-supported, but also cathode-supported in some designs) use a thick, porous electrode substrate for mechanical support and gas transport, allowing the electrolyte to be deposited as a thin, fully dense membrane. Classic demonstrations of anode-supported protonic cells with thin electrolytes show how this geometry unlocks high power densities once electrolyte thickness is reduced to the tens-of-micrometers regime, even when electrode processes remain nontrivial[125].

A representative demonstration of why thin electrolytes must be designed together with the support architecture is provided by Bae et al. Rather than treating electrolyte thinning as a membrane-only problem, they engineered a multi-scale anode support to provide a surface suitable for depositing a dense BZY thin film, noting that direct deposition onto conventional powder-processed anodes with micron-scale pores tends to generate pinholes and incomplete coverage. Using this architecture, they fabricated an anode-supported PCFC with a columnar, grain-boundary-free BZY electrolyte about 2.5 μm thick, tightly integrated with a nanoporous anode functional layer and a nanogranular cathode, thereby minimizing the grain-boundary penalty that usually limits BZY-

based cells[152]. The resulting cell delivered a peak power density of about 740 mW cm^{-2} at 600 °C, which the authors described as up to an order of magnitude higher than previously reported BZY-based fuel cells, illustrating that the benefit of a thin electrolyte is realized only when membrane densification, grain structure, and support surface morphology are co-optimized (Figure 2.27). In this sense, this work makes a broader architectural point: successful thin-electrolyte PCCs depend not simply on making the electrolyte thinner, but on creating a support/electrolyte pair that simultaneously enables gas tightness, low ohmic resistance, and mechanical integrity.

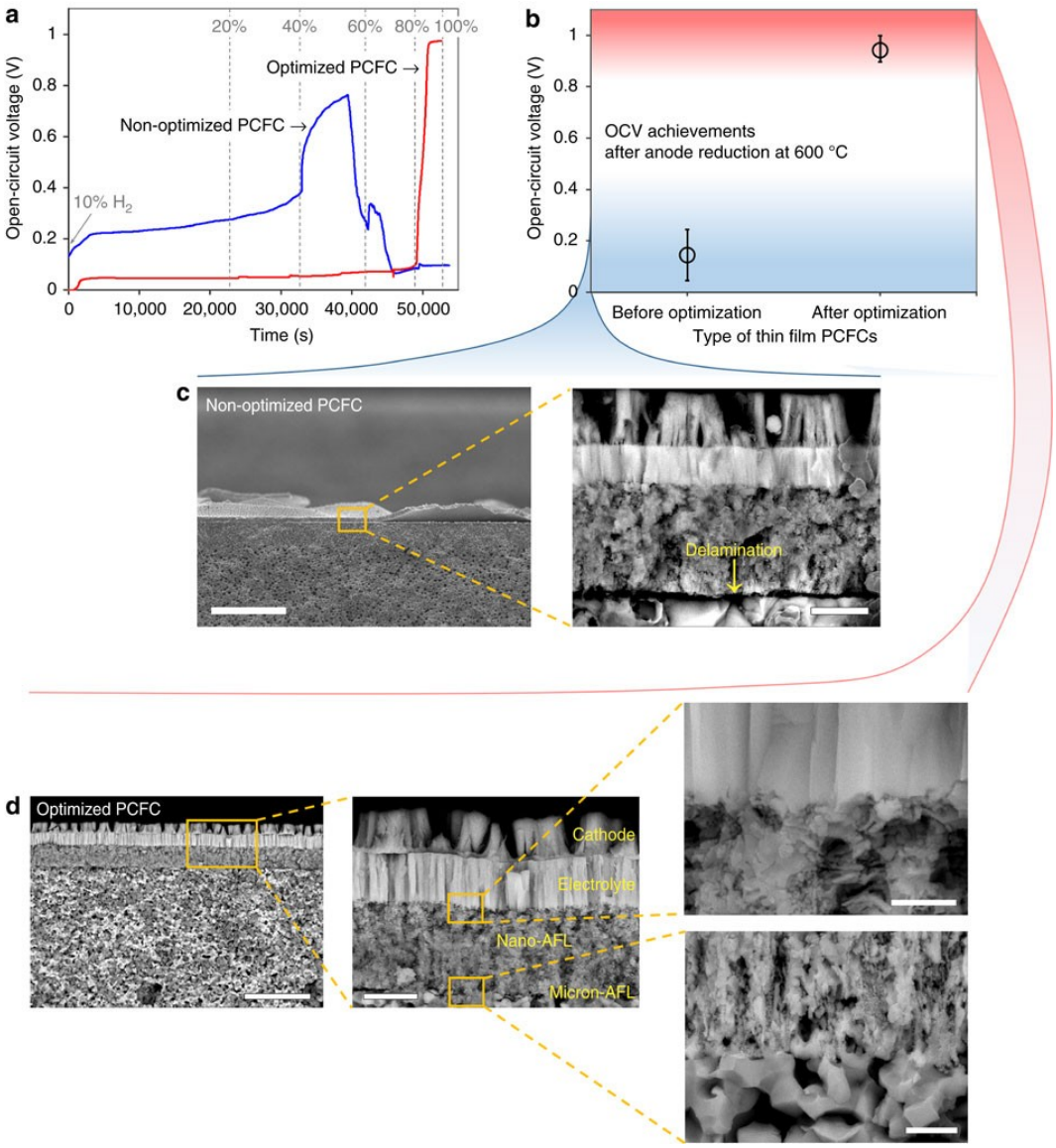


Figure 2.27. Comparison between PCFCs with optimized and non-optimized nano-AFLs. The optimized nano-AFL was fabricated by post annealing at 1300 °C for 1 h after PLD with

a volumetric composition of 50:50 (Ni:BZY), while the non-optimized nano-AFL by post annealing at 1200 °C for 1 h. (a) OCV profiles obtained during anode reduction in which H_2 concentration was varied from 0% to 100% with N_2 balanced in the feeding gas at the anode side. (b) OCV achievements after the reduction at 600 °C obtained from repeating measurement of the PCFCs fabricated under the same conditions with the PCFCs used in a, and error bars present the gap between the maximum and minimum values. (c) SEM images of the PCFC fabricated under non-optimized conditions exhibiting poor adhesion between nano- and micron-AFLs after reduction. Scale bars from left, 100 and 2 μm, respectively. (d) SEM images of the optimized PCFC after reduction exhibiting fully integrated morphologies. Scale bars from left and top, 10, 2, 0.5 and 1 μm, respectively[152].

The practical motivation for pushing thickness below ~10 μm is clear— ASR_{Ω} can drop dramatically—but this regime introduces strict constraints. When the electrolyte becomes very thin, it must be fully dense and defect-free: any pinholes, open porosity, or microcracks can cause gas leakage and internal shorting, undermining both OCV and durability[153]. Fabrication studies of thin BCZY-type electrolytes emphasize that <10 μm membranes demand exceptional densification control; aggressive sintering can densify the film but also promotes grain growth, impurity-phase formation, and microstructure damage in the porous support. These tradeoffs are even sharper for refractory compositions such as BZY, where high sintering temperatures are often required for full density, increasing the risk of Ba loss, interfacial reactions, and boundary-wetting secondary phases.

Supported architectures also differ in how they manage mechanical and chemical stresses. A thin ceramic membrane on a porous support experiences constrained shrinkage during co-sintering and can warp or crack if sintering mismatch is large[154]. During operation, chemical expansion and thermal cycling can concentrate stress in the thin electrolyte and at the electrode–electrolyte interface. This is one reason why thin-electrolyte success is tightly tied to interface engineering (interlayers, graded junctions, and controlled near-interface porosity) and to support microstructure (porosity, tortuosity, and mechanical compliance).

Several fabrication routes are commonly used to realize thin electrolytes. Co-sintered ceramic processing (tape casting, screen printing, slurry coating) is the most scalable pathway: a thin green

electrolyte layer is deposited onto a porous support and co-fired to achieve full density. Its advantages are manufacturability and large-area compatibility; its challenges are densification without pore infiltration or cracking and avoiding chemical reactions during firing—issues that are particularly relevant for Ba-based proton conductors. Vacuum-based thin-film deposition methods (e.g., pulsed laser deposition) can produce very thin (down to micrometers or even sub-micrometers), high-quality films with excellent uniformity and controlled interfaces, and have been used in protonic cells to realize engineered thin functional layers and dense thin electrolytes[155]. However, thin-film routes are often highlighted as cost- and throughput-limited for scale-up compared with ceramic co-sintering.

Overall, thin electrolytes and supported architectures should be viewed as a system optimization: thinning the membrane reduces ohmic loss, but it also increases sensitivity to defects, interface reactions, stress, and support microstructure. The most successful designs therefore combine (i) a fabrication route that reliably delivers a dense, crack-free thin membrane, (ii) a support that provides gas transport and mechanical compliance, and (iii) interfacial strategies (functional layers/interlayers/graded junctions) that preserve proton transparent contact and suppress long-term interdiffusion. Within this framework, BZCYYb-based thin electrolytes often target maximal conductivity and manufacturability, while BZY-rich layers and surface protections are leveraged when chemical robustness and long-term stability become the limiting constraints.

Chapter 3- Enhancing Surface Activity and Durability in Triple Conducting Electrode for Protonic Ceramic Electrochemical Cells

3.1 Abstract

With the material system operating at lower temperatures, protonic ceramic electrochemical cells (PCECs) can offer high energy efficiency and reliable performance for both power generation and hydrogen production, making them a promising technology for reversible energy cycling. However, PCEC faces technical challenges, particularly regarding electrode activity and durability under high current density operations. To address these challenges, we introduce a nano-architecture oxygen electrode characterized by high porosity and triple conductivity, designed to enhance catalytic activity and interfacial stability through a self-assembly approach, while maintaining scalability. Electrochemical cells incorporating this advanced electrode demonstrate robust performance, achieving a peak power density of 1.50 W cm^{-2} at 600 °C in fuel cell mode and a current density of 5.04 A cm^{-2} at 1.60 V in electrolysis mode, with enhanced stability on transient operations and thermal cycles. The underlying mechanisms are closely related to improved surface activity and mass transfer due to the dual features of the electrode structure. Additionally, the enhanced interfacial bonding between the oxygen electrode and electrolyte contributes to increased durability and thermomechanical integrity. This study underscores the critical importance of optimizing electrode microstructure to achieve a balance between surface activity and durability.

3.2 Introduction

High-temperature solid oxide cells (SOCs) are a promising technology for reversible fuel cell and electrolysis applications due to their high energy efficiency. They can store excess renewable energy as hydrogen and generate electricity when needed. Recent advancements in the materials, structures, and manufacturing of conventional oxygen-ion conducting SOCs have significantly enhanced their performance and long-term stability, potentially reducing costs[156–158]. However, the high operating temperatures required still pose challenges, including rapid degradation, high stack costs, and thermal incompatibility. Therefore, lowering the operating temperature is crucial to addressing these issues[159–161]. Protonic ceramic electrochemical cells offer a compelling alternative, demonstrating improved reliability, energy efficiency, and cost-effectiveness for

hydrogen production or electricity generation, making them suitable for lower-temperature operations (350~500 °C). These benefits arise from the high proton conductivity of their electrolyte, better material compatibility, and favorable electrode reaction kinetics[8,162].

Nevertheless, the reduction of PCEC operation temperature accordingly requires the matching of fast reaction activity on oxygen electrodes to result in the low electrode polarization resistance since it is crucial for facilitating the electrochemical reactions, in particular, under high current density and steam concentration. Thus, the proper electrode is needed to adapt into the electrochemical material system that is consisted of proton conducting electrolyte, which typically demands efficient transport and dissociation of reaction species, stability, thermochemical compatibility with electrolyte[6,163,164]. To be considered as the rational composition, the triple phase conductivity of electron, proton and oxygen ion is needed to extend the reaction sites throughout the entire electrode layer for maximizing catalytic activity[165,166]. Recent progresses have been made on the development of several promising triple conducting oxides such as $BaCo_{0.4}Fe_{0.4}Zr_{0.4}Y_{0.1}O_{3-\delta}$ (BCFZY), $PrBa_{0.5}Sr_{0.5}Co_{1.5}Fe_{0.5}O_{5+\delta}$ (PBSCF), $Pr_2NiO_{4+\delta}$ (PNO), and $PrNi_{0.7}Co_{0.3}O_{3-\delta}$ (PNC) electrodes which demonstrate superior fuel cell or electrolysis performances at reduced temperature range (350-500℃)[78,167–169]. These electrodes undoubtedly are proved to possess a significant fraction of proton conduction that is triggered by the formation of proton defects in the lattice by different mechanisms. The underlying mechanisms have been investigated to elucidate the intrinsic factors that support the favorable electronic structure for proton defect formation and transport. Additionally, to further enhance PCEC electrochemical activity, recently there are several other approaches being adopted to enhance the reaction kinetics at interface where ions, electrons and gas meet[76,170].

The durable operation of PCECs depends on several critical factors: rapid kinetic reactions, effective charge and mass transfer, and reliable interfacial bonding. These factors are dynamically linked and influence long-term degradation under complex operating conditions. To meet these requirements, precise control over electrode composition, morphology, layer microstructure, and interface is essential[171–173]. This ensures optimal surface activity, ion diffusion, and mass transfer while maintaining the cell structure and local geometry without deterioration. The electrode particle structure plays a key role, with micron-sized particles stacked to create porosity and active surfaces for reactions. Traditionally, electrodes in PCECs are made by sintering regularly shaped

particles, which are randomly stacked to form the electrode layer. This structure relies on the contact between solid phases and the open spaces between them, which may not be optimal[59,174,175]. Additionally, the interfacial bonding between electrode particles and the electrolyte membrane after thermal treatment is limited by the contact area, affecting long-term stability and interfacial polarization resistance[10,176].

To address these challenges, we have developed a nanofiber-architecture ultra-porous (NAUP) electrode, which integrates ultra-fine nanoparticles and hollow gas pathways to significantly enhance surface activity, mass transfer, and interfacial stability. This novel design leverages the unique properties of a triple-conducting composition, enabling the simultaneous conduction of protons, oxygen ions, and electrons. Such triple-conducting behavior facilitates seamless electron and ion diffusion while supporting rapid reaction kinetics and bulk diffusion processes, creating a highly synergistic system. At the macroscopic level, the NAUP electrode's channel-structured fibers provide high porosity, enabling efficient mass transfer of steam to supply adequate reactants for hydrogen production. Concurrently, the nano-scale electrode particles offer an enhanced surface area for catalytic activity, accelerating reaction kinetics. This synergy forms a feedback loop in which efficient mass transfer supports rapid reaction kinetics, and in turn, the accelerated reactions further drive mass transport. At the microscopic level, the unique triple-conducting nature of the PNC material ensures efficient surface reactions and bulk transport. Protons are swiftly conducted through the electrode, while oxygen ion and electron conduction facilitate the removal of intermediates, reducing the accumulation of reaction by-products and further enhancing reaction efficiency.

The synergistic integration of these structural and functional advancements translates into exceptional electrochemical performance. The NAUP electrode exhibits reduced activation energy for ORR, as well as minimized polarization resistance, leading to enhanced current density and cost-effectiveness. Under practical conditions, the NAUP electrode achieved a peak power density of 1.50 W cm^{-2} at 600°C in fuel cell mode and a current density of 5.04 A cm^{-2} at 1.60 V in electrolysis mode, with the potential to achieve faradaic efficiency greater than 90% at 1.0 A cm^{-2}, which proves the excellence in recent PCEC progresses (Supplementary Fig. 1, Supplementary Table 1 and Supplementary Table 2). The substantial improvement in electrochemical activity is attributed to the reduced electrode polarization resistance, which results from enhanced surface

activity, improved gas transport, and optimized interfacial morphology. The durability of the NAUP electrode under transient reversible operation, thermal cycling, and various challenging conditions has been demonstrated to be robust and reliable for practical applications. The readily manufactured electrode and its scalability will potentially accelerate its adoption into PCEC systems.

3.3 Materials and Methods

3.3.1 Fabrication of NAUP-PNC73 mesh-structure electrode

The prepared cotton fiber (FabricLA) was cut into 5 x 5 cm^2 squares and soaked in the PNC73 precursor solution. To get the specified concentrations, 1 M and 2 M, dissolve the stoichiometric amount of PNC73 powder in the desired solvent (a 1:1 mixture of 95% ethanol and deionized water) and agitate for half an hour until a clear phase is obtained. The desired solution was kept at the transparent glass containers for later use. Regular stirring before each use. The as-prepared PNC73 powder was fabricated using following procedure. Specifically, stoichiometric amounts of $Pr(NO_3)_3 \cdot 6H_2O$ (99.9%, Alfa Aesar), $Ni(NO_3)_2 \cdot 6H_2O$ (99.9985%, Alfa Aesar), and $Co(NO_3)_2 \cdot 6H_2O$ (98+%, Alfa Aesar) were dissolved in deionized water along with EDTA and citric acid to prepare a transparent precursor solution. The chelation process was carried out with a molar ratio of EDTA:citric acid:cations = 1:1.5:1, and a cation concentration of 0.02 mol L^{-1} for this batch. The precursor solution was then magnetically stirred and heated until a viscous gel formed. The gel underwent further heating at approximately 200°C, leading to self-ignition and the formation of powdery ash. This ash was transferred to a muffle furnace for calcination at 1000°C for 5 hours, resulting in a crystalline perovskite phase of PNC73.

After fully immersing the fiber for 2 hours, it was calcined at 650°C/750°C/850°C for 3 hours with the heating rate of 1°C/minute and the cooling rate of 3°C/minute in ambient air to get mesh-structure electrodes with varying porosity. Once the black textile mesh was removed from the muffle furnace, it was trimmed to a specific area of 0.178 cm^2 to serve as the actual electrode layer for later use.

3.3.2 Integration of NAUP electrode to PCEC full cells

The full cells were fabricated using a mix of tape-casting and electrode-brushing or mesh-constructed techniques. The complete cells were prepared by first making the BCZYYb4411/NiO

hydrogen electrode and electrolyte green tapes using the tape casting procedure. By sandwiching layers of electrode support and electrolyte membrane at 70 °C for 5 hours, half-cell green tapes were manufactured. To remove the organic solvents and binder, the cells were pre-sintered at 920 °C after being taken from the tapes. Finally, the electrolyte was solidified by sintering the cells for 5 hours at 1500 °C to get the half cells.

For NAUP-PNC73 full cells, 10 µl of PNC73 ink was used to affix the mesh-structured electrode onto the electrolyte/hydrogen electrode bilayer. The electrode ink was prepared by blending 5 g of as-prepared $PrNi_{0.7}Co_{0.3}$ (PNC73) powder, 0.5 g of binder (5 wt% V-006, Heraeus, dissolved in α-terpinol), and 1 g of dispersant (20 wt% Solsperse 28000, Lubrizol, mixed in α-terpinol) with about 15 mL of ethanol using a high-speed centrifugal mixer (Thinky). After about 20-minute operation, the slurry attained a semi-flow condition with an appropriate viscosity for later use. Following that, dry the cells in the over first and then they were subjected to the identical sintering process to acquire the NAUP-PNC73 full cells. For powder-packed PNC73 full cells, PNC73 ink was brushed onto the dense electrolyte layer. This resulted in fully functional cells with an active area of 0.178 cm^2. The cells were then subjected to a firing process at a temperature of 1000 °C for 2 hours.

3.3.3 Cells assembly and electrochemical measurements

Both kinds of full cells were enclosed on the top of the lab-made testing fixtures (Supplementary Fig. 11) using Ceramabond™ 552 as sealant with the oxygen electrode facing upwards. A current collector made of silver mesh was utilized, with leads connected by silver wires. Once the cell was assembled, it was heated to 600 °C at a rate of 2 °C/minute. When the temperature reached 600 °C, with the continuous H_2 flow to hydrogen electrode at the rate of 20 sccm, NiO was converted to metallic Ni. Upon reaching the equilibrium and stable OCVs were captured to indicate the complete reduction, 40 sccm O_2 was fed to electrode to collect the data using the potentiostat (Parstat MC, Princeton Applied Research). Under fuel cell mode, the current-voltage-power curves, impedance spectroscopy at OCV for both NAUP-PNC cells and powder-packed PNC cells with variable frequency from 10^6 Hz to 0.01 Hz from 600 °C to 400 °C were noted. The amplitude was set at 50 mV RMS and the voltage range was +/-6V. For steam electrolysis, O_2 with certain relative humidity was introduced into the testing fixture through the custom-built humidifier. Different flow rates of oxygen were controlled by multiple flow meters. The polarization curves and impedance spectroscopy at 1.30 V from 600 °C to 400 °C were also recorded. Different relative

humidities and flow rates of oxygen were considered to revalidate the electrolysis performance of NAUP-PNC cells. All electrochemical data were collected and process using VersaStudio software.

Comprehensive impendence analyses were conducted once the resistance data were collected. DRT analyses were completed through the Gamry Echem Analyst software while the activation energy was calculated using Arrhenius equation. Cells also went through long-term durability tests, transient cycling tests, reversible cycling tests and thermocycling tests. The long-term durability test for steam electrolysis was operated at 1.30 V for the first 50 hours and then at 1.40 V for the second 50 hours. Through the process, impedance curves were recorded for 20 times to verify the decreased total resistance. The reversible test was carried on at 0.70 V for fuel cell mode and at 1.30 V for electrolysis for the total 100 hours. The transient cycling tests were maintained at 1.50 V, 1.35 V and 1.20 V for the step voltages while also varying between 1.20 V and 1.50 V for certain time intervals to witness current responses with any degradations. All mentioned experiments underwent at 600 °C. The thermal cycling tests were under 600 °C, 550 °C and 500 °C for a total 15-time assessment with the corresponding impedance curves presented. The acquisition of all data was performed using VersaStudio Software.

3.3.4 Faradaic efficiency and energy efficiency measurements

To evaluate the electrolysis performance for hydrogen production, humidified oxygen gas was supplied to the NAUP electrode with a steam concentration of 20%. Pure hydrogen gas (40 sccm) was fed to the hydrogen electrode as the sweep gas. To evaluate the FE (%), the hydrogen electrode outlet gas was injected into a specially designed flow meter to quantify the hydrogen production rate. The FE (%) was calculated using

$$\nu = \frac{V_m}{2F} \times i$$

$$FE(\%) = \frac{\nu_e}{\nu} \times 100\%$$

where the theoretical hydrogen production flow rate, $\boldsymbol{\nu}$ (sccm), is determined by several key parameters: the electric current, $\boldsymbol{i}$ (A), which drives the reaction; the factor **2**, representing the two electrons transferred per molecule in the steam electrolysis process; the Faraday constant, **F**, valued at 9.6485×10^4 C·mol^{-1}; and the molar gas volume, $\boldsymbol{V_m}$, set at 22,400 mL·mol^{-1} under

standard conditions. Meanwhile, the experimentally observed hydrogen production rate is denoted as ν_e, providing a practical counterpart to its theoretical prediction.

The electrolysis energy efficiency was calculated according to

$$EE(\%) = \frac{FE(\%)}{\upsilon}$$

υ is the corresponding voltage (V).

3.3.5 Characterizations

Scanning electron microscope (TFS Quattro S) was utilized to examine the surface of NAUP-PNC73 electrode and the cross-sectional area in both secondary electron and backscattered electron modes. Using the backscattered mode, detailed ultra-porous structure of mesh fiber was revealed. After acquiring the SEM images of certain regions, direct the images into Pathfinder X-ray microanalysis software to complete the EDS mapping to confirm all desired elements were successfully incorporated onto the mesh structure. The automatic peak identification, background subtraction and matrix corrections for quantitative analysis were acquired as a Spectral Imaging dataset. The distributed PNC elemental information exhibited contrast indicatives of the existence of praseodymium, nickel and cobalt, confirming the ideal compositional substances for later use. The morphology of the NAUP-PNC mesh was analyzed using transmission electron microscopy (TEM). The nanoparticles exhibited a uniform size distribution, ranging from approximately 20 to 100 nm. Energy dispersive X-ray (EDX) analysis, conducted with the TEM, confirmed the presence of Pr, Ni, and Co within the nanoparticles. A high-resolution TEM (HRTEM) image of the grain edge revealed a highly crystalline structure, corresponding to the (111) crystal plane of the perovskite structure, with a lattice inter-planar spacing of d = 0.339 nm. Furthermore, the selected area electron diffraction (SAED) pattern of the boxed region confirmed the long-range ordered crystal structure. A line-element scan demonstrated the homogeneous distribution of the three cations within the selected range. The crystalline phase structure of PNC73 powder and mesh structure were examined by X-ray diffraction (XRD, Rigaku SmartLab) using Cu rotating anode source.

3.4 Results and Discussion

3.4.1 Formation of self-assembled NAUP electrode structure

To facilitate the spontaneous self-assembled synthesis of the electrode component, we used a natural cotton mesh as a template, which provided the necessary mechanical strength. As illustrated in Figure 3.1a, after being properly tailored, the mesh was entirely immersed into the triple conducting $PrNi_{0.7}Co_{0.3}O_{3-\delta}$ (PNC73) alcoholic solution for 2 hours for absorbing sufficient loading with stoichiometric composition. Upon soaking, the color of the saturated mesh changed from white to dark green. To preserve its flatness during the subsequent calcination process, the soaked mesh was carefully placed between two aluminum plates for sintering at 750 °C for 3 hours to form black NAUP textile electrode, which was consequently cut to a precise area of 0.178 cm^2 as the functional electrode layer. In the conventional manufacturing process for the powder-packed PNC73 electrode, a thoroughly mixed PNC73 ink combined with a binder and disperser ensures strong bonding between interfaces. Accordingly, 10 µl of PNC73 ink was also applied to adhere the mesh-structured electrode to the surface of the electrolyte.

Once the PNC73 ink has been applied to the mesh-structured electrode using a pipette, the full cells are dried in the oven for 1 hour. Following this, a second calcination process is carried out at 1000°C for 2 hours. The morphology of the mesh-structured electrode was examined using a scanning electron microscope (SEM), which clearly displayed the interlaced textile mesh fibers in images of meshes soaked in both 1 M and 2 M solutions. This confirms the porous properties and suitable mechanical flexibility of the structure (Figure 3.1b, Supplementary Fig. 2 and Supplementary Fig. 3a).

By subjecting the PNC73-loaded mesh to sintering at temperatures well above the melting point of cotton fabric, the material was successfully preserved in its original self-architecture mesh shape. The moderate porosity level, around 50%, of the oxygen electrode has been shown to exhibit optimal electrochemical performance[59]. Therefore, the mesh-structured electrode immersed in 1 M PNC73 solution was used for all full cells in this study.

To further clarify the uniformity of the mesh-structured electrode, energy-dispersive X-ray (EDS) mapping images are shown in Figure 3.1c. These images reveal the presence of elements Pr, Ni, Co, and O distributed consistently across all mesh fiber bundles, indicating a uniform distribution

of the desired elements in the processed electrode samples. Figure 3.1d demonstrates the optimal porosity of the electrode, with a SEM image of a single mesh fiber in back-scattered electron mode providing a clear view of the numerous holes on the wrinkled fiber wall. These pores facilitate

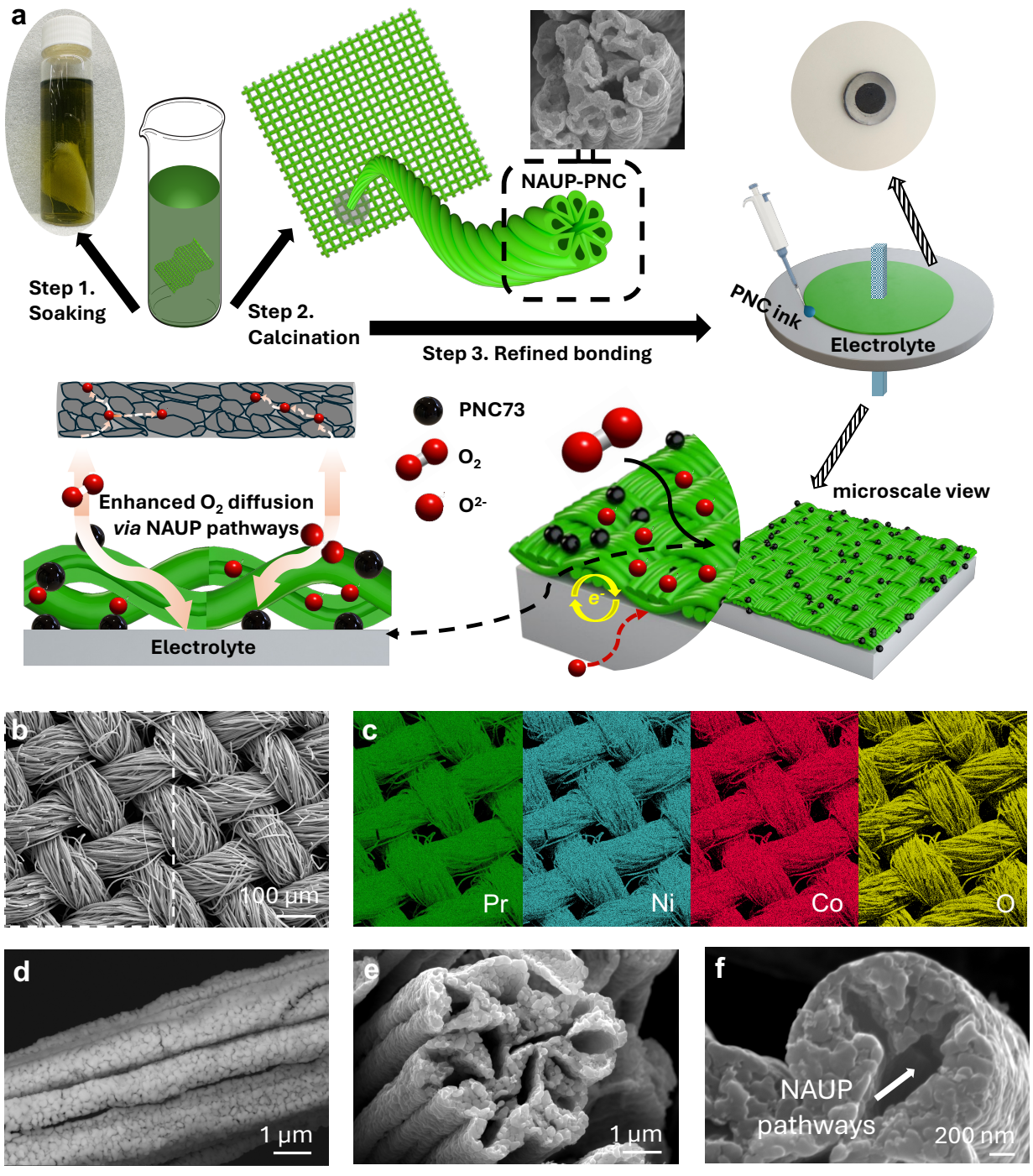


Figure 3.1. Scalable fabrication and characterization of nano-structured ultra-porous PNC73 oxygen electrode. (a) Schematic illustration of the process to fabricate NAUP-PNC73

mesh-structured electrode and its integration into the $BaCe_{0.4}Zr_{0.4}Y_{0.1}Yb_{0.1}O_{3-\delta}$ (BZCYYb4411[177])/BZCYYb4411-NiO half cells. The oxygen electrode has a diameter of 0.476 cm with a corresponding area of 0.178 cm^2, while the hydrogen electrode has a diameter of 0.872 cm with a corresponding area of 0.597 cm^2. (b) SEM image of mesh-structured NAUP-PNC73 (soaked in 1 M solution) surface, displaying visible channels for charge and mass dual-transfer. (c) EDS mapping for constituent substances on selected mesh area, including Pr, Ni, Co and O. (d) SEM image (back-scattered electron mode) of a single mesh fiber, showing observable holes for dual-transfer (side view). (e-f) SEM images of a single mesh fiber, indicating apparent pathways for dual transfer (cross-sectional view) and semi-NAUP pathways in nanoscale.

mass and charge transfer across a larger number of specific surface areas, which are considered active sites during electrochemical test (Supplementary Fig. 3b-3e). Additionally, cross-sectional observations of individual mesh fibers or clusters reveal that the crumpled surface of the fibers creates extra pathways for simultaneous mass and charge transfer, including inner-fiber and inter-fiber pathways. This takes advantage of the ultra-porous nature of the structure (Figure 3.1e). At the interface between the mesh-structured electrode and the electrolyte, the mesh fibers form a shell-like structure that integrates with the dense electrolyte, with an appropriate amount of PNC73 powder particles serving as a homogeneous adhesive in between (Supplementary Fig. 3f). Additionally, X-ray diffraction (XRD) analysis of the two mesh-structured PNC73 electrodes and the powder-packed PNC73 electrode confirmed that all samples exhibit a pure crystalline phase (Supplementary Fig. 4).

Due to the self-assembly process, PNC73 particles within the fiber walls aggregate from the liquid phase to achieve a nanoscale size of less than 400 nm, which can be precisely controlled through loading and calcination temperatures. This particle size is optimal for enhancing activity in both the oxygen reduction reaction (ORR) in fuel cell mode and the oxygen evolution reaction (OER) in electrolysis mode (Figure 3.1f). Considering its morphology and porosity, this innovative structure is termed the nano-architecture ultra-porous PNC73 (NAUP-PNC73) electrode. The expanded NAUP channels improve oxygen diffusion, providing high gas partial pressures at the interfaces and thereby facilitating reaction kinetics on this nano-structured electrode.

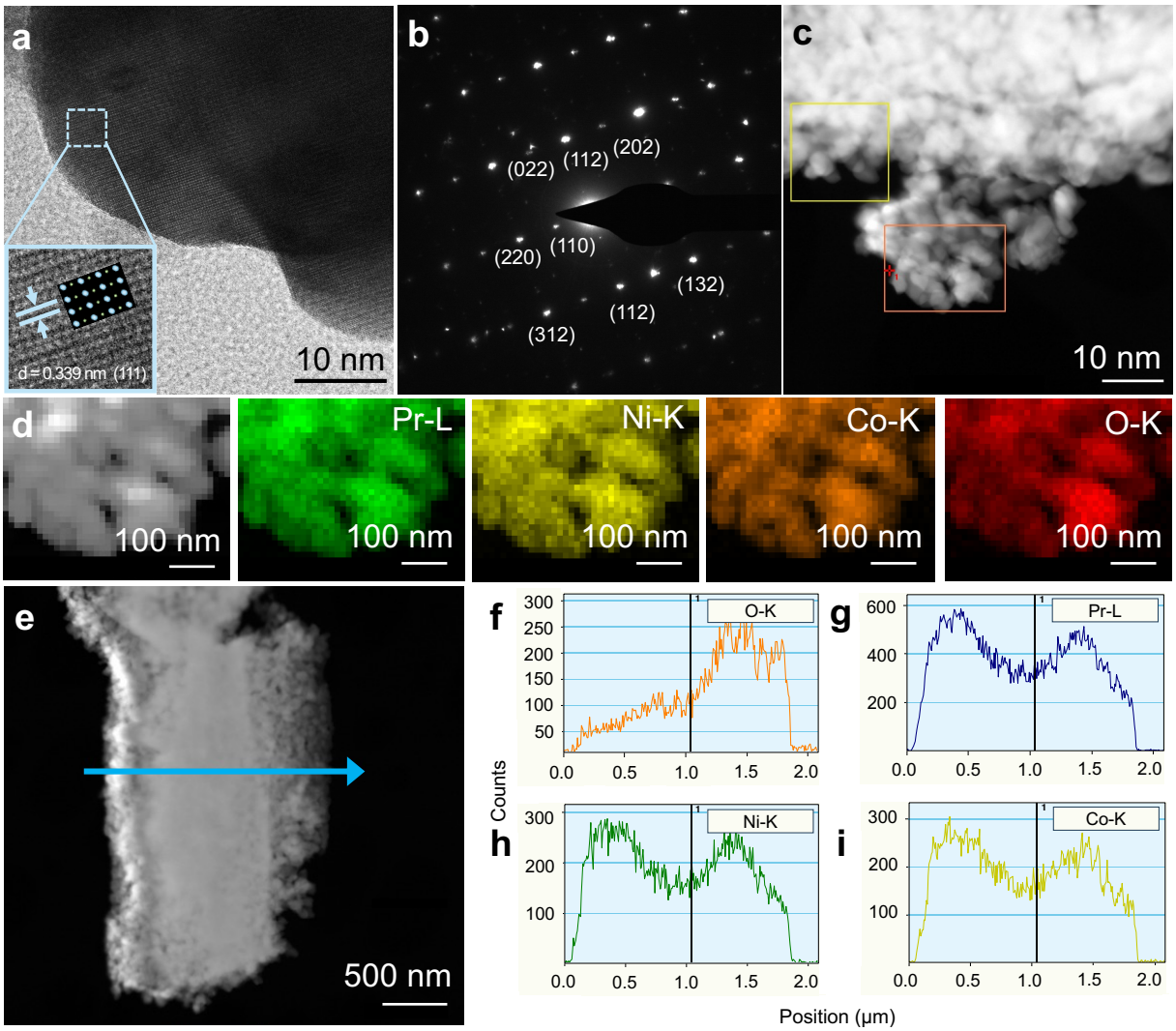


Figure 3.2. TEM characterization of NAUP-PNC oxygen electrode. (a) HRTEM image of NAUP-PNC nanoparticles. The inset contains magnified view of the marked region with a simulated atomic model of the PNC phase (orthorhombic perovskite structure, *Pnma* space group). (b) SAED pattern of NAUP-PNC nanoparticles. (c) HAADF image of NAUP-PNC nanoparticles; the representative areas are squared. (d) EDS elemental maps of the NAUP-PNC electrode confirm the presence of the PNC phase. From left to right, the selected area for EDS (orange rectangle in Fig. 3C) shows praseodymium as a green pattern, nickel as a yellow pattern, cobalt as an orange pattern, and oxygen as a red pattern, arranged in order. € EDS line scan (blue arrow) of a single NAUP-PNC electrode fiber. (f-i) Elemental information of line scan, oxygen-orange (f); praseodymium-blue (g); nickel-green (h) and cobalt-yellow (i).

To investigate the porous nanostructure of the NAUP-PNC electrode, transmission electron microscopy (TEM) was utilized to analyze its microstructure and atomic-level crystal structure. The high-resolution TEM (HRTEM) image of PNC nanoparticles within the mesh fiber, captured near their respective zone axes, is shown in Figure 3.2a. The magnified view of the marked region (inset) reveals atomic arrangements consistent with the [111] zone axis of orthorhombic perovskite symmetry. The measured interplanar spacing of 0.339 nm validates the lattice parameter, aligning with the pure PNC phase index information. To further support these observations, a simulated atomic arrangement of the PNC phase is provided, highlighting the atomic pattern. The selected area electron diffraction (SAED) results in Figure 3.2b corroborate the specific planes of the PNC crystalline structure. Additionally, a high-angle annular dark-field (HAADF) TEM image, along with elemental distribution maps, is presented in Figure 3.2c and Figure 3.2d. These maps confirm the uniform distribution of all elements comprising the PNC phase within the selected region (highlighted by the orange rectangle in Figure 3.2c). Through the line scan analysis (Figure 3.2e-3.2i) and point analysis (Supplementary Fig. 5) of a single NAUP fiber in HAADF mode, the elements Pr, Ni, and Co exhibit similar compositional peaks with varying amplitudes along the entire fiber. This consistency indicates that the prepared NAUP mesh retains uniform elemental composition and is well-suited for fabrication onto half cells.

3.4.2 Synergistic effects of enlarged dual-transfer pathways and enhanced interfacial bonding on reduced polarization resistance of R_o and R_p

Electrochemical performances of PCECs are closely related with the polarization resistances from each cell component and ohmic resistance (R_o) and polarization resistance (R_p) are two crucial parameters for evaluating the materials or microstructure. Thus, significant advancements have been achieved to reduce the resistance mainly by microstructure optimization[178–180].

To rationally study the synergistic effect of this NAUP electrodes on the polarization resistances, the impedance spectra from full cells are systematically investigated to analyze the relationship between the refined electrode microstructure and improved interfacial activity. As clearly seen in Figure 3.3a-3.3c, the R_o value dropped below 0.20 Ω cm^2, e.g., 0.190 Ω cm^2 under open-circuit voltage (OCV) conditions and 0.158 Ω cm^2 in electrolysis mode at 1.30 V and 600 °C, respectively. Compared with the conventional powder-packed PNC73 electrode, both R_o and R_p of this NAUP electrode are significantly reduced. For example, the R_p of NAUP-PNC73 in full cell was only 40%

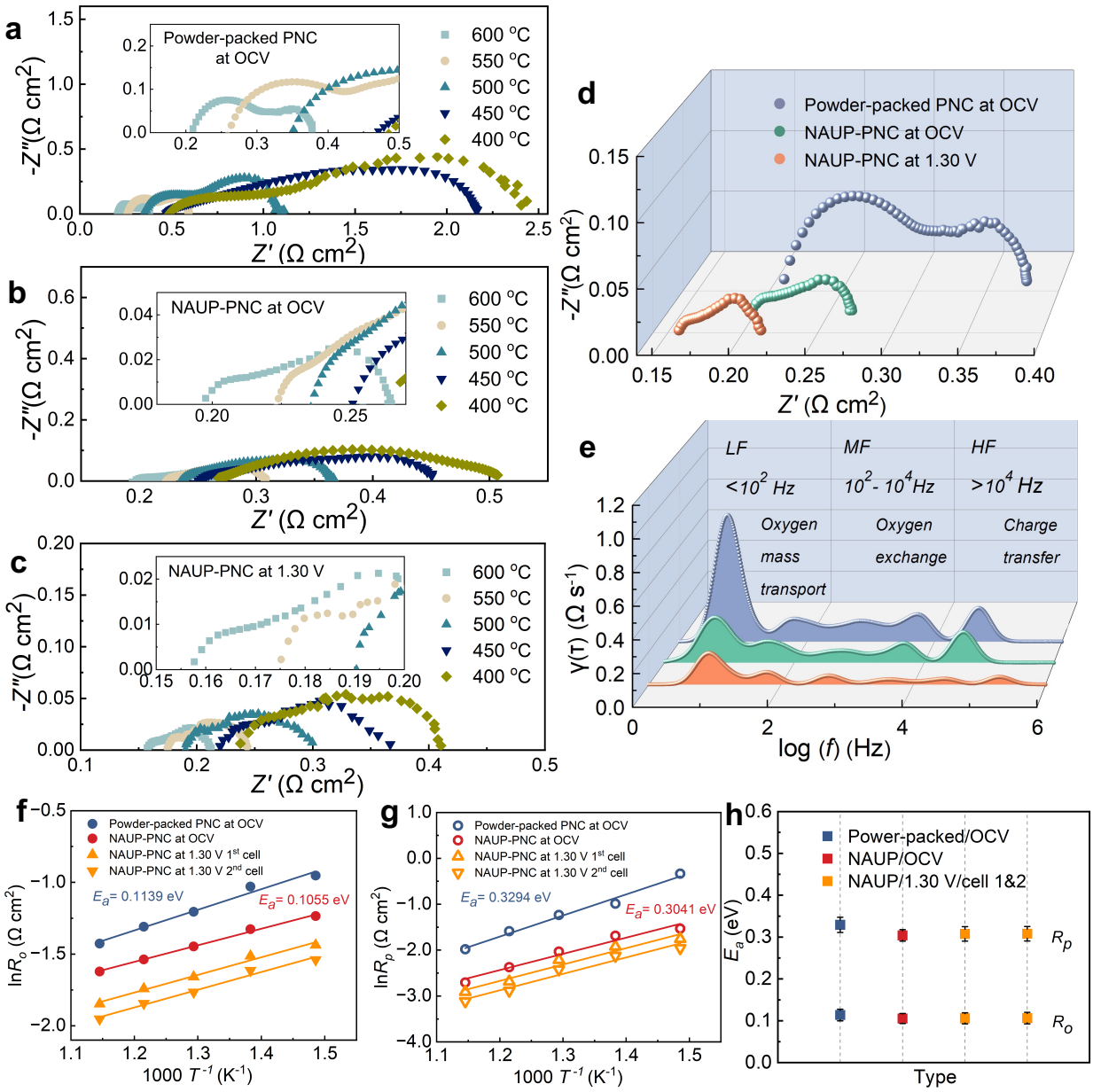


Figure 3.3. Correlated elucidation on synergistic impacts of electrode structures via electrochemical impedance spectra and analysis of distribution of relaxation times (DRT) and activation energy. (a) EIS spectra of powder-packed PNC in full cells measured under OCV conditions at 600°C. Hydrogen (20 standard cubic centimeter per minute, sccm) and oxygen (40 sccm) were respectively fed into the cells. (b) EIS spectra of NAUP-PNC cells measured under OCV conditions at 600 °C with the same gas conditions. (c) EIS spectra of NAUP-PNC cells measured at 1.30 V and 600 °C under electrolysis conditions (H_2, 20 sccm, was fed to hydrogen electrode side and 20 vol.% H_2O + 80 vol.% O_2, 40 sccm was fed to steam electrode). (d)

Comparison on EIS spectra from three representative conditions: regular powder-packed PNC cells at OCV condition; NAUP-PNC cells at OCV, and NAUP-PNC cells at 1.30 V, displaying reduced ohmic and polarization resistances. (e) The corresponding DRT analysis of the EIS spectra shows that all peaks are smaller across the entire frequency range. (f-g) Arrhenius plot of ohmic resistance and electrode polarization resistance of cells under four characteristic conditions with fitted straight lines (two cells were used to validate the repeatability). (h) The corresponding activation energies for R_o and R_p. Each test was conducted for six times to get the statistical standard deviations, presented as error bars. *All voltage values reported in this work was not iR corrected.

of that observed in powder-packed PNC73 electrode. A consistent trend was witnessed across the entire temperature range with exact resistance values and corresponding standard deviations shown in Supplementary Fig. 6. Furthermore, it is evident that the values of R_o and R_p presented under steam electrolysis were much lower than those collected under OCV conditions from the identical cells. This behavior is well explained by the distinct overpotential conditions, the accumulation of reactant concentrations on both electrodes, the efficient utilization of generated heat, and the maintenance of effective dual-transfer pathways. In electrolysis mode, the higher applied voltage reduces polarization resistance, enhances ion conductivity, and improves charge transfer, aided by heat generated during steam electrolysis[181,182]. The heat effect aligns with the observed results (0.192 Ω cm^2 at OCV and 0.158 Ω cm^2 at 1.30 V for R_o, 0.073 Ω cm^2 at OCV and 0.053 Ω cm^2 at 1.30 V for R_p). This phenomenon is probably due to the enhanced proton conduction and localized Joule heating, further lowering resistance and improving the efficiency of NAUP-PNC electrodes.

To gain a deeper understanding of the elemental reaction steps in polarization resistance, a distribution of relaxation times (DRT) analysis was performed to deconvolute their relationship. By separating the three impedance arcs and using appropriate fitting parameters, we can reveal the underlying electrochemical processes (Figure 3.3d). The peak intensities in the primary frequency regions—low-frequency (LF), intermediate-frequency (MF), and high-frequency (HF)—are quantified in terms of their statistical variability, corresponding to bulk ionic conduction, gas diffusion and interfacial reaction process[183]. It was observed (Figure 3.3e) that the NAUP-PNC73 electrode under FC and EC modes demonstrates smaller intensities than the conventional electrode structure in the LF region, which clearly indicated that the mass transfer was significantly

enhanced by the nanoscale ultra-porous structure. Similarly, the shrinking peaks (green and orange) in the MF region further confirmed the optimized oxygen surface exchange featuring faster and more efficient oxygen adsorption, dissociation and incorporation on the interface. This behavior was more pronounced in EC mode, where a 1.30 V electrolysis voltage was applied during measurement. In the HF region, the lower intensity observed in EC mode indicated enhanced charge transfer with fewer limitations due to the dual-transfer channels of the NAUP structure. This effect was not as evident in FC mode. It is important to note that the suppression of HF peaks aligns with the unobstructed pathways for charge movement during steam electrolysis, as illustrated in Figure 3.3c.

The activation energy is the minimum amount of energy required for this electrochemical reaction to proceed, representing the energy barrier that reactants must overcome during ORR or water splitting reaction, which is related to the performance[184,185]. As depicted in Figure 3.3f-3.3g, after combining the initial results of R_o and R_p noted in Supplementary Fig. 6a-6b with Arrhenius Equation for activation energy (Supplementary Eq. 1), the diagram of ln $R_{o/p}$ versus 1000 T^{-1} was plotted along with fitted straight line, clearly exhibiting the activation energy values. The calculated $E_{a,o}$ of conventional powder-packed PNC cells at fuel cell mode is 0.114 eV, whereas, that of two representative NAUP-PNC cells, whether acquired at open circuit condition or 1.30 V, is around 0.106 eV. Considering the polarization resistance as major contributor to the overall impedance, 0.329 eV, 0.304 eV, 0.308 eV and 0.308 eV (only first value is from the conventional powder-packed PNC cell). Considering polarization resistance as the major contributor to overall impedance, the $E_{a,p}$ is 0.329 eV for the conventional powder-packed electrode, 0.304 eV for NAUP-PNC electrode under open circuit, and 0.308 eV under 1.30 V. The reduction of activation energy is clearly attributed to the enhanced reaction kinetics, which is more compared in Figure 3.3h, Supplementary Table 3-Table 4. $E_{a,p}$ is strongly influenced by the nanoscale properties of the catalyst. Nanometer-sized catalysts provide a significantly higher surface area-to-volume ratio, increasing the number of active sites available for reaction. This enhanced interaction between reactant molecules, and the catalyst surface improves reaction efficiency and lowers the apparent activation energy. As revealed by TEM analysis (Figure 3.2), the nanoparticles in the NAUP-PNC electrode, measuring tens of nanometers, exhibit quantum effects and altered surface electronic properties. These characteristics stabilize transition states and reaction intermediates, further reducing the energy barrier. On the other hand, the optimized porosity and pore connectivity in the

NAUP electrode design enhance mass transfer pathways and minimize diffusion resistance. Within this optimized framework, a slight but consistent reduction in activation energy was observed, with a 7.37% decrease for $E_{a,o}$ and a 7.68% decrease for $E_{a,p}$. These reductions underscore the effectiveness of the NAUP electrode in stabilizing reaction intermediates and improving the adsorption and desorption efficiency of intermediates (Supplementary Fig. 7). The ultra-porosity and expanded active sites of the NAUP electrode facilitate rate-determining steps for both the oxygen reduction reaction (ORR) and oxygen evolution reaction (OER), resulting in enhanced catalytic activity and superior electrochemical performance.

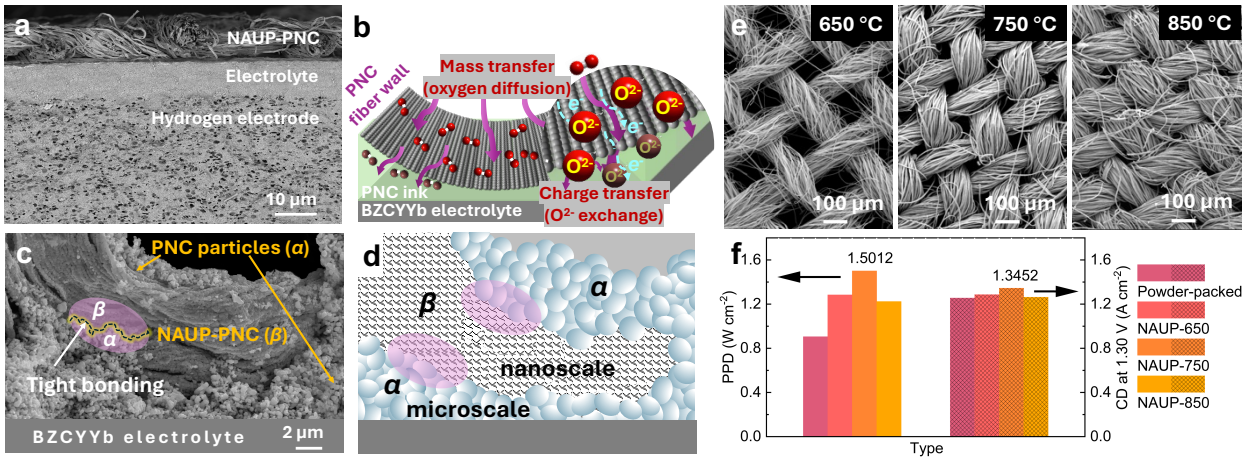


Figure 3.4. Illustration of the integrated NAUP PNC electrode and hybrid structure for optimal dual mass/charge transfer and interfacial strength in PCEC. (a) SEM image of cross section of as-fabricated NAUP-PNC/BZCYYb4411/BZCYYb4411-NiO "sandwiched" structure. Despite the use of a mesh-structured electrode, a strong and secure bonding between the electrode layer and electrolyte is still seen, with no evident signs of delamination. (b) Schematic illustration of occurrence of charge and mass dual-transfer through the single NAUP-PNC fiber inner wall to slight loading of PNC glue ink, ultimately to the electrode/electrolyte interface under the fuel cell mode. During the former fabrication, 10 μl PNC73 ink for certain electrode area (0.178 cm^2) was used to achieve refined bonding (Figure 3.1a, Step 3). (c) SEM image of single mesh fiber section, verifying the tight bonding between PNC73 particles (α) and NAUP-PNC structure (β). (d) Schematic illustration of enhanced bonding existing between α (microscale) and β (nanoscale). (e) SEM images of mesh calcinated at 650°C, 750°C and 850°C. (f) Bar chart of the comparison on the PPD and CD at 1.30 V at 600°C for different meshes.

To understand the synergistic mechanism behind the reduced overall resistance and activation energy, the cross-sectional view of a NAUP-PNC full cell was initially analyzed (Figure 3.4a). The cell configuration with the hydrogen electrode, featuring well-distributed holes, a dense and flat electrolyte, and the intricately intertwined mesh-structured NAUP oxygen electrode, is clearly visible. Although delamination is a potential concern due to the differing structures and morphologies of the mesh electrode and electrolyte, they are effectively bonded together with the aid of the adhesive PNC ink. Here, the NAUP-PNC full cells achieved the unique "homogeneous composition but heterogeneous morphology" compatibility, ensuring the adequate physical and chemical stability. The utilized PNC ink acted as the agent in microscale to better couple the large-grain electrolyte of tens of micrometers with NAUP-PNC oxygen electrode of nanometers (Figure 3.4b). Assuredly, the mesh-structured electrode facilitates the massive gas transport and efficient catalysis via the gas channels and nanoparticles on the fibers. Further throughout PNC ink, oxygen ions realize bulk diffusion and incorporation along interfaces *via* enlarged dual-transfer pathways. Figure 3.4c and 3.4d presents the tighter-bonding areas (light pink areas) along the newly created microscale and nanoscale PNC interface, which are PNC particles (α) and NAUP-PNC structure (β). The bridge-shaped NAUP-PNC plays a crucial role in both mass transport and charge transfer. The thickness of this hybrid electrode has been reduced to around 10 μm, which is the minimum value identified for maintaining sufficient structural strength[186,187]. While a thinner electrode could potentially reduce the transfer efficiency, this has been largely offset by the increased specific surface area created by its ultra-porous structure. To explore the relationship between dual-transfer efficiency and pore size in NAUP electrodes, meshes were prepared at calcination temperatures of 650°C, 750°C, and 850°C, denoted as NAUP-650, NAUP-750, and NAUP-850, respectively. This allowed visualization of the impact of calcination temperature on dual-transfer pathways. As shown in the SEM images of temperature-dependent meshes (Figure 3.4e), the lower calcination temperature (650°C) preserved finer structures with smaller particle sizes due to reduced sintering and minimized grain growth, resulting in larger pore sizes that enhance gas diffusion. In contrast, higher calcination temperatures reduced pore size due to enhanced sintering and crystallinity, which led to larger particle sizes and decreased surface area, as observed in the NAUP-850 mesh. To balance pore size and active PNC nanoparticle content for optimal reaction facilitation, electrochemical tests were conducted using single full cells fabricated with meshes of the three porosities (Figure 3.4f). Compared to the conventional powder-packed PNC electrode,

all NAUP-PNC electrodes demonstrated improved performance. Notably, the NAUP-750 achieved a peak power density improvement of up to 66% at 600°C and higher current density for electrolysis at 1.30 V. These results highlight the enhanced performance of the NAUP-750 mesh structure, attributed to its optimal porosity and dual-transfer efficiency. This NAUP-PNC mesh-structured electrode is designed to improve interfacial properties, resulting in lower activation energy for ORR/OER and reduced overall resistance, particularly R_p. This synergistic enhancement is a key highlight of its performance.

3.4.3 Superior electrochemical performances in fuel cell and steam electrolysis modes

To investigate the NAUP-PNC full cell performance, the *I-V-P* curves in fuel cell mode and polarization curves in electrolysis mode have been systematically measured respectively. We fabricated two cells: one with a conventional powder-packed electrode and the other with a NAUP electrode, to highlight the improvements achieved with the new structure. For both cells, the open-circuit voltages (OCVs) of the cells were above 1.03 V, indicating a dense electrolyte membrane and confirming the absence of gas leakage (Figure 3.5a-3.5b). Conclusively, the as-fabricated NAUP-PNC full cells attained an average increment of 58% on peak powder density (PPD) than that of powder-packed PNC full cells over the entire set temperature range (Supplementary Table 5). At 600 ℃, the PPD was optimized from 0.906 W cm^{-2} to 1.501 W cm^{-2} with H_2 (20 sccm) and O_2 (40 sccm) fed to the electrodes, which incredibly towered over the results in latest reported literatures (Supplementary Table 1). With the test temperature set as 550 ℃, 500 ℃, 450 ℃ and 400 ℃, the PPD yield shows improved performance by 59%, 60%, 67% and 37%, respectively (Supplementary Fig. 8). It strongly presents the excellence of NAUP mesh structure operated at low temperatures. When operating NAUP-PNC cells under steam electrolysis for hydrogen production, favorable performance was similarly demonstrated with the contrast to the current densities of powder-packed PNC electrode at 400 ℃ - 600 ℃. At 600 ℃, the electrolysis current density reached 5.04 A cm^{-2} at 1.60 V, however, the conventional PNC cells had only 3.36 A cm^{-2}, highlighting the 150% enhancement for electrolysis (Figure 3.5c-3.5d, Supplementary Table 6). Additionally, current densities at other four tested temperatures till 400 ℃ all increased by over 32%, demonstrating significantly better performance in NAUP-PNC full cells compared to powder-packed PNC full cells under the same applied voltages. The aforementioned advancements

have validated the enhanced electrode kinetics and reduced total resistance from the NAUP nanostructure, clearly indicating the significant boost of the investigated performances in both fuel cell and electrolysis modes among the recent PCEC progresses.

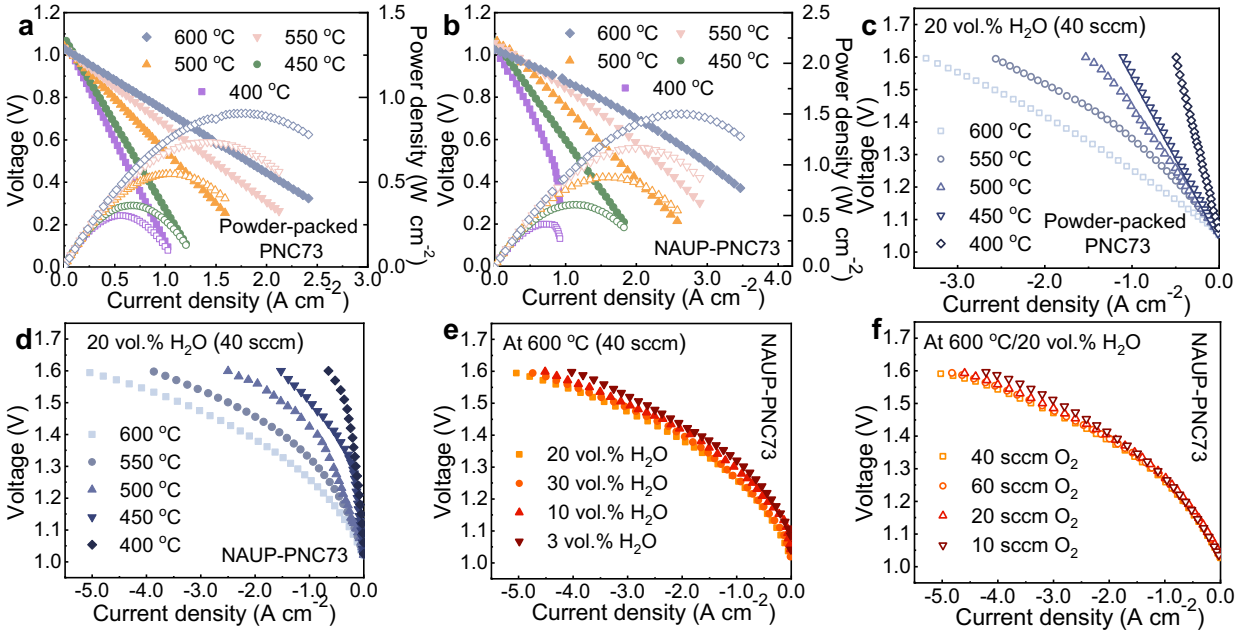


Figure 3.5. Electrochemical performances of NAUP-PNC73 full cells in both fuel-cell and electrolysis modes as compared to full cells with conventional powder-packed electrodes. (a) *I-V-P* curves of the cell with a conventional powder-packed PNC73 electrode measured at 400-600 °C. (b) *I-V-P* curves of a representative NAUP-PNC73 cell at 400-600 °C. (c) Polarization curves of a powder-packed PNC73 cell in electrolysis mode at 400-600 °C. H_2 (20 sccm) and 20 vol.% H_2O + 80 vol.% O_2 (40 sccm) was fed to the electrode. The applied voltage for all tests ranged from 1.60 V to OCV. (d) Polarization curves of a NAUP-PNC73 cell in electrolysis mode at 400-600 °C. (e) Comparison of electrolysis performance of NAUP-PNC73 in terms of different vol.% H_2O in O_2 at the flow rate of 40 sccm and 600 °C. (f) Comparison of electrolysis performance of NAUP-PNC73 in terms of different flow rate of O_2 at 600 °C. All tests conducted were under the same relative humidity of O_2, which was 20 vol.% H_2O in O_2.

To evaluate the dependences of PCEC conditions on electrochemical performances, the steam and oxygen partial pressures are varied to find how these parameters may affect hydration and other defect formation within electrolyte to consequently influence electrolysis behaviors. Firstly, a slight increase in electrolysis current density is observed with rising steam pressure (Figure 3.5e).

Specifically, the current density improved from 4.03 A cm^{-2} at 1.60 V with 3% H_2O to 5.04 A cm^{-2} with 20% H_2O. This behavior contrasts with that of conventional electrode structures, which do not exhibit a positive effect from increased steam pressure. This improvement is attributed to the enhanced gas diffusion and surface kinetics of the NAUP electrode. Additionally, higher steam pressure facilitates greater hydration in the triple-conducting PNC electrode, thereby enhancing both surface reaction efficiency and bulk proton conduction throughout the electrode layer and interface. However, further increase to 30% H_2O did not improve the current density anymore but slightly dropped to 4.74 A cm^{-2} (Supplementary Table 7). Secondly, by increasing the oxygen sweep gas from 10 to 60 sccm, the electrolysis current density also showed the uptrend and reached equilibrium (Figure 3.5f), which further validated that the NAUP structure allows large steam flow rate that enhances electrolysis activity. When comparing the performance of this work with other recent and representative studies, the current density and PPD of NAUP-PNC cells exhibit significant improvements, whether in fuel cell mode or steam electrolysis (Supplementary Fig. 9). All reference data were gathered from the tests using the same experimental gas conditions (H_2/O_2) as our study to reinforce the comparison (Supplementary Table 8). For example, the PPD from the cell with microwave-assisted sintered BCFZY electrode achieved 0.88 W cm^{-2} at 600 °C. While this demonstrates improved performance under extreme sintering conditions, it still does not meet the benchmark of 1.0 W cm^{-2} [167]. Notably, the NAUP-PNC electrode in this work surpassed 1.50 W cm^{-2}, same at 600°C, marking at least a 32% increment compared to other referenced studies. In terms of steam electrolysis performance, the current density at 1.30 V for NAUP-PNC full cells significantly exceeds that of other studies, showing approximately a 1.8-fold improvement. Specifically, the $(PrBa_{0.8}Ca_{0.2})_{0.95}Co_2O_{6-\delta}$ (PBCC95) oxygen electrode exhibited 0.71 A cm^{-2} at 1.30 V and 600 °C owing to the A-site cation ordered and deficient material, whereas the current density achieved in this work was ~1.35 A cm^{-2} under identical conditions, ensuring it is highly competitive for large-scale reversible operations. Overall, cell performance may be slightly affected by relative humidity or oxygen flow rate, with current densities decreasing by up to 20%. This marginal impact further confirms the robust physical and chemical stability of the nanostructured NAUP-PNC electrode. Faradaic efficiency (FE) and energy efficiency (EE) were evaluated for NAUP-PNC full cells to demonstrate their high performance in energy-intensive processes, such as water splitting. During steam electrolysis under 20 vol.% H_2O at 600°C, the cells achieved an impressive FE exceeding 95% at a current density of 0.6 A cm^{-2}. Additionally,

the energy efficiency for converting electrical energy into chemical energy surpassed 80% under the same conditions (Supplementary Fig. 10). These results highlight the exceptional feasibility of hydrogen production using the NAUP-PNC oxygen electrode.

3.4.4 Electrochemical performance durability in various degradation measurements

The electrode composition used in this study has been validated as a promising TCO material, free of alkaline earth metals, and exhibits significantly enhanced proton conductivity due to its readiness for hydrating lattice structure to form reasonable proton defects. The electrochemical durability of this electrode in fuel cell mode has recently been demonstrated through an accelerated transient test[169,170]. When the conventional electrode is transformed to incorporate NAUP structure, its performance durability under various transient conditions is systematically examined. Initially, the full cell was operated at a constant voltage of 1.30 V in 20% H_2O at 600°C for 50 hours, followed by a switch to 1.40 V for an additional 55 hours. The resulting current density exhibited only a 1.03% decrease during the first electrolysis period and a 1.24% decrease during the second (Figure 3.6a, Supplementary Table 10). During the test, EIS measurements at 1.30 V were recorded every 10 hours to monitor changes in polarization resistance (Figure 3.6b). Notably, the value of R_o remained stable at approximately 0.15 Ω cm^2, while R_p was maintained at around 0.05 Ω cm^2, with an acceptable fluctuation of about 5% (Supplementary Table 9). To assess the feasibility of operating in reversible modes, the cell was tested by alternating the voltage between 1.3 V and 0.7 V, and the response in current density was observed (Figure 3.6c). Throughout the 5 cycles, the current density responded immediately to voltage changes, demonstrating that the PNC electrode and its structure can swiftly adapt to mode transitions. The transient degradation rates were 1.87% for steam electrolysis and 1.55% for fuel cell operation (Supplementary Table 11), indicating that NAUP-PNC cells are both reliable and flexible as reversible protonic solid oxide cells.

Escalated transient testing is a valuable approach for assessing the resilience of cell properties by examining the adaptability of materials and interfaces under dynamic conditions. NAUP-PNC full cells were subjected to step-voltage and time-interval-based transient tests during steam electrolysis to gain deeper insights into the degradation mechanisms. In the step-voltage testing, the cell was cycled among 1.50 V, 1.35 V, and 1.20 V, with each voltage applied for 20 minutes

(Figure 3.6d). The electrolysis current density swiftly and consistently transitioned between 3.30 A cm^{-2}, 1.70 A cm^{-2}, and 0.75 A cm^{-2}, aligning with the initial performance measurements of the NAUP-PNC electrodes. Importantly, degradation at 1.20 V was minimal, at only 0.45%, while other degradation rates were below 2% (Supplementary Tables 12-Table 14). Despite the high overpotential during steam electrolysis causing minor damage to the nanostructure of the electrode layer, the NAUP-PNC full cells proved robust, maintaining reliable current density responses during rapid voltage changes.

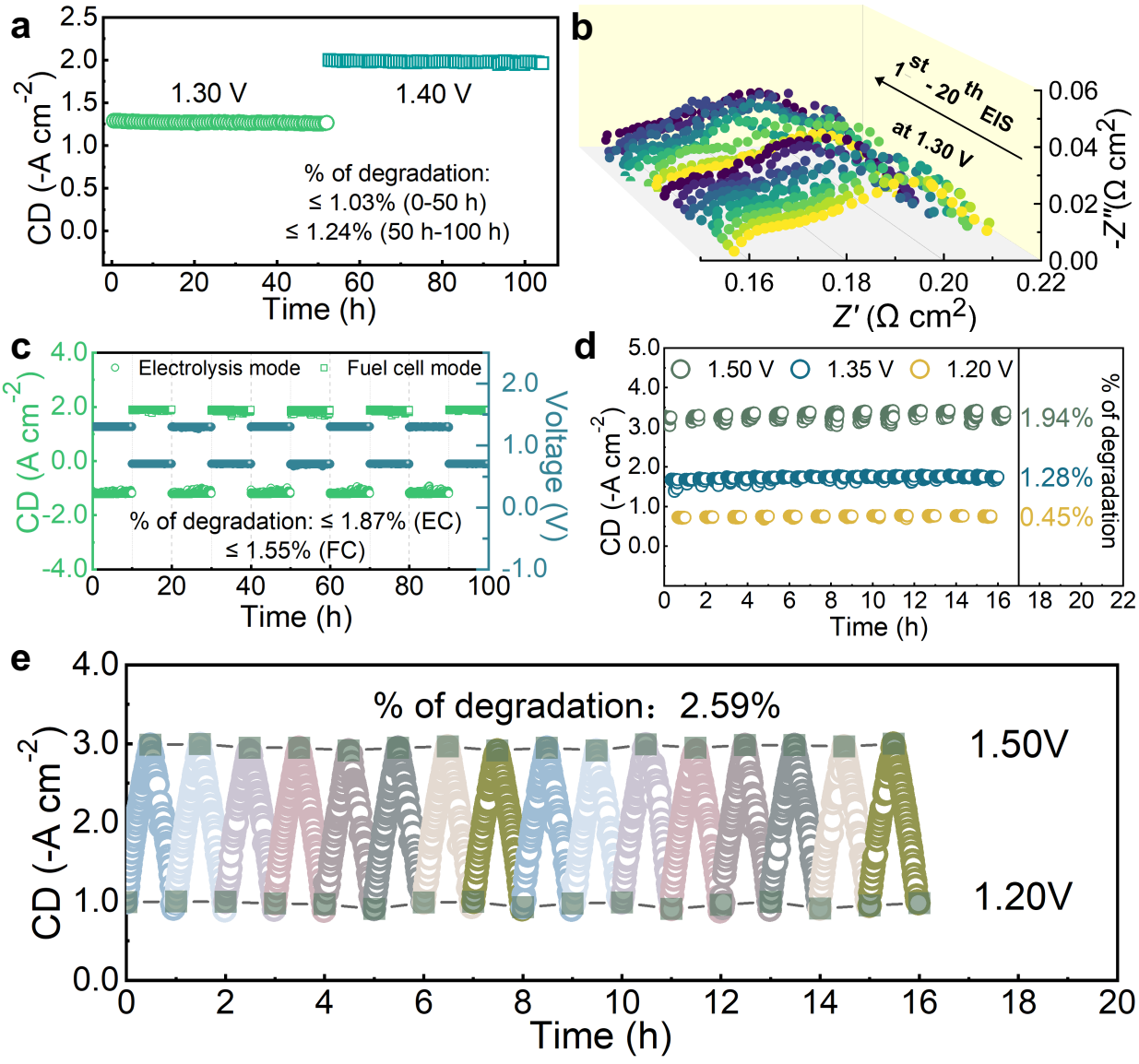


Figure 3.6. Extraordinary stability and durability on accelerated stress tests of NAUP-PNC full cells under both fuel cell and electrolysis modes. (a) Long-term stability tests for 100 hours,

during which a single switch of applied voltage was made from 1.30 V to 1.40 V, constant electrolysis testing at a fixed voltage of 1.30V for 50 hours, followed by 1.40V for approximately 55 hours, showing degradation rate of current density under electrolysis mode was less than 1.25%. (b) Corresponding EIS spectra collected at 1.30 V for 20 times during the long-term stability test. (c) Reversible tests between fuel cell mode at 0.70 V and electrolysis mode at 1.30 V for 100 hours (5 cycles). (d) Transient tests (step-voltage based) under electrolysis mode at 1.50 V, 1.35 V and 1.20 V respectively, dynamically operated across different modes. (e) Transient tests (time-interval based) under electrolysis mode between 1.20 V and 1.50 V. A cycle (from 1.20 V to 1.50 V, and then back to 1.20 V) lasted for 1 hour, dynamically operated across different modes. All tests were conducted at 600 ℃. Fuel cell mode was operated using H_2 (20 sccm) for the anode and O_2 (40 sccm) for the electrode. Electrolysis mode was operated using H_2 (20 sccm) for the anode and 20 vol.% H_2O + 80 vol.% O_2 (40 sccm) for the electrode.

In addition to step changes, the applied potential was varied based on specific intervals between 1.20 V and 1.50 V. The voltage was first increased and then decreased back to the original level, with each voltage-changing cycle lasting 1 hour and repeated 16 times. Figure 3.6e illustrates a clear periodic pattern in the current response with minimal deviations, and the statistical degradation rate was 2.59% (Supplementary Tables 15-Table 17). This significant durability of NAUP-PNC full cells highlights their potential for industrial-scale applications.

3.4.5 Structural resilience of the NAUP electrode on thermal cycles

Typically, solid oxide cells undergo heating and cooling processes across their operational temperature range, particularly during start-up and shut-down cycles[188,189]. The PNC material system has been elucidated to excel in the thermal stability during the multi-transient-cycling examination due to its improved thermal expansion behavior via the stoichiometric balance on various properties. In view of the frequent temperature fluctuations in realistic operation, it is crucial to perform comprehensive assessment of NAUP structure durability under various transient thermal cycle conditions.

As shown in Figure 3.7a-3.7C, the transient polarization curves at three temperatures reveal distinct behaviors in both fuel cell and electrolysis modes, with higher temperatures enabling faster recovery of reaction activity. At 600°C, current density degradation after four cycles is minimal—1.12% in electrolysis mode and 1.76% in fuel cell mode (Supplementary Table 18)—highlighting

the durability of NAUP-PNC full cells under optimal conditions. This improved recovery at higher temperatures is possibly due to thermally activated processes, such as enhanced ionic and protonic transport. Proton conduction is more efficient at elevated temperatures due to reduced energy barriers, while the diffusion of oxygen vacancies and chemical re-equilibration further contribute to performance restoration. These effects align with the observed low degradation rates, confirming the benefits of thermal activation on durability and performance recovery at 600°C.

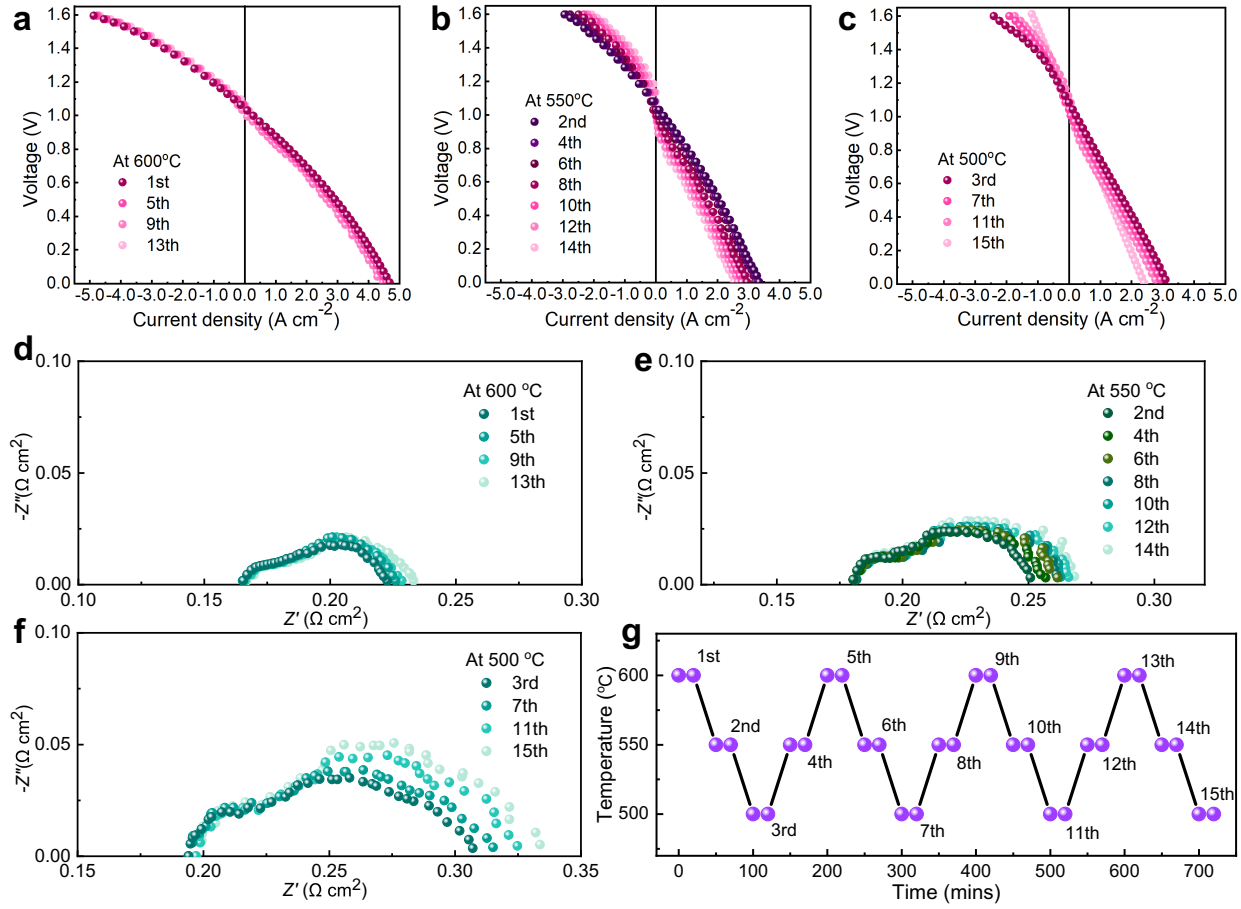


Figure 3.7. Thermal cycle stability evaluation of NAUP-PNC electrode under both fuel cell and electrolysis modes, explicated by dynamically operation across different temperatures. (a-c) *I-V* curves of fast-changing thermal cycling tests at 600, 550, 500 °C respectively. (d-f) Corresponding EIS curves at 1.30 V of fast-changing thermal cycling tests at 600, 550, 500 °C respectively. H_2 (20 sccm) was used for the anode and O_2 (40 sccm) for the electrode in fuel cell mode. Electrolysis mode was implemented for the anode using H_2 (20 sccm) and the electrode using 20 vol.% H_2O + 80 vol.% O_2 (40 sccm). (g) Illustration of the complete thermal cycling

process. The temperature ramp rate was 50 ℃ per 30 minutes. The measurement was completed after 20 minutes at the temperature point.

The impedance spectra were collected in electrolysis mode to reveal the possible mechanism for the discrete behaviors. As can be seen in Figure 3.7d measured at 600 ℃, there is no observable change on ohmic resistance while the electrode polarization resistance increases from 0.057 Ω cm^2 to 0.065 Ω cm^2 at 600°C after several cycles, reflecting a modest rise of less than 14%. Similarly, there is no increase in ohmic resistance at 550°C and 500°C during thermal cycling; however, the polarization resistance increased by 23.2% and 20.9%, respectively (Figure 3.7e and Figure 3.7f). More detailed data were recorded in Supplementary Table 19. Admittedly, the polarization resistance, which is the primary contributor to overall resistance, increased due to unstable temperature regions in the furnace cavity caused by rapidly fluctuating thermal conditions (Figure 3.7g). This led to significant mechanical stress on the full cell configuration and weakened the adhesive PNC junction sites beneath the ultra-porous mesh structure. Similar negative effects are observed when using only electrode slurry to fabricate powder-packed electrode full cells. These results indicate that more studies can be carried out to further improve the interfacial mechanical strength based on this NAUP electrode.

3.5 Conclusion

Engineering of nanostructured electrode into PCECs is crucial to enhance effectiveness and reliability for electrochemical performances. The hurdles remain on how to compromise the complexity of synthesizing nanostructure, effective activity and gas transport, and durability on morphology and interfaces. The created NAUP structure in this study explicitly addresses the concerns on the synthesis scalability, porosity loss, structure instability, and interfacial bonding. This template-assisted one-step formation of the triple conducting electrode is straightforward to improve activity and durability simultaneously.

The structure perfection in nanoscale highly facilitates the mass/charge transfer and interfacial bonding along boundaries, resulting in reduced ohmic and polarization resistance and lowering energy barriers. The ohmic resistance dropped from 0.24 to 0.15 Ω cm^2, whereas the polarization resistance was reduced from 0.138 to 0.05 Ω cm^2. Moreover, after stressed tests for stability, the total resistance consistently remained at lower level within minor changes. These makes it achievable to obtain enhanced PPD from 0.9 to 1.5 W cm^{-2} at 600 ℃, witnessing the increment of

166% under fuel cell mode and improved current density at 1.60 V from 3.361 to 5.042 A cm^{-2}, of 150% boost under steam electrolysis, indicating the elevated hydrogen and power. Still notably, the NAUP-PNC cells exhibit the tolerance to the various humidities and flexible gas conditions.

When evaluating the potential of switching to the NAUP structure to enhance PCEC performance, durability is a critical factor. The improved interfacial bonding between the NAUP-PNC electrode and the electrolyte, facilitated by the PNC73 ink as a transitional medium, ensures the robustness of NAUP-PNC full cells during both transient cycling and long-term testing. It also shows good thermal stability, ensuring the potential to adapt the real cell operation conditions. The expanded dual-transfer pathways not only accelerate triple-conducting rates but also enable effective thermal management across both operating modes and reversible operations, preventing thermal fatigue. This durability and thermal stability make NAUP-PNC a promising choice for resilient protonic ceramic devices used in hydrogen production.

In summary, we present a straightforward method for producing the mesh-structured PNC73 fabric, followed by a conventional co-sintering process with the electrolyte-anode bilayer, to create a spontaneously formed nano-architecture ultra-porous electrode suitable for both hydrogen and power production. The NAUP-PNC73 full cells demonstrate exceptional performance in reversible operations, with higher peak power density, reduced overall resistance, and remarkable durability, making them suitable for integration into advanced solid oxide systems. With the underlying mechanisms now understood, scaling down the electrode microstructure to the nanoscale with extensive porosity is expected to benefit other electrochemical materials and devices, such as alkaline fuel cells, electrolyzers, and biosensors.

3.6 Data and materials availability

All data are available in the main text or the supplementary materials. The supplementary materials can be found at https://doi.org/10.1038/s41467-025-59477-9

Chapter 4- Hybridizing Electrode Interface Structures in Protonic Ceramic Cells for Durable, Reversible Hydrogen and Power Generation

4.1 Abstract

Protonic ceramic electrochemical cells (PCECs) represent a transformative technology for sustainable hydrogen production and power generation by converting energy between chemical and electrical forms. Operating at intermediate temperatures, PCECs utilize proton-conducting electrolytes, achieving high efficiency and reduced degradation. However, a major bottleneck lies at the oxygen electrode due to sluggish kinetics and limited active sites. To address this, we present a hybrid oxygen electrode featuring $PrNi_{0.7}Co_{0.3}O_{3-\delta}$ (PNC) backbone infused with oxygen vacancy-rich praseodymium oxide (PrO_x) nanoparticles. This design leverages the interplay between surface and bulk properties to enhance oxygen adsorption, diffusion, and catalytic kinetics. The PrO_x introduces abundant oxygen vacancies and modulate the *d*-band center for optimal adsorption energy, while the PNC backbone provides robust proton conduction and stabilizes reaction intermediates. Cells incorporating this hybrid electrode demonstrate a peak power density of 1.56 W cm^{-2} at 600 °C in fuel cell mode and a current density of 2.25 A cm^{-2} at 1.30 V in electrolysis mode. Faradaic and energy efficiency reach 96.8% and 89.9%, respectively, with exceptional thermal cycling stability and reduced polarization resistance (0.079 Ω cm^2). This study underscores the potential of advanced electrode architectures to enhance the efficiency, durability, and applicability of PCECs in renewable energy systems.

4.2 Introduction

Protonic ceramic electrochemical cells (PCECs) are regarded as an advanced electrochemical device that plays a pivotal role in hydrogen production and power generation, offering a promising solution for efficient energy cycling. By utilizing proton-conducting ceramic electrolytes, PCECs enable effective conversion between electrical energy and chemical energy[6,143,190]. Operating at intermediate temperatures, PCECs achieve high efficiency and reduced degradation, making them ideal for sustainable hydrogen production through electrolysis and clean power generation in fuel cell mode. Their dual functionality and ability to integrate seamlessly into renewable energy

systems position PCECs as a transformative technology for achieving a circular energy economy[132,191].

To reduce system operation cost and improve material and interface reliability, there have been significant efforts made in advancing electrolyte and electrode materials, optimizing microstructure and processing to improve intrinsic activity. Among some crucial factors, the oxygen electrode plays a pivotal role in determining efficiency, interfacial compatibility, and durability[192,193]. This underscores the need for a high-performance, reliable material system capable of sustaining reversible operation under demanding conditions. An early technical focus lies in developing advanced oxygen electrode materials to address the primary causes of performance degradation and efficiency loss in current PCECs[194]. In their present form, both the water oxidation reaction (WOR) and oxygen reduction reaction (ORR) within mixed ionic and electronic conducting (MIEC) electrodes are largely restricted to the triple-phase boundaries (TPBs) where ions, electrons, and gases intersect. To overcome this limitation, incorporating proton conduction into MIEC materials to create triple-conducting oxides (TCOs)—capable of conducting electrons, oxygen ions, and protons—represents a promising strategy. This approach enables the extension of TPBs from the electrolyte/electrode interface into the electrode bulk, significantly enhancing reaction kinetics and overall efficiency. While a limited number of single TCO electrodes have been reported to exhibit superior electrochemical performance, their effectiveness underscores the potential of this strategy to improve PCEC activity and durability.

From a broader perspective on the nature of catalytic reactions, the interplay between electrode surface and bulk properties plays a pivotal role in determining electrochemical activity. Performance bottlenecks often stem from disparities between surface reaction rates and bulk transport properties. Factors such as insufficient active sites, a low concentration of oxygen vacancies, or inadequate proton conduction can significantly hinder reaction kinetics. By harmonizing surface reactivity with bulk transport capabilities, oxygen electrodes can overcome these limitations, achieving higher catalytic activity, faster reaction kinetics, and improved durability. This integrated approach is key to advancing the performance and longevity of PCECs. The core issue lies in the oxygen vacancy concentration, as it simultaneously governs surface catalytic reactions and bulk ionic diffusion by significantly impacting the surface electronic structure and ionic conductivity. Recent density functional theory (DFT) simulations demonstrate

that proton conduction effectively stabilizes reaction intermediates, thereby boosting overall efficiency. Leveraging the integration of surface and bulk properties, oxygen electrodes can achieve heightened catalytic activity, accelerated reaction kinetics, and enhanced durability, driving significant advancements in the performance of PCECs.

Transition metals like cobalt (Co) and nickel (Ni), along with rare-earth elements such as lanthanum (La) and praseodymium (Pr), are commonly used for their effectiveness in facilitating ORR and oxygen evolution reaction (OER)[195–197]. The partially filled *d*-orbitals of transition metals enable the optimal positioning of oxygen intermediates binding energy, while the partially filled *f*-orbitals of rare-earth elements provide the ability to adopt multiple oxidation states, facilitating oxygen storage and release. This characteristic enhances oxygen adsorption, catalytic processes, and redox stability in mixed conducting oxides[198–201]. Improving catalytic performance further requires increasing the density of active sites and the catalytic turnover frequency, which accelerates reaction kinetics[202]. A key factor in this enhancement is the precise positioning of the "*d*-band center" relative to the Fermi level, optimizing the adsorption energy for reactants and intermediates—known as the Sabatier Principle[203,204]. The *d*-band center, as proposed by Nørskov et al., is a proven and effective indicator of the binding strength of key intermediates during electrocatalytic reactions[205,206]. Sun et al. further demonstrated that a moderate increase in the *d*-band center energy improves catalytic activity by optimizing the balance between adsorption and desorption of oxygen-containing intermediates (e.g., O^*, OH^*, and OOH^*), which is essential for improving reaction kinetics and overall catalytic performance[207]. Although this principle is mainly applied to transition metals, incorporating Pr into perovskite structures, such as praseodymium oxide (PrO_x), can also influence the *d*-band center and further enhance catalytic activity. This optimization facilitates oxygen dissociation, reduction to hydroxyl ions (OH^-) in ORR, and stabilization of intermediates in OER, ensuring efficient and reversible PCEC operations[208].

By integrating these principles, a hetero-structured electrode comprising a proton-conducting backbone and oxygen vacancy-rich nanoparticles can optimize catalytic reactions through enhanced adsorption/desorption dynamics, improved electron-proton coupling, and stabilized intermediates. Coincidently, the ability of PrO_x to switch and balance between its oxidation states (Pr^{3+} and Pr^{4+}) serves as a driving force in generating and stabilizing more oxygen vacancies, thus

improving the catalytic activity of mixed oxides. Its mixed valence nature, charge-compensation behavior to maintain electroneutrality and the partially filled 4*f* orbitals for electronic structure all contributes to a reduced vacancy formation energy[209–211]. As a result, PrO_x serves as an ideal medium for promoting proton conduction in Pr-doped electrode materials. In this work, we propose a novel approach to reconstruct the hetero-structured oxygen electrode for PCECs by modifying the $PrNi_{0.7}Co_{0.3}O_{3-\delta}$ (PNC) surface with PrO_x oxide nanoparticles, to form a hybrid structure for high-efficient surface reaction and fast bulk diffusion simultaneously. The infiltration of PrO_x onto the PNC backbone creates a dual-phase electrode structure, consisting of a proton-conducting PNC backbone and oxygen vacancy-rich PrO_x nanoparticles. This heterostructure fosters a unique synergy: the abundant oxygen vacancies in PrO_x nanoparticles enhance the reactions by facilitating oxygen ion diffusion and adsorption, while the proton-conducting PNC backbone stabilizes reaction intermediates, promoting efficient catalytic kinetics at the surface. This hybrid electrode in full cells has achieved a peak power density of 1.56 W cm^{-2} at 600°C in fuel cell mode and a current density of 2.25 A cm^{-2} at 1.30 V in electrolysis mode, which excels in recent PCEC progresses (Figure S1, Supporting Information). At 600 °C and a current density of 0.60 A cm^{-2}, the hybrid cell yielded the faradaic efficiency of 96.8% and the energy efficiency of 89.9%, validating the superior cell-level electrical energy-to-chemical energy conversion efficiency. Exceptional stability during transient operations and thermal cycling was demonstrated, with a polarization resistance reduction to 0.079 Ω cm^2, underscoring the synergy between the PrO_x phase and the PNC electrode. This improvement can be attributed to enhanced surface reactivity, optimized bulk diffusion, and the formation of a reconstructed interfacial catalytic zone. By harnessing this innovative mechanism, our study offers valuable insights into the design of advanced electrode materials that effectively combine oxygen vacancy engineering with proton-conducting support. This easily fabricated hybrid electrode architecture presents a promising pathway for significantly improving the performance and durability of PCECs, further advancing their potential as a transformative technology for renewable energy systems.

4.3 Materials and Methods

4.3.1 Materials synthesis

To fabricate the full cells, a combination of tape-casting and electrode-brushing techniques was employed, ensuring precise layer formation and integration of the cell components. The initial step

involved creating green tapes for the BCZYYb7111/NiO hydrogen electrode and electrolyte using tape casting. By stacking the electrode support and electrolyte membrane layers, half-cell green tapes were fabricated after a controlled press at 70°C for 5 hours. These tapes were then pre-sintered at 920°C to eliminate organic solvents and binders, followed by a high-temperature sintering process at 1500°C for 5 hours, which solidified the electrolyte and established a dense, robust half-cell structure.

For assembling the complete PNC full cells, an electrode ink was prepared by mixing 5 g of synthesized PNC powder with 0.5 g of binder (5 wt% V-006, Heraeus, in α-terpineol), 1 g of dispersant (20 wt% Solsperse 28000, Lubrizol, in α-terpineol), and approximately 15 mL of ethanol. This blend was homogenized using a high-speed centrifugal mixer for 20 minutes, producing a slurry with suitable viscosity for electrode application. The PNC ink was then brushed onto the dense electrolyte layer, creating functional cells with an active area of 0.178 cm^2. Subsequently, the cells underwent a sintering process at 1000 °C for 2 hours to yield fully functional full cells.

To prepare a 0.2 M $Pr(NO_3)_3$ solution for infiltration, $Pr(NO_3)_3 \cdot 6H_2O$ (99.99% purity, ThermoFisher) was dissolved in a mixed solvent of ethanol and glycine. The final mixture contained 5 wt% $Pr(NO_3)_3$, 55 wt% glycine (as a fuel and complexing agent), and 40 wt% ethanol, calculated based on the total weight of the solution. The glycine was added as the agent for regulating PrO_x nucleation and promoting pore formation. During infiltration, a pipette was used to dispense the solution onto the full cells under vacuum conditions, allowing precise control of different loadings (Type I, II, IV, VI, and VIII). Finally, the cells were calcined at 1000 °C for 2 hours, forming a pure phase of praseodymium oxides at the interface and establishing an enhanced heterostructure critical for improved catalytic activity and cell stability.

4.3.2 Cells assembly and electrochemical measurements

The hybrid full cells were mounted on lab-made testing fixtures, sealed with Ceramabond™ 552, with the oxygen electrode facing upward. A silver mesh current collector was used, with leads connected by silver wires. After assembly, the cell was heated to 600°C at 2°C/min. Upon reaching 600°C, continuous H_2 flow to the hydrogen electrode at 20 sccm facilitated the reduction of NiO to metallic Ni. Once equilibrium was achieved and stable OCVs indicated complete reduction, 40 sccm of O_2 was introduced to the oxygen electrode, and data were collected using a potentiostat

(Parstat MC, Princeton Applied Research). In fuel cell mode, current-voltage-power curves and impedance spectra at OCV were recorded for the hybrid full cells across a frequency range from 10^6 Hz to 0.01 Hz, from 600°C down to 400°C. For steam electrolysis, oxygen with controlled relative humidity was introduced through a custom-built humidifier, with flow rates adjusted by multiple flow meters. Polarization curves and impedance spectroscopy at 1.30 V were similarly recorded from 600°C to 400°C.

Comprehensive impedance analysis followed, with DRT analyses conducted using Gamry Echem Analyst software, and activation energy was calculated via the Arrhenius equation. Durability assessments included long-term tests at 0.75 V and 1.25 V for 80 hours, transient cycling tests varying between 0.80 V and 0.20 V to observe current response and degradation, and reversible cycling tests at 0.70 V for 10 hours followed by 1.30 V for 5 hours, with multiple cycles. All tests were conducted at 600°C, except for thermal cycling tests, which alternated between 600°C and 500°C for five cycles. Data acquisition for all tests was performed using VersaStudio Software.

4.3.3 Structural characterizations

A scanning electron microscope (TFS Quattro S) was used to examine both the surface and cross-sectional areas of the hybrid electrode, utilizing secondary electron and backscattered electron modes. Once SEM images of specific regions were obtained, they were processed with the ColorSEM plugin to map and confirm that all targeted elements were successfully incorporated into the heterostructure. This process included automatic peak identification, background subtraction, and matrix corrections, resulting in a Spectral Imaging dataset for quantitative analysis. High-resolution transmission electron microscopy (HRTEM) and selected area electron diffraction (SAED) patterns were captured using the Titan Themis S/TEM with an ultra-bright XFEG gun. Imaging in STEM mode was supported by HAADF and triple DF/BF detectors for simultaneous visualization. The crystalline phase structure of the hybrid electrode was analyzed via X-ray diffraction (XRD) using a Rigaku SmartLab equipped with a Cu rotating anode source.

4.3.4 Measurement of surface oxygen vacancy

X-ray photoelectron spectroscopy (XPS) measurements were conducted using a monochromatic Al Kα source ($h\nu$ = 1486.6 eV). High-resolution O 1s spectra were recorded in the 534–526 eV range, with the energy scale calibrated to the C 1s peak at 284.8 eV. Data were processed using

CasaXPS, applying Shirley background subtraction and fitting with Gaussian–Lorentzian functions. The O 1s peaks were deconvoluted into two components: lattice oxygen (O_L^{2-}) around ~528.6 eV and surface OH^*/O^* species at oxygen vacancies near ~530.5–531.8 eV. Relative concentrations were derived from integrated peak areas.

Electron paramagnetic resonance (EPR) spectroscopy was employed at 140 K to quantitatively assess the oxygen vacancy concentration as EPR is a powerful technique for detecting unpaired electrons associated with oxygen vacancies. The measurement was conducted in the X-band with a microwave frequency of 9.35 GHz and a microwave power of 5 mW, which ensures sufficient sensitivity while minimizing signal saturation. The recorded EPR spectrum over the 3400–3600 G magnetic field range displayed sharp, symmetric Lorentzian-shaped derivative peaks centered around ~3480 G, yielding a g-value of approximately 1.98, characteristic of isolated oxygen vacancies. Quantitative analysis involved double integration of the normalized derivative spectrum using a 0.001 mol/L $CuSO_4 \cdot 5H_2O$ solution as the standard under the same conditions.

4.3.5 Measurement of bulk oxygen vacancy

Iodometric titration method was employed to quantify the bulk oxygen vacancy in PrO_x (Pr_6O_{11}). In this procedure, a known mass of Pr_6O_{11} powder (~0.1g) was dissolved in dilute hydrochloric acid (0.5 mol/L, Thermo Scientific) under acidic conditions, followed by the addition of excess potassium iodide (KI). The KI powder (99.9%, Thermo Scientific) was dissolved into 10 wt% aqueous solution for later use. The oxidized Pr^{4+} species in the sample reacted with iodide ions to form molecular iodine (I_2), which was subsequently titrated using a standardized sodium thiosulfate ($Na_2S_2O_3$) solution (0.1 mol/L, Thermo Scientific). The amount of iodine released—and thus the amount of Pr^{4+} originally present—was determined based on the volume of thiosulfate required to reach the endpoint, detected using a starch indicator (1% w/v aqueous solution, Thermo Scientific). The Pr^{4+}/Pr^{3+} ratio was then used to calculate the average praseodymium oxidation state, from which the bulk oxygen vacancy per Pr_6O_{11} formula unit was derived.

Thermogravimetric analysis (TGA) was employed to assess the oxygen release behavior and quantify the bulk oxygen vacancy concentration. Measurements were conducted using a NETZSCH STA 449 F3 thermal analyzer. For the pure PrO_x sample, 48.7 mg of powder was heated from 25 °C to 900 °C at a rate of 10.0 K/min under an air atmosphere (80% N_2 / 20% O_2). The composite PNC-PrO_x sample, composed of 10.6 wt% PrO_x and 89.4 wt% PNC (as specified

in this study), was analyzed under the same conditions. These measurements revealed distinct thermal and redox behaviors for the individual and hybrid systems, which were further utilized to calculate bulk oxygen vacancy based on stoichiometric deviations induced by thermal treatment.

4.4 Results and Discussion

4.4.1 Reconstruction of high-catalytic hetero-interface

To evaluate the high efficiency of PCEC reversible operations, it is crucial to understand how catalytic performance impacts the occurrence of ORR. The incorporation of a new PrO_x phase on a hybridized electrode significantly enhances catalytic activity, optimizing the positions of the conduction and valence band edges (Figure 4.1A). This optimization highly improves charge transfer, allowing more electrons to mobilize in the conduction band, thereby lowering the Fermi level. Following band gap alignment, the band edges become better suited for specific redox reactions[212–215]. For example, in water splitting reaction, protons are reduced to hydrogen gas relatively easily under this preferable condition with the abundant supply of electrons. The mixed-valence nature of PrO_x, which can readily transition between Pr^{3+} and Pr^{4+}, enables it to compensate for oxygen anion loss, facilitating the formation of vacancies without destabilizing the crystal lattice. This strong tendency to generate oxygen vacancies enhances ionic conductivity and, more importantly, proton transport. The preferential adsorption of oxygen at these vacancies promotes interfacial reactions, while the increased release of free electrons within the vacancies boosts charge transfer efficiency[216–218]. In comparing the activation energy (E_a), determined by polarization resistance, the E_a for ORR on the hybridized electrode is 87% of that on the pristine PNC electrode, indicating a more efficient reduction of oxygen (Figure 4.1B).

PrO_x is an exceptionally effective catalyst, largely due to its ability to enhance oxygen ion mobility, thereby significantly boosting catalytic activity. Its mixed ionic and electronic conductivity, combined with an abundance of oxygen vacancies, facilitates efficient oxygen ion transport. The oxidized praseodymium also demonstrates a remarkable ability to store and release oxygen, which is crucial for redox reactions. Furthermore, its inherent stability at high temperatures makes it highly suitable for PCEC operations that require sustained exposure to elevated thermal conditions. Notably, PrO_x exhibits a high reduction potential, resulting in a low energy barrier for oxygen vacancy formation through the release of lattice oxygen atoms, making it an excellent promoter

for vacancy generation[219–221]. The X-ray photoelectron spectroscopy (XPS) result of PrO_x is demonstrated in (Figure S2, Supporting Information). The substantial presence of surface oxygen vacancies (59.9%) in PrO_x plays a pivotal role in enhancing its electrochemical performance by serving as active catalytic sites that lower the activation energy for oxygen-involving reactions. These vacancies facilitate the adsorption and activation of molecular oxygen or water, stabilize key intermediates, and accelerate surface redox kinetics. Simultaneously, the enriched oxygen vacancy population enhances bulk ionic conductivity by creating low-energy pathways for oxygen ion migration. This synergistic effect—boosting both surface catalytic activity and ionic transport—underpins the significance of the vacancy-rich PrO_x-based oxygen electrode. Moreover, among the various phases of praseodymium oxide, the β-phase (Pr_6O_{11}) stands out for its exceptional electrical conductivity, with values increasing from $\sigma = 7.6 \times 10^{-6}$ S cm^{-1} at 60°C to 6.77×10^{-2} S cm^{-1} at 400°C, and reaching an impressive 1.40 S cm^{-1} at 850°C [222,223]. However, despite these advancements, PrO_x alone cannot meet the conductivity requirements to function as the sole material for PCEC operations. This limitation is addressed by the PNC backbone, a triple-conductor oxide that effectively reduces performance constraints at the triple-phase boundaries, where ions, electrons, and gases converge to facilitate reactions[224]. The PNC backbone exhibits high proton conductivity (σ_{H^+}), primarily attributed to the Ni dopant in the B-sites of its perovskite lattice, which enhances hydration and generates substantial proton defects[170]. This property not only positions PNC as a crucial structural support for the catalytic layer but also establishes it as a primary contributor to σ_{H^+}. Furthermore, PNC demonstrates overall conductivity exceeding 100 S cm^{-1} within the operating temperature range of 400°C to 600°C, ensuring excellent electronic conductivity (σ_{e^-})[169]. More importantly, Pr^{3+} closely matches the ionic size of common A-site cations, enabling seamless integration into perovskite structures without significant lattice distortion. This makes Pr particularly suitable for surface modification or infiltration strategies. When incorporated into the PNC backbone, PrO_x enhances the oxygen surface exchange coefficient and oxygen ion conductivity, significantly boosting the system electrochemical performance[225]. Thus, PrO_x is selected not only for its catalytic effectiveness but also for its seamless structural integration with PNC, making it an ideal electrocatalyst for the hybridization. The synergistic interaction between PrO_x, the reconstructed interface, and the PNC backbone optimizes the pathways for ORR, significantly enhancing the overall performance and durability of PCECs.

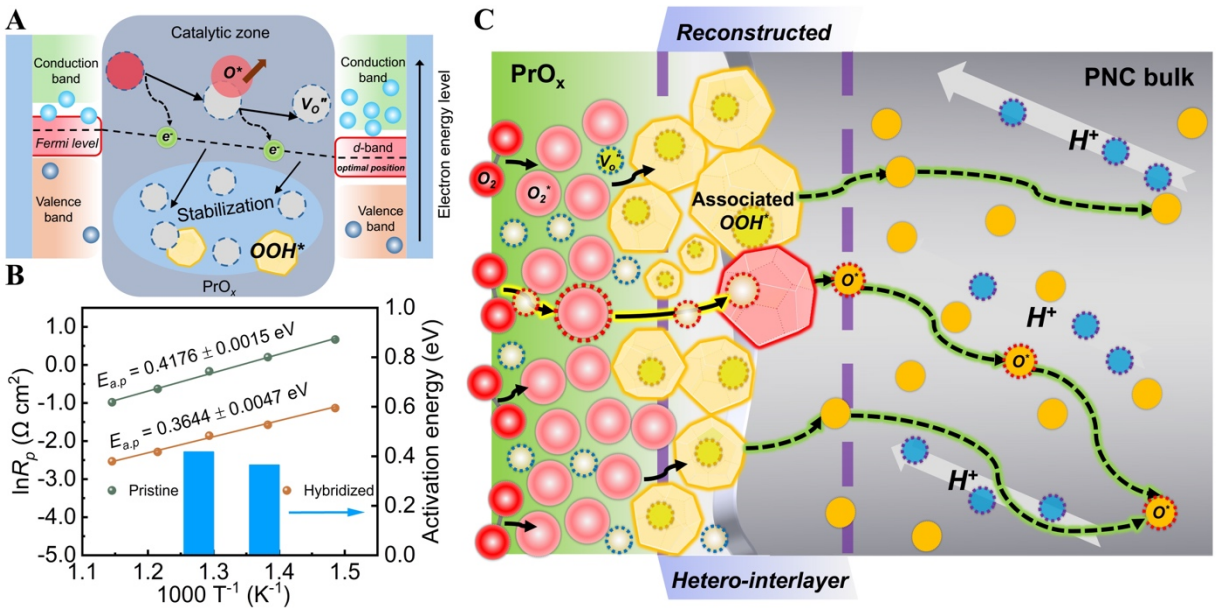


Figure 4.1. Mechanistic approach for designing a synergistic interlayer to enhance the ORR. (A) Impacted band gap structure resulted from oxygen vacancy formation in PrO_x phase. Light blue sphere, free electrons in conduction band; dark blue sphere, free electrons in valence band; hollow blue sphere, oxygen vacancy; red sphere, oxygen ion; yellow polygon, OOH^*. (B) Reduced activation energy for ORR due to catalytic enhancement. (C) Enhanced ORR facilitated by the reconstructed hetero-interlayer, blue ball, hydrogen protons.

The detailed multi-step mechanism is illustrated in Figure 4.1C, which emphasizes the critical interplay between intermediates and oxygen vacancies at the reconstructed hetero interface. This dynamic interaction not only alleviates potential catalyst surface poisoning but also accelerates ORR kinetics, leading to a more stable and efficient electrochemical process. By optimizing the intermediate stabilization and vacancy interactions, the reconstructed interface effectively improves both the activity and durability of the electrode.

4.4.2 Comprehensive characterizations on multiphase PrO_x catalytic zone

After fabricating the PNC/$BaCe_{0.7}Zr_{0.1}Y_{0.1}Yb_{0.1}O_{3-\delta}$ (BZCYYb7111[177,226])/BZCYYb7111-NiO full cells using the conventional powder-packed oxygen electrode for the half cells, the catalyst interlayer was developed via vacuum infiltration of a $Pr(NO_3)_3$ solution across the electrode bulk and the electrode/electrolyte interface (Figure S3, Supporting Information). The $Pr(NO_3)_3$ aqueous

solution was uniformly distributed over the electrode surface, followed by calcination to form PrO_x phases with varied morphologies. The infiltrated catalyst loadings were categorized by volume and weight percentage relative to the specific electrode area (0.178 cm^2): pristine, Type I (1 μL, 1.32 wt%), Type II (2 μL, 2.64 wt%), Type IV (4 μL, 5.28 wt%), Type VI (6 μL, 10.6 wt%), and Type VIII (8 μL, 21.1 wt%). The multi-morphology evolution of PrO_x is illustrated in Figure 4.2A, where an initial solution concentration of 1.32 wt% was applied to the pristine electrode to initiate interface reconstruction. At this stage, only a few nanoparticles formed, confirming the beginning of the process (Figure 4.2B). As hybridization progressed with a moderate solution concentration of 5.28 wt%, elongated nanobars were observed. The hybridized interlayer at this stage served as a catalytic zone, stabilizing intermediates like OOH^* and mitigating the rate-limiting steps of the oxygen reduction reaction (ORR) (Figure 4.2C). Till the optimization of hybridization (10.6 wt%), the PrO_x nanoparticles were firmly bonded to the PNC backbone, while the nanowires formed an interlaced network, creating a "reconstructed high-catalytic hetero-interface." This structural enhancement significantly expanded the active reaction zones and improved mass and charge transfer pathways (Figure 4.2D). To validate the distribution and composition of the PrO_x nanophases, ColorSEM, an advanced integration of SEM and Energy Dispersive X-Ray Spectroscopy (EDS) technologies, was utilized to reveal the compositional details of the particle- and wire-like pure PrO_x nanophases, highlighted in yellow (insets of Figure 4.2D). Resultantly, the resulting multi-phase PrO_x electrocatalyst appeared as nanoparticles or nanowires, expanding the active surface area (Figure S4, Supporting Information).

Compared to the pristine PNC backbone, the nanoparticle-impregnated electrode bulk, especially near the interface, exhibited an "inflated" poly-porous structure due to the use of glycine as a complexing agent, which naturally increased the number of mass transfer channels (Figure 4.2E and 4.2F). As the PrO_x loading increased from 1 μL to 4 μL, even to 6 μL, the number of nanoparticles observed grew exponentially (Figure S5A and S5B, Supporting Information), demonstrating a favorable growth trend and enhanced nucleation performance. However, increasing the $Pr(NO_3)_3$ loading to 8 μL (21.1 wt%) led to surface saturation, which impeded further penetration of the solution into the electrode bulk (Figure S5C, Supporting Information). Consequently, the catalytic enhancement became localized to the superficial shell rather than contributing to deeper interface activity. The final hybridized electrode surfaces after infiltration

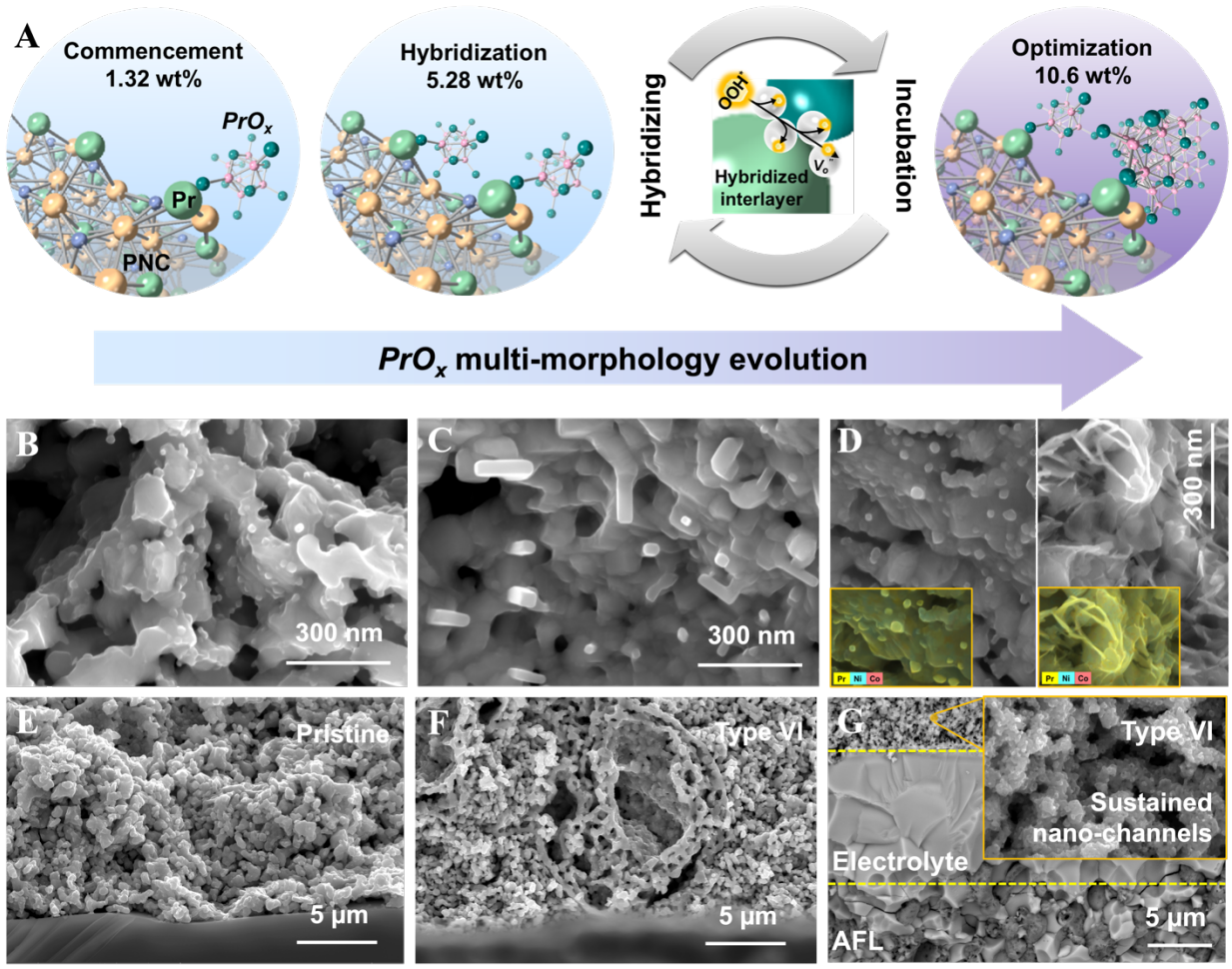


Figure 4.2. Schematic of the readily hybridized electrode and its characterizations. (A) Procedures for the incubation and hybridization of the PNC-PrO_x electrode. (B-D) Evolution of PrO_x morphology: (B) commencement with nanoparticles, (C) hybridization with nanobars, and (D) optimization with coexisting nanoparticles and nanowires (with inset showing compositional distribution; yellow for Pr, sky blue for Ni and peachy pink for Co). (E) Electrode/electrolyte interface of pristine PNC backbone. (F) Electrode/electrolyte interface of the hybridized electrode (Type VI, 6 μL), showing the porous structure. (G) Cross-section of the post-stability test single cell, highlighting sustained nano-channels on the hybridized electrode.

are shown in Figure S5D, Supporting Information, with detailed morphological observations available in Figure S6, Supporting Information. These findings emphasize the importance of balancing PrO_x loading to achieve optimal catalytic performance through effective bulk and interface integration. Furthermore, the cross-section of the post-test single cell reveals no signs of

delamination, ensuring long-term durable operation. The nano-channels formed through hybridization were preserved, supporting efficient mass transfer and revitalizing the catalytic electrode (Figure 4.2G).

X-ray diffraction (XRD) patterns of all hybridized electrodes confirm the coexistence of two distinct phases: a cubic fluorite structure (space group: *Fm-3m*) with a lattice parameter of a = 5.474 Å, and an orthorhombic perovskite structure (space group: *Pnma*) with lattice parameters a = 5.374 Å, b = 5.428 Å, and c = 7.632 Å (Figure 4.3A). A characteristic peak at 2θ = 28.24° corresponding to the PrO_x (111) plane exhibits noticeable variations with different infiltration loadings (Figure 4.3B)[227]. The smallest particle size, determined using the full-width at half maximum (FWHM) method, is 4.68 nm for the hybrid Type VI electrode (Figure 4.3C), indicating its enhanced catalytic performance (Equation S1, Supporting Information). To investigate the hybridized interface at the nanoscale, transmission electron microscopy (TEM) was employed to analyze the microstructure and atomic-level crystal structure of the hybrid Type VI electrode. A high-angle annular dark-field (HAADF) TEM image, accompanied by elemental distribution maps, is presented in Figure 4.3D. The PrO_x and PNC phases are distinguished based on the Ni- and Co-depleted regions (PrO_x) and Ni- and Co-rich regions (PNC), labeled as regions 'e' and 'f', respectively. The elemental distribution (in atomic %) of cations Pr, Ni, and Co across the interphase between the PrOx and PNC phases (along the line labeled 'e' in the HAADF image) is presented in Figure 4.3E. In the PNC region (right side of Figure 4.3E), the atomic ratio of Pr:Ni:Co is approximately 1:0.7:0.3, closely matching the nominal composition of the designed PNC73 backbone. High-resolution TEM (HRTEM) images for PrOx and PNC phases, acquired near their respective zone axes, are shown in Figure 4.3F and 4.3G. In Figure 4.3H, the magnified view of the marked region in Figure 4.3F, reveals atomic arrangements consistent with the [001] zone axis of cubic fluorite symmetry. The interplanar spacing further validates the lattice parameter of 5.47 Å, in agreement with XRD results. A simulated atomic arrangement of the PrOx phase along the [001] zone axis is provided as an inset in Figure 4.3H. The fast Fourier transform (FFT) of Figure 4.3F aligns with the electron diffraction pattern of cubic fluorite along the [001] zone axis (Figure 4.3I). Similarly, the atomic arrangements in Figure 4.3J, which is a magnified view of the marked region in Figure 4.3G, align with the [111] zone axis of orthorhombic perovskite symmetry. The inset of Figure 4.3J displays a simulated atomic arrangement of the

PNC phase along the [111] zone axis. The FFT of Figure 4.3G corresponds to the electron diffraction pattern of orthorhombic perovskite along the [111] zone axis, as shown in Figure 4.3K.

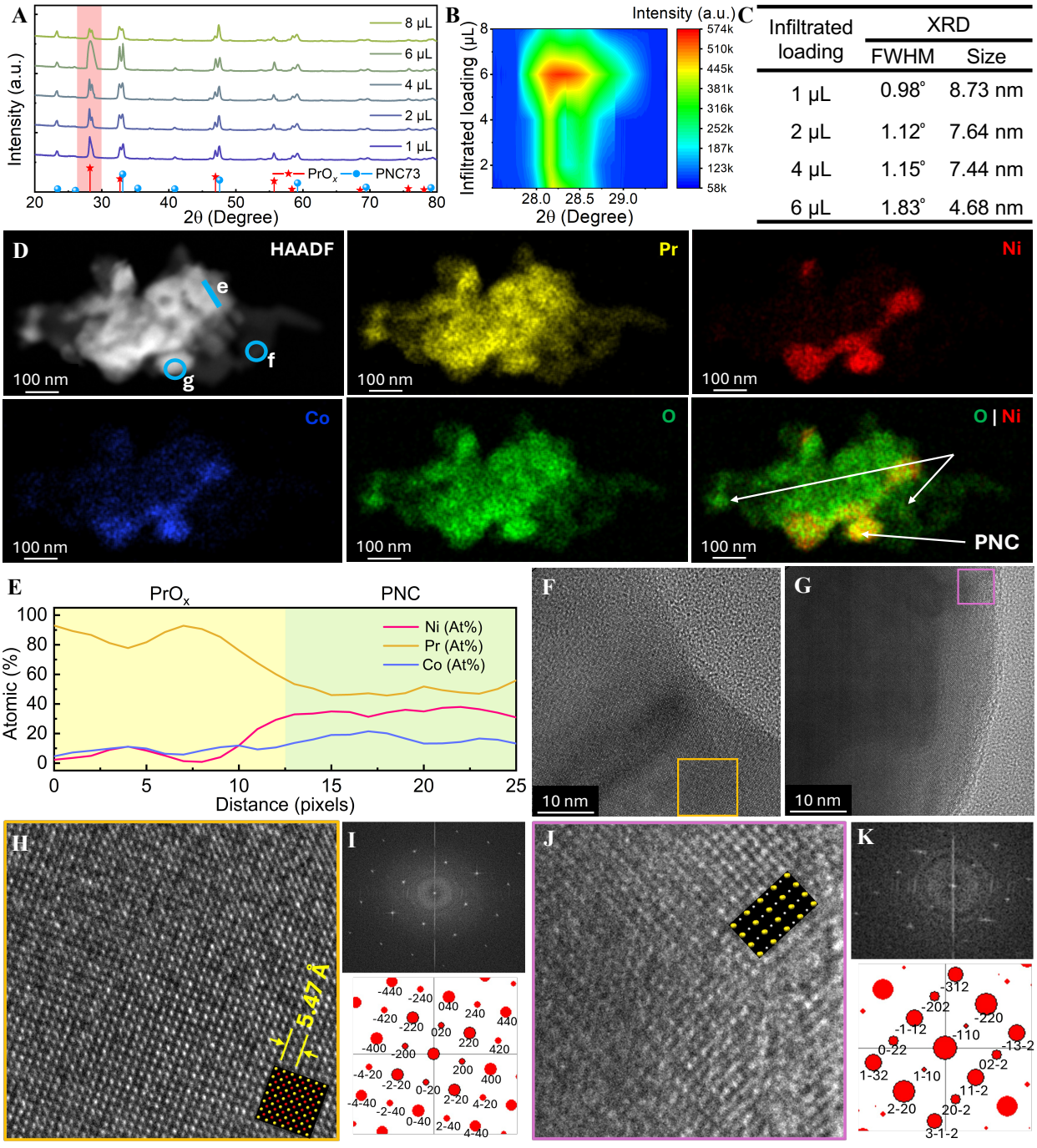


Figure 4.3. In-depth characterization of the hybrid Type VI electrode through XRD and TEM analysis. (A) XRD of hybridized electrode powders with different infiltrated loadings. (B) Selected XRD range to indicate (111) crystalline plane of as-infiltrated PrO_x on different loaded

hybrid electrode. (C) Averaged XRD size of PrO_x multiphase catalysts, calculated from the FWHM of the XRD peaks using the Scherrer Equation. (D) HAADF image with Electron Dispersive Spectroscopy (EDS) elemental maps of the hybrid type-VI electrode, which confirms the impregnation of PrO_x coating on PNC phase. (E) Cationic elemental distribution (in atomic %) across the interphase between PrOx and PNC phases, indicated as line 'e' in the HAADF image. (F) HRTEM image of the Ni- and Co-depleted region (indicated as 'f' in the HAADF image), identified as the PrO_x phase. (G) HRTEM image of the Ni- and Co-enriched region (indicated as 'g' in the HAADF image), identified as the PNC phase. (H) Magnified view of the marked region in (F) with a simulated atomic model of the PrO_x phase (cubic fluorite structure, *Fm-3m* space group) along the [001] zone axis, where yellow and red circles represent Pr and O atomic columns, respectively. (I) Fast Fourier Transform (FFT) pattern of (F) with simulated electron diffraction pattern of the PrO_x phase (cubic fluorite structure) along the [001] zone axis. (J) Magnified view of the marked region in (G) with a simulated atomic model of the PNC phase (orthorhombic perovskite structure, *Pnma* space group) along the [111] zone axis, where yellow and gray circles represent Pr and Ni/Co atomic columns, respectively. (K) FFT pattern of (G) with simulated electron diffraction patten of the PNC phase **(orthorhombic perovskite structure) along the [111] zone axis.**

4.4.3 Minimizing ASR_o and ASR_p to enhance ORR efficiency

To comprehensively evaluate the synergistic effects of the reconstructed high-catalytic interface on reaction kinetics and bulk diffusion, impedance spectra were analyzed for full cells, revealing their complex interrelationships. As shown in Figure 4.4A, the ohmic resistance (R_o) of the hybrid Type VI electrode full cell decreased significantly to 0.092 Ω cm^2 under open-circuit voltage (OCV) conditions and further to 0.090 Ω cm^2 in electrolysis mode at 1.30 V and 600°C. In comparison, the R_o of the pristine electrode full cell was 0.202 Ω cm^2, highlighting a considerable improvement in ORR electrochemical kinetics. Notably, all hybridized oxygen electrodes demonstrated the ability to reduce R_o by half, to approximately 0.1 Ω cm^2, attributed to the exceptional catalytic activity of PrO_x. Even in hybrid Type VIII cells, where a superficial stagnated praseodymium oxide shell formed, the R_o was reduced to 0.146 Ω cm^2. Hybridization of PrO_x with the PNC73 backbone improves adhesion and reduces interfacial voids, lowering contact resistance. Simultaneously, PrO_x nanoparticles refine the microstructure by coating pore walls and filling microvoids,

enhancing electron and ion transport. These combined effects lead to a significant decrease in ohmic resistance, as shown by impedance spectra. The polarization resistance (R_p) demonstrated a similar trend with significant reduction. For the optimal hybridized loading, the R_p dropped from 0.375 Ω cm^2 for the pristine electrode to 0.079 Ω cm^2, further validating the mitigation of sluggish ORR kinetics via the reconstructed interface. When examining the performance across different operating temperatures, the hybrid Type VI electrode showed R_o and R_p reductions of 63% and 75%, respectively, as the temperature increased from 400°C to 600°C (Figure 4.4B). At 600°C and OCV, the optimized heterostructure facilitated more efficient mass and charge transfer, achieving a R_o as low as ~0.1 Ω cm^2 (Figure S7, Supporting Information). This improvement was further supported by the enhanced catalytic activity of PrO_x, leading to a reduced R_p of ~0.08 Ω cm^2. In electrolysis mode at 1.30 V under humid conditions, the R_p decreased further due to the availability of water molecules, which facilitated proton exchange and proton mobility (Figure S8, Supporting Information). This demonstrates the synergistic mechanism driving enhanced performance in both fuel cell and steam electrolysis modes (Figure 4.4C and 4.4D).

To gain deeper insights into the electrochemical processes underlying the impedance spectrum, a deconvolution of overlapping processes was conducted through a Distribution of Relaxation Times (DRT) analysis (Figure 4.4E). This approach identified four primary peaks (P1-P4), associated with charge transfer, oxygen surface exchange, and oxygen gas diffusion mechanisms. The intensity of P1, observed in the high-frequency region, was significantly reduced for hybrid Type VI electrode, indicating an accelerated charge transfer rate and diminished charge transfer resistance. Similarly, the reduced intensities of P2 and P3 in the intermediate frequency range highlighted improved oxygen surface exchange processes, including adsorption, dissociation, and incorporation, thereby reducing the energy barriers for the ORR on the hybridized catalytic electrode. In the low-frequency region, representing oxygen gas diffusion, P4 exhibited negligible intensity, signifying that the PrO_x-reconstructed interface effectively mitigated limitations in oxygen bulk and surface diffusion, thereby reducing concentration polarization during the reduction reaction[8]. Given these findings, the activation energy (E_a) for ORR was analyzed (Figure S9, Supporting Information). By plotting resistance values against temperature and applying linear fitting, a decrease in activation energy was observed. Using the Arrhenius equation (Equation S2, Supporting Information), the $E_{a,o}$ for ORR in the pristine PNC electrode was calculated at 0.273 eV, whereas the hybrid Type VI electrode exhibited a lower $E_{a,o}$ of 0.253 eV

(Figure 4.4F). Similarly, the activation energy for polarization resistance ($E_{a,p}$) decreased from 0.418 eV for untreated cells to 0.364 eV following hybridization (Figure 4.4G). These analytical results strongly correlate with the observed enhancements in electrochemical performance, reinforcing the impact of the reconstructed heterostructure.

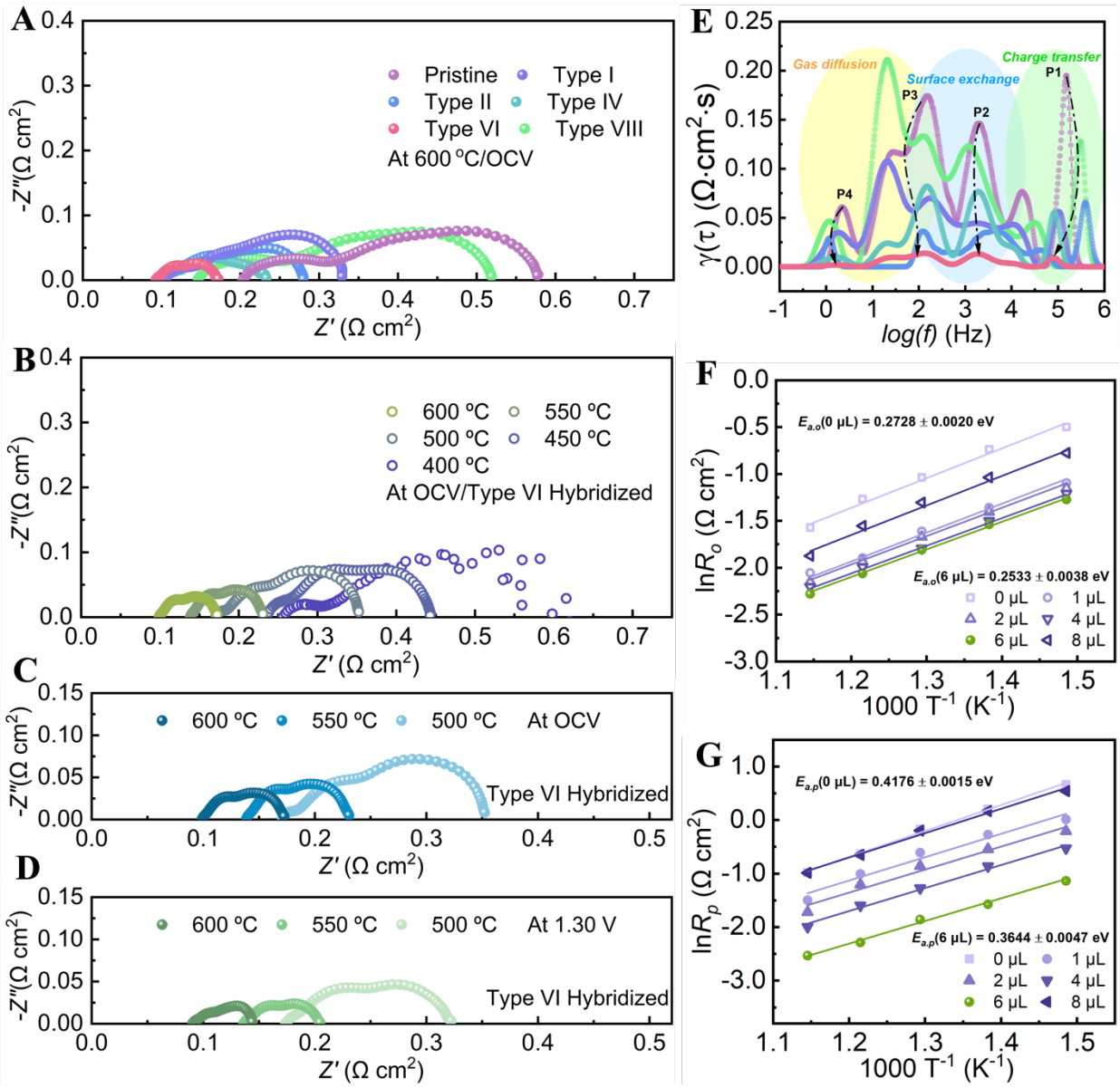


Figure 4.4. Correlation between electrochemical impedance spectra, distribution of relaxation times (DRT) analysis, and activation energies. (A) EIS spectra of different infiltrated loadings of the hybrid Type VI electrode full cells under OCV conditions at 600 °C. Hydrogen (20 standard cubic centimeter per minute, sccm) and oxygen (40 sccm) were respectively fed into the

cells. (B) EIS spectra of the hybrid Type VI electrode full cells under OCV conditions from 600 ℃ to 450 ℃ with the same gas conditions. (C) EIS spectra of the hybrid Type VI electrode full cells under OCV conditions from 600 ℃ to 500 °C. (D) EIS spectra of the hybrid Type VI electrode full cells at 1.30 V from 600 ℃ to 500 ℃ under electrolysis conditions (H_2, 20 sccm, was fed to hydrogen electrode side and 20 vol.% H_2O + 80 vol.% O_2, 40 sccm was fed to steam electrode). (E) The corresponding DRT analysis of the EIS spectra of different infiltrated loadings of the hybrid Type VI electrode full cells. (F) and (G) Arrhenius plot of ohmic resistance and polarization resistance of different loaded hybrid electrode full cells with fitted straight lines.

4.4.4 Hybridized electrode for PCEC: electrochemical efficiency and durability validation

After successfully reconstructing the high-catalytic interlayer onto the pristine PNC electrode, the hybrid Type VI electrode underwent electrochemical testing, demonstrating exceptional performance in both fuel cell and steam electrolysis modes. The OCVs for all PCEC operations consistently exceeded 1.05 V, confirming the integrity of the full cell structure without signs of electronic or gas leakage and demonstrating robust structural stability throughout the testing period (Figure 4.5A). In fuel cell mode, under a flow of H_2 (20 sccm) and O_2 (40 sccm) to the electrodes, the PPD reached 1.56 W cm^{-2} at 600°C. This represents an 83% increase compared to the pristine PNC electrode, which achieved a PPD of only 0.85 W cm^{-2}. Incremental impregnation of nanophase PrO_x — ranging from 1 μL to 6 μL— resulted in a steady PPD improvement from 1.03 W cm^{-2} to its highest value, confirming the significant impact of enhanced electrochemical kinetics and improved oxygen mass transport. Conversely, the hybrid Type VIII electrode achieved a PPD of 0.946 W cm^{-2}, only marginally surpassing the pristine result, likely due to insufficient hybridization at the electrode/electrolyte interface. The nanowire morphology of PrO_x (Type VI in Figure 4.2D) significantly enhances electrochemical performance by promoting surface and strain-driven energy minimization. At low loading, PrO_x forms high-surface-energy nanoparticles with limited activity. In contrast, increased infiltration yields ~4.68 nm particles that reduce nucleation barriers and promote the formation of one-dimensional nanowires. These structures offer increased surface area, improved alignment of reactive facets, and facilitated electron and oxygen ion transport, thereby enhancing oxygen exchange kinetics, stability, and efficiency at elevated current densities. The correlation between tailoring morphology and optimizing electrochemical behavior

is illustrated in Figure S10, Supporting Information, emphasizing the critical role of controlled hybridization. Even at reduced temperatures, the optimized hybrid full cells demonstrating superior performance, achieving a PPD of 0.587 W cm^{-2} at 400°C and 1.04 W cm^{-2} at 500°C, making it competitive for low-temperature PCEC operations (Figure 4.5B). Representative PPD values for all operation temperatures and varying PrO_x loadings are provided in Figure 4.5C and Table S1, Supporting Information, further validating the exceptional performance under optimal conditions.

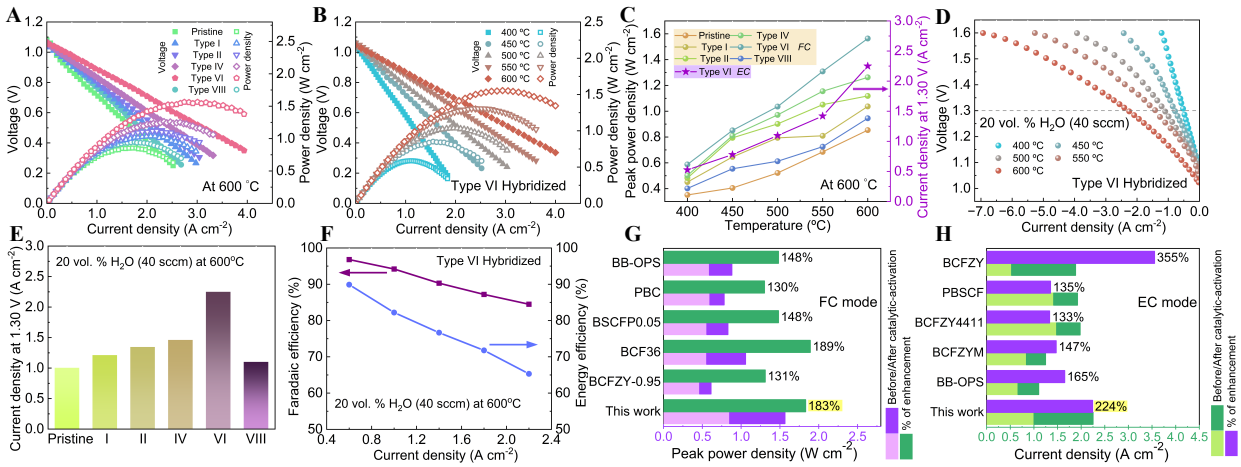


Figure 4.5. Electrochemical performance of the hybrid Type VI electrode full cells in both fuel cell and electrolysis modes. (A) *I-V-P* curves of different loaded hybrid electrode full cells at 600 °C. (B) *I-V-P* curves of the hybrid Type VI electrode full cells at 400-600 °C. (C) Comparisons of peak power density and current density of different loaded hybrid electrode full cells at 400-600 °C. (D) Polarization curves of the hybrid Type VI electrode full cells in electrolysis mode at 400-600 °C. H_2 (20 sccm) and 20 vol.% H_2O + 80 vol.% O_2 (40 sccm) were fed to the electrode. The applied voltage for all tests ranged from 1.60 V to OCV. (E) Comparisons of current density at 1.30 V of different loaded hybrid electrode full cells at 600 °C for steam electrolysis. (F) Faradaic efficiency of hybrid Type VI electrode full cells. G) and H) Comparison of the hybrid Type VI electrode full cell performances in both fuel cell and electrolysis at 1.30 V with some recent literatures. $Ba(Co_{0.4}Fe_{0.4}Zr_{0.1}Y_{0.1})_{0.95}O_{3-\delta}$ (BCFZY-0.95); $BaCe_{0.36}Fe_{0.64}O_{3-\delta}$ (BCF36); $Ba_{0.5}Sr_{0.5}(Co_{0.8}Fe_{0.2})_{0.95}P_{0.05}O_{3-\delta}$ (BSCFP0.05); $PrBaCo_2O_{5+\delta}$ (PBC); $Ba_{0.5}Sr_{0.5}Co_{0.7}Fe_{0.2}Ni_{0.1}O_{3-\delta}$ /$BaZr_{0.1}Ce_{0.7}Y_{0.1}Yb_{0.1}O_{3-\delta}$ (BB-OPS); $Ba(Co_{0.4}Fe_{0.4}Zr_{0.1}Y_{0.1})_{0.95}Mg_{0.05}O_{3-\delta}$ (BCFZYM);

$BaCo_{0.4}Fe_{0.4}Zr_{0.1}Y_{0.1}O_{3-\delta}$ (BCFZY4411); $PrBa_{0.5}Sr_{0.5}Co_{1.5}Fe_{0.5}O_{5+\delta}$ (PBSCF); $BaCo_{0.4}Fe_{0.4}Zr_{0.4}Y_{0.1}O_{3-\delta}$ (BCFZY)[167,228–235].

In steam electrolysis mode, with a gas mixture of 20 vol.% H_2O and 80 vol.% O_2 (total flow rate: 40 sccm) supplied to the hybrid oxygen electrode, the hybridized PCEC achieved a current density of -2.25 A cm^{-2} at 1.30 V and 600°C, and -1.09 A cm^{-2} at 500°C (Figure 4.5D). Additional data at different temperatures and for various hybrid electrode configurations are provided in Figure S11, S12 and Table S2, Supporting Information. Specially, the current density yielded at 1.30 V for Type VI electrode full cells exceeded substantially than other types, reaching 2.25 A cm^{-2} (Figure 4.5E). Furthermore, it achieved faradaic efficiency larger than 90% at 1.0 A cm^{-2} and 600°C. Moreover, at 600 °C and a current density of 0.60 A cm^{-2}, the energy conversion efficiency reached 90%, validating the feasibility of producing hydrogen with this hybrid electrode cells (Figure 4.5F and S13, Supporting Information). The optimal hybridized electrode cell (Type VI) excelled, with over a 1.8-fold improvement in PPD under fuel cell mode, surpassing the catalytic performance benchmarks reported in recent literature (Figure 4.5G and 4.5H). For example, B-site cation-deficient perovskites, $Ba(Co_{0.4}Fe_{0.4}Zr_{0.1}Y_{0.1})_{0.95}O_{3-\delta}$ (BCFZY-0.95) achieved a PPD of 0.611 W cm^{-2} at 600°C, representing only a 31% improvement in catalytic activity[229]. Similarly, tailoring Ce/Fe ratios in $BaCe_{0.36}Fe_{0.64}O_{3-\delta}$ electrodes enhanced catalytic and achieved 1.056 W cm^{-2} in fuel cell mode[230]. Another comparable material, $PrBaCo_2O_{5+\delta}$, attained a PPD of 0.780 W cm^{-2}, reflecting a 30% improvement[232]. In contrast, the hybrid Type VI electrode demonstrated a significantly greater enhancement, achieving superior catalytic performance and power output. In terms of hydrogen production, the hybrid electrode also outperformed its peers, achieving a remarkable 2.2-fold improvement in current density at 1.30 V — close to the electrochemical neutral voltage, demonstrating outstanding performance under equilibrium conditions. Notably, while composite oxygen electrodes such as $Ba_{0.5}Sr_{0.5}Co_{0.7}Fe_{0.2}Ni_{0.1}O_{3-\delta}$ /$BaZr_{0.1}Ce_{0.7}Y_{0.1}Yb_{0.1}O_{3-\delta}$ achieved a current density of − 1.099 mA cm^{-2} at 600°C and 1.3 V, and microstructurally optimized $PrBa_{0.5}Sr_{0.5}Co_{1.5}Fe_{0.5}O_{5+\delta}$ cells reached −1.80 A cm^{-2} under the same conditions[228,233], the hybrid electrode in this work still demonstrated high hydrogen production capability, outperforming other composite or optimized electrodes.

The harsh operating conditions of PCECs, including high temperatures and large electrochemical potentials, can lead to performance degradation, surface cracking, and delamination over time.

Therefore, long-term stability and transient tests are essential to assess the scalability and commercialization viability of these cells. During a long-term stability test of 0.75 V and 1.25 V at 600°C for over 80 hours, the hybrid Type VI electrode full cell exhibited remarkable durability,

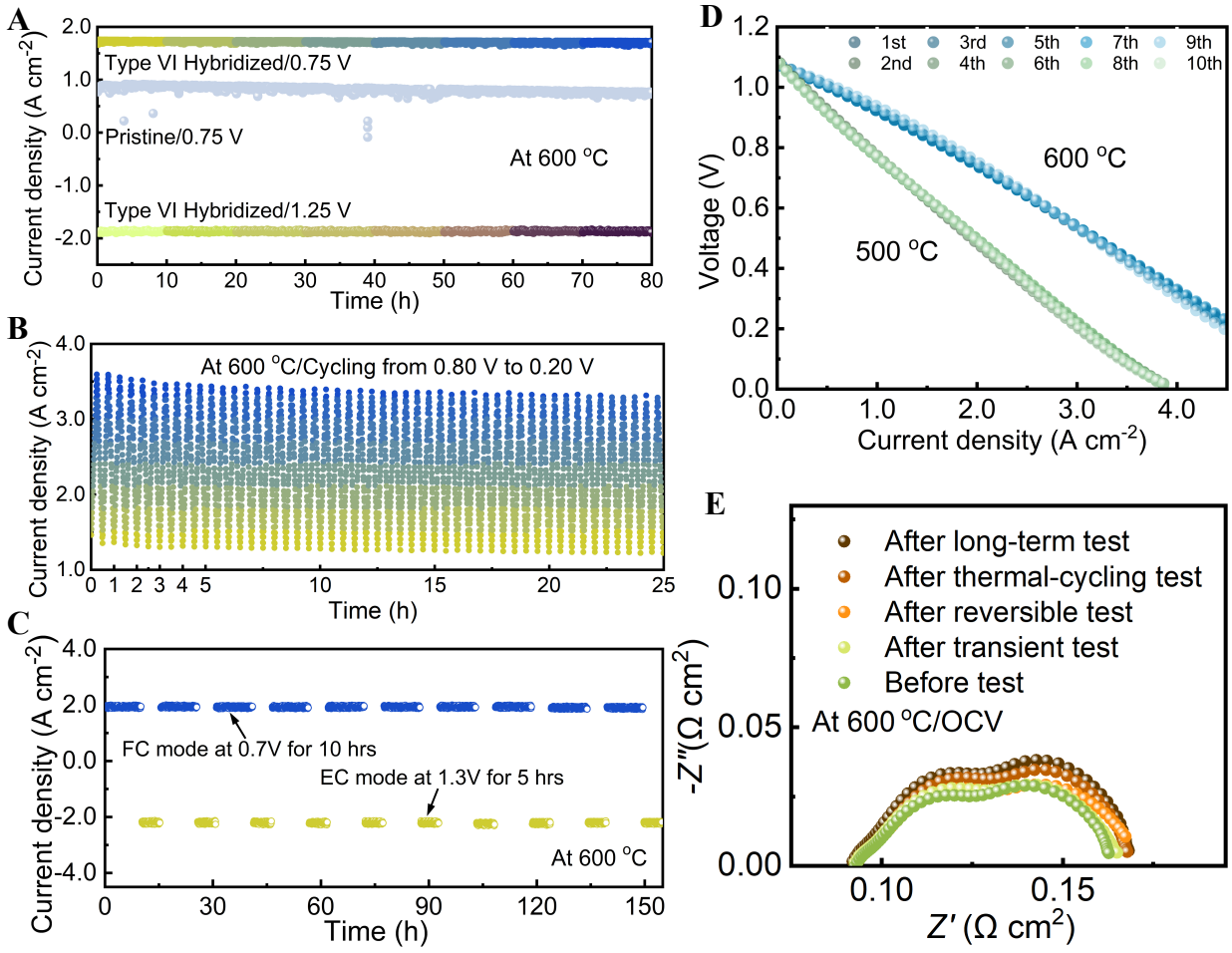


Figure 4.6. Exceptional stability and durability of the hybrid Type VI electrode full cells in both fuel cell and electrolysis modes. (A) Long-term stability tests for 80 hours at 0.75 V for full cell mode and at 1.25 V for 20% steam electrolysis at 600°C, with contrast to the pristine PNC full cells under identical test conditions of full cell mode. (B) Transient tests (time-interval based) under fuel cell mode between 0.80 V and 0.20 V. A cycle (from 0.8 V to 0.2 V, and then back to 0.8 V) lasted for 0.5 hour. (C) Reversible tests between fuel cell mode at 0.70 V and electrolysis mode at 1.30 V for 10 cycles. Each cycle consisted of operating in fuel cell mode for 10 hours, followed by 5 hours in 20% steam electrolysis mode, with a 15-minute transition between the two modes. (D) *I-V* curves of fast-changing thermal cycling tests at 600 and 500°C for 5 cycles. (E) Corresponding EIS spectra collected before any test and after multiple durability tests.

maintaining the stable current density with average degradation rates of 0.35% in fuel cell mode and 0.57% in electrolysis mode. The corresponding degradation rates were quantified as 0.077 mA cm^{-2} h^{-1} and 0.134 mA cm^{-2} h^{-1}, respectively (Figure 4.6A). In comparison, the pristine full cell reached a current density of less than 0.80 A cm^{-2} and showed a much higher degradation rate of 4.94%. The oxygen vacancy-rich PrO_x stabilizes the catalytic interface by promoting dynamic vacancy regeneration and suppressing defect accumulation during redox cycling. It also serves as a protective barrier against elemental segregation, preventing resistive phase formation and preserving active sites under harsh steam electrolysis conditions. Transient tests were also performed to assess dynamic response and durability. In the first mode, the cell was cycled between 0.80 V and 0.20 V at 600°C for 25 hours, with a 30-minute interval between cycles. The hybridized full cell showed current density fluctuations between ~1.40 A cm^{-2} at 0.80 V and ~3.5 A cm^{-2} at 0.20 V, with degradation rates ranging from ~0.55% to ~0.69% (Figure 4.6B). his test highlighted the cell's ability to handle cycling stresses while maintaining robust performance. Moreover, reversible operation in a cycling mode, similar to rechargeable batteries, proved to mitigate degradation mechanisms effectively. Alternating between 5 hours in fuel cell mode and 1 hour in electrolysis mode extended the operational lifespan by reducing cumulative stress[236].

Further testing under reversible operation at 600°C, with voltages set to 0.70 V for fuel cell mode and 1.30 V for electrolysis mode for 150 hours, confirmed excellent durability. The current density remained steady during each 10-hour fuel cell operation, with a degradation rate of 0.33% (Figure S14, Supporting Information). During each 5-hour steam electrolysis operation, the degradation rate was slightly higher at 0.37%, confirming the durability for hybridized cells under real operating conditions (Figure 4.6C). To assess thermal and mechanical robustness, a fast-changing thermal cycling test was performed. The *I-V* curves for five cycles between 600°C and 500°C showed near-perfect overlap, demonstrating the hybrid electrode's ability to withstand rapid temperature shifts without structural or functional compromise (Figure 4.6D). Stability in terms of resistance was further validated through impedance tests at OCV and 600°C (Figure 4.6E). The R_o values remained consistently around ~0.09 Ω cm^2, while the R_p hovered around ~0.07 Ω cm^2, with only slight fluctuations (Figure S15, Supporting Information). These results underscore the profound stability, durability, and catalytic enhancements achieved with the hybridized PrO_x electrode, showing no structural delamination and no signs of nanophase coarsening or pore

closure on electrode microstructure. The findings strongly support the potential of these advanced full cells for long-term, practical applications in energy systems.

4.4.5 DFT simulations and determination of oxygen vacancy concentration for studying synergistic interaction on hybridized electrode structure

During the hybridization process, a one-step infiltration was used to coat the multiphase PrO_x onto the PNC substrate, effectively reconstructing the catalytic interface (Figure 4.7A). This process induced a natural synergistic effect at the interface, leading to a significant enhancement in overall performance. As depicted in Figure 4.7B, the ORR in the reconstructed catalytic zone follows a four-electron pathway. This process involves the sequential transfer of protons and electrons, culminating in the formation of water molecules while generating intermediates such as OOH^*. These intermediates can pose challenges by reducing efficiency and compromising the stability of electrochemical cells. However, the additional oxygen vacancies introduced by PrO_x play a pivotal role in stabilizing OOH^* intermediates, thereby facilitating enhanced oxygen adsorption and desorption[237–240]. To elaborate the synergy, DFT simulation was conducted to validate the promoted reaction kinetics of ORR.

Spin-polarized DFT calculations were performed using the Vienna *ab initio* Simulation Package (VASP)[241–243]. The Perdew–Burke–Ernzerhof (PBE) functional is chosen to account for electron exchange-correlation effects, and the projector-augmented wave (PAW) method is used to approximate core electrons[244,245]. In this study, we assumed the valency of Pr is +3, and all three of its *f*-electrons were treated as valence electrons. In addition, the Hubbard U approach[246] is used to correct self-interaction errors related to the Pr(*4f*) orbitals. We used a U_{eff} value of 4.5 eV, which was reported by Milberg and coworkers[247] to describe the strong onsite Coulombic repulsion in Pr oxides reliably.

The monoclinic Pr_6O_{11} bulk lattice (space group $P2_{1/c}$) was selected to represent the PrO_x and optimized using a plane-wave cutoff energy of 520 eV. The integrations over its first Brillouin Zone were performed using a Monkhorst-Pack *k*-point mesh with a 6 × 4 × 4 grid[248]. Afterward, a periodic $p(1 \times 1)$ slab was obtained by cleaving the bulk along the (101) orientation, denoted as PrO_x(101) throughout the study, revealing the hexagonal close-packed surface. The slab consists of three Pr layers, with the bottom two layers and associated O atoms fixed at the bulk value. A

vacuum layer of more than 17 Å was added above the surface. A 4 × 4 × 1 Γ-centered Monkhorst-Pack grid was employed for all calculations involving such a slab. Grimme's DFT-D3 method was used for the van der Waals dispersion energy correction[249]. Moreover, dipole corrections were included if an adsorbate molecule is placed on one side of the surface[250,251].

The proposed ORR steps are represented by R1-R5:

$$O_2(g) + V_O^{\cdot\cdot} \rightarrow O_2^* \quad \text{(R1)}$$

$$O_2^* + OH_O^{\cdot} \rightarrow OOH^* + O_O^X \quad \text{(R2)}$$

$$OOH^* + V_O^{\cdot\cdot} \rightarrow O_O^X + OH_O^{\cdot} \quad \text{(R3)}$$

$$O_O^X + OH_O^{\cdot} \rightarrow OH_O^{\cdot} + O_O^X \quad \text{(R4)}$$

$$OH_O^{\cdot} + OH_O^{\cdot} \rightarrow V_O^{\cdot\cdot} + H_2O(g) \quad \text{(R5)}$$

According to the Kroger-Vink notation, $V_O^{\cdot\cdot}$, $OH_O^{\cdot}$, and O_O^X describe the oxygen vacancy, proton attached to the lattice oxygen, and lattice oxygen, respectively. Moreover, O_2^* and OOH^* represent the adsorbed molecular O_2 and OOH intermediates. The O_2 molecule binds weakly on the vacancy-free PrO_x (101) surface, with a binding energy of -0.03 eV. Moreover, the oxygen vacancy formation energy ($E_{f,Ov}$) in PrO_x (101) defined by Eq. 1, is energetically favorable (-0.37 eV).

$$E_{f,Ov} = E_{Ov} + 0.5E_{O_2(g)} - E_{surf} \quad (1)$$

where E_{Ov}, $E_{O_2(g)}$, and E_{surf} represent the DFT total energies of the slab with one oxygen vacancy ($V_O^{\cdot\cdot}$), gas-phase molecular oxygen, and vacancy-free pristine slab surface. DFT calculations also showed that the binding of O_2 at the $V_O^{\cdot\cdot}$ site is significantly enhanced (-0.51 eV). Similarly, the intermediates involved in ORR also favor the $V_O^{\cdot\cdot}$ site (Figure 4.7C).

Figure 4.7D displays ORR's free energy profile on the PrO_x (101) surface. The entropies associated with free gas-phase molecules were estimated using standard statistical methods[252]. It is evident that, the adsorption of O_2, a critical step toward its activation, is thermodynamically favored in the presence of an $V_O^{\cdot\cdot}$. Moreover, OOH^* can also be stabilized at the $V_O^{\cdot\cdot}$ site. According to our DFT calculations, the same OOH^* intermediate will spontaneously dissociate into molecular O_2 and $OH_O^{\cdot}$ on the $V_O^{\cdot\cdot}$-free PrO_x (101). Hence, based on DFT modeling, we propose that the conversion

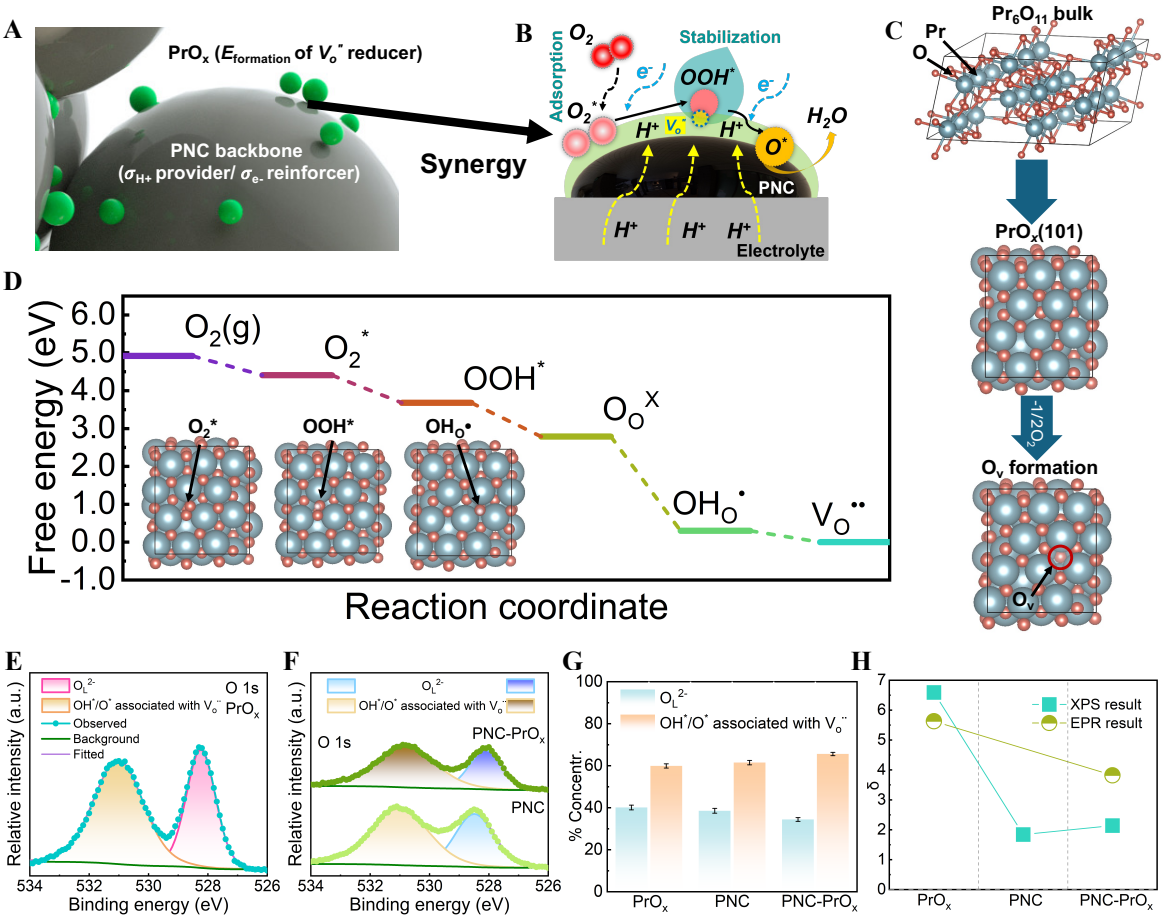


Figure 4.7. DFT analysis. (A) Schematic illustration of the reconstructed hetero interlayer between the PrO_x coating and PNC bulk. (B) Synergistic effect of the PrO_x coating and PNC bulk, facilitating the stabilization of the OOH^* intermediate. (C) The optimized lattice of monoclinic Pr_6O_{11} bulk with slab models representing PrO_x. (101) and the $\boldsymbol{V_O^{\cdot\cdot}}$ site in the top layer. (D) free energy diagram depicting ORR on PrO_x in the presence of $\boldsymbol{V_O^{\cdot\cdot}}$ at 600°C and 1 atm. The optimized ORR intermediate species (O_2^*, OOH^*, and OH^*_o) at the $\boldsymbol{V_O^{\cdot\cdot}}$ site is depicted in the inset of D). (E) Deconvoluted O 1s spectrum of PrO_x showing two main components attributed to lattice oxygen (O_L^{2-}) and surface $\boldsymbol{V_O^{\cdot\cdot}}$. (F) Comparative O 1s spectra for PNC–PrO_x and PNC samples, illustrating enhanced intensity of surface $\boldsymbol{V_O^{\cdot\cdot}}$ sites in the hybrid. (G) Quantified relative concentrations of O_L^{2-} and surface $\boldsymbol{V_O^{\cdot\cdot}}$ across the three materials. (H) Surface oxygen vacancy concentration δ determined by XPS and EPR for PrO_x, PNC, and PNC-PrO_x.

of O_2^* into OOH* is a plausible pathway for the cleavage of the strong O–O bond, producing an O_O^X, which fills the $V_O^{\cdot\cdot}$- and a hydroxyl group (i.e., $OH_O^{\cdot}$) (R3). R4 represents the proton transfer

step. $OH_O^{\cdot}$ will be further protonated into water. The ORR cycle is eventually completed once a new $V_O^{\cdot\cdot}$ site is re-generated. Again, the protonation of surface lattice O_O^X species is highly exothermic.

XPS analysis was conducted to quantify the enrichment of $V_O^{\cdot\cdot}$ in the hybridized electrode, with O 1s spectra revealing two primary peaks across all samples: lattice oxygen (O_L^{2-}) at lower binding energy and OH^*/O^* associated with surface oxygen vacancies ($V_O^{\cdot\cdot}$) at higher binding energy. As shown in Figure 4.7E and 4.7F, the PNC–PrO_x hybrid exhibits a notably stronger vacancy-related peak, indicating a significant increase in surface oxygen vacancies. Quantitative analysis (Figure 4.7G) confirms this trend, showing an increase in surface vacancy-associated species from ~60% in PrO_x and PNC to nearly 70% in the hybrid. The oxygen vacancy concentration, represented by δ in nonstoichiometric oxides, quantifies the deficiency of oxygen atoms in a crystal lattice relative to the ideal stoichiometric composition. A higher δ typically indicates enhanced ionic conductivity and catalytic activity, which is particularly advantageous in applications such as the hybridized electrode for PCEC in this study. Deconvoluted results of O 1s XPS spectrum in Table S3 were calculated further to attain the values of δ for surface oxygen vacancy concentration ($\delta_{surface}$), which are 6.59, 1.84 and 2.14 for PrO_x (Pr_6O_{11}), PNC and PNC-PrO_x, respectively. It is evident that PrO_x is intrinsically rich in surface oxygen vacancies. The notable increase in $\delta_{surface}$ from pure PNC to the PNC-PrO_x hybrid (from 1.84 to 2.14) further confirms that the incorporation of PrO_x effectively enhances the oxygen vacancy concentration on the surface of the PNC backbone. This result strongly supports the role of PrO_x as a vacancy donor, facilitating the creation of a vacancy-enriched interface upon hybridization. Electron paramagnetic resonance (EPR) also confirmed high oxygen vacancy concentrations in PrO_x and PNC-PrO_x, with distinct peaks observed for both (Figure S16). Quantitative analysis yielded $\delta_{surface}$ values of 5.63 for PrO_x and 3.82 for PNC-PrO_x per Pr_6O_{11} formula unit, demonstrating the vacancy-rich nature of PrO_x and its role in enhancing vacancy through hybridization (Figure 4.7H). While the vacancy-rich surface promotes the association of oxygen species and facilitates ORR, the bulk oxygen vacancy concentration (δ_{bulk}) was also examined to provide a comprehensive understanding of vacancy enrichment through hybridization. The assessment of δ_{bulk} was conducted using iodometric titration and thermogravimetric analysis (TGA). Based on the titration results for four times, the δ_{bulk} is approximately 0.132, corresponding to a Pr^{4+} fraction of ~62%, giving a composition of $Pr_6O_{10.868}$

(Table S4). This value is consistent with the TGA results under room temperature, besides, the δ_{bulk} increased with the rising operation temperature (Figure S17).

Collectively, through hybridization, both $\delta_{surface}$ and δ_{bulk} are validated to be improved (Table S5). This enrichment arises not only from the intrinsic defect chemistry of PrO_x but also from synergistic interfacial interactions in the hybrid, which likely facilitate electron redistribution and weaken Pr–O bonds, promoting oxygen vacancy formation. These vacancies are critical for catalytic and electrochemical processes, thus supporting the observed enhancement in catalytic performance and highlighting the potential of the hybridized electrode for PCEC applications.

4.5 Conclusion

Enhancing catalytic activity within intrinsic material systems is crucial for improving the efficiency, versatility, and reliability of PCEC performance. Praseodymium oxides were strategically introduced for their superior oxygen vacancy concentration and catalytic properties in redox reactions. To further elevate performance and minimize rate-limiting steps in the ORR, a heterostructure interface was reconstructed. This PrO_x-PNC interface demonstrated a synergistic relationship: PrO_x provided abundant oxygen vacancies for catalytic reactions, while the PNC substrate ensured stable proton conductivity. A high-catalytic interlayer of multiphase PrO_x was integrated into full cells using a one-step vacuum infiltration process. At an optimized $Pr(NO_3)_3$ solution loading of 6 μL over the oxygen electrode area (0.178 cm^2), our comprehensive analysis confirmed the morphological and compositional integrity of PrO_x. The formation of ultra-small PrO_x nanoparticles for this configuration provided numerous active sites, establishing it as a highly effective catalyst for ORR.

This hybridization strategy significantly enhanced the electrochemical performance in reversible PCEC operations. In fuel cell mode at 600°C, the PPD reached 1.56 W cm^{-2}, making an 83% improvement over pristine PNC electrode cells. For hydrogen production, the hybrid electrode achieved exceptional current densities of -6.93 A cm^{-2} at 1.60 V and -2.25 A cm^{-2} at 1.30 V and 600°C, surpassing recent benchmarks reported in the literature. Furthermore, the R_o and R_p resistances were reduced to 0.09 Ω cm^2 and 0.07 Ω cm^2, respectively, validating the enhanced ORR kinetics both electrochemically and thermodynamically. Detailed DRT analysis and activation energy calculations confirmed improved oxygen gas diffusion, oxygen surface exchange, and charge transfer rates. The activation energy barrier for ORR was significantly reduced in the

hybrid Type VI full cells. Supporting DFT simulations revealed that PrO_x-generated oxygen vacancies stabilized key intermediates like OOH^*, facilitating a continuous ORR cycle as new vacancies regenerated dynamically.

Durability assessments further validated the hybrid system's reliability. Long-term stability tests demonstrated negligible degradation under constant and transient operational conditions, confirming its robustness. These results highlight the effectiveness of the hybridized electrode in sustaining high catalytic activity and structural stability over extended use.

In conclusion, the straightforward hybridization method employed here offers a promising avenue for scaling up and commercializing high-performance PCECs. The reinforced reaction kinetics, enhanced bulk diffusion, and remarkable electrochemical durability make this hybrid electrode design a compelling candidate for advancing sustainable energy technologies.

4.6 Data and materials availability

All data are available in the main text or the supplementary materials. The supplementary materials can be found at https://doi.org/10.1002/adma.202503649.

Chapter 5- Interfacial Nanostructuring Enables Integrated, Low-Polarization Reversible Protonic Ceramic Cells

5.1 Abstract

Interfaces often impose the practical limits of protonic ceramic cells, where the oxygen electrode–electrolyte junction simultaneously governs polarization losses, tolerance to steam, and mechanical stability during reversible operation. Conventional porous electrodes typically rely on discontinuous point contacts and chemically reactive interfaces, which exacerbate interfacial resistance and promote delamination. Overcoming these coupled limitations requires an interlayer that is thin and conductive yet continuous, chemically compatible, and structurally integrated interlayer. Here, we report a pulsed laser deposition enabled interfacial nanostructuring strategy that forms a dense, nanocrystalline $Pr_{0.5}La_{0.5}BaCo_2O_{5+\delta}$ interlayer directly on a chemically robust $BaZr_{0.8}Y_{0.2}O_3$ electrolyte. This interlayer establishes a conformal contact and a defect-enriched reaction zone beneath a porous PLBC oxygen electrode, strengthening the electrode–electrolyte junction while preserving gas accessibility. The engineered interface increases interfacial bonding strength by threefold and substantially reduces interfacial polarization. As a result, the cells deliver peak power densities of 1.16 W cm^{-2} at 600 °C and exhibit stable steam electrolysis operation for ~1000 h under 0.3–0.7 atm steam, maintaining steady operando impedance at 1.30 V with faradaic efficiency exceeding 92%. These results establish interfacial nanostructuring as an effective strategy to construct structurally integrated, low-polarization electrode–electrolyte interfaces for versatile electrochemical devices.

5.2 Introduction

Protonic ceramic cells (PCCs) have emerged as a compelling electrochemical platform for reversible energy conversion as they can operate efficiently at intermediate temperatures, where materials compatibility and balance-of-plant requirements are substantially relaxed compared with conventional high-temperature systems[7,170]. By employing proton-conducting ceramic electrolytes, PCCs achieve high ionic conductivity in the 400–600 °C regime while retaining the thermodynamic and kinetic flexibility needed for both electricity generation and hydrogen production. This dual functionality positions PCCs as a promising “one-device” solution for integrating intermittent renewable electricity with chemical fuel synthesis and storage[70,228]. PCCs

are particularly attractive for steam electrolysis, where favorable reaction thermodynamics and high steam utilization enable elevated hydrogen throughput at reduced electrical energy input[192,253]. When operated with steam feeds, potentially under pressurized conditions, PCC electrolysis offers a pathway toward compact and scalable hydrogen production that can be integrated with upstream heat sources and downstream utilization[42,254]. Advancing PCCs toward practical deployment therefore requires not only high peak performance, but also stable and durable operation across a broad range of temperatures, steam partial pressures, and dynamic operating conditions relevant to reversible applications[10,20,255].

Despite these advantages, further improvements in PCC efficiency and durability are increasingly dictated by interfacial processes rather than bulk ionic transport in the electrolyte[224,256]. In particular, the oxygen electrode-electrolyte interface has repeatedly emerged as a performance-limiting junction, where electrochemical reaction kinetics, ionic transport, and mechanical integrity must be sustained simultaneously[9,21]. A pervasive challenge at this ceramic–ceramic junction is incomplete physical contact, which concentrates local current densities and elevate interfacial resistance[6]. At intermediate temperatures, oxygen electrode polarization is further governed by sluggish surface exchange and interfacial charge-transfer processes, both of which are highly sensitive to water partial pressure through changes in defect chemistry[257,258]. These processes can be expressed schematically as

$$O_2^* + * \rightleftharpoons 2O^* \text{ (surface exchange)} \quad (1)$$

$$O^* + H^+ + e^- \rightleftharpoons OH^* \rightleftharpoons H_2O^* \rightarrow H_2O\,(g) + * \text{ (interfacial charge transfer)} \quad (2)$$

where overall polarization reflects the coupled limitations of oxygen surface exchange and proton–electron transfer across the interface. Beyond kinetics, the oxygen electrode–electrolyte junction is frequently mechanically fragile, with thermal expansion mismatch and repeated operating gradients promoting crack initiation and delamination, ultimately compromising long-term durability[259].

To address these interfacial limitations, extensive efforts have focused on improving oxygen electrode activity and microstructure through porous architecture design, catalyst decoration, and composite electrodes or interlayers[194,260]. While such strategies can increase the density of active sites and mitigate specific kinetic bottlenecks, they often remain limited by discontinuous contact

at the electrode–electrolyte interface. Moreover, approaches that enhance surface activity do not necessarily improve interfacial mechanical robustness, leaving the bonding junction susceptible to delamination under thermal gradients and reversible cycling. A further practical challenge is the limited ability to stabilize interfacial functionality under steam-rich conditions, where changes in steam partial pressure can strongly modulate surface chemistry and defect equilibria in ways that are difficult to control through bulk electrode design alone[12,14].

Pulsed laser deposition (PLD) offers a more direct route to engineering the electrode–electrolyte bonding junction. By depositing a thin, dense, and conformal ceramic layer directly onto the electrolyte surface, PLD can transform discontinuous point contacts into a continuous and conformal interface with precisely controlled thickness and coverage[226,261]. This nanocrystalline architecture expands the effective reaction zone, alleviates constricted transport, and introduces a defect-enriched interfacial region that can accelerate oxygen surface exchange and interfacial charge transfer at intermediate temperatures[262]. Simultaneously, the deposited layer serves as a mechanically integrated bonding layer, reducing the propensity for delamination during reversible operation and under steam-driven gradients. A clear precedent is provided by $PrBa_{0.5}Sr_{0.5}Co_{1.5}Fe_{0.5}O_{5+\delta}$ (PBSCF) | $BaZr_{0.4}Ce_{0.4}Y_{0.1}Yb_{0.1}O_{3-\delta}$ (BZCYYb4411) protonic ceramic fuel cells, where introducing a PLD cathode film increased the peak power density to 1098 mW cm^{-2} at 600 °C and 548 mW cm^{-2} at 500 °C, and impedance deconvolution revealed a dramatic decrease in the offset resistance, directly implicating improved cathode–electrolyte contact[117]. Beyond interfacial modification, PLD is also capable of producing gas-tight ceramic films at comparatively low temperatures. For instance, Stange et al. deposited ~2μm thick proton-conducting electrolyte by PLD at 600–800 °C for metal-supported protonic electrolysers, while noting that post-annealing could induce cracking, highlighting the importance of PLD-enabled designs that balance both contact enhancement with mechanical tolerance[263].

The selection of a suitable oxygen electrode is equally critical, as the interfacial layer must remain chemically stable while supporting fast electrode kinetics under steam-rich conditions. In this work, $Pr_{0.5}La_{0.5}BaCo_2O_{5+\delta}$ (PLBC) is adopted as both the oxygen electrode and interlayer material due to its double-layer perovskite structure, which accommodates flexible oxygen coordination and interacts favorably with water-containing atmospheres[264,265]. The intrinsic defect chemistry of double-layer perovskites, characterized by adjustable oxygen nonstoichiometry and hydration

behavior, further provides a pathway to construct an interfacial region that supports coupled ionic and electronic transport beyond a narrow triple-phase boundary[266–268]. As the electrolyte, $BaZr_{0.8}Y_{0.2}O_3$ (BZY) is selected as a chemically robust baseline material, offering excellent stability and low electronic leakage, which are advantageous for sustained reversible operation and high faradaic efficiency during steam electrolysis[138,269,270].

Building on these principles, we design a PLD-enabled interfacial architecture that integrates a conformal, dense PLBC-derived interlayer with a porous PLBC oxygen electrode on a chemically robust BZY electrolyte. This architecture transforms the electrode–electrolyte junction from a contact-limited boundary into a nanoscale conformal reaction zone, thereby alleviating constricted transport, accelerating surface-exchange and charge-transfer kinetics under steam-containing atmospheres, and improving mechanical tolerance during reversible cycling. As a result, the PLD-engineered cells deliver a peak power density of 1.16 W cm^{-2} at 600 °C, together with reduced polarization resistances of 0.077 Ω cm^2 in fuel cell mode and 0.022 Ω cm^2 during electrolysis. Under steam electrolysis conditions, the cells sustain current density of 1.55 A cm^{-2} at 1.30 V under 0.3 atm steam, with stable faradaic efficiency of over 92% and stable operation for over 1000 h at 600 °C. These results demonstrate that PLD-enabled interfacial nanostructuring provides an effective materials strategy for advancing protonic ceramic cells toward practical reversible operation and steam electrolysis.

5.3 Materials and Methods

5.3.1 Synthesis of PLBC powder

PLBC powder was synthesized via wet chemistry route. Stoichiometric amounts of $Pr(NO_3)_3 \cdot 6H_2O$ (≥99.9%), $La(NO_3)_3 \cdot 6H_2O$ (≥99.9%), $Ba(NO_3)_2$ (≥99%), and $Co(NO_3)_2 \cdot 6H_2O$ (≥99%) (corresponding to the target PLBC composition of $[Pr_{0.5}La_{0.5}BaCo_2O_{5+\delta}]$) were dissolved in deionized water to form a clear precursor solution. Citric acid and EDTA were then added to the solution at a molar ratio of EDTA : citric acid : total metal cations = 1 : 1.5 : 1, and the total cation concentration was adjusted to 0.1 mol L^{-1}. The solution was heated under magnetic stirring for 2 h until a homogeneous viscous gel formed. The product was further calcined in ambient air at 1050 °C for 3 h (heating/cooling rate: 1°C min^{-1}) to obtain phase-pure crystalline PLBC powder.

5.3.2 Cell fabrication

Full cells were prepared by coupling tape casting (for the structural layers) with a brushing step (for later electrode deposition), allowing tight control over thickness and layer integration. First, green sheets corresponding to the BCZYYb7111–NiO fuel-electrode support and the BZY electrolyte were produced via tape casting. The two sheets were then aligned and laminated into a single half-cell precursor, followed by hot pressing at 70 °C for 5 h to consolidate the stack and strengthen interlayer contact. After lamination, the half-cells were co-sintered at 1480 °C for 15 h, yielding a dense electrolyte and a mechanically stable half-cell framework ready for subsequent processing. A thin PLBC interlayer was deposited onto the half-cell substrate using a Neocera pulsed laser deposition system and a dense PLBC ceramic target. The PLD target was prepared by uniaxially pressing 8 g of phase-pure PLBC powder, followed by sintering at 1100 °C for 5 h. PLBC deposition was conducted at a radiative-heater temperature of 800 °C under 20 mTorr oxygen, with a target–substrate spacing of 40 mm. A 248 nm excimer laser was used for ablation, operated at a fluence of 7.4 J cm^{-2} and a repetition rate of 5 Hz. After deposition, the coated half-cells were cooled to room temperature at 20 °C min^{-1}.

To assemble the PLD–PLBC full cells, the PLBC electrode ink was formulated by dispersing the as-synthesized PLBC powder in a solvent/binder system. Specifically, 5 g of PLBC powder was combined with 0.5 g of binder (5 wt% V-006, Heraeus, in α-terpineol), 1 g of dispersant (20 wt.% Solsperse 28000, Lubrizol, in α–terpineol), and ~15 mL of ethanol. The mixture was homogenized in a high-speed centrifugal mixer for 20 min to obtain a uniform slurry with appropriate rheology for coating. The resulting ink was brush-coated onto the dense electrolyte surface to define an electrode area of 0.178 cm^2. After drying, the coated cells were fired at 1000 °C for 3 h to form the porous PLBC oxygen electrode and complete the full-cell assembly.

Symmetric cells were prepared by uniaxially pressing BZY electrolyte powder with 2 wt.% NiO as a sintering aid, followed by sintering at 1450 °C for 10 h to obtain dense pellets. PLBC ink was brush-coated on both pellet faces (active area 0.178 cm^2) and fired at 920 °C for 5 h to remove organics and complete the symmetric cells.

5.3.3 Cells assembly and electrochemical measurements

Both PLD–PLBC symmetric cells and full cells were mounted on in-house fixtures and sealed with Ceramabond™ 552. A silver mesh and silver wires served as the current collector/leads. The cell was heated to 600 °C at 2 °C min^{-1} while H_2 (20 sccm) was supplied to reduce NiO; reduction was confirmed by a stable OCV. O_2 (40 sccm) was then introduced to the oxygen electrode, and electrochemical measurements were performed using a potentiostat (Parstat MC, Princeton Applied Research). In fuel-cell mode, I–V–P and EIS at OCV (10^6–10^{-2} Hz) were collected from 600 to 350 °C. For steam electrolysis, humidified O_2 (controlled RH via a custom humidifier) was supplied, and polarization curves plus EIS at 1.30 V were recorded over 600–350 °C. Data were acquired using VersaStudio.

To evaluate electrolysis efficiency, the Faradaic efficiency (FE) was calculated as:

$$\mathrm{FE}(\%) = \frac{2\mathrm{F} \cdot \nu_{\mathrm{net}}}{22400 \cdot \mathrm{I}} \times 100$$

Here, ν_{net} represents the net flow rate ($\nu_{\mathrm{outlet}} - \nu_{\mathrm{inlet}}$) of H_2 generated in mL s^{-1}. F is Faraday constant (96485 C mol^{-1}), and I is the applied current in amperes.

Energy efficiency (EE) for electrolysis was computed using:

$$\mathrm{EE}(\%) = \frac{\Delta G^{\circ} \cdot \mathrm{FE}(\%)}{2\mathrm{F} \cdot \mathrm{v}}$$

where v is corresponding voltage (V) and ΔG° is the Gibbs free energy at 600 °C, 198500 J mol^{-1}.

5.3.4 Characterizations

A scanning electron microscope (TFS Quattro S) was used to examine both the surface and cross-sectional areas of oxygen electrode with and without PLD, utilizing secondary electron and backscattered electron modes. For nanoscale microstructural and compositional characterization, a cross-sectional TEM lamella was prepared from the tested cell using a dual-beam FIB–SEM (Thermo Scientific Scios 2 DualBeam). The extracted lamella was then examined using a Thermo Scientific Talos F200X G2 STEM. High-resolution TEM (HR-TEM) and high-angle annular dark-field STEM (HAADF-STEM) imaging were performed to resolve interfacial features at the nanoscale, while EDS elemental mapping and selected-area electron diffraction (SAED) were used

to assess local chemistry and crystallographic information. The Talos system, equipped with a field-emission gun (FEG), was operated at an accelerating voltage of 200 kV for high-resolution imaging and analytical measurements.

Thermogravimetric analysis (TGA) was used to evaluate oxygen release behavior and quantify the bulk oxygen vacancy concentration using a NETZSCH STA 449 F3 thermal analyzer. High-resolution O 1s spectra were collected by X-ray photoelectron spectroscopy (XPS) using a monochromatic Al Kα source (hν = 1486.6 eV). Prior to fitting, spectra were charge-corrected using the adventitious carbon reference (C 1s = 284.8 eV, when applicable) and processed with an appropriate background subtraction. The O 1s envelopes were then deconvoluted using a U2 Tougaard background and Gaussian–Lorentzian (GL) peak shapes to resolve contributions from distinct oxygen environments (e.g., lattice oxygen and surface-related oxygen species such as hydroxyl/adsorbed oxygen), with the fitting constrained to physically reasonable peak widths and positions. Phase purity and crystal structure were verified by X-ray diffraction (XRD) on a Rigaku SmartLab diffractometer. Diffraction patterns were compared against standard reference files to confirm the absence of secondary phases and to identify the crystallographic phase of the samples.

Shear-force measurement was evaluated using a motorized force tester (MARK-10). Multiple replicate measurements were performed for each condition to assess repeatability and report representative values. Surface topography and roughness of the half-cell electrolyte were examined by atomic force microscopy (AFM, Park NX10). For each sample, AFM height maps were collected over a 20 μm × 20 μm scan area, and the root-mean-square (RMS) roughness was quantified using XEI (v5.1.6) analysis software.

5.4 Results and Discussion

5.4.1 Fabrication route for the conformal PLD interface in PCCs

Interfacial engineering has become a central lever for advancing protonic ceramic cells, as intermediate-temperature operation shifts dominant losses from bulk ionic transport toward electrode polarization and junction stability. In particular, the oxygen electrode–electrolyte interface frequently dictates both electrochemical performance and durability. Incomplete contact and microstructural discontinuity at this junction can constrict current pathways, amplify local overpotentials, and promote crack initiation and delamination during thermal and chemical cycling.

Against this backdrop, Figure 5.1 summarizes the device-level motivation for targeting the interfacial junction and introduces pulsed laser deposition (PLD) as a strategy to transform a contact-limited boundary into a robust and reaction-active interface.

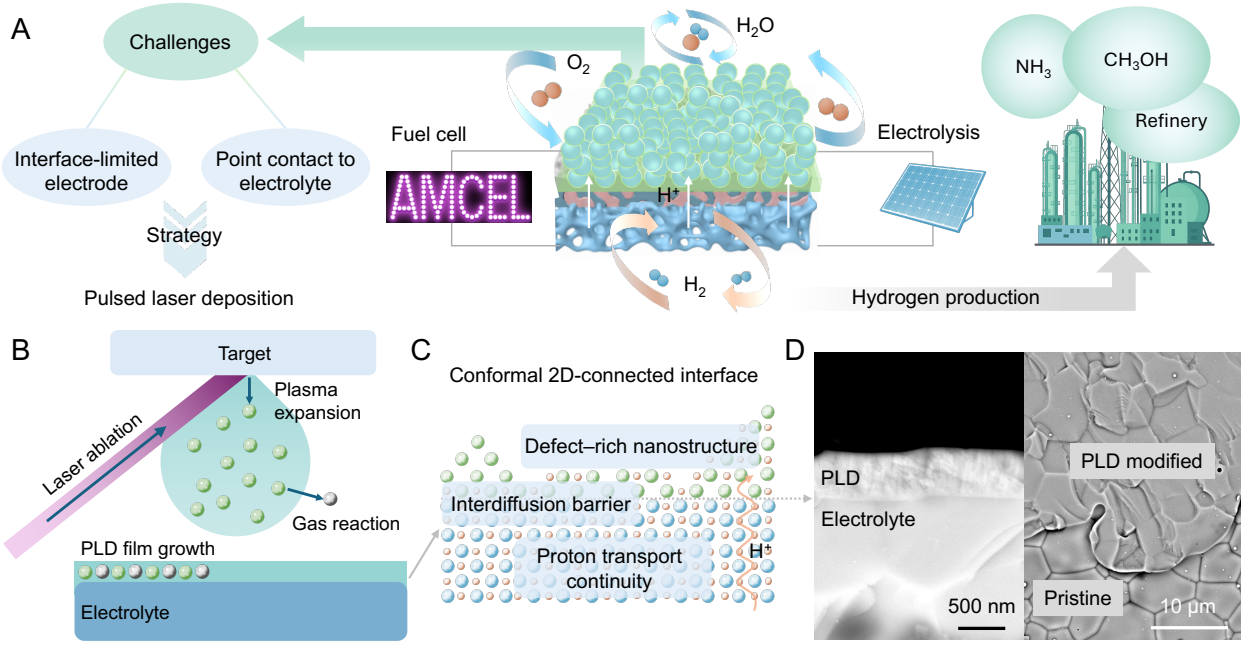


Figure 5.1. PLD-enabled interfacial nanostructuring strategy for protonic ceramic cells. (A) Schematic overview of targeted applications, persistent oxygen electrode–electrolyte interfacial limitations, and the PLD-based strategy to overcome them. (B) Illustration of the PLD process, highlighting the formation of thin, dense, and adherent ceramic layers with controlled composition and thickness. (C) Conceptual depiction of a conformal electrode–electrolyte interface that enhances interfacial bonding, transport continuity, and reaction-zone accessibility. (D) Representative electrode layer directly deposited on the electrolyte, shown in cross-sectional (left) and top-view (right) configurations.

As illustrated schematically in Figure 5.1A, PCCs offer a versatile platform for reversible fuel-cell and steam-electrolysis operation; however, their practical performance is often constrained by the oxygen electrode–electrolyte bonding junction. At this interface, multiple challenges are coupled: incomplete physical contact, sluggish oxygen surface exchange and interfacial charge transfer, strong sensitivity to steam partial pressure, and mechanical fragility under operating gradients. These factors collectively motivate an interfacial design strategy that simultaneously enhances reaction kinetics, transport continuity, and bonding integrity, rather than relying on porous

electrode optimization alone. PLD offers a distinct advantage over conventional slurry-based deposition and co-sintering routes, which often produce discontinuous point contacts and poorly controlled interfacial reactions. By contrast, PLD enables the direct deposition of a thin, dense, and compositionally well-defined ceramic layer onto the electrolyte with excellent conformality and thickness control[271,272]. As depicted in Figure 5.1B, the laser ablation process generates a highly reactive plume that condenses onto the electrolyte surface, forming a nanocrystalline interlayer with uniform coverage. This deposition route provides precise control over interlayer thickness and microstructure, which is critical for balancing interfacial conductivity, chemical compatibility, and mechanical integration. The targeted interfacial functionalities enabled by this approach are summarized in Figure 5.1C. First, the formation of a conformal contact eliminates the point-contact limitations inherent to sintered porous electrodes. Second, the dense nanocrystalline interlayer establishes continuous mixed ionic–electronic conduction pathways across the junction, alleviating constricted transport and reducing interfacial polarization. Third, the defect-rich nature of the PLD-derived layer expands the effective reaction zone, enhancing oxygen surface exchange and interfacial charge-transfer kinetics, particularly under steam-containing atmospheres. Finally, the interlayer can serve as a diffusion-modulating barrier, suppressing detrimental interdiffusion and stabilizing the interface during prolonged reversible operation.

The morphological realization of this interfacial design is confirmed by cross-sectional and top-view microstructural analysis (Figure 5.1D and Figure S1). The dense BZY electrolyte layer has a thickness of approximately 12 μm, as determined from cross-sectional SEM analysis, providing a low-ohmic yet mechanically robust proton-conducting membrane. Importantly, this architecture preserves the porous morphology of the subsequently applied oxygen electrode while establishing a mechanically coherent bonding layer at the junction. Together, these results confirm that the PLD strategy successfully constructs the intended defect-enabled, and structurally integrated electrode–electrolyte interface. This well-defined interfacial architecture provides a controlled platform for evaluating how nanoscale interfacial connectivity and defect chemistry translate into enhanced electrochemical performance and stability in reversible protonic ceramic cells.

5.4.2 Phase stability and defect chemistry of double perovskite PLBC

Establishing the structural stability and defect chemistry of PLBC under dry-to-humid atmospheres is essential, as oxygen electrode kinetics in protonic ceramic cells are strongly coupled to lattice response, defect equilibration, and water–oxide interactions under changing oxygen and steam partial pressures. In particular, oxygen vacancy availability and hydration-driven chemical expansion directly influence oxygen incorporation, proton-coupled charge transfer, and interfacial polarization behavior. The materials-level rationale for selecting PLBC as the oxygen electrode and interlayer material is therefore established in Figure 5.2. The crystallographic framework (Figure 5.2A) highlights the double-layer perovskite motif, which is frequently associated with enhanced oxygen transport and flexible defect accommodation. High-temperature X-ray diffraction collected in both dry air and humid air (2.9–3.1 vol% H_2O) reveals systematic peak evolution between 33° and 33.25° (Figure 5.2B–5.2C), indicative of reversible chemical expansion under both environments (Figure S2). Importantly, no secondary phases or peak splitting are observed, confirming that PLBC accommodates steam-driven defect equilibration without loss of crystallographic integrity[273]. Such atmosphere-responsive lattice behavior is a known characteristic of double-layer perovskites and has been linked to high oxygen surface reaction constants and measurable H_2O uptake, features that are advantageous for oxygen electrodes in PCCs[256,274]. Chemical homogeneity is critical for interpreting defect signatures and correlating them with electrochemical behavior. Scanning transmission electron microscopy energy-dispersive spectroscopy (STEM–EDS) mapping (Figure 5.2D and Figure S2) confirms a spatially uniform distribution of Pr, La, Ba, and Co in the PLBC powder, minimizing the likelihood that local cation segregation governs the observed redox or hydration responses.

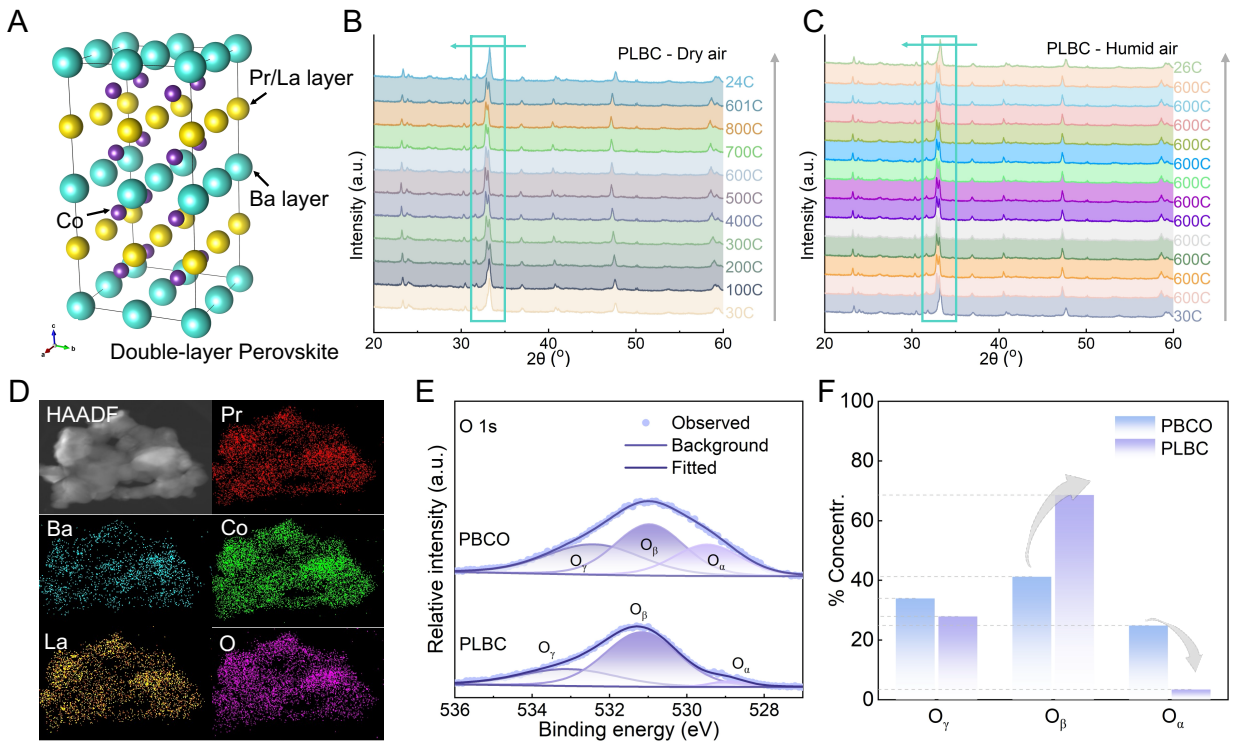


Figure 5.2. Structural stability, chemical expansion, and defect chemistry of PLBC. (A) Crystal structure of the double-layer perovskite PLBC. (B, C) High-temperature X-ray diffraction (HT-XRD) patterns of PLBC powder collected in (B) dry air (100 sccm) and (C) humid air (2.9–3.1 vol% H_2O in air, 100 sccm), revealing atmosphere-dependent chemical expansion. (D) STEM-EDS elemental mapping of PLBC powder confirming spatially uniform cation distribution. (E) XPS O 1s spectra comparing PBCO and PLBC powders, where O_α, O_β, and O_γ denote lattice oxygen, hydroxyl-related species, and surface adsorbates, respectively. (F) Quantitative distribution of the resolved oxygen species shown in (E).

To directly assess defect availability, thermogravimetric analysis was employed to compare the oxygen release behavior of PLBC with that of the parent $PrBaCo_2O_{5+\delta}$ (PBCO) (Figure S3), from which the corresponding oxygen vacancy content per formula unit was extracted (Figure S4). Quantitative analysis reveals that PLBC retains an appreciable oxygen vacancy reservoir relative to PBCO, providing a defect basis for enhanced oxygen incorporation and proton-coupled electrochemical reactions. This defect chemistry is reflected in the kinetic response measured by symmetric-cell electrochemical impedance spectroscopy. Impedance spectra collected across 700–500 °C under varying steam partial pressures (Figure S5–S9), together with the consolidated R_p–

T trend and Arrhenius analysis (Figure S10–S11), demonstrate that PLBC polarization is systematically modulated by steam. This behavior is consistent with an oxygen electrode mechanism in which surface defect equilibration and hydration participate in the rate-controlling steps of oxygen reduction and evolution[275].

X-ray photoelectron spectroscopy further resolves the near-surface oxygen chemistry of PLBC. Deconvolution of the O 1s spectra identifies contributions from lattice oxygen (O_α), hydroxyl-related species (O_β), and weakly bound adsorbates (O_γ) (Figure 5.2E–5.2F). Quantitatively, PBCO exhibits 24.85% O_α, 41.20% O_β, and 33.94% O_γ, whereas PLBC shows a markedly lower O_α (3.46%) together with substantial fractions of O_β (68.63%) and O_γ (27.91%). This redistribution indicates that PLBC possesses a more reactive and hydration-accessible surface. Protonated oxygen species (–OH) directly facilitate proton-coupled oxygen redox by promoting surface protonation and water dissociation, while weakly bound adsorbed oxygen provides a reservoir for oxygen activation and intermediate stabilization during surface exchange and charge-transfer processes[276–278]. In contrast, the higher lattice oxygen contribution in PBCO is characteristic of a comparatively less hydration-responsive surface, consistent with lower sensitivity to steam-driven surface exchange[279]. Collectively, these results position PLBC as a steam-responsive, defect-tunable double perovskite, creating a strong materials basis for the next step to use PLD to translate this chemistry into a more effective and stable electrode-electrolyte reaction zone.

5.4.3 Nanocrystalline PLD-PLBC interlayer: crystallography and interfacial continuity

Establishing a clear structure–chemistry–interface relationship is essential for interpreting any electrochemical enhancement, as interfacial nanostructuring only functions as a performance enabler when it produces a deliberate, well-defined interlayer rather than an uncontrolled reaction zone. For this strategy to succeed, the deposited film must remain compositionally defined, structurally coherent, and chemically compatible with the BZY electrolyte, enabling it to act as both a kinetically favorable bridge for charge and ion transfer and a mechanically robust bonding scaffold. Figure 5.3 therefore integrates phase identification with multiscale microscopy to verify that the inserted PLBC interlayer retains its structural identity and forms a stable, continuous junction with BZY. Cross-sectional SEM imaging (Figure 5.3A) confirms the intended tri-layer architecture comprising porous PLBC, a dense PLD-derived PLBC interlayer (~500 nm), and the

BZY electrolyte, defining the interfacial region examined in subsequent analyses. The thickness of ~500 nm is as a practical design choice to ensure robust, fully continuous coverage of the BZY surface and stable conformal contact beneath the porous PLBC electrode. Structurally, the porous, slurry-derived PLBC provides the 3D gas-accessible framework, but its *contact* to *electrolyte* can still be limited to discrete particle necks on the dense BZY surface, which promotes non-uniform current injection and current constriction. The PLD-grown PLBC film is pinhole-free and conformal, fully covering BZY and replacing these isolated contacts with a laterally continuous electrolyte-facing junction, improving interfacial uniformity and chemical compatibility rather than simply increasing geometric area (Figure S12). We note the porous PLBC/PLD-PLBC interface remains particle-to-film contact, but because it is compositionally identical, it is less likely to introduce mismatch or detrimental phases. Room-temperature XRD with Rietveld refinement (Figure 5.3B) verifies that the deposited PLBC film preserves the targeted tetragonal phase, providing a crystallographic reference for nanoscale diffraction and Fourier-transform analyses. The interfacial functionality of the PLD-derived layer is corroborated by coupled structural and chemical evidence. HAADF-STEM imaging combined with STEM–EDS mapping (Figure 5.3C) reveals a conformal PLBC interlayer with a clear chemical transition across the interface (Pr/La/Co versus Y), demonstrating that the process yields an engineered interlayer rather than a broadly intermixed region. This sharp compositional gradient further indicates that the interlayer can function as a barrier to detrimental cation interdiffusion[280,281].

At higher magnification, the interlayer is shown to be nanocrystalline and structurally ordered. Atomic-resolution HAADF-STEM images (Figure 5.3D–5.3E) resolve the characteristic A-site layered ordering of Pr/La and Ba planes, with an interplanar spacing of approximately 3.91 Å, confirming that the double-layer perovskite motif is preserved at the nanoscale. Consistently, the selected-area electron diffraction pattern (Figure 5.3F) is indexed to tetragonal PLBC, while the FFT and corresponding intensity line profile (Figure 5.3G) further confirm the crystallinity and preferred orientation (indexed to PLBC [010]) of the interlayer. Additional high-resolution images provided in Figure S13 corroborate this nanocrystalline microstructure. The above interpretation is reinforced by the line profile across porous PLBC | PLD-PLBC | BZY (Figure 5.3H), which indicates compositional continuity within the PLD layer and a sharp boundary toward the electrolyte along the probed direction, which is the important prerequisite for stable interfacial transport and reproducible kinetics. Collectively, it verifies that PLD produces a continuous,

nanocrystalline, and compositionally coherent PLBC interlayer with preserved layered ordering and a distinct interface with electrolyte BZY.

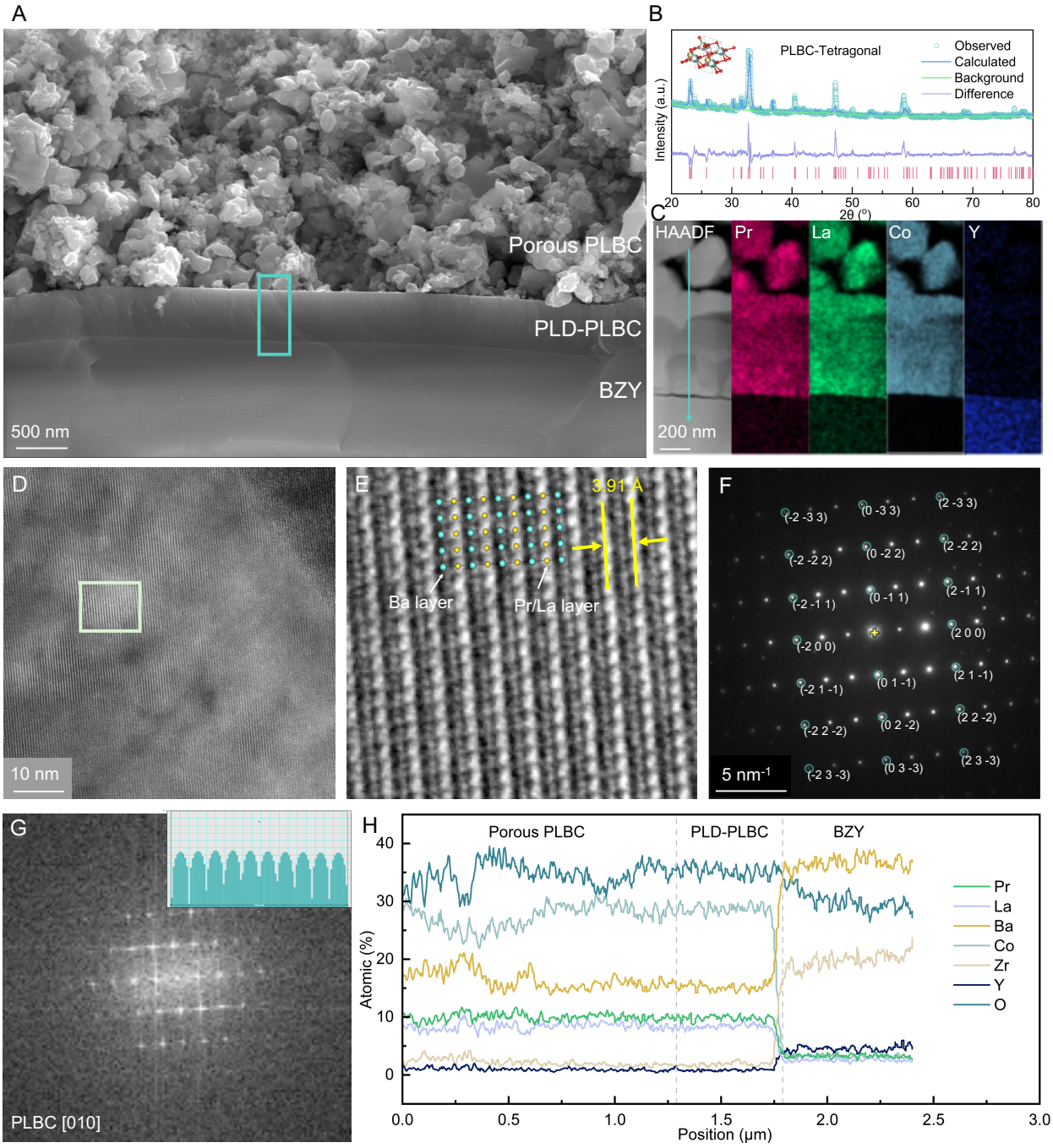


Figure 5.3. PLD-derived nanocrystalline PLBC interlayer with compositional continuity stabilizes the PLBC | BZY interface. (A) Cross-sectional SEM image of a PLD-PLBC full cell, showing the porous PLBC electrode supported by a dense PLD-derived interlayer on the BZY

electrolyte (boxed region marks the area examined by STEM). (B) Room-temperature XRD pattern of the PLBC thin film with Rietveld refinement, confirming the targeted tetragonal phase. (C) Cross-sectional HAADF-STEM image with corresponding STEM-EDS elemental maps (Pr, La, Co, Y), evidencing a conformal PLBC-derived interlayer and a well-defined chemical transition across the electrode–electrolyte interface. (D) High-resolution STEM image of PLD-PLBC layer. (E) Atomic-resolution HAADF-STEM image resolving A-site layered ordering (Pr/La and Ba layers) with an interplanar spacing of ~3.91 Å. (F) Selected-area electron diffraction (SAED) pattern indexed to tetragonal PLBC. (G) Fast Fourier transform (FFT) pattern indexed to PLBC [010], with corresponding intensity line profile (inset), confirming the crystallinity and orientation of the PLD-PLBC layer. (H) Compositional line profile across porous PLBC | PLD-PLBC | BZY along the direction indicated in (C), demonstrating compositional continuity within the PLD interlayer and a sharp, chemically distinct interface with the electrolyte.

5.4.4 Performance gains from PLD interface engineering

Interfacial failure and contact inhomogeneity represent persistent reliability bottlenecks in PCCs, where localized debonding and constricted current pathways simultaneously compromise mechanical integrity and inflate electrochemical polarization. To directly evaluate whether an engineered interlayer alleviates these coupled limitations, we correlate quantitative interfacial bonding and surface characterization with full-cell electrochemical performance and impedance-based kinetic deconvolution, enabling a unified assessment of interfacial robustness and transport losses in cells fabricated with and without the PLD-derived interlayer.

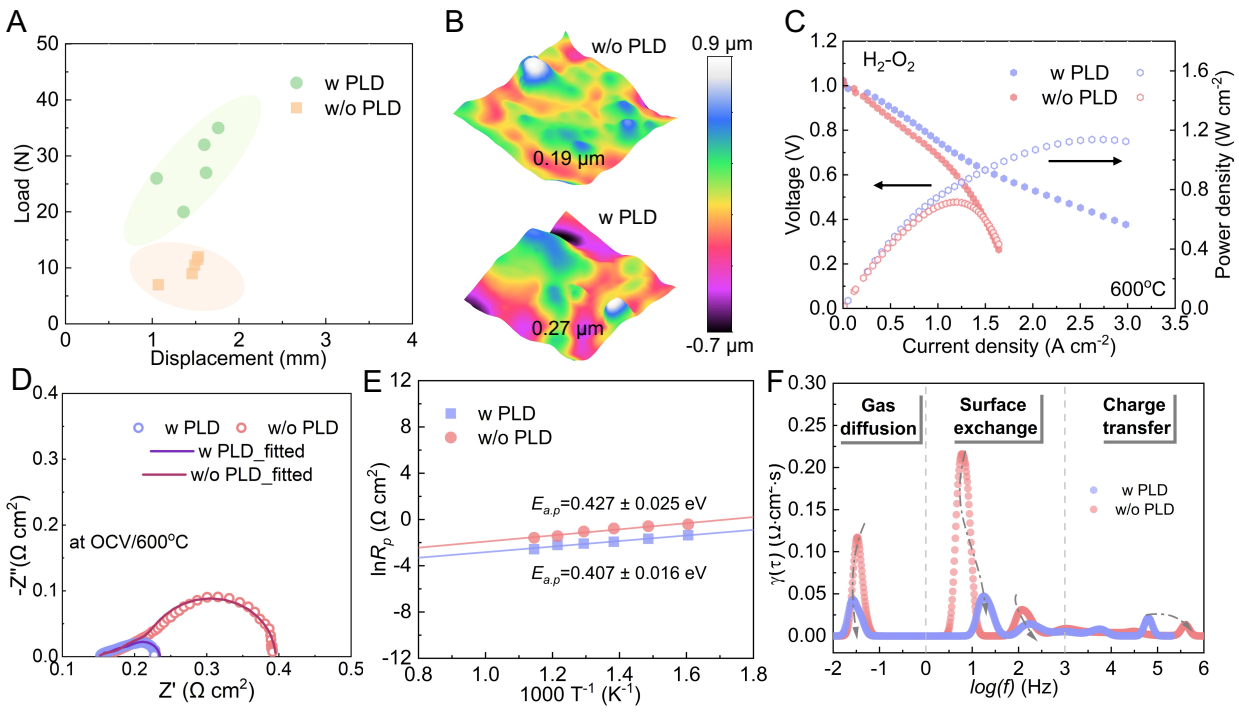


Figure 5.4. Interfacial reinforcement and polarization reduction enabled by PLD. (A) Shear-force measurements of cells without and with PLD, showing a ~3-fold increase in interfacial mechanical robustness after PLD interlayer formation. (B) AFM surface topography of cells without and with PLD, illustrating increased surface roughness and enhanced contact area. (C) I–V and power-density curves at 600 °C in H_2–O_2. (D) Nyquist plots measured at OCV and 600 °C in H_2–O_2, showing reduced polarization with PLD. (E) Arrhenius plots of R_p with linear fits, from which apparent activation energies are extracted, revealing lower effective kinetic barriers. (F) DRT spectra derived from EIS at 600 °C, deconvoluting gas diffusion, surface exchange, and charge-transfer contributions, and highlighting suppression of dominant interfacial kinetic losses.

Mechanical testing provides direct evidence that interfacial integrity is substantially strengthened by interlayer insertion. The shear-force measurements (Figure 5.4A) reveal a pronounced enhancement in interfacial robustness upon introducing the PLD layer, consistent with the formation of a mechanically integrated ceramic–ceramic junction rather than discrete, point-bonded contacts. Expanded datasets (Figure S14) confirm the reproducibility of this response and quantify an approximately threefold increase in interfacial strength. In parallel, AFM topography (Figure 5.4B) shows that the electrolyte surface becomes measurably rougher after PLD, reflecting finite film buildup (0.27 μm versus 0.19 μm) and coalescence-driven growth of the deposited layer

on the initially smoother electrolyte substrate. This trend is reproduced across independent measurements (Figure S15), establishing roughness evolution as a robust signature of PLD film formation. Such roughness-mediated bonding enhancement has been previously demonstrated in BZCYYb-based systems, where increased surface roughness led to higher cathode–electrolyte peeling strength and concomitant performance improvements attributed to increased true contact area and strengthened heterophase bonding[39]. Here, PLD achieves similar bonding benefits while preserving chemical compatibility and conformality at the interface.

Similarly, these interfacial improvements translate directly into electrochemical gains. At 600 °C in H_2–O_2, the PLD-modified cell exhibits a 62% increase in peak power density in the I–V–P response (Figure 5.4C), accompanied by a marked reduction in polarization impedance at open circuit (Figure 5.4D). Notably, the high-frequency intercept (R_o) decreases only slightly at 600 °C (from 0.162 to 0.153 $\Omega \cdot cm^2$). For the BZY-based cell (≈12 μm electrolyte), the ohmic term is dominated by the intrinsic bulk and grain-boundary protonic resistance of BZY, which an ultrathin PLD interlayer cannot materially change. Thus, at 600 °C, where BZY conductivity is relatively high, yet still far lower than the conductivity of electrodes, the contact-related component constitutes only a small fraction of the total series resistance. Improving interfacial continuity therefore produces only a modest net drop in the measured R_o. In sharp contrast, the polarization contributions from fitting are strongly suppressed (Table S1), which decrease from 0.238 to 0.093 $\Omega \cdot cm^2$ (~ 61% reduction), with the most pronounced decrease in surface exchange term (from 0.169 to 0.036 $\Omega \cdot cm^2$). This selective reduction is consistent with the PLD layer creating a continuous, defect-enriched interfacial reaction zone that lowers oxygen-electrode kinetic barriers, thereby producing the markedly smaller polarization arc. Temperature-dependent measurements further support a kinetics-level enhancement: Arrhenius plots show consistently lower R_p values for the PLD cell across the temperature range (Figure 5.4E). The extracted apparent activation energy decreases from 0.427 eV to 0.407 eV following PLD modification, indicating that the engineered interface lowers the effective kinetic barrier governing the rate-limiting cathodic processes at intermediate temperatures. This reduction reflects not only enlarged effective interfacial contact but also a shift toward a more reaction-ready interface in which oxygen incorporation and charge-transfer steps proceed with reduced temperature sensitivity. Mechanistic insight is provided by distribution of relaxation times (DRT) analysis (Figure 5.4F). By deconvoluting the impedance into contributions associated with gas diffusion, surface exchange,

and charge transfer, the DRT spectra show that PLD preferentially suppresses the dominant kinetic features linked to surface exchange processes. This behavior is consistent with a PLD-derived interlayer that alleviates local gas transport through a continuous contact and introduces a defect- and boundary-rich reaction zone that accelerates oxygen incorporation and interfacial charge transfer, thereby reducing R_p while enhancing overall cell performance[282,283]. The PLD-grown PLBC interlayer reduces polarization through coupled structural and kinetic effects at the oxygen electrode–electrolyte junction. It converts discrete particle–electrolyte point contacts into a laterally continuous, conformal interface, redistributing ionic flux across the electrolyte surface, increasing the true active contact area, lowering local current density, and thereby alleviating contact-limited overpotential. At the same time, the ultrathin proton-conducting film provides continuous ionic access along the entire interface, which broadens and homogenizes the near-interface reaction zone and improves utilization of the porous PLBC scaffold, lowering the surface-exchange resistance. The PLD film also forms a chemically uniform, strongly bonded junction that suppresses transfer barriers, and its defect-enriched nature supplies abundant active sites and short pathways that accelerate oxygen adsorption, dissociation, and incorporation. Consistent with these mechanisms, DRT shows the dominant surface-exchange peak is strongly attenuated and shifts to higher frequency after PLD ($\log(f) \approx 0.7 \rightarrow 1.3$; max $\gamma(\tau) \approx 0.22 \rightarrow 0.045$ $\Omega \cdot cm^2 \cdot s$), accompanied by reduced diffusion-like and charge-transfer features, while Arrhenius analysis indicates a slightly lower apparent activation energy and a uniform downward shift in Rp, together confirming faster interfacial kinetics enabled by improved continuity and an expanded, defect-rich reaction zone. Collectively, slurry-based porous PLBC on cells without PLD often contacts dense BZY through discrete particle necks. A PLD-grown PLBC film conformally covers BZY, creating a continuous transport plane that homogenizes current distribution. Even if porous PLBC/PLD contact is particle-to-film, it is PLBC-on-PLBC and current can spread within the continuous PLD layer before entering the porous network, preventing the electrolyte interface from remaining the bottleneck, hence the enhanced performance versus a conventional point-contact interface.

Figure 5.5 evaluates the PLD-engineered cell in details and links performance to impedance evolution. The PLD-PLBC cell maintains strong temperature-dependent power output in H_2–air (Figure 5.5A) and H_2–O_2 (Figure 5.5B), with the higher oxidant activity in O_2 highlighting the intrinsic interfacial kinetics enabled by PLD modification. Across the full temperature range, the

PLD-engineered cell consistently outperforms its non-PLD counterpart (Figure S16). Under electrolysis-relevant conditions, polarization curves measured at 0.3 atm steam (Figure 5.5C) demonstrate substantial current output across 350 to 600 °C, with a clear enhancement relative to the control cell (e.g., 1.13 versus 1.55 A cm^{-2} at 600 °C, 0.85 versus 0.92 A cm^{-2} at 550 °C; Figure S17). Because both cells are evaluated under identical steam conditions, this comparison directly isolates the positive contribution of the PLD interface. Impedance measurements further clarify how the resistance landscape evolves with temperature and operating mode. The EIS collected in H_2–air (Figure 5.5D) and H_2–O_2 (Figure 5.5E) exhibit the expected decrease in polarization resistance with increasing temperature, while comparison with the non-PLD cell (Figure S18) confirms that the interlayer reduces polarization up to 0.077 Ω cm^2 at 600 °C. Besides polarization, contact-related series losses account for a larger fraction of the high-frequency intercept as temperature decreases and BZY conductivity drops (Figure S19- S20). Consistent with this, the PLD interlayer yields a progressively larger reduction in R_o at lower temperatures, increasing from a small change at 600 °C (0.009 Ω·cm^2) to a much larger decrease at 350 °C (0.224 Ω·cm^2). This systematic trend indicates that the PLD layer indeed mitigates interfacial, contact-related series resistance, but its apparent impact on the total measured R_o scales inversely with electrolyte conductivity. Under electrolysis bias (1.30 V, 0.3 atm steam; Figure 5.5F), impedance is further reduced, consistent with bias-activated interfacial kinetics and enhanced charge-transfer under operating conditions. Faradaic efficiency, energy efficiency (Figure S21 and Table S2), and hydrogen flux measurements (>11 ml min^{-1} cm^{-2} at 1.30 V and 600 °C; Figure S22) confirm that the observed currents correspond to productive H_2 generation rather than parasitic leakage.

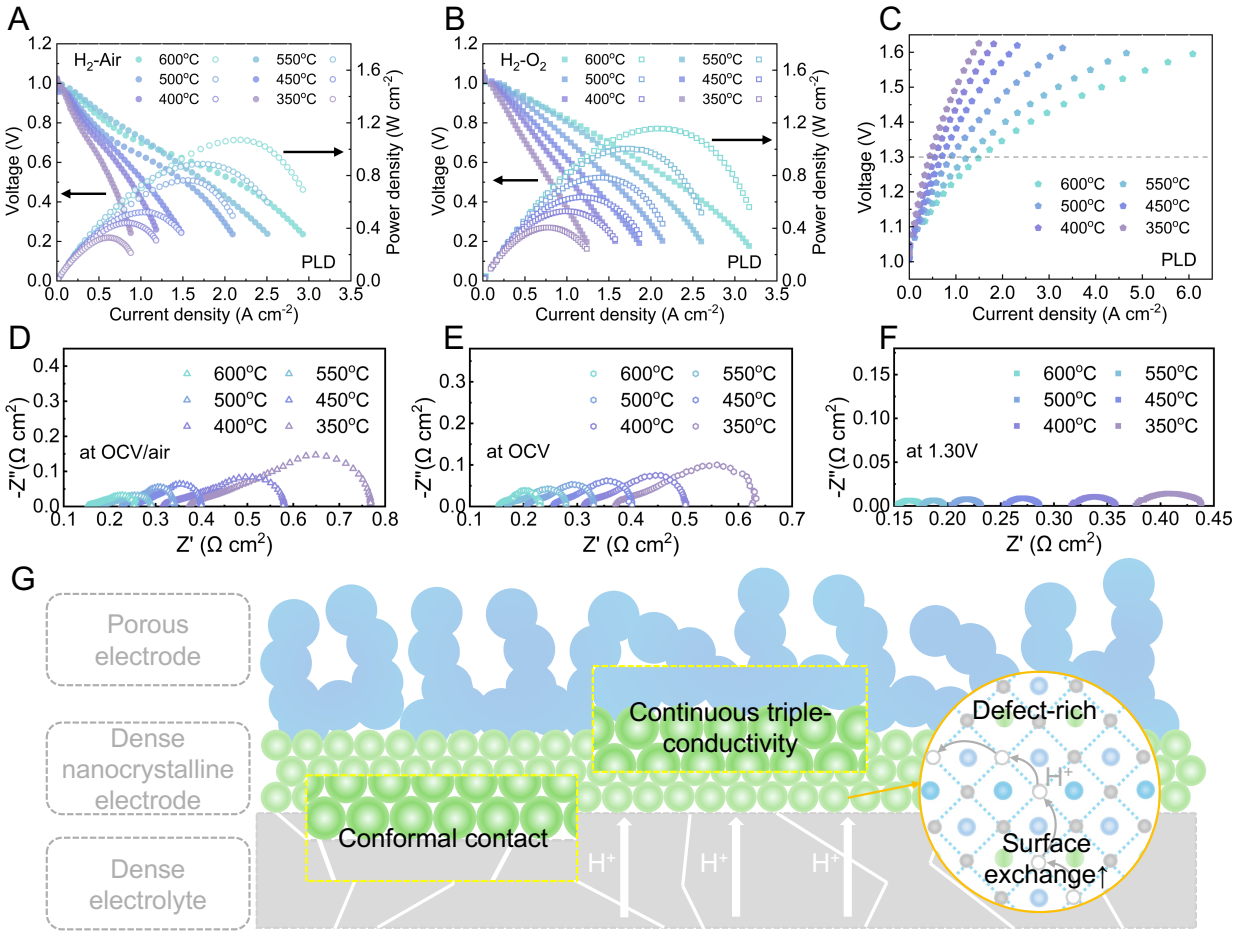


Figure 5.5. Performance enhancement enabled by interfacial nanostructuring in PCCs. (A) Temperature-dependent I–V and corresponding power-density curves of the PLD cell measured in H_2–air from 350 to 600 °C. (B) Temperature-dependent I–V and power-density curves in H_2–O_2 (350–600 °C), highlighting enhanced intrinsic oxygen-electrode kinetics. (C) Polarization behavior of the PLD cell under 0.3 atm steam. (D) Temperature-dependent EIS collected at OCV in H_2–air, showing the evolution of polarization resistance with temperature. (E) Temperature-dependent EIS collected at OCV in H_2–O_2. (F) EIS measured under electrolysis operation at 1.30 V and 0.3 atm steam, revealing markedly reduced impedance under operating bias. (G) Mechanistic schematic illustrating how a dense nanocrystalline PLD-derived layer creates conformal contact and continuous triple-conducting pathways, while a defect-rich interfacial region promotes oxygen surface exchange and interfacial charge transfer.

The collective results are summarized schematically in Figure 5.5G. The dense, nanocrystalline PLD-derived interlayer establishes conformal contact and continuous multi-carrier transport

pathways, while introducing a defect-rich interfacial region that promotes oxygen surface exchange and interfacial charge transfer. This interpretation aligns with prior studies in which thin electrode, where inserting a ~200 nm dense PLD perovskite layer fully covering a rough interlayer produced very good adhesion and reduced polarization resistance by ~3 times (from 0.67 Ω cm^{-2} to 0.21 Ω cm^{-2} at 600 °C)[284]. Similar conclusions appear across thin interlayer approaches, where ~150 nm perovskite films minimize interface resistance primarily by increasing contact area and facilitating oxygen ion transport across the bonding junction[285]. Beyond geometric contact, a PLD-grown nanocrystalline interlayer is expected to introduce a high density of grain boundaries plus defects that can act as kinetically active pathways; direct nanoscale measurements have shown grain boundaries can deliver ~10^4 higher oxygen diffusivity and ~10^3 higher surface-exchange coefficients than grain interiors, providing a quantitative basis for attributing the PLD interlayer's benefit to accelerated oxygen surface exchange and interfacial charge-transfer steps rather than to contact-area effects alone[286]. Recent nanoengineered cathode architectures that integrate dense thin-film transition layers likewise emphasize high interfacial density and improved bonding[287]. In the present system, the STEM image (Figure S23) directly visualizes a continuous PLD-PLBC layer with conformal contact and pronounced grain-boundary features, providing structural support for the interlayer-enabled pathway proposed in Figure 5.5G. Overall, it highly demonstrates that PLD converts the point-contact junction into a stable, areal reaction interface, enabling high performance and durability from fuel-cell mode to pressurized steam electrolysis.

5.4.5 Long-term reversible cycling and high-pressure steam electrolysis with sustained FE

Demonstrating durable reversible operation under high steam pressure, especially under dynamic loads and thermal cycling, is essential for translating PCCs from proof-of-concept demonstrations toward practical electrolysis devices. These operating conditions simultaneously intensify interfacial chemical driving forces, thermal stresses, and the sensitivity of electrode kinetics to steam activity. Figure 5.6 therefore evaluates the PLD-enabled cell under extended pressurized-steam operation, dynamic electrochemical and steam perturbations, and repeated thermal cycling, while benchmarking the achieved performance against representative literature.

In reversible cycling test over ~1000 h (Figure 5.6A), the PLD-PLBC cell maintains stable operation under high steam (0.3 and 0.5 atm), and the simultaneously tracked polarization resistance R_p shows no evidence of accelerated growth, indicating that the dominant interfacial

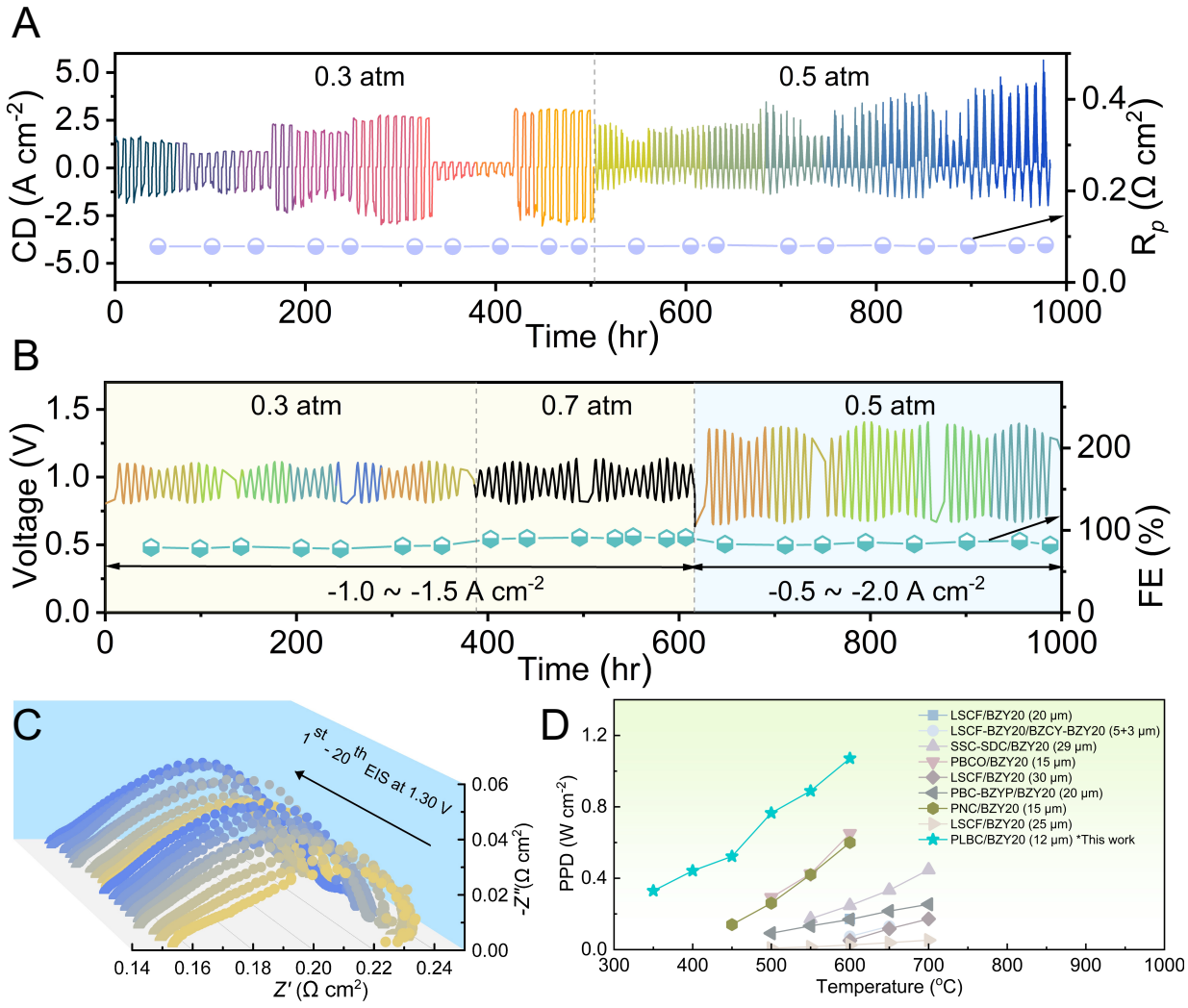


Figure 5.6. Long-term reversible operation and benchmarked performance of the PLD-enabled protonic ceramic cell under thermal cycling test. (A) Current-density (CD) cycling stability over ~1000 h under pressurized steam electrolysis, with the corresponding R_p tracked continuously throughout the test. (B) Voltage response during dynamic current-density cycling under varying steam pressures (0.3, 0.7, and 0.5 atm), together with the evolution of FE over time. (C) Operando EIS collected at 1.30 V, demonstrating impedance stability during sustained electrolysis operation. (D) Literature benchmark of PPD as function of temperature for representative cells, highlighting the performance achieved in this work[139,288–294].

$La_{0.6}Sr_{0.4}Co_{0.2}Fe_{0.8}O_{3-\delta}$ (LSCF), $BaZr_{0.8}Y_{0.2}O_{3-\delta}$ (BZY20), $BaZr_{0.1}Ce_{0.7}Y_{0.2}O_{3-\delta}$ (BZCY), $BaCo_{0.4}Fe_{0.4}Zr_{0.1}Y_{0.1}O_{3-\delta}$ (BCFZY), $Sm_{0.5}Sr_{0.5}CoO_{3-\delta}$–SDC, $PrBaCo_2O_{5+\delta}$ (PBCO), $BaZr_{0.7}Y_{0.2}Pr_{0.1}O_{3-\delta}$ (BZYP), $PrNi_{0.7}Co_{0.3}O_{3-\delta}$ (PNC).

processes remain kinetically stable during prolonged electrolysis-relevant operation. During the first 500 hours, alternating fuel cell and electrolysis modes was performed with symmetric voltage sweeps ranging from 1.3 V to 0.7 V, followed by stepped voltage cycles of 1.2–0.8 V, 1.4–0.6 V, 1.5–0.5 V, 1.1–0.9 V, and 1.6–0.4 V, each held for 250 minutes over 10 cycles. In the second 500 hours, a staircase voltage protocol was applied with symmetric switching, 1.3–0.7–1.3 V, 1.4–0.6–1.4 V, 1.5–0.5–1.5 V at a sweep rate of 0.5 mV s^{-1}. Degradation-rate analysis (Figure S24) quantifies the long-term drift behavior, with the statistical result of 0.567 mA cm^{-2} h^{-1}. To probe resilience under realistic transients, dynamic current-density steps and steam-pressure switching were applied (Figure 5.6B). Current densities were varied from –1.0 to –1.5 A cm^{-2} under 0.3 and 0.7 atm steam, and from –0.5 to –2.0 A cm^{-2} under 0.5 atm steam. The voltage response remained reproducible across changing operating windows, while the FE was continuously tracked. High FE was sustained as the steam partial pressure was switched between 0.3, 0.7, and 0.5 atm, demonstrating that electrochemical selectivity is preserved even under coupled electrochemical and gas-phase perturbations. Quantitatively, the voltage degradation rate remains low (0.193 mV h^{-1}; Figure S25), and FE variations are minimal (Table S3), providing direct evidence of operational stability under pressurized steam.

Operando impedance measurements further corroborate interfacial stability during electrolysis. The EIS series recorded at 1.30 V under steam electrolysis conditions (Figure 5.6C) shows highly consistent impedance responses over time, implying limited evolution of the rate-limiting processes at the oxygen electrode and across the PLD-engineered junction. The summarized R_p degradation rates (Table S4), together with linear-regression analysis of R_p evolution (Figure S26 and Table S5), indicate a variation of only 0.174% per cycle, reinforcing the conclusion that the interfacial nanostructure remains electrochemically intact during prolonged operation. Conclusively, Figure 5.6D benchmarks the peak power density as function of temperature against representative PCC literature employing same electrolyte (benchmark dataset summarized in Table S6). For example, Bi et al. impregnated nanoscale cathode catalysts onto BZY20 backbone to tailor the cathode–electrolyte interface, enabling much higher BZY-electrolyte cell performance

below 600 °C and emphasizing that preserving the *nanostructure* is more critical than perfectly retaining a target phase. In an anode-supported cell with a ~15 µm BZY electrolyte, they reported PBCO/BZY20 cells reached 650 mW cm^{-2} at 600 °C, alongside Rp ≈ 0.08 Ω cm^2 at the same temperature[291]. A recent study also demonstrates a co-sintering approach where the shrinkage stress from a readily sinterable support layer assists the densification of ceria-free electrolytes without sintering aids, aiming to improve durability and efficiency under harsh steam electrolysis conditions. Using their ~15 µm BZY full cell, Tang et al. report peak power density of 0.60 W cm^{-2} at 600 °C[139]. While these studies highlight important advances, their peak power densities remain below those achieved in the present PLD-fabricated PLBC cells, emphasizing the effectiveness of conformal interfacial nanostructuring.

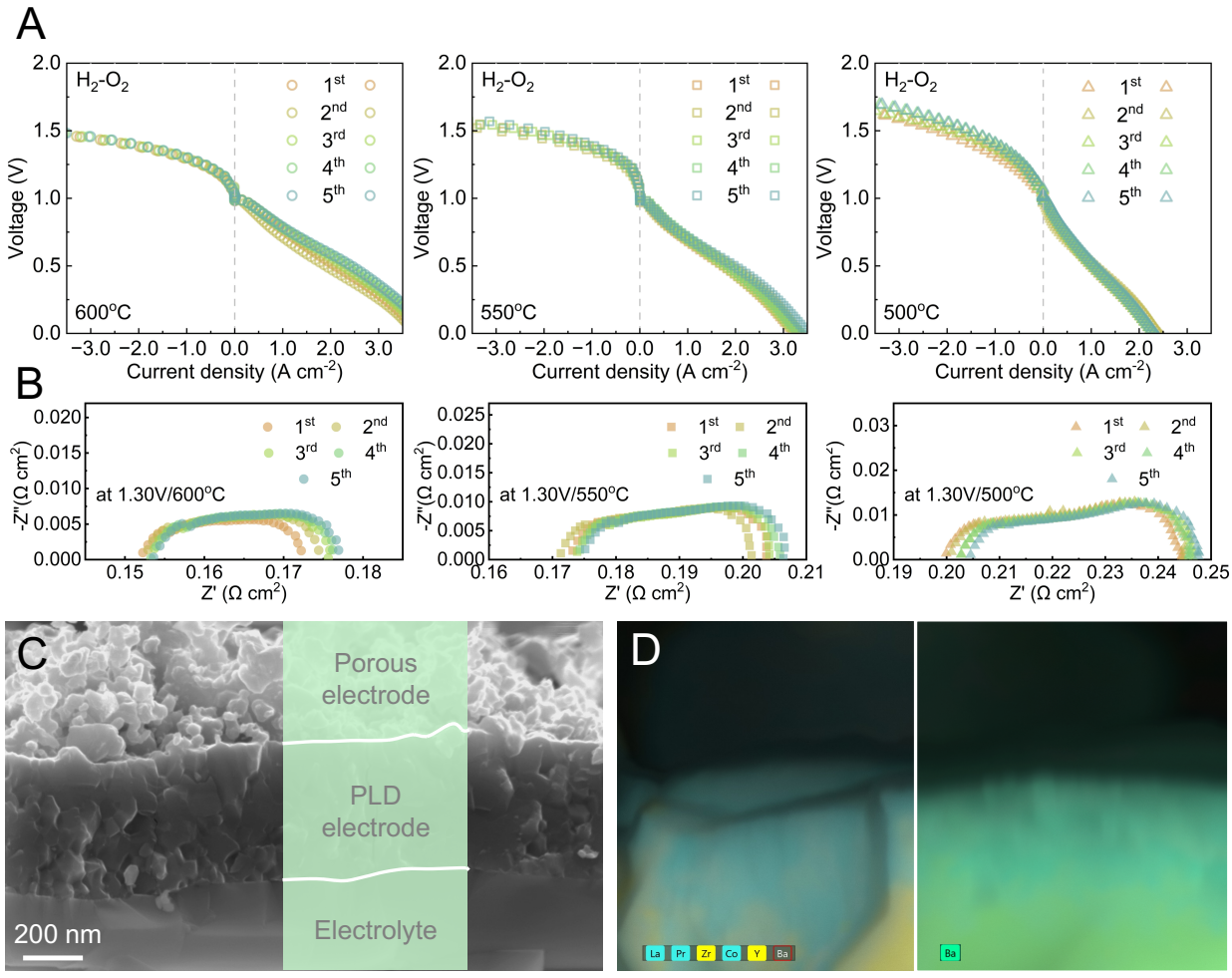


Figure 5.7. Stable reversible performance enabled by a robust bilayer interface under steam and repeated thermal cycling. (A) Polarization curves collected in H_2–O_2 for repeated thermal

cycles (1st–5th) at 600, 550, and 500 °C under 0.3 atm steam, demonstrating highly reproducible electrolysis and fuel-cell operation. (B) Corresponding Nyquist plots measured at 1.30 V for each thermal cycle at 600, 550, and 500 °C, evidencing stable interfacial kinetics and consistently low polarization losses under high steam pressure. (C) Cross-sectional SEM image of the post-cycling cell, showing the porous electrode supported on a thin PLD-grown interlayer that remains structurally intact after repeated thermal cycling. (D) Corresponding EDX elemental maps (La, Pr, Zr, Co, Y, Ba), highlighting a chemically distinct interlayer and a sharp, well-preserved interface.

Beyond steady operation, repeated thermal cycling under pressurized steam directly tests tolerance to temperature transients in harsh electrolysis environments. Polarization curves collected over multiple cycles between 600, 550, and 500 °C under 0.3 atm steam (Figure 5.7A–5.7B) show reproducible electrolysis and fuel-cell behavior. Corresponding Nyquist plots recorded at 1.30 V remain nearly unchanged across cycles, consistent with preserved interfacial kinetics and minimal polarization growth. The applied heating and cooling protocol is detailed in Figure S27. Post-test microstructural and chemical integrity is confirmed by SEM and ColorSEM analysis (Figure 5.7C–5.7D), which show uniform elemental distributions and no evidence of interfacial degradation after testing. Collectively, these results demonstrate that the PLD-enabled, conformal PLBC interlayer not only enhances performance but also stabilizes the electrode–electrolyte junction under prolonged reversible operation, pressurized steam electrolysis, and repeated thermal cycling. By simultaneously maximizing the electrochemically active interfacial area and reinforcing mechanical and chemical compatibility, this interfacial design translates nanoscale engineering directly into sustained, application-relevant performance at intermediate temperatures.

5.5. Conclusion

Interfacial engineering represents a decisive lever for advancing intermediate-temperature protonic ceramic cells, where the oxygen electrode–electrolyte junction frequently dictates electrochemical losses and serves as a primary locus of mechanical failure under reversible operation. PLD offers a unique capability in this context, as it enables the direct construction of thin, dense, and adherent ceramic layers with precisely controlled microstructure, allowing deliberate modification of the buried interface beyond the limitations of conventional porous electrode sintering. In this work, the introduction of a PLD-derived PLBC interlayer simultaneously enhances interfacial mechanical integrity and electrochemical kinetics. Shear-

force measurements reveal an approximately threefold increase in electrode–electrolyte bonding strength, consistent with the formation of a mechanically integrated junction that resists debonding under thermal gradients and reversible cycling. Electrochemically, the PLD-engineered cells deliver peak power densities of 1.16 and 1.01W cm^{-2} at 600 °C and 550 °C, respectively. Under electrolysis-relevant conditions, the cells sustain ~1000 h of reversible current-density cycling in pressurized steam (0.3–0.5 atm), maintain stable operando impedance at 1.30 V with faradaic efficiency exceeding 92%, and exhibit reproducible performance across repeated thermal cycles under steam-containing atmospheres. These results are consistent with the intended function of the PLD-enabled interlayer: a dense, nanocrystalline, and compositionally coherent phase that establishes conformal contact to mitigate current constriction and expand the active reaction zone, provides continuous multi-carrier transport pathways across the junction, and serves as a physically dense barrier that suppresses detrimental interdiffusion commonly reported at oxide–oxide interfaces in related PCC architectures. By integrating mechanical reinforcement with kinetic enhancement at the nanoscale, this interfacial design directly translates into sustained performance under application-relevant operating conditions. More broadly, this PLD-based interfacial nanostructuring strategy is readily transferable to other protonic and solid-oxide electrochemical devices. It offers a general and scalable route to constructing robust, low-loss electrode–electrolyte interfaces capable of supporting high-performance reversible operation under demanding thermal and chemical environments.

5.6 Data and materials availability

All data are available in the main text or the supplementary materials. The supplementary materials can be found at https://doi.org/10.1002/aenm.70850

Chapter 6- Vacancy–Redox Coupling at Interface-Engineered Heterostructures Enhances Reversible Energy Conversion in Protonic Ceramic Cells

6.1 Abstract

Achieving efficient and durable oxygen electrocatalysis in protonic ceramic cells (PCCs) demands precise control of defect chemistry and cation redox under steam. Here we design a hierarchically engineered oxygen electrode comprising a three-dimensional, mesh-like $PrNi_{0.7}Co_{0.3}O_{3-d}$ (PNC) scaffold conformally integrated with a vacancy-rich PrO_x nanophase. This architecture extends the reactive zone while the PrO_x–PNC interphase enables vacancy-mediated redox coupling between Pr and Co, buffering local oxygen chemical potential and stabilizing the defect landscape during reversible operation. The enhanced activity is attributed to vacancy-assisted steam activation and defect-mediated oxygen surface exchange and is consistent with interfacial modulation of metal–oxygen covalency within an O 2p band center framework. The electrode delivers 1.75 W cm^{-2} in fuel-cell mode and 2.77 A cm^{-2} at 1.3 V in electrolysis at 600 °C, maintains >92% Faradaic efficiency, and shows minimal degradation over 200 h. Our results establish a general strategy for coupling hierarchical transport with chemically active, redox-buffered interphases to achieve both high kinetics and durability in protonic electrochemical systems.

6.2 Introduction

Protonic ceramic cells (PCCs) provide a compelling route for clean energy conversion by directly coupling electricity and hydrogen in a single, reversible solid-state device[10]. Operating efficiently at intermediate temperatures (≈400–600 °C), PCCs offer a favorable combination of high performance, materials compatibility, and system simplicity relative to conventional high-temperature ceramic systems[12,228]. Their proton-conducting ceramic electrolytes enable seamless switching between electricity generation in fuel-cell mode and hydrogen production in electrolysis mode, supporting flexible integration with renewable energy sources and addressing energy-storage demands in a decarbonizing energy landscape[22,44,194]. However, widespread adoption remains constrained by the oxygen electrode, where sluggish kinetics and steam-driven degradation impose large polarization losses and limit long-term durability[46,82].

The oxygen electrode plays a decisive role in governing the overall kinetics of both the oxygen reduction reaction (ORR) and the oxygen evolution reaction (OER), which directly impacts power output and hydrogen production efficiency[14]. OER, in particular, requires high overpotentials that reduce system efficiency and accelerate degradation under steam-rich and oxidative environments[256]. Sustained operation under these conditions often leads to structural instability and performance decline, underscoring the need for more catalytically active and durable oxygen electrode materials[170].

Advancing oxygen electrode design requires both precise engineering at the electrode–electrolyte interface and optimization of intrinsic catalytic properties. Incorporating nanoscale features at this junction has proven highly effective in expanding the active reaction zone, enhancing charge and mass transport, and increasing the availability of surface sites[295]. Nanostructured architectures with high surface area and controlled porosity support efficient gas diffusion and facilitate coupling between proton, oxygen ion, and electron transport, while nanoscale domains promote oxygen vacancy formation and locally tune the electronic structure to improve adsorption and turnover of key oxygen intermediates[254,260,296]. Hierarchical porosity, surface gradients, and local strain can further modulate defect chemistry and boost interfacial reactivity without compromising structural integrity[297,298]. In parallel, progress has largely followed two complementary directions, architectural optimization to enlarge reactive zones and chemical modulation to boost kinetics, yet these strategies are often implemented independently, leaving a persistent gap between transport-enabled designs and chemically regulated interphases under steam[9]. We intentionally bridge these two threads here by integrating structural design with interfacial catalytic modulation, aiming to deliver both broadened reactive access and stabilized vacancy-enabled activity during reversible operation.

Equally critical is the selection of oxygen electrode materials with favorable electronic and redox characteristics under steam-containing PCC operation, where reactions proceed at a humid oxide surface dominated by defect chemistry. In PCC electrolysis, water first adsorbs and dissociates into surface hydroxyl species, followed by coupled proton and electron transfer steps and defect-mediated oxygen surface exchange; importantly, the oxygen chemical potential and surface chemistry in steam differ from those in dry O_2, and high steam activity can hydroxylate oxygen-deficient surfaces, weaken metal–oxygen (M-O) bonding, and trigger lattice distortion and cation

migration, ultimately accelerating polarization growth and interfacial degradation under bias[20]. Within this framework, Ni/Co-based perovskite electrodes are particularly attractive because their activity in humid PCC environments is governed by M-O covalency, lattice-oxygen energetics, and vacancy thermodynamics that regulate steam activation, oxygen exchange, and interfacial charge transfer; oxygen vacancies, in particular, directly facilitate steam adsorption and thus improve electrode kinetics[9]. Consistent with this picture, triple-conducting $PrNi_{0.5}Co_{0.5}O_{3-\delta}$ shows pronounced hydration and measurable proton conduction, enabling the oxygen-electrode reaction zone to extend from a narrow interface to the broader porous electrode surface[10]. A physically grounded descriptor for these trends is the bulk O 2p-band center, shifting the O 2p level toward the Fermi level generally increases M–O covalency and is associated with higher oxygen defect reactivity and faster oxygen surface-exchange kinetics, while also highlighting a stability trade-off under steam-rich operation[299,300].

Rare-earth oxides such as praseodymium oxide (PrO_x) offer a direct lever to resolve this design tension by actively stabilizing the redox and defect landscape while preserving high exchange activity. Owing to the reversible Pr^{3+}/Pr^{4+} couple, Pr-containing oxides exhibit pronounced oxygen nonstoichiometry and strong coupling between oxygen chemical potential, defect populations, and electronic carriers, as quantified by defect-equilibria models and direct nonstoichiometry measurements in Pr oxides[301]. This intrinsic oxygen storage provides a thermodynamic basis for local redox buffering, smoothing chemical potential fluctuations under polarization and helping suppress defect excursions that destabilize steam-exposed surfaces[302]. Experimentally, Pr-based oxide additions have been directly linked to faster surface exchange–limited kinetics. Pr_6O_{11} impregnation increased the low-frequency electrochemical step and reduced cathode polarization resistance from 0.23 to 0.06 Ω cm^2 at 800 °C, consistent with accelerated oxygen surface exchange[303]. More importantly for humid durability, integrating a Pr-containing interphase on a double-perovskite oxygen electrode was shown to improve surface exchange and ion diffusion, delivering low resistance and good cycling durability under humid operation[304]. When integrated as a hybrid interphase with Ni/Co-based perovskites, PrO_x can further mitigate large redox swings on the adjacent transition M-O sublattice, reducing the driving force for steam-induced reconstruction and slowing polarization growth during electrolysis[77,305]. In this sense, PrO_x acts as a chemically active stabilizer that couples defect chemistry with redox buffering, preserving

catalytically competent surface states and interfacial integrity during prolonged reversible operation in humid environments.

Building on these insights, we designed a hierarchically engineered oxygen electrode (HEN) composed of a high-porosity, mesh-like $PrNi_{0.7}Co_{0.3}O_{3-d}$ (PNC) framework integrated with a finely dispersed, locally conformal PrO_x nanophase. The PNC scaffold provides an interconnected triple-conducting backbone and open gas channels, while the PrO_x nano-layer establishes a defect-enriched, redox-responsive interphase that extends the functional reaction zone and stabilizes interfacial chemistry during reversible operation in steam. Importantly, this work advances by integrating architecture and chemistry into a coupled design, where hierarchical transport and redox–vacancy regulation are intentionally co-engineered to deliver both high kinetics and long-term durability. As a result, the hybrid electrode delivers robust performance in both fuel-cell and electrolysis modes, achieving a peak power density of 1.75 W cm^{-2} and a current density of 2.77 A cm^{-2} at 1.3 V, respectively, at 600 °C, while maintaining high Faradaic efficiency and exhibiting minimal degradation during extended operation in humid environments. Altogether, this hierarchical strategy highlights how combining physical nano-architecture with chemical adaptability can unlock both efficiency and longevity in protonic electrochemical systems.

6.3 Materials and Methods

6.3.1 Fabrication of 3D-architectured electrodes (3DE) and hierarchically engineered nanostructure electrode (HEN)

Cotton meshes (5 × 5 cm^2, FabricLA) were immersed for 2 h in a 1 M precursor solution of stoichiometric $Pr(NO_3)_3 \cdot 6H_2O$, $Ni(NO_3)_2 \cdot 6H_2O$, and $Co(NO_3)_2 \cdot 6H_2O$ dissolved in a 1:1 ethanol–water mixture, prepared by stirring for 30 min and stored in sealed containers until use. After immersion, meshes were calcined in air at 650, 700, 750, or 800 °C for 3 h (1 °C /min heating, 3 °C/min cooling) to produce porous black 3DE structures, which were trimmed to 0.178 cm^2 for electrode fabrication. For HEN electrodes, calcined 3DE meshes were infiltrated under vacuum with a $Pr(NO_3)_3$-glycine-ethanol solution (5 wt.% $Pr(NO_3)_3$, 55 wt.% glycine, 40 wt.% ethanol) to achieve ~10.6 wt.% loading, followed by annealing at 1000 °C for 2 h to form a crystalline PrO_x layer integrated into the nanostructured framework.

6.3.2 Cells assembly and electrochemical measurements

PNC powder was synthesized via a citrate–EDTA sol–gel method, calcined to the perovskite phase, and formulated into ink for direct oxygen electrodes or to attach 3DE/HEN meshes onto BCZYYb/NiO button cells. Cells were sealed with Ceramabond™ 552, using silver mesh and wires as current collectors. They were heated to 600 °C (2 °C/min) under 40 sccm H_2 to reduce NiO, then supplied with 40 sccm O_2 after OCV stabilization. Electrochemical tests (I–V–P, EIS) were conducted between 600–350 °C (10^6–0.01 Hz, 50 mV RMS) using a Parstat MC. For electrolysis, humidified O_2/steam was fed, and 1.30 V performance was measured under varied steam partial pressures. Data were acquired via VersaStudio, with DRT and Arrhenius analyses in Gamry Echem Analyst. Durability, transient, and cycling tests followed (details in figure captions).

To assess electrolysis efficiency, a 30% steam-oxygen mixture was introduced to the HEN side, while 40 sccm of H_2 was supplied to the hydrogen electrode. The hydrogen output was quantified using a custom-designed flow meter, and Faradaic efficiency (FE) was calculated as:

$$FE(\%) = \frac{2F \cdot \mathcal{V}_{net}}{22400 \cdot \mathrm{I}} \times 100$$

Here, $\mathcal{V}_{net}$ represents the net flow rate ($\mathcal{V}_{outlet} - \mathcal{V}_{inlet}$) of H_2 generated in mL s^{-1}. F is Faraday constant (96485 C mol^{-1}), and I is the applied current in amperes.

Energy efficiency (EE) for electrolysis was computed using:

$$EE(\%) = \frac{\Delta G^{\circ} \cdot FE(\%)}{2F \cdot \upsilon}$$

where υ is corresponding voltage (V) and ΔG° is the Gibbs free energy at 600 °C, 198500 J mol^{-1}.

O_2-TPD was conducted using an AutoChem III 2920 (Micromeritics, USA). About 200–250 mg of sample was loaded into a quartz tube, pretreated with 10% O_2/He (20 cm^3/min) while ramping to 650 °C at 5 °C /min and held for 30 min. After cooling to room temperature, the chamber was flushed with He (10 cm^3/min at sample side, 50 cm^3/min at thermal conductivity detector side) for 10 min. Once stable, the temperature was raised to 650 °C at a rate of 10 °C/min (or 5, 15, or 20 °C/min in separate runs), and desorbed oxygen was quantified via TCD using gas calibration.

6.3.3 Structural and microstructural characterizations

Surface morphology of all electrode types was examined using scanning electron microscopy (TFS Quattro S). Elemental distribution was analyzed by EDX mapping using Pathfinder software, confirming the uniform incorporation of Pr, Ni, and Co, and the localized enrichment of Pr within the HEN region. TEM analysis was conducted with a Titan Themis STEM instrument equipped with an XFEG source. PrO_x particles were observed to coat the PNC structure, forming a core–shell interface. High-resolution TEM (HRTEM) imaging revealed defined lattice fringes matching perovskite planes. The selected area electron diffraction (SAED) analysis confirmed the crystallinity of the HEN interface. Line-scanning EDX verified uniform cation dispersion, while XRD (Rigaku SmartLab) confirmed phase purity and crystallographic structure.

6.3.4 Electronic structure and oxygen defect analyses

Electron paramagnetic resonance (EPR) was conducted at 4 K, 77 K, and room temperature using X-band (9.35 GHz) over 1000–6000 G. Sharp Lorentzian peaks near 3300 G indicated isolated oxygen vacancies. X-ray photoelectron spectroscopy (XPS) with a monochromatic Al Kα source (1486.6 eV) was used to collect high-resolution O 1s, Pr 3d, and Co $2p^3$ spectra. O 1s peaks were deconvoluted (Shirley background, GL fitting) into lattice oxygen (~528.6 eV) and surface OH*/O* species (~530.5–531.8 eV) related to vacancy sites.

Bulk oxygen non-stoichiometry (δ_{bulk}) of PrO_x (Pr_6O_{11}, 50 wt.%)–PNC and pure PNC powders was determined by iodometric titration. ~0.45 g powder was dissolved in 0.5 M HCl (Thermo Scientific), then reacted with excess KI (99.9%, Thermo Scientific) pre-dissolved in a 10 wt.% aqueous solution. Pr^{4+} oxidized I^- to I_2, which was titrated with 0.1 M $Na_2S_2O_3$ (Thermo Scientific) using a 1 wt.% starch indicator (Thermo Scientific). The thiosulfate volume indicated Pr^{4+} content, enabling calculation of average Pr valence and δ_{bulk} per formula unit.

6.4 Results and Discussion

6.4.1 Vacancy enrichment and band modulation induced by hybrid interface in a hierarchically engineered oxygen electrode for PCCs

PCCs are reversible, intermediate-temperature (300–600 °C) devices that couple the grid to molecules: in electrolysis, steam is split across a proton-conducting electrolyte transporting H^+ to

deliver high-purity, pressurizable H_2 with co-product O_2; in fuel-cell mode, the reactions reverse to generate electricity (Figure 6.1A)[164]. The H_2 also enables ammonia, refinery hydrotreating/hydrogenation, and methanol/syngas pathways for broad industrial use. However, PCC steam electrode performance is limited by a microstructure bottleneck that raises mass-transport resistance, kinetics drag that elevates ohmic and surface resistance *via* slow H_2O adsorption/dissociation and OER/ORR turnover, and tripe phase boundary (TPB) deficit that enlarges charge-transfer resistance (Figure 6.1B)[18]. Mitigation centers on hierarchical, percolating microstructures as graded porosity to shorten diffusion paths; catalytic activation as vacancy control to accelerate surface steps; and interface tuning to extend TPB and lower proton-transfer barriers (Figure 6.1C)[10,186].

Thus, simultaneously accelerating reaction kinetics and increasing the density of accessible active sites is essential for achieving high-efficiency reversible operation in PCC. Through engineering a hierarchical nanostructure based on a pristine PNC oxygen electrode, the oxygen vacancy mediated redox coupling at hybridized electrode interface could potentially alter the electrocatalysis property. The hierarchical electrode architecture in Figure 6.2A presents a rationally engineered platform that couples highly open, multiscale porosity with a vacancy-enriched, hybridized interface to overcome kinetic and transport limitations under both fuel-cell and steam-electrolysis operation. The 3D fibrous scaffold provides continuous gas pathways and large accessible surface area, while one-step PrO_x hybridization reconstructs the fiber surfaces to form locally conformal, PrO_x-decorated catalytic skins that promote interfacial electronic modulation and defect enrichment (Figure S1). We note that, consistent with the porous nature of the electrode, the PrO_x deposition is distributed but spatially heterogeneous at the tens-of-micrometers scale; nevertheless, the repeated appearance of reconstructed, PrO_x-modified regions across the network establishes the desired synergy between architecture-enabled mass transport and defect-regulated reaction kinetics. The HEN oxygen electrode features an ultra-porous dual-channel architecture that significantly enhances both mass and charge transport properties[59]. This design facilitates rapid diffusion of reactant gases and efficient proton migration, effectively increasing the electrochemically active surface area[78]. The dual-channel morphology not only maximizes exposure of active sites but also provides abundant pathways for improved catalytic accessibility. Furthermore, the conformal growth of PrO_x on the mesh-structured framework

promotes the enrichment and modulation of oxygen vacancies ($V_O^{\cdot\cdot}$), a critical factor in tuning surface reactivity and electronic structure[306,307]. This results in the formation of a strongly hybridized interface that synergistically enhances interfacial charge transfer kinetics and catalytic performance.

The side-view SEM image of a single fiber clearly distinguishes two regions: a pristine 3DE segment that retains a relatively smooth, compact surface and an upper hierarchically engineered (HEN) segment with a markedly roughened, porous texture (Figure 6.2B). This pronounced morphological transition is induced by hybirdization–driven surface reconstruction, which generates a conformal, porous HEN skin while preserving the mechanically robust fiber backbone. The reproducibility of this reconstructed morphology is further confirmed by additional representative fibers and characterizations in Figure S2. Elemental analyses in Figure S2 verify that the reconstructed skin is Pr-enriched, where the Pr mapping delineates the HEN skin over the underlying conductive scaffold, consistent with the formation of a PrO_x–PNC hybridized surface layer. Cross-sectional views reveal a dense population of PrO_x nanostructures distributed across the fiber thickness, establishing an open, high-surface-area network for interfacial reactions and reactant transport (Figure 6.2B). Importantly, the growth is more accurately described as a layer-by-layer upward buildup. Figure S3 captures the progressive PrO_x accumulation on the PNC backbone with increasing hybridization level, from 1.32 wt% to 5.28 wt% and finally to the targeted 10.6 wt% (optimized loading), illustrating the evolution pathway toward the fully developed HEN skin. Although these layered features are observed in localized regions, reflecting the intrinsic heterogeneity of infiltration on porous scaffolds, their presence consistently evidences the stepwise PrO_x population increase that underpins the reconstructed architecture. Ultimately, this multiscale reconstruction provides abundant accessible active sites and enlarged transport pathways that synergistically enhance charge and gas transport across the electrode, consistent with the electrode-scale functionality.

Building upon these synergistic effects, the HEN electrode (PrO_x–PNC) enables efficient catalytic activity by coupling architecture-enabled mass transport with a vacancy-regulated PP region (Figures 6.2C–6.2D). The tailored cone-like hierarchical morphology provides low-tortuosity pathways and abundant exposed surface, promoting rapid steam access and effective adsorption to

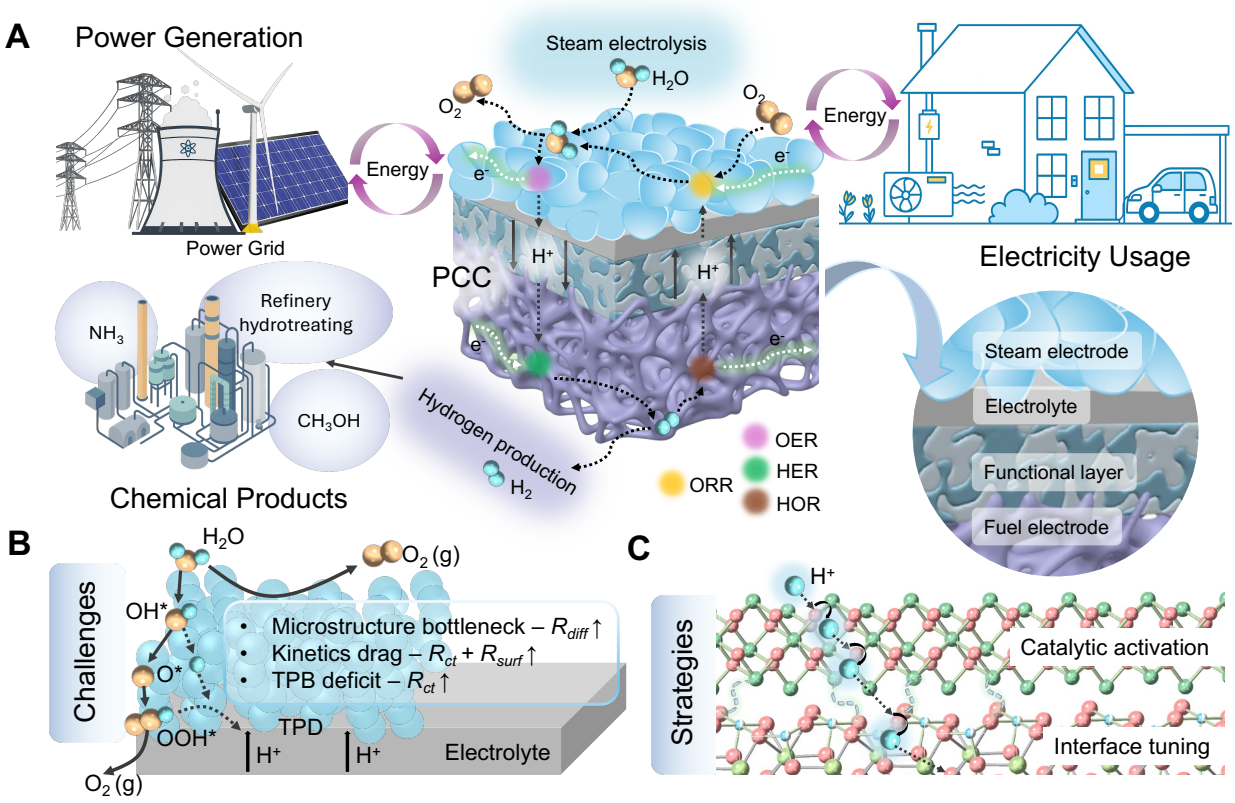


Figure 6.1. PCCs energy pathway: from grid electricity to hydrogen and chemicals. (A) Integrated schematic of reversible PCCs operation with its applications on power grid and chemical production. (B) Challenges at the steam-electrode/electrolyte interface in terms of microstructure, kinetics and TPB. (C) Strategies to boost PCCs' performance. Catalytic activation accelerates surface reactions; interface tuning engineers defect coherence to widen TPB contact and facilitate proton migration, as indicated by the dashed pathway.

generate reactive oxygenated intermediates. Crucially, PrO_x serves as a redox-flexible, vacancy-rich surface regulator that stabilizes these intermediates on unsaturated Pr–O sites and buffers local charge via the Pr^{3+}/Pr^{4+} couple, enabling their productive evolution rather than accumulation as blocking species. As schematized in Figure S4, oxygen evolution in PCC steam electrodes proceeds through a defect-based oxide mechanism. Steam preferentially interacts with vacancy–rich sites at the interphase, followed by coupled electron flow through the electrode backbone and proton transfer into the protonic electrolyte, while oxygen release occurs via defect-mediated oxygen exchange with concurrent vacancy regeneration. In parallel, the PrO_x–PNC coupling creates a vacancy-enriched reaction zone that lowers the barrier for oxygen incorporation into the

PNC lattice; under humid electrolysis, these vacancies can be readily hydrated to form mobile protonic defects, facilitating proton transfer through bulk pathways. Meanwhile, the continuous PNC scaffold provides the triple-conduction backbone and, together with the heterointerface, supports efficient charge redistribution and reduced interfacial charge-transfer resistance. Overall, the HEN architecture synchronizes stabilized surface chemistry with defect-assisted incorporation and exchange, expands the active reaction region beyond discrete point contacts, and accelerates oxygen evolution kinetics under steam.

The schematic illustrates the atomistic configuration and synergistic interaction between the PNC backbone and the PrO_x–modulated hierarchic layer (Figure 6.2D). PNC functions as a triple conducting phase, simultaneously supporting proton, oxygen ion, and electron transport, which is primarily enabled by the Ni/Co dopants at the B-site, which promote hydration and create mobile proton defects, resulting in high proton conductivity (σ_{H^+})[70,224]. In addition, PNC demonstrates excellent electronic conductivity ($\sigma_{e^-} > 100$ S cm^{-1}) within the intermediate temperature range of 400–600 °C, making it an ideal structural and functional platform for catalytic applications in PCCs[189]. In contrast, PrO_x exhibits relatively low electronic conductivity ($\sigma_{e^-} < 4$ S cm^{-1} across the operation temperature window), which limits its standalone applicability in electrochemical systems[222,308]. Despite its fluorite structure enabling mixed ionic–electronic conduction and a favorable redox flexibility (Pr^{3+}/Pr^{4+}), its conductivity is significantly inferior to that of general mixed ionic-electronic conductors. This limitation underscores the importance of hybridizing PrO_x with a highly conductive host such as PNC.

When integrated into the PNC scaffold, PrO_x plays a critical role as a vacancy-modulating layer, which is attributed to its effective catalytic behavior. As depicted in the center and right regions of Figure 6.2D, PrO_x preferentially stabilizes oxygen vacancies, forming a localized vacancy well that enhances surface exchange and ionic transport. The mixed-valence nature of Pr allows for oxygen vacancy formation without structural destabilization, and its ionic radius facilitates seamless integration into perovskite-type lattices. Notably, Pr_6O_{11}, one typical type of PrO_x, has been reported to exhibit a high oxygen surface exchange coefficient of $k = 5.4 \times 10^{-7}$ cm s^{-1} at 600 °C, further supporting its role in enhancing interfacial oxygen exchange and redox kinetics[309]. More importantly, the PrO_x–PNC hybrid achieves a synergistic balance: PNC ensures bulk conductivity and proton transport, while PrO_x enriches the surface with active sites and modulates

interfacial catalytic behavior. Together with the ultra-porous dual-channel architecture, this vacancy-engineered and electronically optimized hierarchic interface offers enhanced performance for oxygen evolution, making it a highly effective and durable electrode strategy for PCCs.

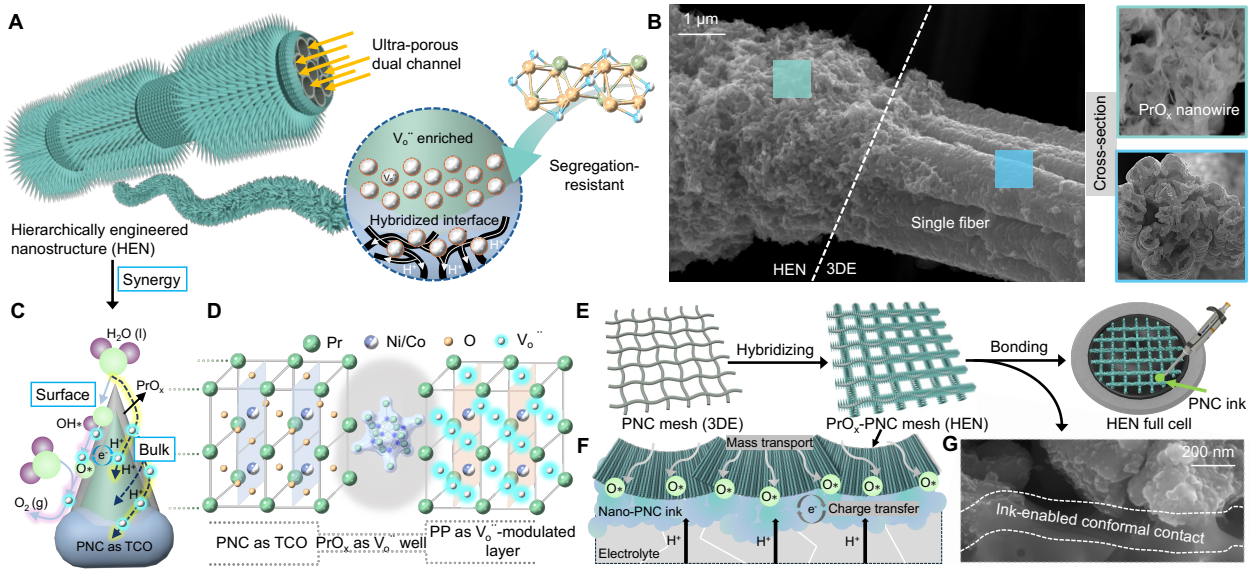


Figure 6.2. Structure, morphology, and oxygen-vacancy-induced lattice structure evolution of the hybrid interface in PrOx–PNC hierarchical structure. (A) Synergistic interaction between PrO_x and PNC on the HEN electrode, illustrating the regulation of oxygen vacancy enrichment and its benefit for suppressing segregation. (B) Structure morphology depicting a single fiber in the mesh, showing the pristine epart and the hierarchical pre-treatment part (side view and cross-section view). (C) Schematic of the oxygen evolution pathway facilitated by PrO_x-decorated PNC functioning as a triple-conducting oxide (TCO). (D) Spatial engineering of $\mathbf{V_o^{\cdot\cdot}}$ distribution across PrO_x–PNC heterostructure. PP denotes the PrO_x–PNC coupled region. (E) Schematic representation of the fabrication process for the HEN electrode onto the as-prepared half-cell ($BaCe_{0.7}Zr_{0.1}Y_{0.1}Yb_{0.1}O_{3-\delta}$-BCZYYb7111[177,226,255]/BCZYYb7111-NiO), employing a two-step approach involving hybridization and bonding. (F) Schematic of coupled charge–mass transfer pathway. The conformal coating of nano-PNC "glue ink" on the inner wall preserves the ultraporous channels for rapid gas/steam diffusion while creating a continuous electronic pathway along the PNC backbone. (G) Micrograph of the HEN steam-electrode showing an ink-enabled

conformal contact along interface following the fabrication in (E), which supports electron continuity and proton transport.

To create efficient, co-optimized pathways for both charge and mass transport, we engineered this hierarchical hybrid steam electrode building on the previously identified optimal hybridization (~10.6 wt.%), in which PrO_x interlaced nanowires are intimately coupled to a triple-conducting PNC mesh backbone using hybridization-bonding method (Figure 6.2E)[260]. The PrO_x nanowire supplies dense, robust catalytic sites, while the PNC nano-network bridges neighboring grains to reconstruct a high-activity heterointerface. Within this framework, the HEN full cells maintain open gas channels and nanowire-decorated fiber surfaces that promote rapid reactant access and turnover (Figure 6.2F). As a result, oxygen species can diffuse and incorporate efficiently along enlarged dual-transfer pathways, synchronizing charge transport with mass delivery and reinforcing the reconstructed heterointerface that underpins both physical and chemical stability. Importantly, the electrolyte–HEN electrode junction is strengthened by the nano-PNC ink, which infiltrates and wets the contact region and, upon firing, forms a conformal interfacial bridge that increases the true contact area and enables continuous charge transfer across the dense electrolyte surface (Figure 6.2G). This ink-enabled conformal layer does not replace the HEN architecture; rather, it anchors the HEN framework to the electrolyte while the high-catalytic HEN mesh preserves the enlarged transport pathways. Together, the conformal contact at the junction and the expanded active network above transform discrete TPB-type contacts into an extended, uniformly utilized interfacial reaction region.

6.4.2 Atomic-scale structural evolution and vacancy engineering in PrO_x–PNC hybrid interface

Through oxygen vacancy engineering, enhancing the electrochemical performance when using transition metal oxides as electrode is expected, but it can also lead to significant structural modifications at both local and long-range scales[310,311]. The formation of oxygen vacancies disrupts the local coordination environment, particularly in octahedrally coordinated lattices, where the removal of O^{2-} ions alters the symmetry, bond angles, and bond lengths within the metal-oxygen framework. This disruption can cause tilting or distortion of MO_6 octahedra, unit cell deformation, and even phase transitions in vacancy-sensitive systems[312,313]. In the case of the

PNC scaffold, the perovskite structure exhibits a relatively high degree of flexibility, allowing for the accommodation of moderate non-stoichiometry without compromising phase integrity. However, increased vacancy concentrations especially when induced near the surface through PrO_x hybridization provably result in subtle lattice changes such as unit cell expansion[314].

As shown in Figure 6.3A, the pristine PNC likely retains a stable perovskite lattice of corner-sharing BO_6 octahedra with minimal distortion. PrO_x interfacial hybridization could induce local lattice distortion and chemical expansion near the interface, possibly due to oxygen vacancies that weaken lattice connectivity and elongate metal-oxygen bonds. At higher vacancy levels, the structure may begin transitioning toward a mixed BO_6–BO_4 polyhedral arrangement, reminiscent of brownmillerite-type ordering, yet this transformation appears partially suppressed[315,316]. The redox-buffering capacity of Pr^{3+}/Pr^{4+} and the intrinsic stability of the PNC framework may help maintain a distorted but continuous octahedral network, preventing full phase conversion. Such controlled expansion and defect formation could create an interfacial region with enhanced Pr 4*f*–O 2*p* orbital overlap, strained bonding, and high vacancy concentration—conditions favorable for charge transport and catalytic activity[317]. The following results provide structural and spectroscopic evidence supporting this proposed lattice behavior.

X-ray diffraction (XRD) analysis provides compelling evidence for both interfacial hybridization and the resulting lattice expansion. As shown in Figure 6.3B, the Rietveld-refined pattern of the PrO_x–PNC hybrid exhibits distinct Bragg reflections corresponding to the PNC perovskite phase (green ticks) and the PrO_x phase (blue ticks), confirming the coexistence of both components. The high degree of fitting between the observed and calculated profiles demonstrates that PrO_x has been successfully incorporated into the PNC framework in a structurally coherent manner. Further insights are revealed in the high-resolution XRD scans shown in Figure 6.3C. The low-angle region shows a pseudo-superlattice peak appearing in the PrO_x–PNC sample but absent in pristine PNC, suggesting periodic modulation at the interface likely originates from the alternating structural motifs or strain fields induced by PrO_x hybridization[318,319]. In the middle panel, the (112) reflection of PrO_x–PNC shifts to lower 2θ relative to PNC, and similar leftward shifts are also observed for the (110) and (022) reflections, indicating a net chemical expansion, which can be interpreted as evidence consistent with vacancy enrichment induced by PrO_x hybridization, since oxygen-vacancy formation in transition-metal perovskites is commonly coupled with local lattice

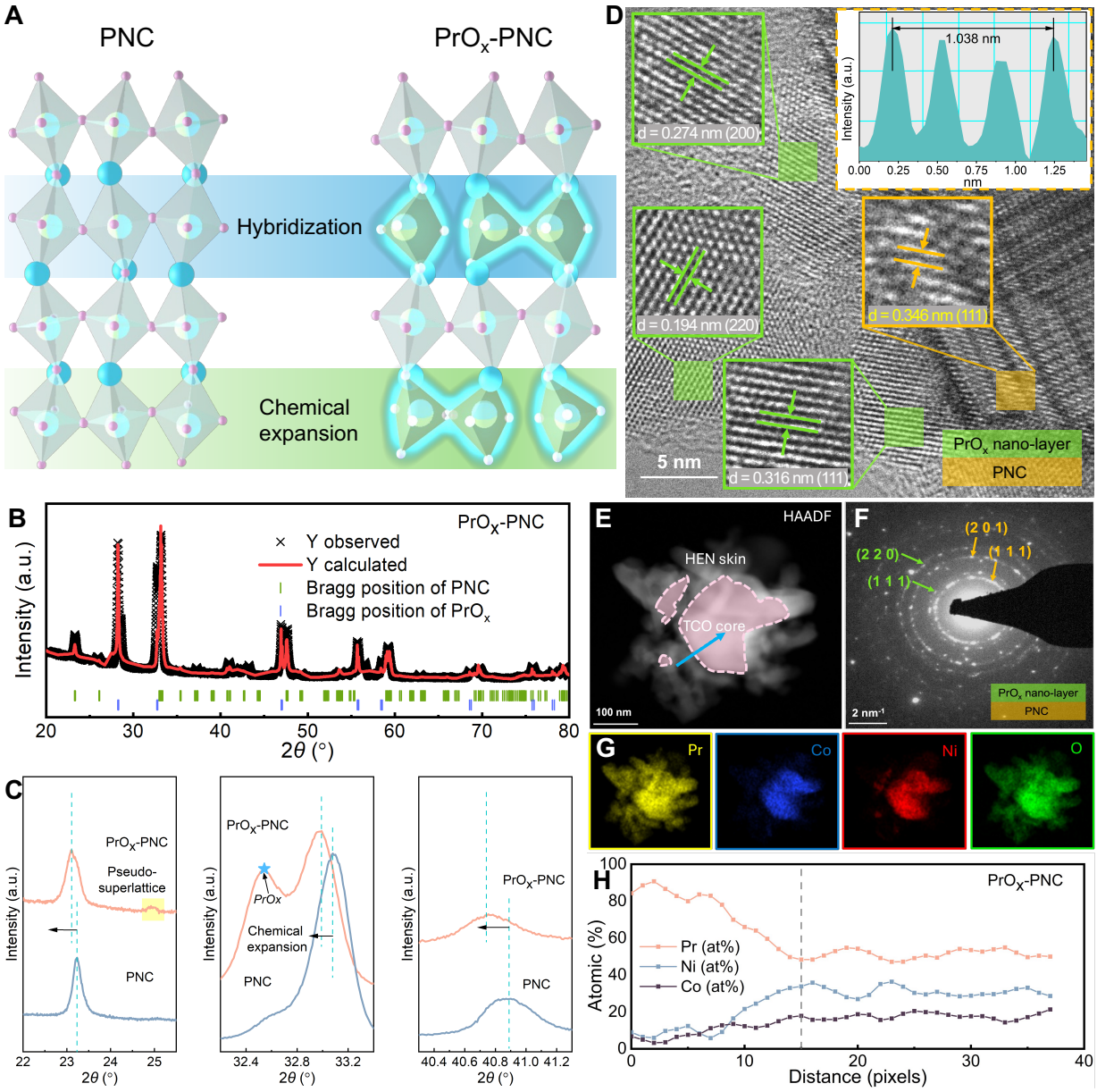


Figure 6.3. Structural characterizations of the hybrid PrO_x–PNC interfaces. (A) Schematic illustration of hybridization strategy, enabling chemical expansion through vacancy engineering and interfacial reconstruction. (B) High-resolution TEM image confirming the hybridized interface within the hierarchical nanostructure. Inset: line profile of PNC [111] plane illustrating increased interplanar spacing consistent with oxygen vacancy-induced lattice expansion. (C) XRD comparison between PNC and PrO_x–PNC showing peak shifts indicative of chemical expansion. From left to right panel, the reference peak are (110) at 2θ = 23.252°, (112) at 2θ = 33.096°, (022)

at 2θ = 40.885° of PNC pure phase (blue pattern), respectively. (D) XRD comparison between PNC and PrO_x–PNC showing peak shifts indicative of chemical expansion. (E) HAADF image revealing the TCO core (PNC) and HEN skin (PrO_x). (F) SAED patterns of PrO_x along [111] and [220] zone axes, and of PNC along [111] and [201] zone axes. (G) EDS elemental mapping: yellow (Pr), red (Ni), blue (Co), green (O). (H) STEM–EDS line scan across the hybrid interface (blue line in E), showing elemental distribution.

relaxation and cation redox that expand the unit cell (Figure S5). A weak shoulder feature further suggests the presence of defect-rich microdomains associated with the PrO_x–PNC coupled region, consistent with a heterogeneous but distributed hybridized structure. Quantitatively, Table S1 shows that the unit-cell dimensions expand along all three axes upon PrO_x hybridization, with a slight increase in the a-axis (0.08%), a moderate increase in the c-axis (0.21%), and the most pronounced expansion along the b-axis (from 5.401 Å to 5.427 Å, 0.48%). This anisotropic b-axis response is consistent with a perovskite lattice tendency toward vacancy-associated ordering, where oxygen-vacancy modulation and BO_6 rearrangement preferentially elongate the b-direction[320,321]. Overall, the diffraction results support that PrO_x hybridization drives a vacancy-enriched PrO_x–PNC region that manifests as measurable chemical expansion in the averaged crystal lattice.

Additional atomic-scale confirmation of structural evolution upon PrO_x impregnation is revealed by high-resolution transmission electron microscopy (HRTEM). As shown in Figure 6.3D, distinct lattice fringes corresponding to both the PNC core and the PrO_x-modified surface confirm the formation of a coherent PrO_x–PNC interface. The identified lattice planes, (200), (220), and (111), with consistent spacing values characteristic of the PrO_x phase validate the crystalline continuity across the bulk and interface. More importantly, a clear expansion of the (111) plane is observed, with the spacing increasing from 0.316 nm in pristine PNC to 0.346 nm in the hybridized nano-layer. The change reflects a measurable lattice expansion consistent with oxygen vacancy accumulation and local strain induced by the interfacial incorporation of PrO_x. The interplanar distance profile further reveals a grouped periodicity of 1.038 nm, consistent with layered modulation across the interface.

Elemental and crystallographic characterization further confirms the hierarchical architecture and chemical differentiation between the PNC core and the PrO_x nano-layer. In Figures 6.3E and S6, the high-angle annular dark-field (HAADF) image reveals a distinct core–shell morphology, where the dense inner region corresponds to the TCO core, and the outer shell displays a hierarchically engineered nanostructure (HEN skin). The corresponding selected area electron diffraction (SAED) pattern in Figure 6.3F exhibits features assignable to both PNC and PrO_x phases. Specifically, the (111) and (201) plane indexed to the perovskite lattice are present alongside (220) and (111) reflections attributable to the fluorite-like PrO_x structure. This coexistence of diffraction features from both lattices further confirms the hybridized nature and the formation of an interface between structurally distinct but chemically compatible phases. The mapping results in Figure 6.3G offer spatial confirmation of the phase distribution. Pr is enriched in the outer skin region, while Ni and Co are concentrated in the inner core, consistent with the HAADF image. Oxygen is homogeneously distributed, supporting the presence of continuous oxide frameworks throughout the structure. The line scan along the blue arrow (Figure 6.3H) quantifies the chemical profile. Pr content sharply increases at the surface, whereas Ni and Co concentrations rise toward the interior. Within the core region, the elemental ratio of Pr:Ni:Co is approximately 50%:35%:15%, closely matching the designed stoichiometry of $PrNi_{0.7}Co_{0.3}O_{3-\delta}$, further validating the integrity of the PNC backbone. The composition gradient supports the formation of a PrO_x-rich outer layer on a PNC core, affirming the success of the hierarchically surface modification strategy. Collectively, the structural, diffraction, and compositional results establish a coherent picture. The PrO_x–PNC hybrid architecture features a vacancy-modulated, chemically expanded PrO_x skin seamlessly integrated with a triple-conducting perovskite core. This spatially resolved hybridization is key to enabling faster proton transport and surface catalytic activity.

6.4.3 Degradation-resistant microstructure for high performance and Faradaic efficiency

The PrO_x–PNC hierarchical hybrid contributes to the long-term robustness by mitigating key degradation mechanisms. Through interfacial hybridization, the PrO_x layer serves as a chemically compatible surface modifier that limits cation segregation and surface decomposition by the mediated Pr^{3+}/Pr^{4+} redox buffering of surface vacancies and a space-charge field at the PrO_x–PNC junction that penalizes vacancy formation and A-site mobility, suppressing outward cation

enrichment[260,322,323]. Simultaneously, controlled oxygen vacancy modulation and structural accommodation help reduce mechanical and chemical stress during operation. The preservation of the TCO framework, along with suppressed phase transition and elemental migration, ensures structural and electrochemical integrity, enabling stable performance over extended cycling.

The suppressed degradation behavior of the PrO_x–PNC hybrid electrode is further validated through long-term electrolysis testing under steam-rich conditions (30 vol.% H_2O, 600 °C, 500 mA cm^{-2}). For electrochemical performance evaluation, all three electrodes: pristine, 3DE, and HEN, are integrated onto a BCZYYb/BCZYYb–NiO half-cell for testing using the lab-made fixture (Figure S7).

As shown in Figure 6.4A, the HEN electrode (bottom curve) maintains voltage stability over 200 h of continuous operation, whereas the pristine cell fails prematurely, consistent with uncontrolled interfacial chemical reconstruction and subsequent degradation, a common failure mode for conventional powder-packed electrodes. By comparison, the 3DE electrode (top curve) exhibits a gradual voltage increase, indicating progressive polarization growth, and post-test analysis reveals partial interfacial delamination (Figure S8). Under the same current density, the 3DE cell degrades at ~0.02 mV h^{-1}, while the HEN cell shows a slight voltage activation with no measurable degradation (Figure S9), underscoring the durability advantage conferred by the hierarchically engineered PrO_x nano-layer. The improved stability is further proved by the EIS results shown in Figure 6.4B, where the impedance spectra of the HEN full cell, recorded for 30 times at a constant voltage of 1.30 V, exhibit minimal change. The arc shape and size remain consistent, with the ohmic resistance (R_o) stabilized around 0.085 Ω cm^{-2} and the polarization resistance (R_p) maintained near 0.04 Ω cm^{-2} throughout the testing period. Such invariance in both the high-frequency intercept and the polarization arc indicates suppressed interfacial deterioration and sustained electrode kinetics over time. Crucially, we emphasize that this long-term stability is best rationalized by a chemically driven stabilization mechanism enabled by PrO_x, rather than by microstructural effects alone. Prior studies have established that interfacial chemical destabilization, often coupled with defect-chemistry drift under polarization, is central drivers of polarization growth and delamination in conventional perovskite oxygen electrodes[324]. In particular, thermodynamic analyses show that segregation is promoted by elastic and electrostatic driving forces and can be mitigated by surface-charge control, directly linking interface chemistry

to long-term stability[325]. Likewise, Pr-containing surface decoration has been demonstrated to stabilize oxygen surface exchange kinetics during aging with more stable surface exchange coefficient over extended time, underscoring a chemistry-based route to durability rather than a purely morphological one[326]. From the standpoint of intrinsic materials chemistry, Pr-containing oxides are widely recognized for their high redox flexibility and the associated ability to promote oxygen mobility and oxygen exchange, enabling them to act as an oxygen chemical-potential buffer under changing operating environments[327]. Therefore, in our HEN architecture, the hierarchically engineered PrO_x nano-layer is best understood as a chemically active stabilizer that regulates interfacial defect chemistry, helping to prevent the chemo-mechanical failure that typically culminates in polarization growth in conventional powder-packed electrodes, rather than merely acting as a microstructural reinforcement.

The hierarchical structure offers critical advantages for maintaining electrode integrity under electrolysis conditions, particularly in the presence of high steam pressures. The porous and mechanically resilient architecture helps mitigate degradation pathways, thus supporting long-term stability. The SEM image reveals the interwoven mesh fibers of a 3DE electrode, illustrating the open, porous structure that facilitates both mass transport and charge conduction. It highlights the tightly braided fiber network, which provides continuous pathways for electron flow and reactant diffusion. The inset zooms in on a localized region after hierarchical hybridization, revealing surface modifications and nanostructured deposits on the fiber strands, indicative of the engineered PrO_x coating designed to enhance catalytic activity (Figure 6.4C). Another image of single fiber also confirms the uniform deposition of the PrO_x-based hierarchical nanostructure onto the 3DE framework. The continuous and conformal coating ensures not merely intimate physical contact and structural cohesion but introduces catalytic benefits (Figure 6.4D). The PrO_x layer brings redox-active Pr sites and enriched oxygen vacancies, which facilitate oxygen exchange kinetics and promote oxygen evolution at the surface. This transformation is further proved by the corresponding Energy Dispersive X-ray Spectroscopy (EDX) elemental mapping. Additionally, cross-sectional SEM and elemental mapping of the HEN full cell (Figure S10) confirm its structural and chemical integrity. The HEN electrode shows strong adhesion with no delamination at the electrolyte-AFL interface. Elemental maps reveal uniform element distribution, with Pr enriched near the outer region, forming a distinct PrO_x skin layer, consistent with the designed hybrid structure. Ni and Co remain confined to the inner region, while Ba, Ce, Zr, Y, and Yb show

sharp boundaries in the electrolyte, indicating minimal interdiffusion and good phase compatibility. These features validate effective hybridization and long-term electrochemical stability.

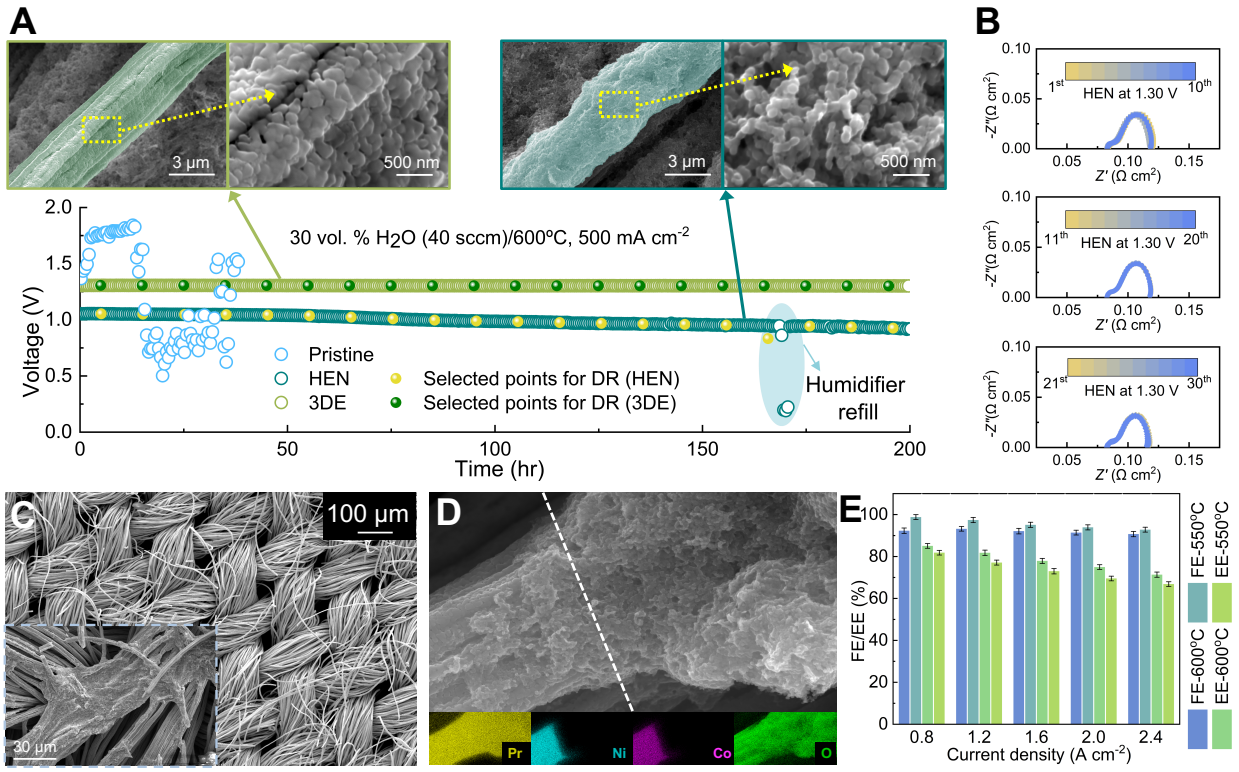


Figure 6.4. Electrochemical performance and structural stability of a PCC incorporating the HEN electrode. (A) Long-term galvanostatic durability, showing superior stability of the HEN architecture compared to pristine and 3DE counterparts, attributed to its optimized morphology (inset: corresponding SEM images). (B) Impedance spectra measured at 1.30 V over 30 cycles, indicating consistent interfacial properties over extended operation. (C) SEM image of interwoven mesh fibers in 3DE electrode, illustrating mass and charge transport pathways; inset shows the region after hierarchical hybridization. (D) SEM images of a single 3DE mesh fiber before (left) and after (right) hierarchical pretreatment with corresponding elemental EDX mapping. (E) Faradaic and energy efficiencies of HEN cells across different temperatures, highlighting enhanced catalytic effectiveness.

Faradaic efficiency (FE) serves as a key indicator of electrolysis effectiveness, representing the fraction of electrical charge successfully converted into hydrogen. A high FE implies that most of the input current drives the target reaction with minimal electronic leakage. Complementing this,

energy efficiency (EE) accounts for both FE and the operating voltage, offering a more comprehensive measure of how efficiently electrical energy is transformed into chemical fuel. To more rigorously attribute the FE behavior to the electrode function, rather than electrolyte-limited transport alone, we further performed a direct comparison under identical conditions as same BCZYYb electrolyte, cell architecture, and steam feed. Across the examined current-density window, the HEN cell consistently shows higher FE than the 3DE baseline, with the difference being most pronounced at 600 °C. The average FE increases from 83.3% to 91.9% at 600 °C and from 90.1% to 95.6% at 550 °C (Figure 6.4E and S11). Because the electrolyte is unchanged, this comparison demonstrates that the FE enhancement cannot be explained solely by ionic conductivity; instead, it reflects a specific functional role of the PrO_x–PNC catalytic architecture in suppressing parasitic loss currents.

Importantly, this FE improvement correlates directly with the I–V behavior under electrolysis (Figure S12). At both 550 °C and 600 °C, HEN achieves a given current density at a lower applied voltage than 3DE, and delivers substantially higher current at the same voltage threshold at 1.30 V. This matters because, in protonic ceramic electrolysis, a larger overpotential increases the effective chemical-potential gradients at the electrode-electrolyte interface, which can activate or amplify electronic leakage pathways and thereby depress FE. By accelerating oxygen-electrode kinetics and reducing the required operating voltage for the same output current, the PrO_x–PNC interface minimizes the driving force for leakage and pushes a larger fraction of the applied current into productive protonic transport and H_2 formation, hence the simultaneously higher FE and improved EE. Consistent with this interpretation, the EE decreases with increasing current density due to the inherent rise in overpotential, yet remains at appreciable levels throughout for HEN, reflecting the combined benefit of high FE and reduced voltage penalty. Finally, H_2 flux measurements conducted at 550 °C and 600 °C under varied voltages (Figure S13) further validate the strong electrolysis capability of the HEN cell. At 600 °C, the H_2 production rate increases from 5.14 to 15.2 ml min^{-1} cm^{-2} as the voltage rises from 1.08 to 1.27 V. Similarly, at 550 °C, the flux increases from 5.50 to 15.5 ml min^{-1} cm^{-2} between 1.21 V and 1.39 V. Together with the reduced-voltage I–V response and the direct FE comparison, these results indicate that the PrO_x–PNC design does not merely benefit initial activity; it reduces polarization-driven leakage and sustains more selective faradaic conversion across practical operating conditions.

To more comprehensively evaluate the effectiveness of the HEN architecture, performance comparisons with pristine and 3DE electrodes were conducted, along with temperature-dependent testing to assess operational robustness. As prerequisite step, we investigated the impact of calcination temperature on the porosity variation in 3DE electrode structure and electrochemical behavior, denoted as 3DE 650/700/750/800. It is well-established that calcination temperature directly influences the pore structure, grain growth, and surface area of porous electrodes. In SEM images of the temperature-dependent 3DE meshes (Figures S14-S17), lower calcination at 650 °C retains finer particles and more open porosity due to limited sintering, which results in larger pore sizes that promote gas diffusion. Conversely, the higher calcination temperature of 800 °C leads to more extensive grain growth and particle coalescence, which reduce pore size and surface area due to densification and enhanced crystallinity. The peak power density of 3DE-750 (1.521 W cm^{-2} at 600 °C) outperforms other electrodes, confirming its electrochemical superiority (Table S2). The SEM image of 3DE-750 reveals a well-defined fibrous network, while EDX mapping confirms uniform distribution of Pr, Ni, Co, and O (Figure S18). Additionally, the EIS result at 600 °C shows that 3DE-750 exhibits a moderate polarization resistance (R_p, ~0.09 Ω cm^2), balancing performance and structural stability (Figures S19 and S20). Among all variants, it achieves the lowest R_p values across the measured temperatures and a relatively low activation energy, $E_{a.p}$ = 0.26 eV, calculated by Equation S1, as shown in Arrhenius plots (Figures S21 and S22). These results demonstrate that the 3DE-750 strikes an optimal balance between porosity, electrical conductivity, and active surface area, making it the most effective electrode configuration. Therefore, the subsequent hierarchical engineering strategy is developed based on the 3DE-750 electrode platform. As depicted in Figure 6.5A, H_2–O_2 fuel cell testing reveals clear performance distinctions among pristine, 3DE and HEN cells. The pristine cell exhibits the peak power density as 0.753 W cm^{-2}, and fastest voltage drop with increasing current density, indicative of inferior electrode kinetics and high interfacial resistance. The 3DE cell shows adequate improvement, yet still suffer from limited power output, reaching 1.488 W cm^{-2}. In contrast, both HEN cells demonstrate significantly enhanced power density, exceeding 1.719 W cm^{-2}, and maintain stable voltage output across a broad current range, confirming their enhanced electrochemical activity and reduced polarization losses.

Evaluation of HEN cells at various temperatures under fuel cell conditions (Figure 6.5B) highlights the excellent thermal activation of the HEN structure and its ability to sustain high proton

conductivity and catalytic activity across a wide temperature window. As operating temperature increases, the cell exhibits continuously rising current and power densities, achieving high peak power density at 600 °C, which are over 3 times higher than that at 350 °C. Under electrolysis conditions, the performance of the HEN cell was further assessed with 30 vol.% H_2O feed (Figure 6.5C). At the neutral electrolysis potential of 1.30 V, the HEN electrode delivers a current density of approximately 0.187 A cm^{-2} at 350 °C, which increases significantly with temperature—reaching ~1.5 A cm^{-2} at 550 °C and exceeding 2.7 A cm^{-2} at 600 °C. The ability to sustain high current output at thermoneutral voltage demonstrates the efficiency and viability of the HEN electrode for practical steam electrolysis applications.

The EIS measurements offer essential insight into the underlying electrochemical behavior of different electrode configurations and operational conditions. In Figure 6.5D, all three electrode structures (pristine, 3DE, and HEN) exhibit nearly identical ohmic resistance (~0.089 Ω cm^2), confirming uniform bulk properties. However, the polarization resistance varies noticeably with electrode modification. HEN electrode exhibits the lowest R_p, ~0.069 Ω cm^2, owing to its hierarchical design and enhanced oxygen vacancy concentration that promotes faster surface exchange and improved electrode kinetics, whereas 3DE and pristine electrode show progressively higher resistance, consistent with their inferior performance in I–V–P curves. With increasing temperature, both ohmic and polarization resistances decrease due to enhanced ionic conductivity and thermally activated electrode reactions, which is particularly favorable for the PrO_x-functionalized interface in HEN electrode (Figure 6.5E). EIS profiles also collected under a constant electrolysis voltage of 1.30 V reveal a significant reduction in R_p compared to OCV at each temperature, which highlights the effect of the applied bias in enhancing carrier transport and promoting more active surface reactions, particularly in the HEN cell with its tailored interface and functional components (Figure S23).

Both DRT analysis and activation energy evaluation further validated the excellency of HEN cells. As illustrated in the DRT spectrum under OCV condition (Figure 6.5F), the HEN electrode displays significantly diminished intensity in characteristic peaks across distinct frequency domains. Specifically, the low-frequency region (10^0–10^2 Hz) corresponds to gas diffusion processes, the mid-frequency range (10^2–10^4 Hz) is attributed to surface exchange reactions, and the high-frequency region (10^4–10^6 Hz) reflects charge transfer resistance at the electrode–

electrolyte interface[8]. The notable reduction in these peaks for the HEN cell suggests that the hierarchical architecture effectively alleviates kinetic limitations throughout all major electrochemical steps. This suppression of resistive contributions indicates improved mass transport, enhanced surface reactivity, and facilitated interfacial charge transfer, collectively contributing to uplifted electrode kinetics under electrochemical conditions. Complementing this, the Arrhenius plot of polarization resistance in Figure 5D highlights the lowest activation energy, calculated by Equation S1, for the HEN cell at 0.5292 eV, lower than those of the 3DE (0.5814 eV) and pristine (0.5897 eV) cells (Figure 6.5G). The reduced energy barrier indicates that the HEN cell facilitates electrochemical reactions with higher efficiency and lower thermal input, which is particularly beneficial at intermediate temperatures. The lower $E_{a.p}$, in conjunction with the minimized resistive contributions observed in DRT, underscores the effectiveness of the hierarchical engineering strategy and the functional role of oxygen vacancy modulation in enhancing catalytic activity, charge transfer, and overall cell performance.

The comparison was made with recently reported peak power densities from other state-of-the-art cells across a similar temperature range to reinforce the performance achieved in this work (Figure 6.5H and Table S3)[8,140,328–336]. The HEN cell demonstrates consistently higher PPD values from 350 °C to 600 °C, significantly outperforming not only the 3DE and pristine references in this study, but also surpassing the majority of literature benchmarks. For instance, a Nb- and Y-co-doped cobalt-based perovskite ($PrBaCo_{1.8}Nb_{0.1}Y_{0.1}O_{5+\delta}$, PBCNY) air electrode was developed, featuring in situ self-assembly into a disordered cobalt oxide layer to enhance oxygen reaction kinetics in reversible PCCs. The PBCNY cell delivered peak power density of 0.97 W cm^{-2} at 600 °C, significantly lower than the 1.75 W cm^{-2} reported in this work under the same temperature. Moreover, the In- doped air electrode was developed to enhance oxygen vacancy concentration, resulting in a nanocomposite structure consisting of double perovskite ($PrBa_{0.95}Co_{1.85}In_{0.09}O_{5+\delta}$) and cubic perovskite ($BaCo_{0.85}In_{0.15}O_{3-\delta}$) phases, which boosts both ORR and OER activity by improving surface exchange and bulk diffusion. Similarly, at 600 °C, this In-doped electrode achieved a peak power density of 1.33 W cm^{-2} in fuel cell mode and 2.11 A cm^{-2} at 1.3 V in electrolysis mode. By comparison, HEN cells reach 2.77 A cm^{-2} under the same conditions, indicating more efficient fuel-to-electricity conversion and proton-driven water splitting. High-order Ruddlesden–Popper air electrodes were also developed with tailored Ni/Co ratios to enhance phase composition and gas transport. The optimized $Pr_4Ni_{1.8}Co_{1.2}O_{10-\delta}$ (PNCO64)

electrode (Ni/Co = 6:4), incorporating 5 wt% graphite to increase porosity, achieved a peak power density of 1.18 W cm^{-2} in fuel cell mode and a current density of 2.08 A cm^{-2} at 1.3 V in electrolysis mode at 600 °C. These enhancements were attributed to improved oxygen mobility and the formation of catalytically active Pr_6O_{11} phase. Through adopting the similar strategy to boost the kinetics, both values remain inferior to the performance achieved here using the HEN cell.

Following the confirmation the high electrochemical performance of the HEN cells, further evaluations were carried out to assess their long-term durability and dynamic response. Specifically, stability and transient switching tests were conducted to validate the reliable operation and robust structural integrity of the HEN configuration under realistic cycling and fluctuating conditions. Based on the I–V characteristics under different O_2/H_2O partial pressures (0.2, 0.3, 0.5, and 0.7 atm), the HEN cell exhibits clear electrolysis variations. At higher partial pressures (0.5 and 0.7 atm), though it achieves upper current density at certain overpotential range (>1.45 V), the voltage increases more rapidly at initial, indicating limited electrochemical kinetics[337]. It may introduce excess steam at the same time to compromise stability. In contrast, under 0.3 atm, the cell maintains a favorable voltage profile with a balanced overpotential, achieving over 2.5 A cm^{-2} at 1.3 V. Therefore, 0.3 atm was selected as the optimal condition for subsequent long-term and transient stability tests due to its combination of high current output and reliable electrochemical response. (Figure S24)

As shown in the reversible cycling test under alternating fuel cell and electrolysis cell modes, the HEN cell was subjected to six sets of symmetric voltage conditions ranging from 1.5–0.5 V to 1.2–0.8 V, 1.4–0.6 V, 1.3–0.7 V, and finally 1.1–0.9 V, each held for 1 hour over 15 cycles per stage (Figure 6.5I). The corresponding current density responses demonstrate excellent reproducibility with minimal performance decay across 200 hours. Notably, the pink-shaded region indicates a temporary disturbance caused by a humidifier refill, after which the performance rapidly recovered, reaffirming the robustness of the HEN architecture. The average degradation rate through the whole span, as quantified, was only 0.21 mA h^{-1}, suggesting remarkable stability under dynamic and harsh operating conditions (Figure S25).

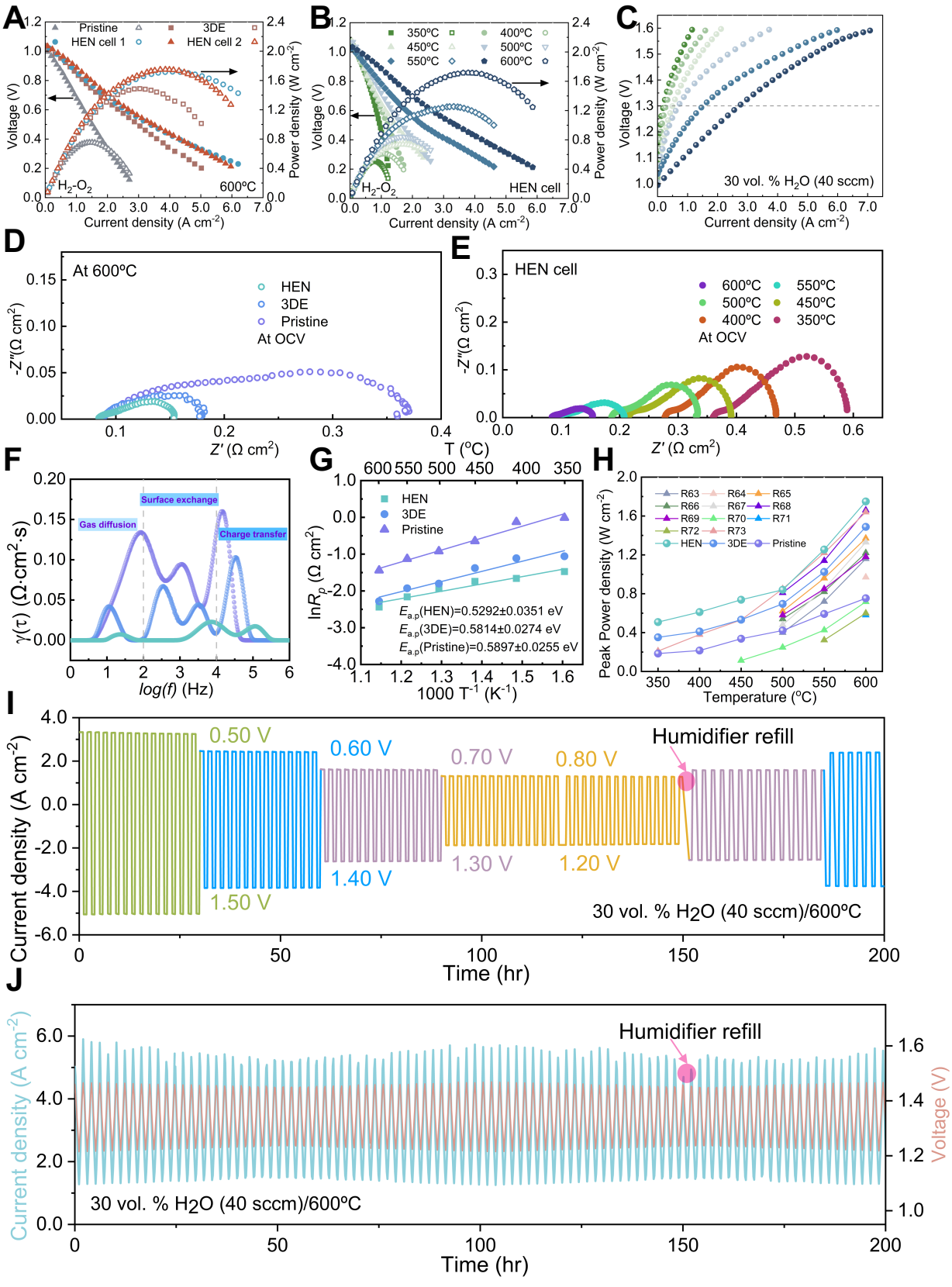

A
Pristine
3DE
HEN cell 1
HEN cell 2
Voltage (V)
Power density (W cm-2)
H2-O2
600ºC
Current density (A cm-2)
B
350ºC
400ºC
450ºC
500ºC
550ºC
600ºC
H2-O2
HEN cell
C
30 vol. % H2O (40 sccm)
D
At 600ºC
HEN
3DE
Pristine
At OCV
-Z''(Ω cm2)
Z' (Ω cm2)
E
HEN cell
600ºC
550ºC
500ºC
450ºC
400ºC
350ºC
At OCV
T (ºC)
F
Surface exchange
Gas diffusion
Charge transfer
γ(τ) (Ω·cm2·s)
log(f) (Hz)
G
HEN
3DE
Pristine
lnRp (Ω cm2)
Ea,p(HEN)=0.5292±0.0351 eV
Ea,p(3DE)=0.5814±0.0274 eV
Ea,p(Pristine)=0.5897±0.0255 eV
1000 T-1 (K-1)
H
R63
R64
R65
R66
R67
R68
R69
R70
R71
R72
R73
HEN
3DE
Pristine
Peak Power density (W cm-2)
Temperature (ºC)
I
0.50 V
0.60 V
0.70 V
0.80 V
Humidifier refill
1.50 V
1.40 V
1.30 V
1.20 V
30 vol. % H2O (40 sccm)/600ºC
Current density (A cm-2)
Time (hr)
J
Humidifier refill
30 vol. % H2O (40 sccm)/600ºC
Current density (A cm-2)
Voltage (V)
Time (hr)

Figure 6.5. Electrochemical performances of pristine, 3DE, and HEN cells and the durability under reversible and dynamic operations. (A-B) I–V–P curves of pristine, 3DE, and HEN single cells at 600 °C and for HEN cells across 350–600 °C, respectively. (C) Polarization behavior of HEN cells in electrolysis mode from 350–600 °C. (D) Electrochemical spectra of the three cell types at 600 °C. (E) Temperature-dependent EIS of HEN cells. (F) DRT analysis derived from EIS in (D). (G) Arrhenius plots of polarization resistance with linear fits. (H) Peak power density comparison with benchmark data. (I) Reversible long-term fuel cell–electrolysis cycling test of HEN cell. (J) Transient electrolysis durability test with voltage switching.

Additionally, the structural integrity of the HEN electrode following prolonged electrochemical operation was examined by post-test cross-sectional SEM. As shown in Figure S26, the HEN electrode retains a porous, interconnected network morphology after 200 h operation under high-steam conditions, and no macroscopic interfacial separation is observed at the HEN-electrolyte junction. We note that the post-test cross-section was obtained after cell sectioning, and the hybrid electrode together with the PNC powder can introduce local debris, which may make the electrolyte boundary appear less sharply defined in some regions. However, it clearly delineates the dense electrolyte layer and confirms that its thickness remains well preserved after long-term operation around 10 μm (Figure S26). Overall, these post-test observations support the mechanical robustness of the HEN architecture and its stable interfacial contact during extended humid electrolysis.

The transient performance of the HEN cell was evaluated under a staircase voltage profile in electrolysis mode to simulate variable power input conditions. As illustrated in Figure 6.5J, the applied voltage was continuously shifted in a pattern between 1.2 and 1.5 V, while the corresponding current density responded dynamically within the certain range. The cell demonstrated excellent responsiveness and repeatability during ~200 h of cycling, with only minimal fluctuations observed. Notably, no abrupt current drops or voltage instabilities were detected, indicating robust interfacial and bulk transport characteristics under fluctuating loads. The average degradation rate extracted was as low as 0.68 mA h^{-1}, affirming the HEN cell's remarkable operational durability even under frequent voltage perturbations (Figure S27). The excellent reversibility and minimal degradation highlight the HEN cell's promise for long-term practical application in reversible PCCs.

6.4.4 Linking electrochemical stability to vacancy-driven catalysis

Electrochemical stability in PCCs is closely tied to the mobility and reactivity of oxygen vacancy, which governs both catalytic activity and redox adaptability. In particular, vacancy-rich electrodes can buffer local chemical potential changes and promote sustained charge transfer across the electrode–electrolyte interface, thus enhancing durability and performance[109,338]. Key insights are drawn from O_2-TPD, which reveals vacancy-induced oxygen release behavior, and from EPR and iodometric titration, which quantify bulk vacancy concentrations. XPS further confirms vacancy-related shifts in surface valence states. These findings are reinforced by galvanostatic electrolysis under varying O_2/H_2O partial pressures, showing that vacancy-rich structures sustain stable operation under dynamic conditions.

The O_2–TPD profiles of PNC and PrO_x–PNC hybrids reveal distinct desorption behaviors that reflect differences in oxygen vacancy concentration and binding strength (Figure 6.6A). The PrO_x–PNC sample exhibits two major oxygen desorption peaks centered at 291 °C and 553 °C, along with a shoulder at 206 °C, whereas the PNC sample shows a much weaker profile with a primary peak at 228 °C and a broad shoulder near 319 °C. These multiple peaks in PrO_x–PNC correspond to the sequential release of oxygen species with varying binding energies, ranging from weakly bound surface adsorbed oxygen (206 °C) to moderately bound subsurface oxygen (291 °C), and more strongly incorporated lattice oxygen species (553 °C)[339]. Notably, the low-temperature desorption peak of PrO_x–PNC at 206 °C occurs at a lower temperature than that of pristine PNC at 228 °C, suggesting that the hybrid exhibits more activated surface oxygen species and enhanced oxygen mobility. This low-temperature shift is also consistent with increased catalytic reactivity and facilitated oxygen exchange. The dominant peak at 291 °C highlights a significant population of moderately bound oxygen, which is typically associated with labile lattice oxygen and reflects an increased density of oxygen vacancies. Additionally, the high-temperature peak at 553 °C, absent in the PNC profile, suggests the activation and release of deeply embedded lattice oxygen, further supporting enhanced bulk oxygen mobility. Collectively, the stronger and broader desorption features in the hybrid confirm a superior oxygen release capacity and more dynamic vacancy-mediated redox behavior, which underpin its improved catalytic performance.

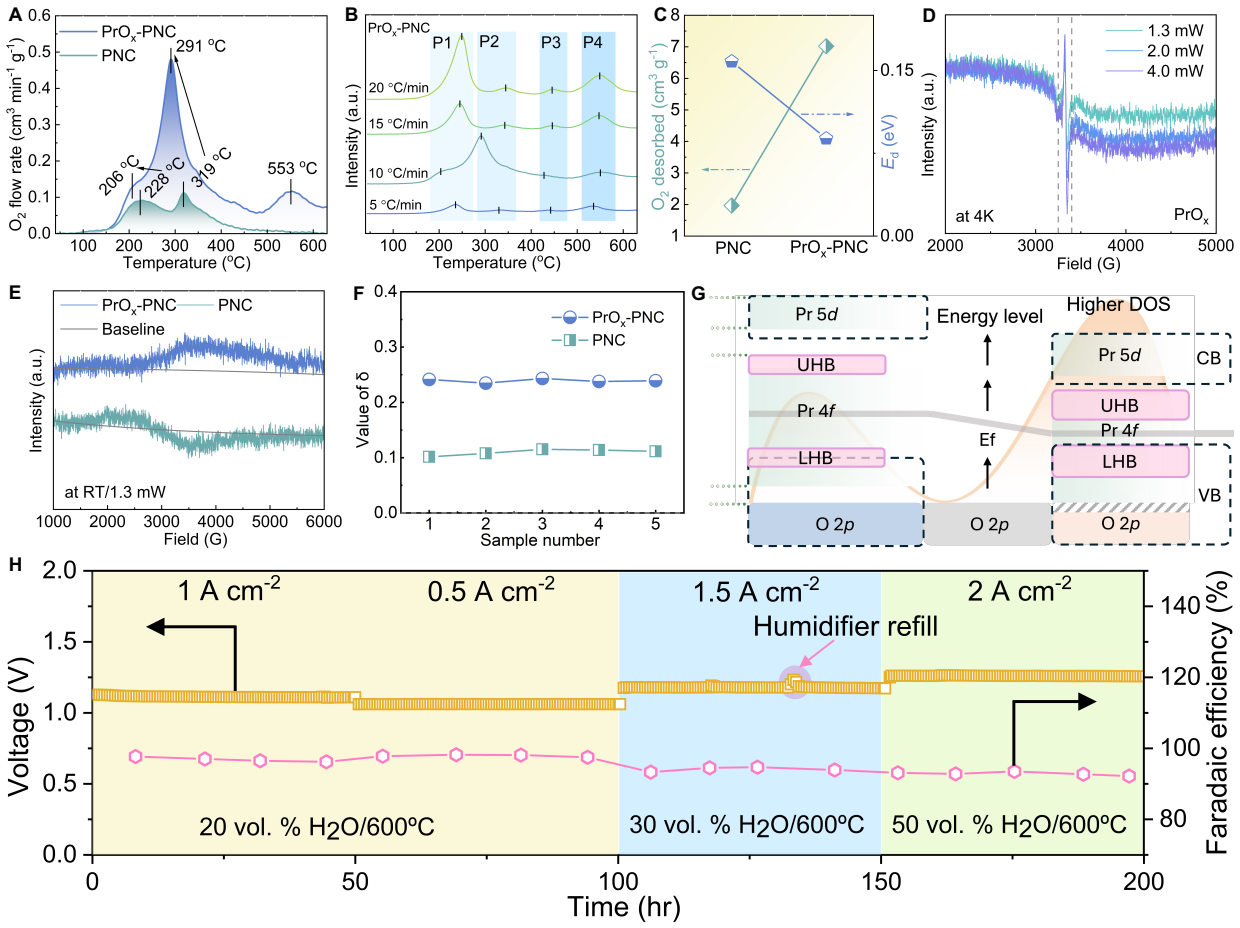


Figure 6.6. Comprehensive investigation of oxygen vacancy behavior and mobility for understanding the mechanism related with the hybrid interfaces. (A) O_2-TPD profiles collected at 10 °C min^{-1}. (B) O_2-TPD spectra under various heating rates (5–20 °C min^{-1}) exhibit four resolved peaks (P1–P4), corresponding to surface adsorbed, lattice, subsurface, and bulk oxygen species. (C) Comparison of total desorbed O_2 and activation energy. (D) Low-temperature (4 K) EPR spectra of PrO_x under 1.3–4.0 mW reveals strong paramagnetic signals, validating oxygen defect centers. (E) Room-temperature EPR spectra at 1.3 mW show the stronger signal in PrO_x–PNC compared to PNC, confirming higher surface vacancy concentration. (F) Iodometric titration results show consistently higher bulk oxygen non-stoichiometry (δ) in PrO_x–PNC across five samples. (G) Schematic of the proposed band structure modulation mechanism at the PrO_x–PNC interface showing enhanced orbital hybridization and increased density of states (DOS) near the Fermi level (Ef). (H) Electrolysis performance at 600 °C under varied H_2O partial pressure and current densities (0.5–2 A cm^{-2}) demonstrates excellent Faradaic efficiency and voltage stability, confirming robust oxygen vacancy modulation.

With the confirmation of enhanced oxygen desorption behavior of PrO_x–PNC, the O_2-TPD profiles acquired under varied temperature ramping rates (5–20 °C min^{-1}) further validate the robustness and mobility of oxygen species in the hybrid interface (Figure 6.6B). Four distinct desorption peaks (P1–P4) are consistently observed across all ramping rates, corresponding to surface adsorbed oxygen (P1), surface lattice oxygen (P2), subsurface lattice oxygen (P3), and bulk lattice oxygen (P4), respectively. The preservation and intensification of these peaks, particularly P1 and P2, with increasing ramp rates indicate a high density of accessible and mobile oxygen species. In contrast, the pristine PNC under the same test exhibits markedly inferior oxygen release behavior compared to the hybrid (Figure S28). Across all tested heating rates, the PNC curves remain largely featureless, lacking the distinct desorption peaks seen in the hybrid. Notably, only at the 10 °C min^{-1} ramping rate does the PNC sample display a discernible desorption peak, indicating minimal activation of oxygen species. This observation reinforces that the hybrid possesses a dynamic oxygen exchange capability and high lattice oxygen mobility, both of which are essential traits for promoting vacancy-driven catalytic processes. Additionally, as quantitative results illustrated in Figure 6.6C, the total amount of desorbed oxygen calculated *via* gas calibration using thermal conductivity detector signals shows a substantial increase from 1.97 cm^3 g^{-1} for pristine PNC to 7.02 cm^3 g^{-1} for the hybrid, which is consistent with the more intense and thermally shifted O_2-TPD peaks. Concurrently, the heat of desorption (E_d), derived from multi-ramp TPD profiles using Equation S2, is markedly reduced from 0.158 eV in PNC to 0.088 eV in PrO_x–PNC. Together, these results undoubtedly show that the hybrid system promotes greater oxygen release and lowers the energy barrier for vacancy formation.

The enhanced electrochemical performance of the PrO_x–PNC hybrid interface is closely related to the oxygen vacancy modulation, motivating further investigation into their enrichment and spatial distribution. To elucidate this, a combination of surface- and bulk-sensitive techniques was employed. Electron paramagnetic resonance (EPR) spectroscopy was used to detect surface oxygen vacancies by identifying unpaired electrons at paramagnetic defect sites. Initially, the rationale for employing PrO_x in the hybrid electrode design was validated by low-temperature electron paramagnetic resonance (EPR) measurements, performed on PrO_x powder at 4 K under varied powers of 1.3, 2.0, and 4.0 mW. Cooling to 4 K suppresses thermal broadening and enhances spectral resolution, enabling precise detection of vacancy-related species[340]. All spectra exhibit a prominent, well-defined signal centered near 3300 G, corresponding to unpaired electrons

associated with oxygen vacancies (Figure 6.6D). The persistence of this signal across increasing power levels confirms its intrinsic nature and robustness. The observed line shape remains consistent, while the signal intensity increases with microwave power, indicating good spin saturation behavior without significant power broadening. This strong and stable paramagnetic signature confirms the abundant presence of oxygen vacancy-related species in PrO_x, thereby supporting its role as an effective modulator when interfaced with the PNC scaffold. However, low-temperature conditions, can lead to signal suppression in certain oxides such as PNC and its derivatives, due to restricted spin relaxation and reduced mobility of paramagnetic centers at cryogenic temperatures, thereby diminishing the detectability of vacancy-related signals. As observed in separate temperature-dependent EPR tests for PNC, the signal at low temperature is considerably weaker than that at room temperature (RT), making RT a more appropriate condition for direct comparison (Figure S29). Consequently, under RT and 1.3 mW, the PrO_x–PNC spectrum reveals a significantly more intense and broader EPR response than pristine PNC, deviating significantly from the baseline, highlighting the higher concentration of paramagnetic centers primarily oxygen vacancies in the hybrid. In contrast, pristine PNC showed a relatively flat, baseline-adjacent profile, consistent with a lower vacancy density (Figure 6.6E). The evident comparison confirms that PrO_x hybridization effectively modulates and enriches oxygen vacancies, thereby enhancing catalytic activity.

Complementarily, iodometric titration was conducted to quantify the bulk oxygen non-stoichiometry by determining the average oxidation state of cations (Figure 6.6F). The results reveal a consistently higher bulk oxygen vacancy concentration (δ_{bulk}) in the PrO_x–PNC hybrid compared to the pristine PNC across five independent samples. The δ_{bulk} value for the hybrid averages approximately 0.24, nearly twice that of PNC, which remains around 0.11 (Table S4). The marked increase in bulk oxygen non-stoichiometry confirms the significant role of PrO_x incorporation in modulating lattice oxygen content, complementing the surface vacancy trends observed by EPR and reinforcing the overall vacancy-driven catalytic enhancement. By elevating vacancy concentration within HEN electrode, PrO_x incorporation primes the lattice for band realignment as enhanced Pr 4*f*–O 2*p* overlap and increased density of states (DOS) near Fermi level (E_f), which together translate structural defects into measurable reductions in surface resistance and higher catalytic rates (Figure 6.6G). In the PrO_x–PNC composite, enhanced

hybridization between Pr 4*f* and O 2*p* orbitals could narrow the band gap relative to pristine PNC, shifting both the unoccupied upper Hubbard band (UHB) and the lower Hubbard band (LHB) toward the Fermi level (E_f) and broadening the density of states (DOS) near E_f[341]. Such modifications are expected to provide more accessible redox-active states and accelerate charge transfer kinetics. Within the valence band (VB), partial overlap between Pr 4*f* and O 2*p* orbitals may increase the covalent character of the Pr–O bond, improving charge delocalization and hole transport—both important for surface redox processes. This interaction could also strengthen binding with catalytic intermediates, favoring efficient adsorption/desorption during oxygen evolution. In the conduction band (CB), positioning of the UHB with significant Pr 4*f* character closer to E_f may facilitate electron excitation and mobility[342]. These potential band alignments could support more efficient proton reduction during water splitting and other electrochemical reactions.

Following the comprehensive characterization of oxygen vacancy concentration and mobility, the electrolysis robustness of the hierarchical PrO_x–PNC hybrid was verified under rigid steam conditions (Figure 6.6H). Specifically, galvanostatic electrolysis was conducted at 600 °C under successively harsher steam environments (20–50 vol.% H_2O), coupled with varied current densities (0.5 to 2.0 A cm^{-2}). Despite the elevated H_2O partial pressures, the hybrid cell sustained stable voltage output and consistently high Faradaic efficiency (>92%), indicating highly efficient charge-to-product conversion. Expressly, the hierarchical system maintained a low degradation rate of 0.89 mA h^{-1}, highlighting the structural and chemical resilience of the vacancy-enriched architecture, which affirms the oxygen vacancy characteristics thermodynamically under demanding electrolysis conditions (Figure S30).

Surface-sensitive X-ray photoelectron spectroscopy (XPS) was employed to elucidate the surface chemical origin of the enhanced electrocatalytic behavior and vacancy dynamics in the PrO_x–PNC hierarchic hybrid. Beyond confirming the initial redistribution of surface oxygen species and the coupled redox response of Pr and Co (Figure 6.7), we further performed XPS on powder after long-term exposure under fuel cell-like (3% H_2O + 97% O_2, 200 h) and electrolysis-like (30% H_2O + 70% O_2, 200 h) environments to clarify the functional role of PrO_x during reversible operation. The deconvoluted Pr 3d5/2 spectra of the fresh powders reveal that PrO_x hybridization already shifts the surface Pr toward a slightly more oxidized state. The PrO_x–PNC surface contains 17.63%

Pr^{4+} versus 15.42% Pr^{4+} in pristine PNC (Figure 6.7A). Importantly, after 200 h operation, Pr maintains an engaged redox equilibrium under both modes. Pr^{4+} rises modestly to 20.13% for post-FC condition and 20.25% for post-FC condition on PrO_x–PNC (Figure 6.7D and 6.7G), remaining slightly higher than PNC (19.68% post-FC; 19.38% post-EC). This consistent Pr^{3+}/Pr^{4+} response indicates that PrO_x is not simply a static additive; rather, it functions as a surface redox reservoir that can reversibly accommodate changes in oxygen chemical potential during both operations, which is an essential prerequisite for stabilizing defect chemistry without forcing excessive redox drift onto the Co sublattice.

Similarly, in the fresh powders, Co 2p3/2 fitting already highlights a distinct hybrid surface state. PrO_x–PNC is dominated by an activated Co hydroxylated component, with a reduced Co^{2+} satellite fraction and a small lattice Co^{3+} contribution, whereas pristine PNC shows a much larger apparent lattice Co^{3+} fraction and a higher Co^{2+} satellite (Figure 6.7B). After operation, the key difference emerges in how each surface evolves under different levels of humidity (Figure 6.7E and 6.7H). Under fuel cell condition, PrO_x–PNC maintains a balanced surface where lattice-Co character is strengthened (lattice Co^{3+} increases to 17.02%) while the Co^{2+} satellite remains moderate. In contrast, pristine PNC undergoes pronounced Co reduction, evidenced by a collapse of lattice Co^{3+} to 6.53% and a sharp rise of the Co^{2+} satellite. This divergence becomes even more striking under electrolysis condition**.** PNC shifts into an extreme Co^{2+}-dominated state, consistent with severe steam-driven reduction; meanwhile, PrO_x–PNC significantly suppresses this degradation pathway while preserving substantially more lattice-Co character (lattice Co^{3+} 10.35%). Collectively, these results show that the functional role of PrO_x under both modes is to buffer cobalt redox drift, preventing the surface from collapsing into a deeply reduced Co^{2+}-rich state that would typically degrade kinetic functionality, with the benefit being most critical under high-steam conditions.

O 1s fitting of the fresh powders supports the vacancy-engineering picture established in Figure 6.7C. PrO_x–PNC exhibits a higher fraction of defect-associated oxygen (67.64%**)** compared with pristine PNC (52.11%), with correspondingly lower lattice oxygen. After FC exposure, PrO_x–PNC essentially preserves this defect-associated population, indicating that the hybrid sustains a vacancy-rich surface that is favorable for oxygen incorporation and exchange (Figure 6.7F). Pristine PNC also shows an increase in OH^*/O^* after FC, but this occurs concurrently with a strong shift toward Co^{2+}, implying that its activation is accompanied by destabilizing reduction. Under

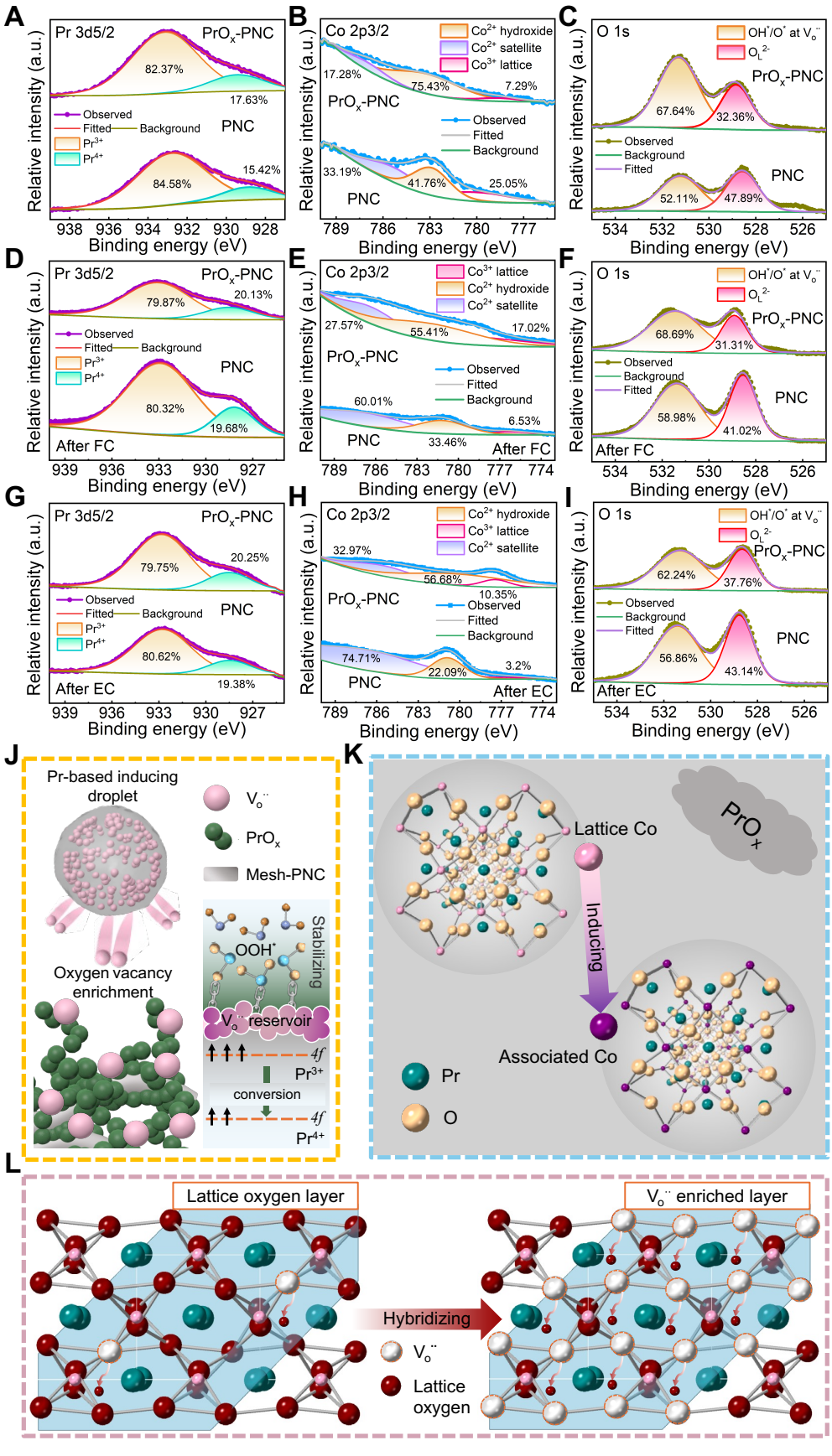

A
Pr 3d5/2
PrOx-PNC
82.37%
17.63%
Observed
Fitted
Background
Pr3+
Pr4+
PNC
84.58%
15.42%
Relative intensity (a.u.)
938 936 934 932 930 928
Binding energy (eV)
B
Co 2p3/2
Co2+ hydroxide
Co2+ satellite
Co3+ lattice
17.28%
75.43%
7.29%
PrOx-PNC
Observed
Fitted
Background
33.19%
41.76%
25.05%
PNC
789 786 783 780 777
Binding energy (eV)
C
O 1s
OH*/O* at Vo··
OL2-
PrOx-PNC
67.64%
32.36%
Observed
Background
Fitted
PNC
52.11%
47.89%
534 532 530 528 526
Binding energy (eV)
D
Pr 3d5/2
PrOx-PNC
79.87%
20.13%
Observed
Fitted
Background
Pr3+
Pr4+
PNC
80.32%
19.68%
After FC
939 936 933 930 927
Binding energy (eV)
E
Co 2p3/2
Co3+ lattice
Co2+ hydroxide
Co2+ satellite
27.57%
55.41%
17.02%
PrOx-PNC
Observed
Fitted
Background
60.01%
6.53%
PNC
33.46%
After FC
789 786 783 780 777 774
Binding energy (eV)
F
O 1s
OH*/O* at Vo··
OL2-
PrOx-PNC
68.69%
31.31%
Observed
Background
Fitted
PNC
58.98%
41.02%
After FC
534 532 530 528 526
Binding energy (eV)
G
Pr 3d5/2
PrOx-PNC
79.75%
20.25%
Observed
Fitted
Background
Pr3+
Pr4+
PNC
80.62%
19.38%
After EC
939 936 933 930 927
Binding energy (eV)
H
Co 2p3/2
Co2+ hydroxide
Co3+ lattice
Co2+ satellite
32.97%
56.68%
10.35%
PrOx-PNC
Observed
Fitted
Background
74.71%
22.09%
3.2%
PNC
After EC
789 786 783 780 777 774
Binding energy (eV)
I
O 1s
OH*/O* at Vo··
OL2-
PrOx-PNC
62.24%
37.76%
Observed
Background
Fitted
PNC
56.86%
43.14%
After EC
534 532 530 528 526
Binding energy (eV)
J
Pr-based inducing droplet
Vo··
PrOx
Mesh-PNC
Oxygen vacancy enrichment
Stabilizing
OOH*
Vo·· reservoir
4f
Pr3+
conversion
4f
Pr4+
K
Lattice Co
PrOx
Inducing
Associated Co
Pr
O
L
Lattice oxygen layer
Vo·· enriched layer
Hybridizing
Vo··
Lattice oxygen

Figure 6.7. XPS analyses and schematic illustrations revealing the synergistic modulation of Pr, Co, and O chemical states in the PrO_x–PNC hybrid. (A, D and G) High-resolution XPS spectra of the Pr 3d5/2 region for pristine PNC and PrO_x–PNC powders before operation, after FC operation and after EC operation. (B, E and H) High-resolution XPS spectra of the Co 2p3/2 region for pristine PNC and PrO_x–PNC powders before operation, after FC operation and after EC operation. (C, F and I) High-resolution XPS spectra of the O 1s region for pristine PNC and PrO_x–PNC powders before operation, after FC operation and after EC operation. (J–L) Schematics illustrate the Pr-induced vacancy enrichment (J), Co coordination transformation (K), and lattice restructuring with vacancy accumulation (L), collectively supporting the synergistic mechanism in catalytic enhancement.

EC exposure, the hybrid shows a moderate decrease in OH^*/O^* and an increase in lattice oxygen, consistent with high-steam conditions promoting partial vacancy compensation (Figure 6.7I). Crucially, this EC-driven oxygen rebalancing in PrO_x–PNC occurs without the catastrophic Co reduction seen in PNC, and the hybrid remains more defect-active than PNC even after EC (62.24% vs 56.86% OH^*/O^*). Thus, the updated post-operation O 1s data refine the mechanistic picture. PrO_x primarily helps *retain* a vacancy-associated oxygen surface during fuel cell operation, whereas PrO_x enables a controlled re-equilibration of oxygen species under steam while maintaining Co in a more catalytically competent state through electrolysis.

Together, the Pr 3d, Co 2p, and O 1s XPS results, supported by the schematics in Figure 6.7J–6.7L, show that PrO_x drives a redox–vacancy coupling in the PrO_x–PNC hybrid rather than a simple surface composition change. PrO_x activates the Pr^{3+}/Pr^{4+} redox buffer, which stabilizes a defect-rich interfacial region and sustains reactive oxygen species; this buffered oxygen landscape, in turn, maintains Co in a more catalytically competent coordination environment and prevents the surface from drifting into an overly reduced, deactivated state. Consistent with this, the O 1s evolution indicates a surface that remains exchange-active, with oxygen vacancies and adsorbed oxygen species participating as dynamic intermediates for oxygen incorporation and release. Importantly, the post-operation XPS clarifies that this behavior is mode-adaptive during reversible operation, functioning as a stabilizing redox mediator and vacancy regulator that couples Pr oxidation, Co coordination, and oxygen exchange, thereby sustaining fast kinetics and durability in both modes.

6.5 Conclusions

By hierarchically hybridizing PrO_x with mesh-structured PNC, an oxygen vacancy-engineered electrode was achieved with enhanced catalytic activity and structural robustness. Structural characterizations revealed lattice expansion and interfacial reconstruction. XPS analyses demonstrate a tightly correlated evolution of Pr, Co, and O states: vacancy enrichment drives Pr^{3+} oxidation to Pr^{4+} for charge compensation and simultaneously shifts Co coordination toward more hydroxylated, catalytically active surface species. These cationic changes mirror the enrichment of surface oxygen species, reflecting an altered anionic framework that facilitates rapid oxygen exchange. EPR measurements confirm the enhanced vacancy density in the hybrid, while O_2-TPD and iodometric titration quantify both greater total oxygen release and higher mobility, accompanied by a lower heat of desorption, indicative of weakened M–O bonding and dynamic redox flexibility. Electrochemically, the hybrid electrode delivered a peak power density of 1.75 W cm^{-2} in fuel cell mode and a current density of 2.77 A cm^{-2} at 1.3 V in electrolysis mode (both at 600 °C), while sustaining Faradaic efficiencies above 92% and minimal degradation even under steam-rich cycling.

Mechanistically, within the PrO_x–PNC hybrid, the PrO_x-modified interface forms a defect-enriched reaction zone in which oxygen vacancies are stabilized and become the primary initiators of redox evolution under polarization. These vacancies act as high-affinity sites for gas-phase oxygen and steam adsorption and dissociation, generating surface adsorbate species that couple to proton transfer into the proton-conducting electrolyte and electron flow through the triple-conducting electrode backbone. As the interfacial oxygen chemical potential shifts during reversible operation, the Pr^{3+}/Pr^{4+} couple in PrO_x responds first, reversibly accommodating oxygen uptake and thereby buffering the local defect population. This redox buffering pins the vacancy landscape and prevents large, irreversible redox excursions from being imposed on the Co–O sublattice. Consequently, Co remains within a catalytically competent valence window rather than drifting toward a deeply reduced, reconstructed state, which would otherwise promote surface deactivation, cation redistribution and interfacial weakening. In this way, vacancy enrichment by PrO_x hybridization triggers a coupled sequence, from vacancy-assisted adsorption to Pr redox buffering and moderated Co redox, ultimately achieving sustained defect-mediated oxygen exchange plus providing a chemically driven basis for stable kinetics and long-term durability.

This work thereby positions the PrO_x–PNC hybrid as a promising platform for durable, high-efficiency energy conversion in protonic ceramic cells.

6.6 Data and materials availability

All data are available in the main text or the supplementary materials. The supplementary materials can be found at https://doi.org/10.1002/anie.7079252.

Chapter 7- Summary and Prospects

This dissertation advances reversible protonic ceramic cells by establishing a unified design framework for the oxygen side of the cell, where performance and durability are most strongly coupled under steam-rich operation. Across four studies, the work demonstrates that high reversible performance is not achieved by a single improvement in composition or morphology, but by coordinated control of multiscale transport architecture, defect-enabled catalytic functionality, and electrode–electrolyte interfacial integrity. By systematically linking electrode microstructure to mass-transfer tolerance, coupling vacancy-rich phases to catalytic activity and redox buffering, and constructing structurally integrated, proton transparent junctions, the dissertation provides practical strategies to reduce polarization while maintaining durability during reversible cycling between PCFC and PCEC modes.

A central outcome of this thesis is the clarification that the oxygen electrode should be treated as a coupled system rather than an isolated material. Microstructure determines the accessibility and utilization of reaction sites; defect chemistry and redox flexibility determine intrinsic ORR/OER kinetics and steam activation; and the buried interface determines whether these benefits can be translated into stable, device-level performance without constriction losses, interdiffusion, or delamination. In particular, the work highlights that engineered interphases—whether formed through hybridized defect-rich phases or through thin-film nanostructuring—can simultaneously lower interfacial polarization and strengthen bonding, thereby stabilizing performance under high current, thermal cycling, and long-term steam electrolysis. Collectively, these results provide a blueprint for designing oxygen electrodes that deliver both high activity and durability, which is essential for practical reversible energy conversion and hydrogen production.

Looking forward, several research directions emerge naturally from the findings of this dissertation.

First, deeper exploration on the catalytic and materials chemistry side of the oxygen electrode remains highly promising. While this dissertation demonstrates how vacancy-rich phases and redox buffering can enhance kinetics and stability, there is substantial opportunity to develop more predictive relationships between composition, defect chemistry, and catalytic function under steam. Future studies can more systematically tune metal–oxygen covalency, vacancy formation energetics, and redox couples to position materials within an optimal activity–stability window.

Particular value lies in designing catalysts and heterostructures that maintain high oxygen exchange activity without becoming overly oxygen-labile in electrolysis mode, as well as in developing oxygen electrodes that are more intrinsically bifunctional for ORR and OER. Extending these concepts to broader composition families, beyond the current perovskite-centered choices, could yield electrodes with improved steam tolerance and reduced segregation-driven degradation.

Second, continued development on the interfacial engineering side is likely to produce outsized benefits, because the interface often dictates both the initial loss breakdown and the long-term degradation trajectory. Future work can expand interfacial nanostructuring and interlayer concepts toward more general "interface design rules" that specify how thickness, defect state, crystallinity, and chemical compatibility jointly control proton transfer, contact uniformity, and mechanical stability. Promising directions include graded junctions that smooth defect-chemical discontinuities, interlayers that combine fast proton transport with catalytic functionality, and integrated architectures that simultaneously address constriction resistance and interdiffusion. Translating thin-film interface concepts into scalable fabrication routes, while preserving conformality and protonic transparency, will also be important for bridging laboratory demonstrations and practical devices.

Third, the dissertation points to the importance of post-operation diagnosis and operando-informed validation as a pillar for future progress. As PCC electrodes become more complex and multiscale, performance decay can originate from subtle changes—nanometer-scale interphases, local segregation, contact loss at discrete regions, or catalyst coarsening—that are not evident from end-point metrics alone. Future research should therefore prioritize systematic post-test forensics and time-resolved diagnostics that can unambiguously connect electrochemical signatures to physical mechanisms. This includes combining periodic EIS/DRT with targeted cross-sectional characterization (FIB/TEM with EDS/EELS), depth profiling for cation migration and interphase growth, and spatially resolved mapping to capture heterogeneity and hot-spot driven degradation. Where possible, operando or near-operando probes that track defect and valence evolution under steam would further strengthen mechanistic understanding and accelerate rational design.

Overall, this dissertation establishes that durable, high-rate reversible protonic ceramic cells can be realized when catalytic activity, transport architecture, and interface stability are engineered as

a coupled system. The prospects outlined above—advancing catalytic/material descriptors under steam, generalizing and scaling interfacial nanostructuring strategies, and strengthening post-operation diagnosis—represent a coherent pathway to further improve both performance and reliability and to move reversible protonic ceramic electrochemical cells closer to practical deployment.

Bibliography

[1] I. Staffell, D. Scamman, A. Velazquez Abad, P. Balcombe, P. E. Dodds, P. Ekins, N. Shah, K. R. Ward, *Energy Environ. Sci.* **2019**, *12*, 463.

[2] C. J. Quarton, O. Tlili, L. Welder, C. Mansilla, H. Blanco, H. Heinrichs, J. Leaver, N. J. Samsatli, P. Lucchese, M. Robinius, S. Samsatli, *Sustainable Energy Fuels* **2020**, *4*, 80.

[3] I. Petkov, P. Gabrielli, *Applied Energy* **2020**, *274*, 115197.

[4] G. Yang, D. Yang, B. Liu, H. Zhang, *Applied Energy* **2024**, *374*, 123914.

[5] A. Nemmour, A. Inayat, I. Janajreh, C. Ghenai, *International Journal of Hydrogen Energy* **2023**, *48*, 29011.

[6] C. Duan, J. Huang, N. Sullivan, R. O'Hayre, *Applied Physics Reviews* **2020**, *7*, 011314.

[7] C. Duan, R. Kee, H. Zhu, N. Sullivan, L. Zhu, L. Bian, D. Jennings, R. O'Hayre, *Nat Energy* **2019**, *4*, 230.

[8] F. Liu, H. Deng, D. Diercks, P. Kumar, M. H. A. Jabbar, C. Gumeci, Y. Furuya, N. Dale, T. Oku, M. Usuda, P. Kazempoor, L. Fang, D. Chen, B. Liu, C. Duan, *Nat Energy* **2023**, *8*, 1145.

[9] X. Chen, Y. Tan, Z. Li, T. Liu, Y. Song, S. Zhai, N. Yu, Z. Shao, M. Ni, *Advanced Materials* **2025**, 2418620.

[10] H. Ding, W. Wu, C. Jiang, Y. Ding, W. Bian, B. Hu, P. Singh, C. J. Orme, L. Wang, Y. Zhang, D. Ding, *Nat Commun* **2020**, *11*, 1907.

[11] X. Chen, N. Yu, Y. Song, T. Liu, H. Xu, D. Guan, Z. Li, W. Huang, Z. Shao, F. Ciucci, M. Ni, *Advanced Materials* **2024**, *36*, 2403998.

[12] K. Pei, Y. Zhou, K. Xu, H. Zhang, Y. Ding, B. Zhao, W. Yuan, K. Sasaki, Y. Choi, Y. Chen, M. Liu, *Nat Commun* **2022**, *13*, 2207.

[13] W. Li, H. Tian, L. Ma, Y. Wang, X. Liu, X. Gao, *Mater. Adv.* **2022**, *3*, 5598.

[14] L. Schley, V. Vibhu, L. Nohl, I. C. Vinke, L. G. J. (Bert) De Haart, R.-A. Eichel, *Energy Adv.* **2024**, *3*, 861.

[15] H. Pourrahmani, A. Yavarinasab, M. Siavashi, M. Matian, J. Van Herle, *Energy Reviews* **2022**, *1*, 100002.

[16] A. V. Kasyanova, I. A. Zvonareva, N. A. Tarasova, L. Bi, D. A. Medvedev, Z. Shao, *Materials Reports: Energy* **2022**, *2*, 100158.

[17] S. Zarabi Golkhatmi, M. I. Asghar, P. D. Lund, *Renewable and Sustainable Energy Reviews* **2022**, *161*, 112339.

[18] H. Su, Y. H. Hu, *Energy Science & Engineering* **2022**, *10*, 1706.

[19] Q. Wang, S. Ricote, M. Chen, *Electrochimica Acta* **2023**, *446*, 142101.

[20] M. Li, F. Liu, D. Ding, *Nat Catal* **2025**, *8*, 293.

[21] A. Chiara, F. Giannici, C. Pipitone, A. Longo, C. Aliotta, M. Gambino, A. Martorana, *ACS Appl. Mater. Interfaces* **2020**, *12*, 55537.

[22] F. Liu, D. Diercks, P. Kumar, A. Seong, M. H. A. Jabbar, C. Gumeci, Y. Furuya, N. Dale, T. Oku, M. Usuda, P. Kazempoor, I. Ghamarian, L. Liu, L. Fang, D. Chen, Z. Wang, S. Skinner, C. Duan, *Sci. Adv.* **2025**, *11*, eadq2507.

[23] L. Ge, X. Yu, Z. Zhao, Z. Jin, Z. Yu, B. He, S. Cui, *Transactions of Materials Research* **2025**, *1*, 100141.

[24] H. Dai, H. Kou, H. Wang, L. Bi, *Electrochemistry Communications* **2018**, *96*, 11.

[25] M. Wang, C. Su, Z. Zhu, H. Wang, L. Ge, *Composites Part B: Engineering* **2022**, *238*, 109881.

[26] M. B. Hanif, S. Rauf, Z. U. Abadeen, K. Khan, Z. Tayyab, S. Qayyum, M. Mosiałek, Z. Shao, C.-X. Li, M. Motola, *Matter* **2023**, *6*, 1782.

[27] D. Catalán-Martínez, L. Navarrete, M. Tarach, J. Santos-Blasco, E. Vøllestad, T. Norby, M. I. Budd, P. Veenstra, J. M. Serra, *International Journal of Hydrogen Energy* **2022**, *47*, 27787.

[28] W. Zhang, X. Zhang, Y. Song, G. Wang, *Next Sustainability* **2024**, *3*, 100028.

[29] F. Zhao, A. Virkar, *Journal of Power Sources* **2005**, *141*, 79.

[30] A. Tarutin, J. Lyagaeva, A. Farlenkov, S. Plaksin, G. Vdovin, A. Demin, D. Medvedev, *Materials* **2018**, *12*, 118.

[31] W. He, J. Zou, B. Wang, S. Vilayurganapathy, M. Zhou, X. Lin, K. H. L. Zhang, J. Lin, P. Xu, J. H. Dickerson, *Journal of Power Sources* **2013**, *237*, 64.

[32] Z. Luo, Y. Zhou, X. Hu, N. Kane, T. Li, W. Zhang, Z. Liu, Y. Ding, Y. Liu, M. Liu, *Energy Environ. Sci.* **2022**, *15*, 2992.

[33] H. Takahashi, I. Yashima, K. Amezawa, K. Eguchi, H. Matsumoto, H. Takamura, S. Yamaguchi, *Chem. Mater.* **2017**, *29*, 1518.

[34] K.-D. Kreuer, S. J. Paddison, E. Spohr, M. Schuster, *Chem. Rev.* **2004**, *104*, 4637.

[35] Y. Yamazaki, F. Blanc, Y. Okuyama, L. Buannic, J. C. Lucio-Vega, C. P. Grey, S. M. Haile, *Nature Mater* **2013**, *12*, 647.

[36] A. Lindman, P. Erhart, G. Wahnström, *Phys. Rev. B* **2015**, *91*, 245114.

[37] B. Guan, H. Tian, Y. N. Picard, J. Liu, H. W. Abernathy, T. Kalapos, L. Zhou, X. Li, W. Li, X. Liu, *Journal of Power Sources* **2024**, *604*, 234454.

[38] T. S. Bjørheim, A. Løken, R. Haugsrud, *J. Mater. Chem. A* **2016**, *4*, 5917.

[39] W. Bian, W. Wu, B. Wang, W. Tang, M. Zhou, C. Jin, H. Ding, W. Fan, Y. Dong, J. Li, D. Ding, *Nature* **2022**, *604*, 479.

[40] C. Meisel, J. D. Huang, L. Q. Le, Y.-D. Kim, S. Stockburger, Z. Luo, T. Zhu, Z. Wang, Z. Shao, R. O'Hayre, N. P. Sullivan, *J. Mater. Chem. A* **2025**, *13*, 10863.

[41] C. Meisel, Y.-D. Kim, D. Diercks, R. O'Hayre, N. P. Sullivan, *Front. Energy Res.* **2025**, *13*, 1565315.

[42] C. Herradon, L. Le, C. Meisel, J. Huang, C. Chmura, Y. D. Kim, C. Cadigan, R. O'Hayre, N. P. Sullivan, *Front. Energy Res.* **2022**, *10*, 1020960.

[43] H. Zhu, S. Ricote, R. J. Kee, *J. Phys. Energy* **2022**, *4*, 014002.

[44] L. Kwati, K. Miyazaki, C. Dellen, M. E. Ivanova, W. Deibert, J. Wolter, W. A. Meulenberg, O. Guillon, V. Vediyappan, T. Ishihara, H. Matsumoto, *Mater. Adv.* **2025**, *6*, 3253.

[45] D. Kim, T. K. Lee, S. Han, Y. Jung, D. G. Lee, M. Choi, W. Lee, *Materials Today Energy* **2023**, *36*, 101365.

[46] W. Wu, C. Wang, W. Bian, B. Hua, J. Y. Gomez, C. J. Orme, W. Tang, F. F. Stewart, D. Ding, *Advanced Science* **2023**, *10*, 2304074.

[47] C. Meisel, J. Huang, Y.-D. Kim, R. O'Hayre, N. P. Sullivan, *Journal of Power Sources* **2024**, *615*, 235021.

[48] L. Q. Le, C. Meisel, C. H. Hernandez, J. Huang, Y. Kim, R. O'Hayre, N. P. Sullivan, *Journal of Power Sources* **2022**, *537*, 231356.

[49] X. Miao, X. Ye, Z. Wen, *Journal of Power Sources* **2022**, *551*, 232216.

[50] S. Yang, J. Gao, M. Trini, S. De Angelis, P. S. Jørgensen, J. R. Bowen, L. Zhang, M. Chen, *Acta Materialia* **2023**, *246*, 118708.

[51] N. Shi, Y. Xie, M. O. Tadé, Z. Shao, *Advanced Materials* **2025**, *37*, 2416528.

[52] M. Choi, S. J. Kim, W. Lee, *Ceramics International* **2021**, *47*, 7790.

[53] Z. Yue, M. Guo, Z. Chen, H. Tang, J. Li, Z. Li, K. Chen, Y. Chen, S. P. Jiang, *International Journal of Hydrogen Energy* **2025**, *190*, 152247.

[54] Y. Lim, J. H. Chong, P. Guha, W.-J. Lee, I. Cho, S. H. Oh, J. Kim, K. J. Yoon, J.-W. Son, J.-H. Lee, S. Choi, D.-H. Kwon, H.-I. Ji, S. Yang, *J. Mater. Chem. A* **2025**, *13*, 17709.

[55] T. Chen, Y. Jing, L. O. Anderson, K. Leonard, H. Matsumoto, N. Aluru, N. H. Perry, *J. Phys. Chem. C* **2021**, *125*, 26216.

[56] A. V. Kuzmin, M. S. Plekhanov, A. S. Lesnichyova, *Electrochimica Acta* **2020**, *348*, 136327.

[57] H. Tian, W. Li, Y.-L. Lee, H. Zheng, Q. Li, L. Ma, D. Bhattacharyya, X. Chen, D. Zhang, G. Li, Y. Wang, L. Li, Q. Wang, F. Xia, M. Kartal, Z. Shao, M. R. Rowles, W. Li, W. A. Saidi, C. Liu, X. Li, J. Luo, X. Li, K. He, X. Liu, *Nat Energy* **2025**, *10*, 890.

[58] A. A. Thatte, M. Pastula, T. Wood, H. Zhu, R. J. Kee, R. J. Braun, *Journal of Power Sources* **2024**, *611*, 234706.

[59] W. Bian, W. Wu, Y. Gao, J. Y. Gomez, H. Ding, W. Tang, M. Zhou, D. Ding, *Adv Funct Materials* **2021**, *31*, 2102907.

[60] J. Jing, Z. Lei, C. Wang, Z. Zheng, H. Wang, P. Zhang, Z. Yang, S. Peng, *ACS Sustainable Chem. Eng.* **2023**, *11*, 10303.

[61] G. C. Mather, D. Muñoz-Gil, J. Zamudio-García, J. M. Porras-Vázquez, D. Marrero-López, D. Pérez-Coll, *Applied Sciences* **2021**, *11*, 5363.

[62] Y. Ling, F. Huang, L. Wang, G. Xiao, T. Li, *Energy* **2025**, *341*, 139473.

[63] P. Marmet, L. Holzer, T. Hocker, G. K. Boiger, H. Bausinger, A. Mai, M. Fingerle, S. Reeb, D. Michel, J. M. Brader, *Energy Adv.* **2023**, *2*, 980.

[64] M. Kishimoto, H. Iwai, M. Saito, H. Yoshida, *Journal of Power Sources* **2011**, *196*, 4555.

[65] D. Chen, H. He, D. Zhang, H. Wang, M. Ni, *Energies* **2013**, *6*, 1632.

[66] W. Yang, Z. Pan, Z. Jiao, Z. Zhong, R. O'Hayre, *Energy Reviews* **2025**, *4*, 100104.

[67] M. Yu, Q. Feng, Z. Liu, P. Zhang, X. Zhu, S. Mu, *Crystals* **2024**, *14*, 225.

[68] W. Deibert, M. E. Ivanova, Y. Huang, R. Merkle, J. Maier, W. A. Meulenberg, *J. Mater. Chem. A* **2022**, *10*, 2362.

[69] A. Tarutin, N. Danilov, J. Lyagaeva, D. Medvedev, *Applied Sciences* **2020**, *10*, 2481.

[70] Y. Geng, S. Zheng, S. Karki, A. Serrano, Y. Jiang, B. Idris, A. Kumari, D. Cao, H. Ding, *ACS Nano* **2025**, acsnano.5c15759.

[71] Z. Wang, X. Miao, X. Ye, Z. Wen, *ACS Appl. Mater. Interfaces* **2023**, *15*, 45035.

[72] Y. Du, N. Hedayat, D. Panthi, H. Ilkhani, B. J. Emley, T. Woodson, *Materialia* **2018**, *1*, 198.

[73] H. Kang, Y. J. Park, S. Y. Baek, J. Kim, S. Ahn, I. Lim, G. Heo, W. Jung, J. H. Kim, *InfoMat* **2025**, *7*, e70025.

[74] Z. Liu, L. Zhang, C. J. Zheng, Y. Zhang, B. Chen, Z. Shao, J. Ge, *Advanced Materials* **2025**, *37*, 2503609.

[75] Q. Wang, X. Tong, S. Ricote, R. Sažinas, P. V. Hendriksen, M. Chen, *Advanced Powder Materials* **2022**, *1*, 100003.

[76] Z. Liu, Y. Bai, H. Sun, D. Guan, W. Li, W.-H. Huang, C.-W. Pao, Z. Hu, G. Yang, Y. Zhu, R. Ran, W. Zhou, Z. Shao, *Nat Commun* **2024**, *15*, 472.

[77] J. Jing, Z. Lei, Y. Xue, Z. Zheng, H. Wang, P. Zhang, B. Ge, Z. Yang, *Energy Storage Materials* **2024**, *72*, 103694.

[78] W. Wu, H. Ding, Y. Zhang, Y. Ding, P. Katiyar, P. K. Majumdar, T. He, D. Ding, *Advanced Science* **2018**, *5*, 1800360.

[79] Z. Liu, R. Qiao, D. Feng, J. Zhou, H. Di, Y. Bai, D. Liu, N. Shi, W.-H. Huang, M.-H. Yeh, C.-W. Pao, Z. Hu, G. Yang, Y. Lin, Z. Luo, R. Ran, W. Zhou, Y. Zhu, Z. Shao, *Nat Commun* **2025**, *16*, 10405.

[80] V. Lescure, M. Gelin, M. François, M. Arab Pour Yazdi, P. Briois, F. Demoisson, L. Combemale, S. Valton, G. Caboche, *Membranes* **2022**, *12*, 68.

[81] T. A. Schmauss, S. A. Barnett, *J. Mater. Chem. A* **2023**, *11*, 3695.

[82] S. Oh, H. Kim, I. Jeong, D. Kim, H. Yu, K. T. Lee, *J. Korean Ceram. Soc.* **2024**, *61*, 224.

[83] C. Zhou, D. Liu, M. Fei, X. Wang, R. Ran, M. Xu, W. Wang, W. Zhou, R. O'Hayre, Z. Shao, *Journal of Power Sources* **2023**, *556*, 232403.

[84] S. Kim, D. Yoon, J. Chae, H. Kim, J. Hong, J.-W. Son, J.-H. Lee, S. Kang, H.-I. Ji, *Energy Environ. Sci.* **2026**, *19*, 1715.

[85] H. Téllez Lozano, J. Druce, S. J. Cooper, J. A. Kilner, *Science and Technology of Advanced Materials* **2017**, *18*, 977.

[86] P. Yao, J. Zhang, Q. Qiu, G. Li, Y. Zhao, F. Yu, Y. Li, *Ceramics International* **2024**, *50*, 2373.

[87] Y. Zhang, X. Hao, J. Liu, X. Yang, H. Xu, Z. Wang, Y. Luo, F. Wang, T. He, *Ceramics International* **2024**, *50*, 4746.

[88] A. Seong, J. Kim, D. Jeong, S. Sengodan, M. Liu, S. Choi, G. Kim, *Advanced Science* **2021**, *8*, 2004099.

[89] M. Siebenhofer, F. Grajkowski, C. Nicollet, B. Yildiz, J. Fleig, M. Kubicek, *J. Mater. Chem. A* **2025**, *13*, 29885.

[90] N. Yu, I. T. Bello, X. Chen, T. Liu, Z. Li, Y. Song, M. Ni, *Nano-Micro Lett.* **2024**, *16*, 177.

[91] H. Liu, W. Gong, F. He, Y. Huang, J. Xia, X. Zhang, X. Chen, K. Sasaki, Y. Choi, Y. Chen, *ACS Energy Lett.* **2025**, *10*, 5644.

[92] H. Di, Z. Liu, M. Xiao, Y. Bai, G. Yang, Z. Luo, W. Wang, R. Ran, W. Zhou, Z. Shao, *Chemical Engineering Journal* **2025**, *507*, 160759.

[93] M. Burriel, J. Peña-Martínez, R. J. Chater, S. Fearn, A. V. Berenov, S. J. Skinner, J. A. Kilner, *Chem. Mater.* **2012**, *24*, 613.

[94] Y. Okuyama, K. Kasuga, M. Shimomura, Y. Mikami, K. Yamauchi, T. Kuroha, H. Sumi, *Journal of Power Sources* **2023**, *586*, 233647.

[95] Y. Zhou, W. Zhang, N. Kane, Z. Luo, K. Pei, K. Sasaki, Y. Choi, Y. Chen, D. Ding, M. Liu, *Adv Funct Materials* **2021**, *31*, 2105386.

[96] L. Wu, J. Sun, H. Qi, B. Tu, C. Xiong, F. Chen, P. Qiu, *J. Mater. Chem. A* **2024**, *12*, 25979.

[97] F. He, H. Liu, Y. Xu, F. Zhu, K. Sasaki, Y. Choi, Y. Liu, Y. Chen, *Joule* **2025**, *9*, 101957.

[98] M. Liang, Y. Zhu, Y. Song, D. Guan, Z. Luo, G. Yang, S. P. Jiang, W. Zhou, R. Ran, Z. Shao, *Advanced Materials* **2022**, *34*, 2106379.

[99] K. Park, M. Saqib, H. Lee, D. Shin, M. Jo, K. M. Park, M. Hamayun, S. H. Kim, S. Kim, K.-S. Lee, R. O'Hayre, M. Choi, S.-J. Song, J.-Y. Park, *Energy Environ. Sci.* **2024**, *17*, 1175.

[100] J. Pan, Y. Ye, M. Zhou, X. Sun, Y. Chen, *Energy Fuels* **2022**, *36*, 12253.

[101] Y. Niu, Y. Zhou, W. Zhang, Y. Zhang, C. Evans, Z. Luo, N. Kane, Y. Ding, Y. Chen, X. Guo, W. Lv, M. Liu, *Advanced Energy Materials* **2022**, *12*, 2103783.

[102] S. Koohfar, M. Ghasemi, T. Hafen, G. Dimitrakopoulos, D. Kim, J. Pike, S. Elangovan, E. D. Gomez, B. Yildiz, *Nat Commun* **2023**, *14*, 7203.

[103] F. Zhu, F. He, D. Liu, H. Zhang, Y. Xu, K. Xu, Y. Chen, *Energy Storage Materials* **2022**, *53*, 754.

[104] J. Nielsen, P. S. Jørgensen, *Electrochimica Acta* **2017**, *252*, 387.

[105] C. Li, X. Tong, C. Yuan, Y. Tong, Y. Zhang, N. Wang, P. Li, S. Pang, L. Wang, Z. Zhan, *Ceramics International* **2024**, *50*, 4656.

[106] I. Yuste-Tirados, X. Liu, C. Kjølseth, T. Norby, *International Journal of Hydrogen Energy* **2023**, *48*, 30027.

[107] S. W. Saeed, T. S. Bjørheim, *J. Phys. Chem. C* **2020**, *124*, 20827.

[108] M. Shirpour, B. Rahmati, W. Sigle, P. A. Van Aken, R. Merkle, J. Maier, *J. Phys. Chem. C* **2012**, *116*, 2453.

[109] S. P. Jiang, *Electrochem. Energy Rev.* **2022**, *5*, 21.

[110] C. Zhou, X. Shen, D. Liu, J. Cui, Y. Yi, M. Fei, J. Zhou, L. Zhang, R. Ran, M. Xu, W. Zhou, Z. Shao, *Journal of Power Sources* **2022**, *530*, 231321.

[111] S. K. Dwivedi, Y. Zeng, L.-A. Schaefer, M. S. Khan, K. Leonard, N. H. Menzler, O. Guillon, M. E. Ivanova, R. Kumar, *International Journal of Hydrogen Energy* **2025**, *177*, 151426.

[112] N. Tarasova, A. Bedarkova, *Materials* **2022**, *15*, 6841.

[113] A. Chiara, G. Raimondi, R. Merkle, J. Maier, C. V. Bordenca, C. Pipitone, A. Longo, F. Giannici, *ACS Appl. Mater. Interfaces* **2023**, *15*, 50225.

[114] K. Akimoto, N. Wang, C. Tang, K. Shuto, S. Jeong, S. Kitano, H. Habazaki, Y. Aoki, *ACS Appl. Energy Mater.* **2022**, *5*, 12227.

[115] S. Uhlenbruck, T. Moskalewicz, N. Jordan, H.-J. Penkalla, H. P. Buchkremer, *Solid State Ionics* **2009**, *180*, 418.

[116] H. Shimada, Y. Mikami, K. Yamauchi, T. Kuroha, T. Uchi, K. Nakamura, S. Kobayashi, R. M. Matsuda, Y. Okuyama, Y. Mizutani, M. Mori, *Ceramics International* **2024**, *50*, 3895.

[117] S. Choi, C. J. Kucharczyk, Y. Liang, X. Zhang, I. Takeuchi, H.-I. Ji, S. M. Haile, *Nat Energy* **2018**, *3*, 202.

[118] M. Abdullah Umer, C.-Y. Cheng, B.-R. Lai, C.-J. Tseng, S. Chen, S.-W. Lee, *Applied Surface Science* **2023**, *638*, 158139.

[119] M. A. Umer, C.-Y. Cheng, K.-C. Tsai, C.-J. Tseng, S. Chen, S.-W. Lee, *Journal of Power Sources* **2024**, *613*, 234872.

[120] C. Yang, Q. Xu, *Journal of Power Sources* **2012**, *212*, 186.

[121] A. Løken, S. Ricote, S. Wachowski, *Crystals* **2018**, *8*, 365.

[122] A. K. E. Andersson, S. M. Selbach, C. S. Knee, T. Grande, *J. Am. Ceram. Soc.* **2014**, *97*, 2654.

[123] K. Taghikhani, A. Dubois, J. Berger, S. Ricote, H. Zhu, R. Kee, *Membranes* **2021**, *11*, 378.

[124] K.-Y. Park, Y.-D. Kim, J.-I. Lee, M. Saqib, J.-S. Shin, Y. Seo, J. H. Kim, H.-T. Lim, J.-Y. Park, *ACS Appl. Mater. Interfaces* **2019**, *11*, 457.

[125] N. Sata, R. Costa, *Prog. Energy* **2024**, *6*, 032002.

[126] N. Tsvetkov, D. Kim, I. Jeong, J. H. Kim, S. Ahn, K. T. Lee, W. Jung, *Adv Materials Technologies* **2023**, *8*, 2201075.

[127] H. Sumi, H. Shimada, Y. Yamaguchi, Y. Mizutani, Y. Okuyama, K. Amezawa, *Sci Rep* **2021**, *11*, 10622.

[128] Y. Aoki, *Electrochemistry* **2023**, 23.

[129] T. Zhou, H. Huang, Y. Meng, J. Conrad, M. Zou, Z. Zhao, K. S. Brinkman, J. Tong, *ACS Energy Lett.* **2024**, *9*, 4557.

[130] H. Shimada, K. Watanabe, M. Fujioka, K. Nomura, A. Sharma, Y. Yamaguchi, H. Sumi, Y. Mizutani, *ACS Appl. Mater. Interfaces* **2025**, *17*, 40639.

[131] Z. Wang, F. Liu, Y. Meng, W. Bian, H. Zhao, C. Duan, M. T. Benson, M. Li, B. Liu, D. Ding, *eScience* **2025**, *5*, 100437.

[132] M. Choi, D. Kim, T. K. Lee, J. Lee, H. S. Yoo, W. Lee, *Advanced Energy Materials* **2024**, 2400124.

[133] Z. Li, C. Wang, I. T. Bello, N. Yu, X. Chen, J. Xuan, L. Xing, M. Han, M. Ni, *Journal of Power Sources* **2024**, *606*, 234581.

[134] X. Chen, N. Yu, I. T. Bello, D. Zhang, J. Zhou, Y. Wang, M. Ni, T. Liu, *Separation and Purification Technology* **2023**, *325*, 124713.

[135] Y. Song, Y. Chen, W. Wang, C. Zhou, Y. Zhong, G. Yang, W. Zhou, M. Liu, Z. Shao, *Joule* **2019**, *3*, 2842.

[136] H. Shimada, Y. Yamaguchi, H. Sumi, Y. Mizutani, *Ceramics International* **2021**, *47*, 16358.

[137] B. Bilbey, S. Pandey, J. Zamudio-Garcia, A. Savikko, M. Khoshkalam, V. Esposito, M. I. Asghar, *WIREs Energy & Environment* **2025**, *14*, e70010.

[138] Á. Triviño-Peláez, D. Pérez-Coll, M. Aparicio, D. P. Fagg, J. Mosa, G. C. Mather, *J. Mater. Chem. A* **2022**, *10*, 4428.

[139] W. Tang, W. Bian, H. Ding, Y. Ding, Z. Zhao, Q. Sun, S. Koomson, Y. Wang, B. Xu, P. Dong, D. Chen, J. Y. Gomez, W. Feng, W. Wu, M. Zhou, Y. Dong, H. Luo, J. Li, D. Ding, *Nat. Synth* **2025**, *4*, 592.

[140] N. Kane, Z. Luo, Y. Zhou, Y. Ding, A. Weidenbach, W. Zhang, M. Liu, *ACS Appl. Mater. Interfaces* **2023**, *15*, 32395.

[141] B. A. Riga-Rocha, V. A. Paganin, M. L. Faro, S. Vecino-Mantilla, Z. Hafsi, F. M. De Oliveira, H. Varela, E. A. Ticianelli, J. Perez, *Electrochimica Acta* **2025**, *514*, 145631.

[142] M. Zhou, Z. Liu, M. Chen, Z. Zhu, D. Cao, J. Liu, *J Am Ceram Soc.* **2022**, *105*, 5711.

[143] H. Tian, Z. Luo, Y. Song, Y. Zhou, M. Gong, W. Li, Z. Shao, M. Liu, X. Liu, *International Materials Reviews* **2023**, *68*, 272.

[144] Z. Zhao, J. Gao, Y. Meng, K. S. Brinkman, J. Tong, *Ceramics International* **2021**, *47*, 11313.

[145] J. N. Ebert, D. Jennings, L.-A. Schäfer, D. Sebold, W. Rheinheimer, *Scripta Materialia* **2024**, *241*, 115852.

[146] C.-T. Chen, C. E. Danel, S. Kim, *J. Mater. Chem.* **2011**, *21*, 5435.

[147] M. Kindelmann, I. Povstugar, S. Kuffer, D. Jennings, J. N. Ebert, M. L. Weber, M. P. Zahler, S. Escolastico, L. Almar, J. M. Serra, P. Kaghazchi, M. Bram, W. Rheinheimer, J. Mayer, O. Guillon, *Advanced Energy Materials* **2025**, *15*, 2404410.

[148] J. Li, C. Wang, X. Wang, L. Bi, *Electrochemistry Communications* **2020**, *112*, 106672.

[149] S. J. Heo, S. P. Harvey, A. G. Norman, M. A. Rahman, P. Singh, A. Zakutayev, *ACS Appl. Mater. Interfaces* **2024**, *16*, 11646.

[150] M. Kindelmann, S. Escolastico, L. Almar, A. Vayyala, D. Jennings, W. Deibert, W. A. Meulenberg, W. Rheinheimer, M. Bram, J. M. Serra, J. Mayer, O. Guillon, *J. Mater. Chem. A* **2024**, *12*, 3977.

[151] I. T. Bello, S. Karki, N. Xu, A. Kumari, S. Zheng, Y. Geng, G. Kim, S. Tao, Y. Liu, H. Ding, *Adv Funct Materials* **2026**, e00006.

[152] K. Bae, D. Y. Jang, H. J. Choi, D. Kim, J. Hong, B.-K. Kim, J.-H. Lee, J.-W. Son, J. H. Shim, *Nat Commun* **2017**, *8*, 14553.

[153] G. Taillades, P. Pers, V. Mao, M. Taillades, *International Journal of Hydrogen Energy* **2016**, *41*, 12330.

[154] Y. S. Kim, W. Chang, H. J. Jeong, K. H. Kim, H. S. Park, J. H. Shim, *Additive Manufacturing* **2023**, *71*, 103590.

[155] F. Liang, J. Yang, Y. Zhao, Y. Zhou, Z. Yan, J. He, Q. Yuan, J. Wu, P. Liu, Z. Zhong, M. Han, *International Journal of Hydrogen Energy* **2022**, *47*, 36926.

[156] M. Shen, F. Ai, H. Ma, H. Xu, Y. Zhang, *iScience* **2021**, *24*, 103464.

[157] M. Fallah Vostakola, H. Ozcan, R. S. El-Emam, B. Amini Horri, *Energies* **2023**, *16*, 3327.

[158] L. Lei, J. Zhang, Z. Yuan, J. Liu, M. Ni, F. Chen, *Adv Funct Materials* **2019**, *29*, 1903805.

[159] Z. Liang, J. Wang, K. Ren, Z. Jiao, M. Ni, L. An, Y. Wang, J. Yang, M. Li, *Nat Commun* **2024**, *15*, 4587.

[160] M. A. Yatoo, F. Habib, A. H. Malik, M. J. Qazi, S. Ahmad, M. A. Ganayee, Z. Ahmad, *MRS Communications* **2023**, *13*, 378.

[161] M. Choolaei, M. F. Vostakola, B. A. Horri, *Crystals* **2023**, *13*, 1008.

[162] M. G. Buonomenna, *Hydrogen* **2023**, *4*, 807.

[163] Z. Luo, X. Hu, Y. Zhou, Y. Ding, W. Zhang, T. Li, M. Liu, *Advanced Materials* **2024**, *36*, 2311159.

[164] F. Liu, D. Ding, C. Duan, *Advanced Science* **2023**, *10*, 2206478.

[165] K. Wei, Z. Guo, F. Chen, H. Liu, Y. Ling, *ACS Appl. Mater. Interfaces* **2023**, *15*, 49785.

[166] C. Kim, H. Lee, I. Jang, S. Kim, H. Jung, M. Ryu, J. Kim, D. Lee, H. Yoon, U. Paik, T. Song, *International Journal of Hydrogen Energy* **2022**, *47*, 5499.

[167] D. Kim, K. T. Bae, K. J. Kim, H.-N. Im, S. Jang, S. Oh, S. W. Lee, T. H. Shin, K. T. Lee, *ACS Energy Lett.* **2022**, *7*, 2393.

[168] W. Li, B. Guan, T. Yang, Z. Li, W. Shi, H. Tian, L. Ma, T. L. Kalapos, X. Liu, *Journal of Power Sources* **2021**, *495*, 229764.

[169] W. Tang, H. Ding, W. Bian, C. Y. Regalado Vera, J. Y. Gomez, Y. Dong, J. Li, W. Wu, W. Fan, M. Zhou, C. Gore, B. M. Blackburn, H. Luo, D. Ding, *Small* **2022**, *18*, 2201953.

[170] S. Zheng, W. Bian, H. Ding, *Mater. Adv.* **2024**, *5*, 2296.

[171] Y. Wang, Y. Ling, B. Wang, G. Zhai, G. Yang, Z. Shao, R. Xiao, T. Li, *Energy Environ. Sci.* **2023**, *16*, 5721.

[172] C. Yang, J. Li, C. Yang, Y. Li, A. Hu, J. Pu, B. Chi, *ACS Materials Lett.* **2024**, *6*, 3540.

[173] K. Hong, M. Choi, Y. Bae, J. Min, J. Lee, D. Kim, S. Bang, H.-K. Lee, W. Lee, J. Hong, *Nat Commun* **2023**, *14*, 7485.

[174] Z. Chen, F. Guo, Y. Zhang, *Materials* **2021**, *14*, 2576.

[175] W. Bauer, M. Müller, L. Schneider, M. Häringer, N. Bohn, J. R. Binder, J. Klemens, P. Scharfer, W. Schabel, H. Ehrenberg, *Nanomaterials* **2024**, *14*, 134.

[176] E. Kuhnert, L. Ladenstein, A. Jodlbauer, C. Slugovc, G. Trimmel, H. M. R. Wilkening, D. Rettenwander, *Cell Reports Physical Science* **2020**, *1*, 100214.

[177] L. Yang, S. Wang, K. Blinn, M. Liu, Z. Liu, Z. Cheng, M. Liu, *Science* **2009**, *326*, 126.

[178] T. Sangeetha, W.-M. Yan, P.-T. Chen, C.-J. Yang, K. D. Huang, *RSC Adv.* **2020**, *10*, 28807.

[179] M. Prioux, E. Da Rosa Silva, M. Hubert, J. Vulliet, J. Debayle, P. Cloetens, J. Laurencin, *Fuel Cells* **2023**, *23*, 408.

[180] C. Tang, Y. Yao, N. Wang, X. Zhang, F. Zheng, L. Du, D. Luo, Y. Aoki, S. Ye, *InfoMat* **2023**, e12515.

[181] T. Cui, Z. Lyu, M. Han, K. Sun, Y. Liu, M. Ni, *Energy Conversion and Management* **2022**, *262*, 115657.

[182] K. Chen, S.-S. Liu, N. Ai, M. Koyama, S. P. Jiang, *Phys. Chem. Chem. Phys.* **2015**, *17*, 31308.

[183] D. Clematis, S. Presto, M. P. Carpanese, A. Barbucci, F. Deganello, L. F. Liotta, C. Aliotta, M. Viviani, *Catalysts* **2019**, *9*, 441.

[184] N. Han, W. Zhang, W. Guo, H. Pan, B. Jiang, L. Xing, H. Tian, G. Wang, X. Zhang, J. Fransaer, *Nano-Micro Lett.* **2023**, *15*, 185.

[185] T. Yan, S. Lang, S. Wang, S. Lin, Q. Cai, J. Zhao, **2024**, DOI 10.2139/ssrn.4750989.

[186] Z. Li, Q. He, L. Xia, Q. Xu, C. Cheng, J. Wang, M. Ni, *International Journal of Hydrogen Energy* **2022**, *47*, 4047.

[187] D.-K. Lim, H.-N. Im, B. Singh, S.-J. Song, *J. Electrochem. Soc.* **2015**, *162*, F547.

[188] S. R. Samms, S. Wasmus, R. F. Savinell, *J. Electrochem. Soc.* **1996**, *143*, 1225.

[189] M. S. I. Sozal, W. Tang, S. Das, W. Li, A. Durygin, V. Drozd, C. Zhang, B. Jafarizadeh, C. Wang, A. Agarwal, D. Ding, Z. Cheng, *International Journal of Hydrogen Energy* **2022**, *47*, 21817.

[190] Y. Lu, M. A. K. Y. Shah, M. Khalid, N. Mushtaq, M. Yousaf, N. Akbar, *Ceramics International* **2024**, *50*, 49748.

[191] Y. Lu, M. A. K. Y. Shah, N. Mushtaq, M. Yousaf, N. Akbar, N. Arshad, S. Irshad, *Fuel* **2024**, *367*, 131558.

[192] Y. Zhou, E. Liu, Y. Chen, Y. Liu, L. Zhang, W. Zhang, Z. Luo, N. Kane, B. Zhao, L. Soule, Y. Niu, Y. Ding, H. Ding, D. Ding, M. Liu, *ACS Energy Lett.* **2021**, 1511.

[193] Y. Yi, R. Ran, W. Wang, W. Zhou, Z. Shao, *Current Opinion in Green and Sustainable Chemistry* **2022**, *38*, 100711.

[194] S. Zheng, W. Wu, Y. Zhang, Z. Zhao, C. Duan, S. Karki, H. Ding, *Nat Commun* **2025**, *16*, 4146.

[195] H. Liang, Y. Dong, Q. Ding, X. Li, M. Yu, P. Li, L. Duan, Y. Wang, *Carbon Trends* **2024**, *15*, 100350.

[196] Y. Chen, W. Zhou, D. Ding, M. Liu, F. Ciucci, M. Tade, Z. Shao, *Advanced Energy Materials* **2015**, *5*, 1500537.

[197] M. B. Hanif, S. Rauf, M. Motola, Z. U. D. Babar, C.-J. Li, C.-X. Li, *Materials Research Bulletin* **2022**, *146*, 111612.

[198] M. T. Curnan, J. R. Kitchin, *J. Phys. Chem. C* **2014**, *118*, 28776.

[199] H. Liu, S. Yang, G. Wang, H. Liu, Y. Peng, C. Sun, J. Li, J. Chen, *Environ. Sci. Technol.* **2022**, *56*, 16325.

[200] M. Huang, L. Song, N. Wang, Y. Fu, R. Ren, Z. Li, Y. Lu, J. Xu, Q. Liu, *Angew Chem Int Ed* **2024**, e202414893.

[201] X. Wang, Y. Tang, J.-M. Lee, G. Fu, *Chem Catalysis* **2022**, *2*, 967.

[202] M. Shetty, A. Walton, S. R. Gathmann, M. A. Ardagh, J. Gopeesingh, J. Resasco, T. Birol, Q. Zhang, M. Tsapatsis, D. G. Vlachos, P. Christopher, C. D. Frisbie, O. A. Abdelrahman, P. J. Dauenhauer, *ACS Catal.* **2020**, *10*, 12666.

[203] P. Guo, W. Chen, Y. Zhou, F. Xie, G. Qian, P. Jiang, D. He, X. Lu, *Small* **2022**, *18*, 2205158.

[204] A. J. Medford, A. Vojvodic, J. S. Hummelshøj, J. Voss, F. Abild-Pedersen, F. Studt, T. Bligaard, A. Nilsson, J. K. Nørskov, *Journal of Catalysis* **2015**, *328*, 36.

[205] J. K. Nørskov, F. Studt, F. Abild-Pedersen, T. Bligaard, *Fundamental Concepts in Heterogeneous Catalysis*, Wiley, **2014**.

[206] S. Jiao, X. Fu, H. Huang, *Adv Funct Materials* **2022**, *32*, 2107651.

[207] S. Sun, X. Zhou, B. Cong, W. Hong, G. Chen, *ACS Catal.* **2020**, *10*, 9086.

[208] T. Hu, F. He, M. Liu, Y. Chen, *Progress in Materials Science* **2023**, *133*, 101050.

[209] M. Alaydrus, M. Sakaue, N. H. Linh, S. M. Aspera, T. D. K. Wungu, H. Kasai, *ECS Trans.* **2015**, *68*, 369.

[210] B. M. Reddy, G. Thrimurthulu, L. Katta, Y. Yamada, S.-E. Park, *J. Phys. Chem. C* **2009**, *113*, 15882.

[211] M. Alaydrus, M. Sakaue, H. Kasai, *Phys. Chem. Chem. Phys.* **2016**, *18*, 12938.

[212] B. Wegner, L. Grubert, C. Dennis, A. Opitz, A. Röttger, Y. Zhang, S. Barlow, S. R. Marder, S. Hecht, K. Müllen, N. Koch, *J. Mater. Chem. C* **2019**, *7*, 13839.

[213] K. H. Tan, Y.-W. Chen, C. N. Van, H. Wang, J.-W. Chen, F. S. Lim, K.-H. Chew, Q. Zhan, C.-L. Wu, S.-P. Chai, Y.-H. Chu, W. S. Chang, *ACS Appl. Mater. Interfaces* **2019**, *11*, 1655.

[214] C. Wang, D. Niu, B. Liu, S. Wang, X. Wei, Y. Liu, H. Xie, Y. Gao, *J. Phys. Chem. C* **2017**, *121*, 18084.

[215] S. Singh, N. Khare, *Nano Energy* **2017**, *38*, 335.

[216] X. Gao, L. Li, Y. Liu, C. Zheng, W. Liu, M. Li, X. Wu, S. Liu, *ACS Catal.* **2024**, *14*, 2924.

[217] M. H. Zoellner, G. Niu, J.-H. Jhang, A. Schaefer, P. Zaumseil, M. Bäumer, T. Schroeder, *J. Phys. Chem. C* **2013**, *117*, 24851.

[218] V. Frizon, J.-M. Bassat, M. Pollet, E. Durand, J. Hernandez, K. Pajot, P. Vernoux, A. Demourgues, *J. Phys. Chem. C* **2019**, *123*, 6351.

[219] H. He, H. X. Dai, C. T. Au, *Catalysis Today* **2004**, *90*, 245.

[220] K. Ahanjan, M. Shamsipur, N. Hassani, M. Neek-Amal, A. Pashabadi, *J. Phys. Chem. C* **2023**, *127*, 24508.

[221] G. Accardo, G. Dell'Agli, L. Spiridigliozzi, S. P. Yoon, D. Frattini, *International Journal of Hydrogen Energy* **2020**, *45*, 19707.

[222] V. Thangadurai, R. A. Huggins, W. Weppner, *J Solid State Electrochem* **2001**, *5*, 531.

[223] B. M. Abu-Zied, Y. A. Mohamed, A. M. Asiri, *Journal of Rare Earths* **2013**, *31*, 701.

[224] S. Karki, S. Zheng, I. T. Bello, A. Le, H. Ding, *J. Mater. Chem. A* **2025**, 10.1039.D4TA08716J.

[225] A. Javed, D. Sikstrom, Y. Furuya, N. Dale, A. M. Hussain, V. Thangadurai, *ACS Appl. Mater. Interfaces* **2025**, *17*, 9305.

[226] S. Patel, S. Goswami, P. Paul, F. Liu, S. Zheng, J. E. Sabisch, C. Duan, T. Venkatesan, H. Paik, H. Ding, P. Kazempoor, S. Xu, D. Ding, I. Ghamarian, *J Am Ceram Soc.* **2025**, *108*, e20371.

[227] F. G. El Desouky, M. M. Saadeldin, I. K. El Zawawi, *Journal of Luminescence* **2022**, *241*, 118450.

[228] S. Choi, T. C. Davenport, S. M. Haile, *Energy Environ. Sci.* **2019**, *12*, 206.

[229] F. He, M. Liang, W. Wang, R. Ran, G. Yang, W. Zhou, Z. Shao, *Energy Fuels* **2020**, *34*, 11464.

[230] H. Tong, M. Fu, Y. Yang, F. Chen, Z. Tao, *Adv Funct Materials* **2022**, *32*, 2209695.

[231] Z. Liu, D. Cheng, Y. Zhu, M. Liang, M. Yang, G. Yang, R. Ran, W. Wang, W. Zhou, Z. Shao, *Chemical Engineering Journal* **2022**, *450*, 137787.

[232] D. Wang, Y. Xia, H. Lv, L. Miao, L. Bi, W. Liu, *International Journal of Hydrogen Energy* **2020**, *45*, 31017.

[233] Z. Liu, Y. Chen, G. Yang, M. Yang, R. Ji, Y. Song, R. Ran, W. Zhou, Z. Shao, *Applied Catalysis B: Environmental* **2022**, *319*, 121929.

[234] M. Liang, Y. Song, D. Liu, L. Xu, M. Xu, G. Yang, W. Wang, W. Zhou, R. Ran, Z. Shao, *Applied Catalysis B: Environmental* **2022**, *318*, 121868.

[235] Y. Shin, Y. Kim, M. Sanders, S. P. Harvey, M. Walker, R. O'Hayre, *J. Mater. Chem. A* **2022**, *10*, 24839.

[236] C. Graves, S. D. Ebbesen, S. H. Jensen, S. B. Simonsen, M. B. Mogensen, *Nature Mater* **2015**, *14*, 239.

[237] C. He, C. Xia, F. Li, J. Zhang, W. Guo, B. Y. Xia, *Advanced Energy Materials* **2024**, *14*, 2303233.

[238] L. Gao, X. Cui, C. D. Sewell, J. Li, Z. Lin, *Chem. Soc. Rev.* **2021**, *50*, 8428.

[239] H. Zhong, Q. Zhang, J. Yu, X. Zhang, C. Wu, Y. Ma, H. An, H. Wang, J. Zhang, X. Wang, J. Xue, *Advanced Energy Materials* **2023**, *13*, 2301391.

[240] X. Tang, Y. Zhang, S. Tang, D. Lützenkirchen-Hecht, K. Yuan, Y. Chen, *ACS Catal.* **2024**, *14*, 13065.

[241] G. Kresse, J. Hafner, *Phys. Rev. B* **1993**, *47*, 558.

[242] G. Kresse, J. Furthmüller, *Computational Materials Science* **1996**, *6*, 15.

[243] G. Kresse, J. Furthmüller, *Phys. Rev. B* **1996**, *54*, 11169.

[244] J. P. Perdew, K. Burke, M. Ernzerhof, *Phys. Rev. Lett.* **1996**, *77*, 3865.

[245] G. Kresse, D. Joubert, *Phys. Rev. B* **1999**, *59*, 1758.

[246] S. L. Dudarev, G. A. Botton, S. Y. Savrasov, C. J. Humphreys, A. P. Sutton, *Phys. Rev. B* **1998**, *57*, 1505.

[247] B. Milberg, A. Juan, B. Irigoyen, *Applied Surface Science* **2017**, *401*, 206.

[248] H. J. Monkhorst, J. D. Pack, *Phys. Rev. B* **1976**, *13*, 5188.

[249] S. Grimme, J. Antony, S. Ehrlich, H. Krieg, *The Journal of Chemical Physics* **2010**, *132*, 154104.

[250] G. Makov, M. C. Payne, *Phys. Rev. B* **1995**, *51*, 4014.

[251] J. Neugebauer, M. Scheffler, *Phys. Rev. B* **1992**, *46*, 16067.

[252] N. Shan, M. Zhou, M. K. Hanchett, J. Chen, B. Liu, *Molecular Simulation* **2017**, *43*, 861.

[253] W. Li, B. Guan, L. Ma, S. Hu, N. Zhang, X. Liu, *J. Mater. Chem. A* **2018**, *6*, 18057.

[254] S. Karki, I. T. Bello, Y. Ding, J. Ruan, A. Kumari, S. Zheng, Y. Geng, H. Ding, *Materials Today* **2025**, S136970212500433X.

[255] A. Kumari, S. Zheng, S. Karki, I. T. Bello, J. Ruan, Y. Geng, H. Ding, *ACS Appl. Mater. Interfaces* **2025**, acsami.5c16287.

[256] H. Zheng, M. Riegraf, N. Sata, R. Costa, *J. Mater. Chem. A* **2023**, *11*, 10955.

[257] H. Tian, W. Li, L. Ma, T. Yang, B. Guan, W. Shi, T. L. Kalapos, X. Liu, *ACS Appl. Mater. Interfaces* **2020**, *12*, 49574.

[258] W. Li, B. Guan, L. Ma, H. Tian, X. Liu, *ACS Appl. Mater. Interfaces* **2019**, *11*, 18323.

[259] Y. Zhang, Z. Liu, J. Li, K. Lin, D. Guan, Y. Song, G. Yang, W. Zhou, J. Ge, M. Shao, B. Chen, M. Ni, Z. Shao, H. Xie, *Nat Commun* **2025**, *16*, 8715.

[260] S. Zheng, B. Liu, G. Kim, I. Ghamarian, S. Patel, H. Ding, *Advanced Materials* **2025**, 2503649.

[261] N. Hildenbrand, B. A. Boukamp, P. Nammensma, D. H. A. Blank, *Solid State Ionics* **2011**, *192*, 12.

[262] J. C. De Vero, K. Develos-Bagarinao, H. Kishimoto, T. Ishiyama, K. Yamaji, T. Horita, H. Yokokawa, *Journal of Power Sources* **2018**, *377*, 128.

[263] M. Stange, A. M. Dayaghi, C. Denonville, Y. Larring, P. M. Rørvik, R. Haugsrud, T. Norby, *ECS Trans.* **2019**, *91*, 941.

[264] F. Hesse, I. Da Silva, J.-W. G. Bos, *JACS Au* **2024**, *4*, 1538.

[265] F. Hesse, I. Da Silva, J.-W. G. Bos, *Chem. Mater.* **2022**, *34*, 1191.

[266] G. Kim, S. Wang, A. J. Jacobson, L. Reimus, P. Brodersen, C. A. Mims, *J. Mater. Chem.* **2007**, *17*, 2500.

[267] J.-H. Kim, A. Manthiram, *J. Mater. Chem. A* **2015**, *3*, 24195.

[268] M. Bahout, S. S. Pramana, J. M. Hanlon, V. Dorcet, R. I. Smith, S. Paofai, S. J. Skinner, *J. Mater. Chem. A* **2015**, *3*, 15420.

[269] I. T. Bello, S. Karki, S. Zheng, J. Ruan, A. Kumari, Y. Geng, S. Patel, Z. Li, P. Kazempoor, W. Bian, Y. Ling, I. Ghamarian, Y. Liu, B. Wang, Z. Shao, M. Ni, H. Ding, *Energy Reviews* **2025**, *4*, 100165.

[270] D. Han, K. Toyoura, T. Uda, *ACS Appl. Energy Mater.* **2021**, *4*, 1666.

[271] Z. Yang, J. Hao, *J. Mater. Chem. C* **2016**, *4*, 8859.

[272] M. P. Wells, A. J. Lovett, Y. Zhang, Z. Shang, K. Kreka, B. Bakhit, H. Wang, A. Tarancón, J. L. MacManus-Driscoll, *Nano Energy* **2024**, *119*, 109049.

[273] D. Hashimoto, D. Han, T. Uda, *Solid State Ionics* **2014**, *262*, 687.

[274] H. Ding, Y. Xie, X. Xue, *Journal of Power Sources* **2011**, *196*, 2602.

[275] H. Sumi, K. Watanabe, A. Sharma, M. Fujioka, H. Shimada, Y. Mizutani, M. S. Alam, I. Kagomiya, *Commun Chem* **2025**, *8*, 71.

[276] Y. A. Mastrikov, R. Merkle, E. A. Kotomin, M. M. Kuklja, J. Maier, *J. Mater. Chem. A* **2018**, *6*, 11929.

[277] A. Whitten, D. Guo, E. Tezel, R. Denecke, E. Nikolla, J.-S. McEwen, *JACS Au* **2024**, *4*, 3104.

[278] A. Nenning, A. K. Opitz, C. Rameshan, R. Rameshan, R. Blume, M. Hävecker, A. Knop-Gericke, G. Rupprechter, B. Klötzer, J. Fleig, *J. Phys. Chem. C* **2016**, *120*, 1461.

[279] Y. Cao, M. J. Gadre, A. T. Ngo, S. B. Adler, D. D. Morgan, *Nat Commun* **2019**, *10*, 1346.

[280] M. Morales, A. Pesce, A. Slodczyk, M. Torrell, P. Piccardo, D. Montinaro, A. Tarancón, A. Morata, *ACS Appl. Energy Mater.* **2018**, *1*, 1955.

[281] L. Bernadet, F. Buzi, F. Baiutti, J. Segura-Ruiz, J. Dolado, D. Montinaro, M. Torrell, A. Morata, A. Tarancón, *APL Energy* **2023**, *1*, 036101.

[282] E. Navickas, T. M. Huber, Y. Chen, W. Hetaba, G. Holzlechner, G. Rupp, M. Stöger-Pollach, G. Friedbacher, H. Hutter, B. Yildiz, J. Fleig, *Phys. Chem. Chem. Phys.* **2015**, *17*, 7659.

[283] M. Tang, Y. Niu, W. Muhammad, S. Muhammad, Z. Zhong, S. Muhammad, Y. Pang, Z. Wan, N. Chen, L. Qiao, W. Lv, *International Journal of Hydrogen Energy* **2024**, *50*, 618.

[284] N. Hildenbrand, Improving the Electrolyte-Cathode Assembly for Mt-SOFC, University of Twente, **2011**.

[285] A. Chrzan, J. Karczewski, M. Gazda, D. Szymczewska, P. Jasinski, *J Solid State Electrochem* **2015**, *19*, 1807.

[286] F. Baiutti, F. Chiabrera, D. Diercks, A. Cavallaro, L. Yedra, L. López-Conesa, S. Estradé, F. Peiró, A. Morata, A. Aguadero, A. Tarancón, *Advanced Materials* **2021**, *33*, 2105622.

[287] K. Develos-Bagarinao, T. Ishiyama, H. Kishimoto, H. Shimada, K. Yamaji, *Nat Commun* **2021**, *12*, 3979.

[288] T. Onishi, D. Han, Y. Noda, N. Hatada, M. Majima, T. Uda, *Solid State Ionics* **2018**, *317*, 127.

[289] B. He, D. Ding, Y. Ling, L. Zhao, J. Cheng, *International Journal of Hydrogen Energy* **2014**, *39*, 19087.

[290] J. Qian, W. Sun, Q. Zhang, G. Jiang, W. Liu, *Journal of Power Sources* **2014**, *249*, 131.

[291] L. Bi, S. P. Shafi, E. H. Da'as, E. Traversa, *Small* **2018**, *14*, 1801231.

[292] L. Bi, E. Fabbri, Z. Sun, E. Traversa, *Energy Environ. Sci.* **2011**, *4*, 1352.

[293] L. Bi, E. Fabbri, Z. Sun, E. Traversa, *Energy Environ. Sci.* **2011**, *4*, 409.

[294] Z. Sun, E. Fabbri, L. Bi, E. Traversa, *Phys. Chem. Chem. Phys.* **2011**, *13*, 7692.

[295] K. Xu, Y. Xu, F. Zhu, Z. Du, X. Zhang, Z. Cheng, Y. Chen, *Energy Environ. Sci.* **2025**, *18*, 6722.

[296] Z. Li, X. Mao, D. Feng, M. Li, X. Xu, Y. Luo, L. Zhuang, R. Lin, T. Zhu, F. Liang, Z. Huang, D. Liu, Z. Yan, A. Du, Z. Shao, Z. Zhu, *Nat Commun* **2024**, *15*, 9318.

[297] J. R. Petrie, V. R. Cooper, J. W. Freeland, T. L. Meyer, Z. Zhang, D. A. Lutterman, H. N. Lee, *J. Am. Chem. Soc.* **2016**, *138*, 2488.

[298] A. E. Pérez Mendoza, A. Schmidt, A. J. G. Zarbin, H. Winnischofer, *ACS Appl. Nano Mater.* **2024**, *7*, 23295.

[299] R. Jacobs, J. Liu, H. Abernathy, D. Morgan, *ACS Appl. Energy Mater.* **2024**, *7*, 3366.

[300] J.-W. Zhao, Y. Li, D. Luan, X. W. (David) Lou, *Sci. Adv.* **2024**, *10*, eadq4696.

[301] S. R. Bishop, T. S. Stefanik, H. L. Tuller, *Phys. Chem. Chem. Phys.* **2011**, *13*, 10165.

[302] C. Chatzichristodoulou, P. V. Hendriksen, *J. Electrochem. Soc.* **2010**, *157*, B481.

[303] D. A. Osinkin, S. M. Beresnev, N. M. Bogdanovich, *Journal of Power Sources* **2018**, *392*, 41.

[304] K. Pei, S. Luo, F. He, J. Arbiol, Y. Xu, F. Zhu, Y. Wang, Y. Chen, *Applied Catalysis B: Environmental* **2023**, *330*, 122601.

[305] Y. Zhao, H. Su, J. Xu, S. Chen, P. Liu, E.-J. Guo, Y. Lin, H. L. Tuller, D. Chen, *J Electroceram* **2023**, *51*, 28.

[306] Y.-Q. Lei, Q. Xu, D.-P. Huang, M. Chen, K. Zhao, D.-C. Chen, F. Zhang, *Solid State Ionics* **2025**, *420*, 116769.

[307] K. Kang, X. Liu, C. Wang, L. Yang, Y. Liu, *Small* **2025**, *21*, 2502478.

[308] L. Yefsah, J. Laurencin, M. Hubert, D. F. Sanchez, F. Charlot, K. Couturier, O. Celikbilek, E. Djurado, *Solid State Ionics* **2023**, *399*, 116316.

[309] R. K. Sharma, N. I. Khamidy, L. Rapenne, F. Charlot, H. Moussaoui, J. Laurencin, E. Djurado, *Journal of Power Sources* **2019**, *419*, 171.

[310] Q. Song, S. Zhou, S. Wang, S. Li, L. Xu, J. Qiu, *Chemical Engineering Journal* **2023**, *461*, 142033.

[311] Y. Kumagai, N. Tsunoda, A. Takahashi, F. Oba, *Phys. Rev. Materials* **2021**, *5*, 123803.

[312] M. V. Ganduglia-Pirovano, A. Hofmann, J. Sauer, *Surface Science Reports* **2007**, *62*, 219.

[313] M. Li, J. Li, L.-Q. Chen, B.-L. Gu, W. Duan, *Phys. Rev. B* **2015**, *92*, 115435.

[314] A. X. B. Yong, L. O. Anderson, N. H. Perry, E. Ertekin, *J. Mater. Chem. A* **2023**, *11*, 4045.

[315] S. Roh, S. Lee, M. Lee, Y.-S. Seo, A. Khare, T. Yoo, S. Woo, W. S. Choi, J. Hwang, A. Glamazda, K.-Y. Choi, *Phys. Rev. B* **2018**, *97*, 075104.

[316] H. Huang, J. Zhang, H. Zhang, F. Han, X. Chen, J. Song, J. Zhang, S. Qi, Y. Chen, J. Cai, F. Hu, B. Shen, J. Sun, *J. Phys. D: Appl. Phys.* **2020**, *53*, 155003.

[317] D. Lee, X. Gao, L. Sun, Y. Jee, J. Poplawsky, T. O. Farmer, L. Fan, E.-J. Guo, Q. Lu, W. T. Heller, Y. Choi, D. Haskel, M. R. Fitzsimmons, M. F. Chisholm, K. Huang, B. Yildiz, H. N. Lee, *Nat Commun* **2020**, *11*, 1371.

[318] D. M. Cornet, R. R. LaPierre, D. Comedi, Y. A. Pusep, *Journal of Applied Physics* **2006**, *100*, 043518.

[319] G. Krizman, B. A. Assaf, T. Phuphachong, G. Bauer, G. Springholz, G. Bastard, R. Ferreira, L. A. De Vaulchier, Y. Guldner, *Phys. Rev. B* **2018**, *98*, 075303.

[320] J. Young, J. M. Rondinelli, *Phys. Rev. B* **2015**, *92*, 174111.

[321] H. Han, A. Sharma, H. L. Meyerheim, J. Yoon, H. Deniz, K.-R. Jeon, A. K. Sharma, K. Mohseni, C. Guillemard, M. Valvidares, P. Gargiani, S. S. P. Parkin, *ACS Nano* **2022**, *16*, 6206.

[322] H.-Y. Li, J. Shin, Y. Wu, P.-C. Su, *Nano Lett.* **2024**, *24*, 15210.

[323] Y. Chen, Y. Chen, D. Ding, Y. Ding, Y. Choi, L. Zhang, S. Yoo, D. Chen, B. deGlee, H. Xu, Q. Lu, B. Zhao, G. Vardar, J. Wang, H. Bluhm, E. J. Crumlin, C. Yang, J. Liu, B. Yildiz, M. Liu, *Energy Environ. Sci.* **2017**, *10*, 964.

[324] D. Marrocchelli, N. H. Perry, S. R. Bishop, *Phys. Chem. Chem. Phys.* **2015**, *17*, 10028.

[325] C. De Leeuwe, W. Hu, D. Neagu, E. I. Papaioannou, S. Pramana, B. Ray, J. S. O. Evans, I. S. Metcalfe, *Journal of Solid State Chemistry* **2021**, *293*, 121838.

[326] H. Kwon, W. Lee, J. W. Han, *RSC Adv.* **2016**, *6*, 69782.

[327] H. Ding, A. V. Virkar, M. Liu, F. Liu, *Phys. Chem. Chem. Phys.* **2013**, *15*, 489.

[328] F. He, Y. Zhou, T. Hu, Y. Xu, M. Hou, F. Zhu, D. Liu, H. Zhang, K. Xu, M. Liu, Y. Chen, *Advanced Materials* **2023**, *35*, 2209469.

[329] Y. Huang, F. He, K. Xu, H. Gao, X. Zhang, Y. Xu, Z. Du, F. Zhu, W. Gong, C. Jian, Y. Chen, *Adv Funct Materials* **2024**, 2409598.

[330] W. Zhang, Y. Zhou, X. Hu, Y. Ding, J. Gao, Z. Luo, T. Li, N. Kane, X.-Y. Yu, T. Terlier, M. Liu, *ACS Energy Lett.* **2023**, *8*, 3999.

[331] Z. Du, K. Xu, F. Zhu, Y. Xu, F. He, H. Gao, W. Gong, Y. Choi, Y. Chen, *Adv Funct Materials* **2024**, *34*, 2409188.

[332] F. He, M. Hou, D. Liu, Y. Ding, K. Sasaki, Y. Choi, S. Guo, D. Han, Y. Liu, M. Liu, Y. Chen, *Energy Environ. Sci.* **2024**, *17*, 3898.

[333] J. Xia, M. Zhou, H. Gao, F. He, Z. Du, Y. Chen, *Adv Funct Materials* **2024**, *34*, 2403493.

[334] S. Oh, D. Kim, H. J. Ryu, K. T. Lee, *Adv Funct Materials* **2024**, *34*, 2311426.

[335] K. T. Bae, I. Jeong, D. Kim, H. Yu, H.-N. Im, A. Akromjon, C.-W. Lee, K. T. Lee, *Chemical Engineering Journal* **2023**, *461*, 142051.

[336] J. Cui, Y. Zhang, Z. Hu, C. Kuo, C. Chang, Y. Ku, Z. Liu, Z. Xia, J. Zhu, J. Zhang, Y. He, J. Ma, A. Li, X. Lin, C. Chen, G. Kim, J. Wang, L. Zhang, *Small Methods* **2024**, *8*, 2400178.

[337] Z. Guan, D. Chen, W. C. Chueh, *Phys. Chem. Chem. Phys.* **2017**, *19*, 23414.

[338] H. Chen, Z. Guo, L. A. Zhang, Y. Li, F. Li, Y. Zhang, Y. Chen, X. Wang, B. Yu, J. Shi, J. Liu, C. Yang, S. Cheng, Y. Chen, M. Liu, *ACS Appl. Mater. Interfaces* **2018**, *10*, 39785.

[339] J. Shi, H. Li, A. Genest, W. Zhao, P. Qi, T. Wang, G. Rupprechter, *Applied Catalysis B: Environmental* **2022**, *301*, 120789.

[340] R.-A. Eichel, *Phys. Chem. Chem. Phys.* **2011**, *13*, 368.

[341] S. K. Pandey, A. Kumar, S. M. Chaudhari, A. V. Pimpale, *J. Phys.: Condens. Matter* **2006**, *18*, 1313.

[342] S. K. Pandey, A. Kumar, S. Banik, A. K. Shukla, S. R. Barman, A. V. Pimpale, *Phys. Rev. B* **2008**, *77*, 113104.